PHD

Hot gas ingress through turbine rim seals
Heat transfer and fluid dynamics

Cho, Geonhwan

Award date:
2015

Awarding institution:
University of Bath

Hot gas ingress through turbine rim seals: heat transfer and fluid dynamics

GeonHwan Cho

A thesis submitted for the degree of Doctor of Philosophy

University of Bath

Department of Mechanical Engineering

September 2014

Abstract

This thesis experimentally investigates the phenomenon of ingress through gas turbine rim seals. The work focuses on developing experimental and numerical techniques for measuring the required sealing flow levels to purge the wheel-space against ingress and the effect of externally-induced ingress on the surface temperature as well as heat transfer to the rotor. Ingress is driven by a pressure difference between the mainstream annulus and wheel-space cavity resulting from the asymmetric external pressure profile in the annulus and/or the rotation of fluid in the rotor-stator wheel-space cavity. It can be prevented by pressurising the wheel-space through the supply of sealant flow.

The University of Bath had measured and shown, for the first time, the thermal effects of ingress on the rotor in the wheel-space for a datum seal (axial-clearance seal) using thermo-chromic liquid crystal. However, as the previously used experimental technique with thermo-chromic liquid crystal was prone to large uncertainties, a non-intrusive temperature measurement technique using an infrared (IR) temperature sensor was developed. The new technique was successfully applied to the Bath one-stage gas turbine test facility and provided a full temperature history of the rotor surface in a transient heat transfer experiment. Moreover, a data analysis method appropriate for transient experiments using the IR temperature measurement technique was developed. The method was used to accurately calculate the heat transfer coefficient and the adiabatic surface temperature based on the full temperature history. A series of numerical experiments was carried out to develop the analysis method and the results from the numerical experiments were used to design new heat transfer experiments for both the 1 and 1.5-stage ingestion rigs of the University of Bath.

Gas concentration measurements were made on the stator of the Bath one-stage gas turbine test rig to determine the variation of sealing effectiveness with sealant flow rate for four different seal geometries at design operational conditions. The IR

temperature measurement technique was used to determine the effect of ingress on the heat transfer coefficient and the adiabatic wall temperature on the rotor of the ingestion test facility. Concurrent gas concentration measurements were made on the stator to compare the effects of ingress on the two discs (stator and rotor). Comparison between the adiabatic effectiveness on the rotor and the concentration effectiveness on the stator showed that the rotor was protected against the effects of ingress relative to the stator. The sealing air, which was drawn into the rotor boundary layer from the source region, thermally buffered the rotor against the ingested fluid in the core. Subsequently, a thermal buffer ratio hypothesis was developed and shown to be in good agreement with the experimental data.

A previously published orifice model was modified so that the sealing effectiveness determined from the concentration measurements in a rig could be used to determine the effectiveness based on pressure measurements in an engine. There was good agreement between the effectiveness acquired from pressure measurement determined using the theoretical model and the sealing effectiveness determined from concentration measurements. It was also shown how parameters obtained from measurements of pressure and concentration in a rig could be used to calculate the sealing effectiveness in an engine.

Acknowledgements

Firstly, I would like to express my deep and sincere gratitude to my supervisors, Professor Gary D. Lock and Dr. Mike Wilson, for their continuous guidance, inspiration and encouragement. They have been incredibly supportive throughout this research project and this thesis would never been completed without their valuable input.

I also would like to thank Professor J. M. Owen for the invaluable guidance he has provided over the course of this research. His kind nature, deep understanding of the subject and enthusiasm towards ingress research will be remembered for the rest of my career. It is a matter of pride and privilege for me to have had the opportunity to work with him.

I take this opportunity to appreciate Dr. Carl Sangan who has always provided me with excellent insightful advice.

Technicians Steve Thomas, Guy Brace, Ian Trussler and instrumentation specialists Vijay Rajput, Stephen Coombes and John Bishop need special recognition for their kind help.

I also would also like to thank my colleagues in the gas turbine research unit, Oliver Pountney, James Scobie, Izzi Mear-Stone, Yogi Lalwani, Xiaohan Wang, Helmey Ramdhaney Mohd Saiah, Mario Patinios and Hui Tang, for providing their help when needed and making the work enjoyable.

Lastly, from the core of my heart, I would like to thank my wife and parents for their endless support and encouragement. A mere thank you is not sufficient for their unconditional love.

Contents

List of figures

List of tables

Nomenclature

Symbols

A	empirical constant
B	empirical constant
b	radius of seal
Bi	Biot number [= hL/k]
Bi_b	Biot number of back-surface
$\overline{Bi}$	corrected Biot number [= $\bar{h}L/k$]
c	concentration; empirical constant;
C	resultant velocity at exit from vanes
	empirical constant
$C_{d,e}$ $C_{d,i}$	discharge coefficients for egress and ingress
C_F	flow coefficient [$=Re_w/Re_\phi$]
c	velocity of electromagnetic radiation (2.998×10^8 m/s)
c_p	specific heat
$c_{p,air}$	specific heat of air
C_p	pressure coefficient [= $(p_a - \bar{p}_a)/(1/2\rho\Omega^2 b^2)$]
$C_{p,max}$	pressure coefficient [= $\Delta p/(1/2\rho W^2)$]
C_w	non-dimensional flow rate [= $\dot{m}/\mu b$]
$C_{w,e}$, $C_{w,i}$	values of C_w for egress and ingress
$C_{w,0}$	non-dimensional sealing flow rate
$C_{w,min}$	minimum value of $C_{w,0}$ to prevent ingress
D	empirical constant
e	relative error in Bi
E	emissive power for a grey body
$E_{\lambda,b}$	emissive power for a black body
$E_{\lambda,b}$	spectral emissive power
Fo	Fourier number [= $\alpha t/L^2$]
G	gap ratio [= S/b]
	parameter used for the Crank-Nicolson method ($G=2Bi\Delta X$)

g	normalised pressure difference across seal clearance [$= (p_2 - p_{2,min}) / \Delta p$]
g^*	value of g when $C_{w,0}$=0
$\hat{g}$	value of g to ensure ε_p=ε_c
G_c	seal-clearance ratio [$= s_c / b$]
h	heat transfer coefficient
	Planck's constant (6.6256×10^{-34}Js)
h'	corrected heat transfer coefficient
h_b	back-surface heat transfer coefficient
h_{buffer}	height of wheel-space
h_s	front-surface heat transfer coefficient
i	i^{th} value of I points
$I_{\lambda,b}$	intensity of the black body radiation for a given wavelength, λ
k	thermal conductivity of solid ; Boltzmann constant (1.3806×10^{-23}J/K).
k_{air}	thermal conductivity of air
K	empirical constant for seal ranking and in thermal buffer hypothesis
L	thickness of solid
M	Mach number
m	empirical constant
$\dot{m}$	mass flow rate
n	power in power-law relationship
	number of temperature data
	n^{th} value of N points
Nu	Nusselt number
Nu_r	local Nusselt number [$= hr/k_{air}$]
p	static pressure
$\bar{p}$	mean pressure
P_{max}	non-dimensional pressure parameter [$= 1/2\ C_{p,max}\ Re_W^2$]
Pr	Prandtl number of air [$= \mu/\rho\alpha$]
$Q_{ND,R}$	non-dimensional heat loss through rotor
q_s	heat flux at surface
q_{ss}	steady state heat flux
r	radius, parameter used for the Crank-Nicolson method ($= \Delta Fo/\Delta X^2$)

r_{inner}	inner radius of annulus
r_{outer}	outer radius of annulus
R	thermocouple recovery factor
Re_W	axial Reynolds number in annulus [$= \rho Wb/\mu$]
Re_ϕ	rotational Reynolds number [$= \rho \Omega b^2/\mu$]
Re_r	local rotational Reynolds number [$= \rho \Omega r^2/\mu$]
S	axial clearance between rotor and stator
s_c	seal clearance
t	time
T	temperature
T_a	temperature of air in annulus
T_{ad}	adiabatic disc temperature
T_{ad}'	corrected adiabatic disc temperature
T_{ad}*	adiabatic disc temperature for $\Phi_0 = \Phi_{min}$
T_{core}	core temperature in the wheel-space
T_{in}	initial temperature of system
T_{int}	temperature of the interface between the materials
T_{IR}	temperature measured by an infrared sensor
T_s	surface temperature
T_{ss}	steady state front surface temperature
T_{true}	true temperature measured by the embedded thermocouple for calibration
U	bulk-mean velocity of sealing air through rim seal [$= \dot{m}_0 / 2\pi\rho bs_c$]
u_e	external axial velocity
u_m	average radial velocity through seal
u_r	radial velocity over a rotating disc
u_z	axial velocity over a rotating disc
u_ϕ	tangential velocity ($u_\phi = \Omega r$)
V	velocity relative to blades
	freestream velocity
W	axial velocity in annulus
$\overline{W}$	uniform value of the axial component of velocity in the external-flow
x	non-dimenasional axial distance in annulus ($=2z/S_c$)
	non-dimensional radius (for thermal buffer ratio)($=r/b$)

	distance from front-face of solid
X	non-dimensional normal co-ordinate [= x/L]; function of G
z	axial co-ordinate in wheelspace
α	vane exit angle; thermal diffusivity [= $k / \rho c_p$]
β	blade angle; swirl ratio in wheel-space [= $v_\phi / \Omega r$]
β_n	eigenvalue in quenching solution
β_0	blade angle for the design case
Γ_c	ratio of discharge coefficients [= $C_{d,i} / C_{d,e}$]
δ	boundary layer thickness
δA_i	elemental area in orifice ring for ingress
δA_e	elemental area in orifice ring for egress
δA_c	elemental area in rim seal
δt	time increment of digital camera
ΔC_p	non-dimensional pressure difference [= $\Delta p / (1/2 \rho \Omega^2 b^2)$]
Δt	active period of liquid crystal colour change
ΔT	bandwidth of liquid crystal
ε	sealing effectiveness [= $C_{w,0} / C_{w,e}$ = Φ_0 / Φ_e]
	emissivity
ε_{ad}	adiabatic effectiveness for rotor [= $(T_{ad} - T_a)/(T_{ad}^* - T_a)$]
ε_c	concentration effectiveness [= $(c_s - c_a) / (c_0 - c_a)$]
ε_o'	thermal buffer ratio (thermal buffer ratio model)
ε_p	pressure effectiveness
$\hat{\varepsilon}_p$	value of ε_p equal to ε_c
$\zeta(x)$	similarity parameter
η	thermal buffer ratio [= $\Phi_{min,c} / \Phi_{min,ad}$]
	normalised axial distance in a boundary layer
θ	normalized angle between vanes
θ_{core}	non-dimensional core temperature in the wheel-space
θ_∞	non-dimensional air temperature [= $(T_{core} - T_{in})/(T_0 - T_{in})$]
Θ	non-dimensional temperature [= $(T - T_{in})/(T_{ad} - T_{in})$]
Θ_{ss}	non-dimensional steady state temperature
λ	wave length
λ_T	turbulent flow parameter [= $C_w / Re_\phi^{0.8}$]

$\lambda_{T,min}$	value of λ_T when $C_w = C_{w,min}$
μ	dynamic viscosity of air
ρ	density
Φ	sealing flow parameter [= C_w / $2\pi G_c\, Re_\phi$]
Φ_e	value of Φ when $C_w = C_{w,e}$
Φ_i	value of Φ when $C_w = C_{w,i}$
Φ_{min}	value of Φ_0 when $C_{w,0} = C_{w,min}$
Φ_0	value of Φ when $C_w = C_{w,0}$
Φ_h, Φ_{Tad}	amplification parameters for h and T_{ad}
χ	parameter in semi-infinite solution [= $BiFo^{1/2}$]
$\chi(x)$	similarity parameter
Ω	angular velocity of rotor

Subscripts

a	annulus; location of inner seal
an	annlus (for thermal buffer ratio model)
ad	adiabatic
ax	axial clearance
av	average value
A	material A; location A on vane platform
B	material B
b	black body
c	concentration
CI	combined ingress
e	egress; entrainment
EI	externally-induced ingress
fd	free disc value
i	ingress
in	initial, inlet
int	interface
L	back face
max	maximum

min	minimum
o	value for rotor (thermal buffer ratio model)
overlap	overlap clearance
r	radial component
	value at radius *r*
rad	radial clearance
RI	rotationally-induced ingress
s	surface; stator surface
ss	steady-state value
T_{ad}	relating to adiabatic disc temperature
TC	thermocouple reading
z	axial component
ϕ	tangential component
0	superposed flow
1	location in wheelspace; first crystal isotherm;
2	location in annulus; second crystal isotherm
∞	infinite time; value for core (for thermal buffer ratio model)

Superscript

–	average value
+	value for upper 95% uncertainty limit
–	value for lower 95% uncertainty limit
*	value with zero ingress
′	value for the quenching solution; corrected value
i	spatial increment;
n	temporal increment

Symbols

AC	Alternating Current
ASME	American Society of Mechanical Engineers

BSI	British Standard Institution
BW	Bandwidth
CCD	Charge Coupled Devices
CCGT	Combined Cycle Gas Turbine
CI	Combined Ingress
EI	Externally-Induced
FRTC	Fast Response Thermocouple
GA	General Assembly
GTRU	Gas Turbine Research Unit
IR	Infrared
ISA	International Standard Atmosphere
ISO	International Organization for Standardization
HP	High Pressure
HRSG	Heat Recovery Steam Generator
LDA	Laser Doppler Anemometry
LDV	Laser Doppler Velocimetry
MHI	Mitsubish Heavy Industries
MGA	Multi Gas Analyser
NACA	National Advisory Committee for Aeronautics
NETD	Noise Equivalent Temperature Difference
NGV	Nozzle Guide Vane
OPR	Overall Pressure Ratio
PIV	Particle Image Velocimetry
RI	Rotationally-Induced
RTD	Resistance Temperature Detector
SFC	Specific Fuel Consumption
TET	Turbine Entry Temperature
TLC	Thermochromic Liquid Crystal

Chapter 1: Introduction

1.1 A brief history of the gas turbine

The first gas turbine was conceived and patented by John Barber in 1791. Although the machine was never built during his lifetime, the design consisted of a compressor, a combustion chamber and a turbine wheel, which are the key components that form modern gas turbines. Furthermore, John Barber's machine was designed to operate using the same thermodynamic cycle as modern gas turbines. A sketch of his gas turbine from his patent is shown in Fig. 1.1(Hünecke, 1997) (Meher-Homji, 2000).

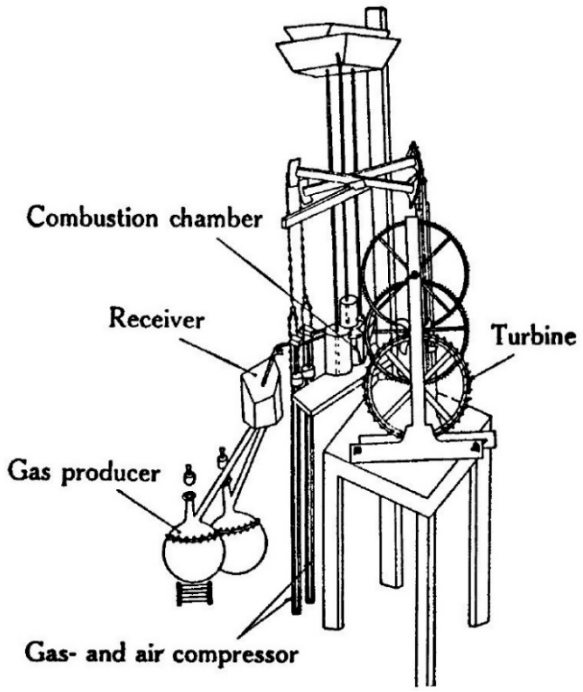

Figure 1.1 Patent (1791) Drawing of John Barber's gas turbine (Meher-Homji, 2000)

In 1872, George Brayton invented and patented the 'Ready Motor', a reciprocating constant pressure internal combustion engine. The thermodynamic cycle of this motor is named after the inventor and the Brayton cycle can be used to describe gas turbines thermodynamically (Brayton, 1872). In the same year, a German engineer, Dr. Franz Stolze, designed an engine consisting of a multi-stage axial compressor, a multi-stage axial turbine, a heat exchanger, a gas producer and a

combustion chamber. The axial compressor and axial turbine were connected to each other by the same shaft, just like in modern gas turbines. Stolze's gas turbine is believed to be the first equipped with a multi-stage compressor and turbine. Although he developed his first gas turbine in 1872, operating tests were not carried out until much later, between 1900 and 1904. It could not produce enough power to run its own compressor due to the limited knowledge of aerodynamics at the time. Consequently, it required external power to run (Meher-Homji, 2000).

The first gas turbine which produced excess power was built in 1903 by a Norwegian engineer, Aegidius Elling. His engine had a 6-stage centrifugal compressor and a single stage centripetal impeller (turbine). Elling's first machine, which is known as the first constant pressure gas turbine, could produce net power of 11hp with a turbine entry temperature (TET) of 400°C. In the next year, he improved the design of his gas turbine and achieved net power output of 44hp with a TET of 500°C. The improvement included new compressor design, such as water injection between compressor stages for intercooling and recuperation of exhaust gas heat (Meher-Homji, 2000, Bakken *et al.*, 2004).

In 1921, a Frenchman, Maxime Guillaume, filed the first patent for using a gas turbine, which was an axial-flow turbojet for use as an aircraft engine. However, his gas turbine was never built due to the immaturity of technology at the time.

In the 1930s, after nearly one and a half centuries of endeavour, the first practical aero-derivative and industrial gas turbines were developed. In 1930, Frank Whittle submitted his patent 'Improvements relating to the Propulsion of Aircraft and other Vehicles'. A drawing from the patent is shown in Fig. 1.2. His first conceptual turbojet comprised a multi-stage axial compressor followed by a centrifugal compressor, an annular combustion chamber, a single-stage axial turbine and a nozzle. He constructed and tested his first jet engine based on the patent in April 1937. Parallel to Whittle's development of the jet engine, German engineer Dr. Hans von Ohain independently developed and tested a hydrogen powered turbojet engine (HeS-1) producing 550lb of thrust in 1937. Two years later, in 1939, a Heinkel HE178 experimental aircraft powered by Von Ohain's new engine, the HeS-3B, successfully made the world's first turbojet-powered flight. In 1941, the British

Gloster E28/39 experimental aircraft made its maiden jet powered flight with Whittle's W1A engine (Hünecke, 1997).

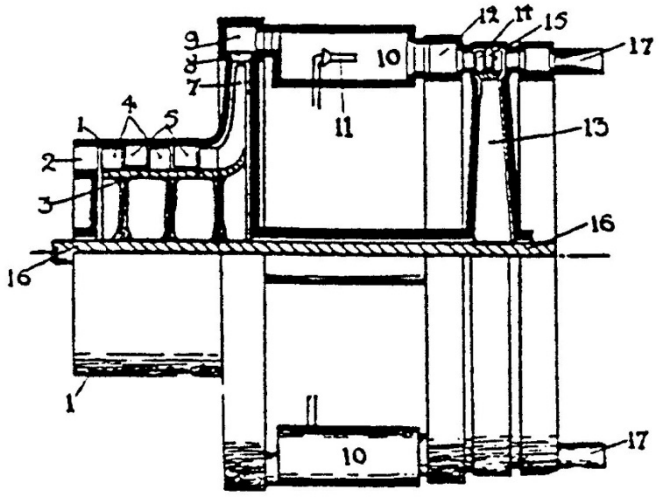

Figure 1.2 Frank Whittle's patent drawing (1930) (Meher-Homji, 1998)

The first successful industrial gas turbine for power generation was developed by Brown Boveri, the company established by Charles Brown and Walter Boveri. By 1939, the world's first gas turbine power plant (GT Neuchâtel) had been built and successfully commissioned as a standby unit in Neuchâtel, Switzerland by Brown Boveri. The power plant was capable of producing 4MW of electricity with a TET and thermal efficiency of 550°C and 17.4%, respectively. The American Society of Mechanical Engineers (ASME) honoured the world's first industrial gas turbine as a Historic Mechanical Engineering Landmark in 1988 and the GT Neuchâtel was permanently shut down in 2002, after 63 years and 1908 start-ups, due to the damaged generator. In 2005, the GT Neuchâtel was restored and displayed by Alstom (Brown Boveri was merged with ASEA and form ABB in 1988, then ABB was merged with Alstom power in 2000) at their factory in Birr, Switzerland. A layout of this first industrial gas turbine is shown in Fig. 1.3 (Van der Linden, 1988).

Although some first generation industrial gas turbine power plants were built in the 1930s and 1940s, these were not competitive enough to match fast-advancing steam turbine technology (Winskel, 2002). However, owing to the quick start up time of gas turbines, the early ones could be used to produce peak or standby power. From the early 1950s onwards, as technology developed, the performance of gas turbines

continually improved. In fact, the power output of a simple cycle industrial gas turbine (for 60Hz frequency) was increased from less than 5MW in the early 1950s to approximately 300MW in 2000, as shown in Fig. 1.4. In the same period, the firing temperature was increased from approximately 800°C to 1400°C (Fig. 1.5).

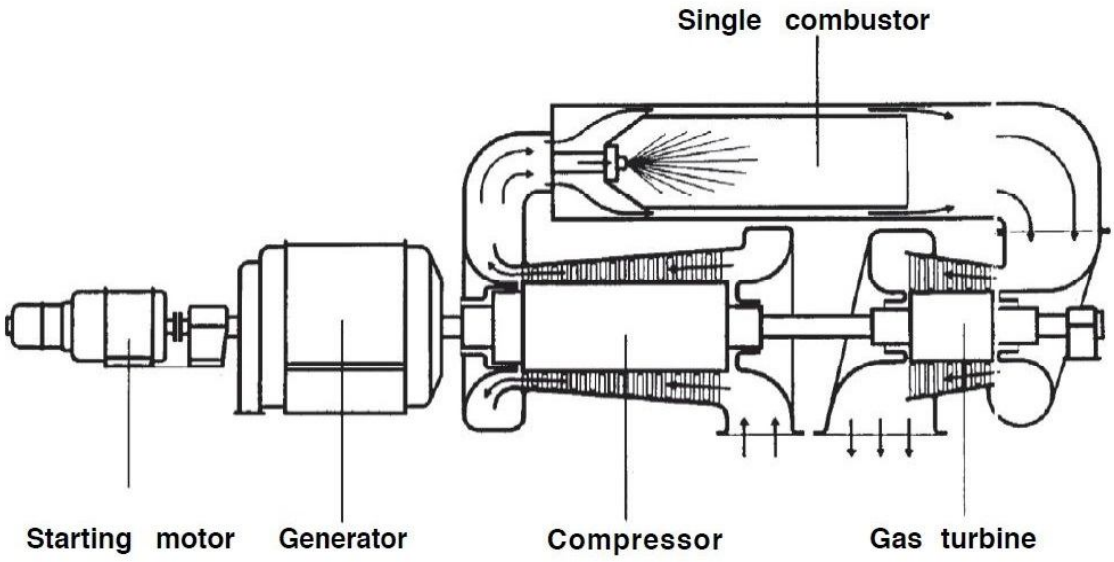

Figure 1.3 Layout of the single stage Brown Boveri gas turbine installed at the Neuchâtel power plant (Van der Linden, 1988)

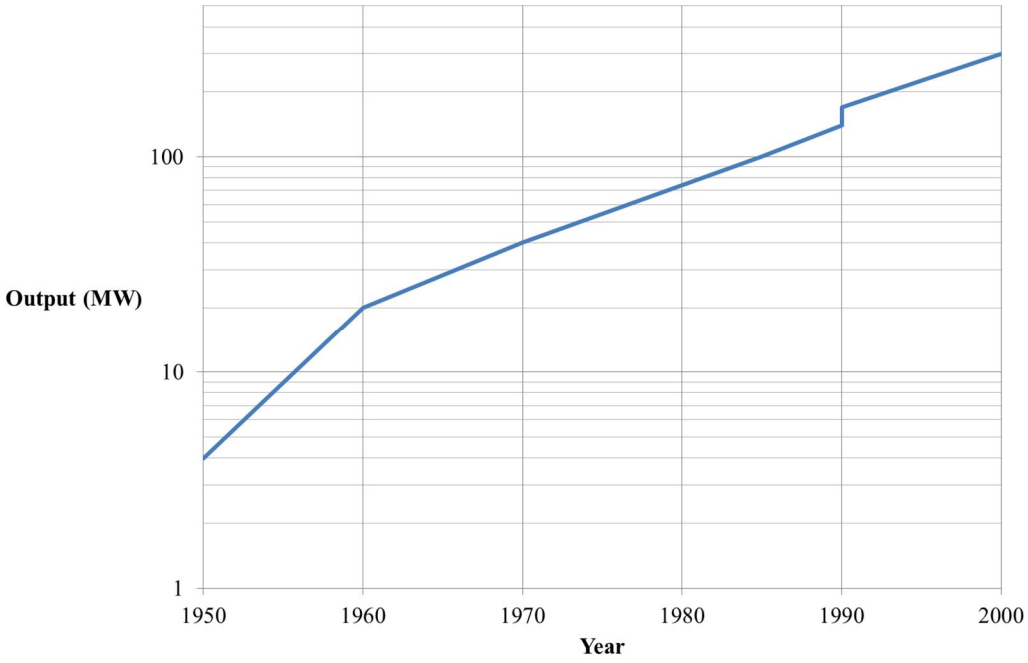

Figure 1.4 Unit rating increase over time for industrial gas turbines for 60Hz applications (Balling *et al.*, 2002)

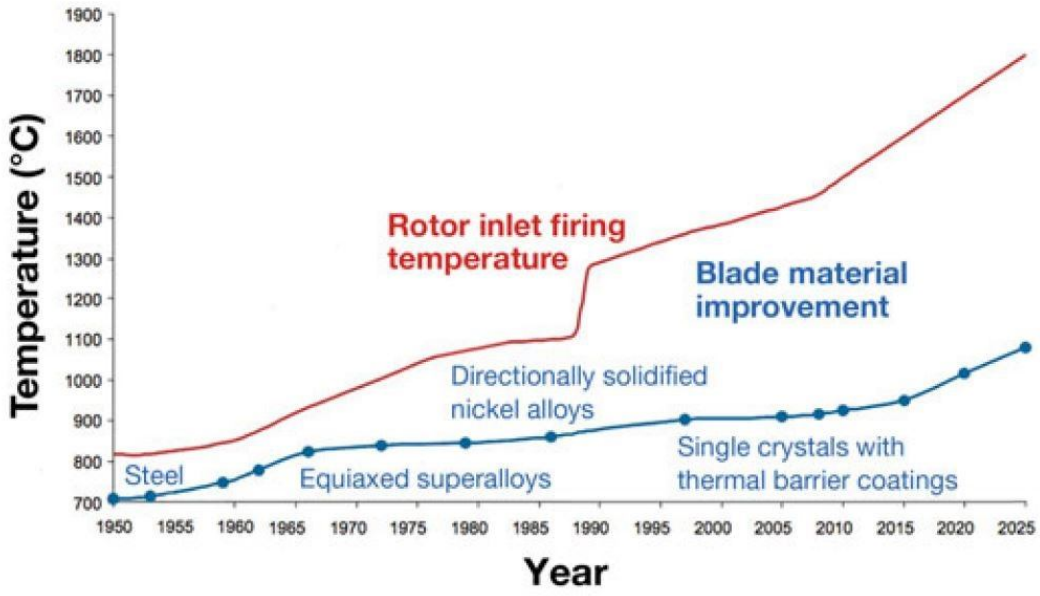

Figure 1.5 Firing temperature and material improvement over time for the industrial gas turbine (Saini, 2012)

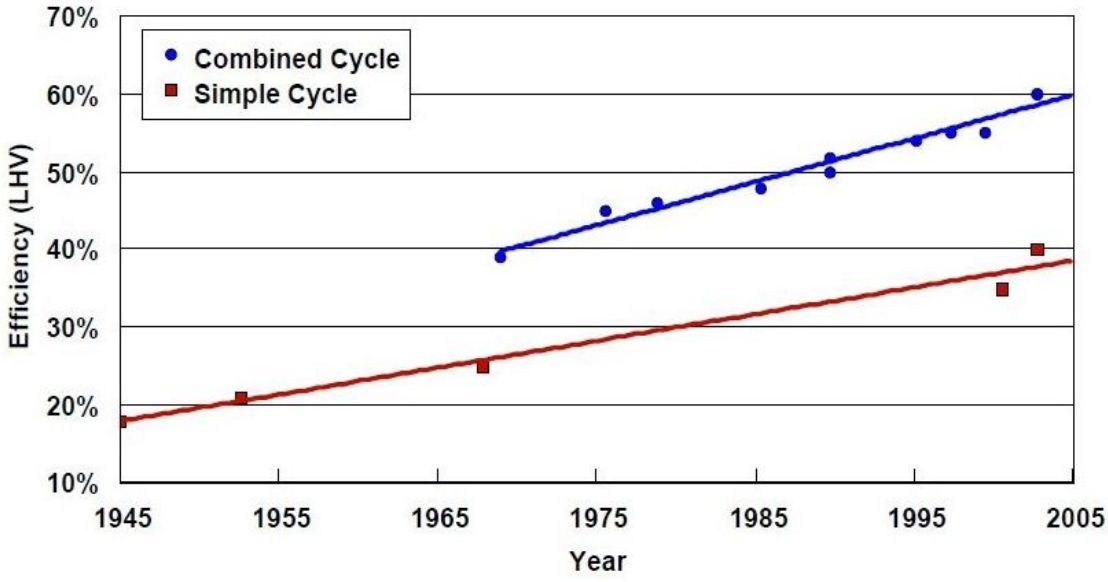

Figure 1.6 General efficiency increase over time for simple and combined cycle gas turbines (Unger and Herzog, 1998)

The performance of the gas turbine rapidly improved in the 1950s and 1960s and consequently the technology became good enough for the development of the combined cycle gas turbine (CCGT) to begin in earnest, with the first combined cycle power plant with a heat recovery steam generator (HRSG) being

commercialised in 1968. The plant achieved the same level of thermal efficiency as the conventional steam turbine at this time, approximately 40% (Fig. 1.6). Since then, that of the CCGT power plant has been consistently improved and broke the 60% efficiency barrier in 2003 (Saini, 2012). In the present day, state of the art high-power industrial gas turbines, such as the Mitsubishi M701J, are capable of operating at a turbine inlet temperature of 1600°C and producing 680MW (50Hz application) in combined cycle operation with an efficiency of 61.7 % (MHI).

1.2 Gas turbines

1.2.1 Gas turbine applications and advantages

The gas turbine has superior power to weight/volume ratio when compared to a conventional reciprocating engine. It also has high reliability, a long life and relatively low maintenance cost owing to the smaller number of moving parts likely to fail. Significantly short start-up time is another strong advantage of the gas turbine over steam; large industrial gas turbines can produce full load in minutes, while large steam turbines require hours of start-up period before peak output. In addition, the gas turbine is capable of utilising a wide variety of fuels, from natural gas to kerosene-like jet fuel through to the gasification of solid fuels, such as coal (Langston and Opdyke, 1997).

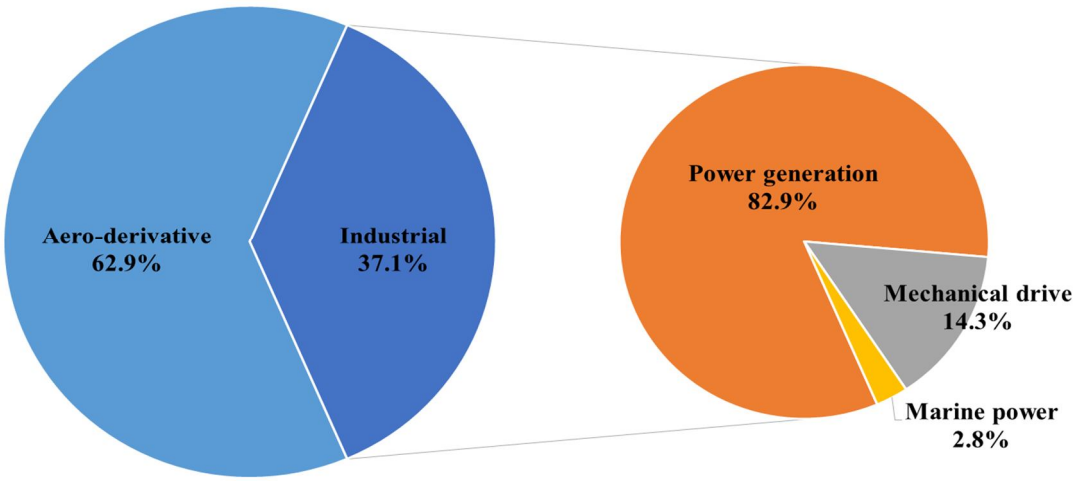

Figure 1.7 Gas turbine production by sector in 2010 (Langston, 2011)

One of the major drawbacks of the early gas turbine was its inferior efficiency and higher operating cost compared to conventional internal combustion engines and steam turbines power plants; efficiency of industrial gas turbines in 1940s was less than 20 %, as shown in Fig. 1.6. However, over a half century of endeavour to achieve higher thermal efficiency resulted in the gas turbine being more efficient than its competitors; for example, Mitsubishi claims that their J-series gas turbine has achieved 41% and 61 % of efficiency from simple and combined cycle operations, respectively. (MHI, 2014)

Today, the gas turbine is most well-known to the public for its application to aircraft propulsion. However, owing to the above stated merits, it is widely used not just for aircraft propulsion, but also for power generation and marine propulsion. The worldwide gas turbine market share by its application in 2010 is shown in Fig. 1.7, where it can be seen that that of aero-derivative gas turbines was 62.9 % and that of industrial gas turbines was 37.1 %. Within the industrial application segment, gas turbines for power generation hold the dominant market share of 82.9 %. Moreover, they are also used for land-based mechanical drive purposes, such as pumps for natural gas transportation and power systems for ground vehicles, e.g. tanks and trains (Langston, 2011).

1.2.2 Gas turbine theory

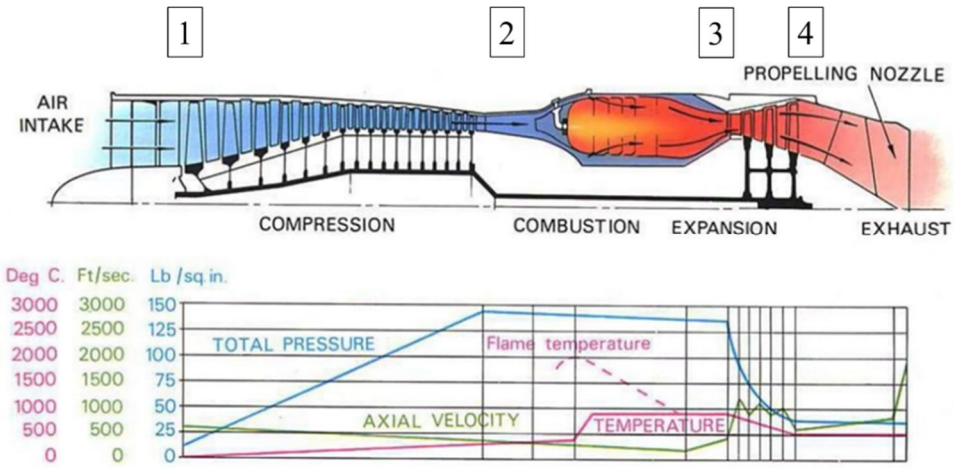

Figure 1.8 Variation of temperature, pressure and velocity through simple turbojet (Rolls-Royce., 1996)

A simple gas turbine consists of the three main sections: compressor, combustion chamber and turbine. Fig. 1.8 shows these components for a turbojet. A simple gas turbine is sometimes referred to as a core engine or gas turbine core. A compressor (1-2) increases the pressure of the air, which is drawn into the system through an intake. This high pressure and temperature compressed air is then delivered to a combustion chamber (2-3), where it is mixed with gaseous liquid fuel and burned. Subsequently, the temperature of the gas is increased by the conversion of chemical energy of fuel into thermal energy and a turbine (3-4) arranged downstream of a combustion chamber is used for extracting energy from the hot gas through an expansion process. As energy is extracted from the hot gas by the expansion process, the temperature and pressure of the air decrease in the turbine section. Some of the energy extracted by the turbine is used to drive the compressor and then the remaining energy is used to produce usable power in the form of jet thrust or shaft work. The pressure, temperature and velocity variations through a typical simple turbojet engine are shown in Fig. 1.8 and a gas turbine system, which uses the remaining high energy gas to run a separate power turbine, is shown in Fig. 1.9.

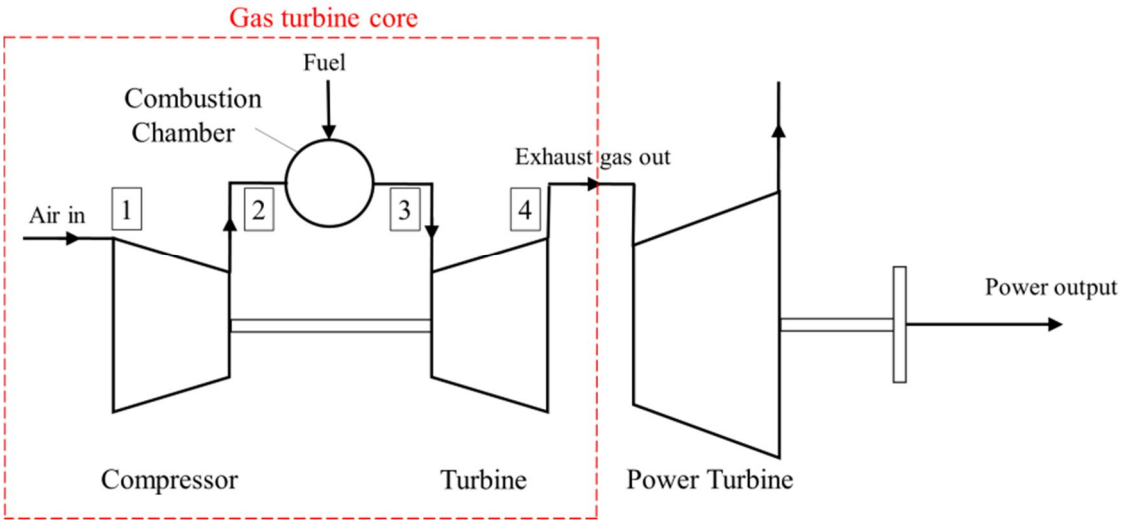

Figure 1.9 Gas turbine with a separate power turbine (Saravanamuttoo, 2009)

The operation of a gas turbine can be represented by the ideal Brayton cycle, which consists of the following three processes, as shown in Fig. 1.10: isentropic compression (1-2'), isobaric combustion (2'-3') and isentropic expansion (3'-4'). However, the actual thermodynamic cycle of a real engine will be non-isentropic.

That is, non-isentropic compression (1-2) and expansion (3-4) will occur in a real gas turbine. In addition, owing to frictional and aerodynamic losses in the combustion chamber, losses in total pressure are expected during the combustion process (2-3) (Cengel *et al.*, 2011).

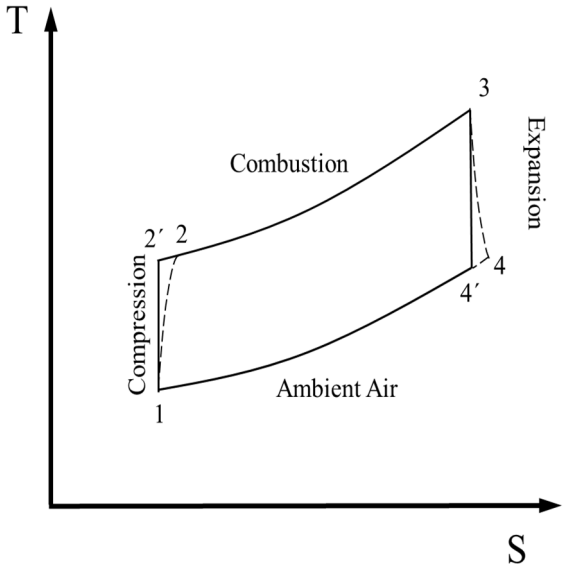

Figure 1.10 Temperature-entropy graph for a gas turbine core

The efficiency of the ideal Brayton cycle is dependent only on the overall pressure ratio (OPR) across a compressor. The higher the OPR of a cycle, the higher cycle the efficiency, whereas the specific work output of a gas turbine is a function of not only of the OPR, but also the TET. Thus, the maximum specific work output can be achieved by the optimum OPR for a given TET of the cycle.

Due to the significantly increasing concern relating to man-made greenhouse gases and high fuel prices, demands for increasing efficiency, hence reducing SFC, is highly required. According to Cumpsty (2003), between 15 ~ 25% of the compressed air is taken from the last stage of the HP compressor for cooling purposes. Although the cooling air is essential for ensuring the integrity of engine components, the efficiency of gas turbines decreases with increased use of cooling air. In addition, the cooling air causes aerodynamic losses, owing to the mixing of the coolant and the hot mainstream gas, which reduces the total temperature of hot mainstream gas governing gas turbine performance (Brooks, n.d., Schüpbach *et al.*, 2011). According

to MirzaMoghadam *et al.* (2008), the thermal efficiency of a gas turbine can be improved by 0.4% points with a 1% reduction in cooling and sealing air from the HP compressor. and this is the reason why engine designers have made every endeavour to increase the OPR of gas turbines, which in turn will increase the TET (Saravanamuttoo, 2009).

1.3 Evolution of gas turbine cooling technology

As described in the previous section, increasing the OPR and TET is one of the key solutions in achieving lower specific fuel consumption (SFC) and emissions. Therefore, ceaseless efforts to increase these have been made since the birth of practical gas turbines in the late 1930s and consequently, the TET has been rising significantly since then. Although the efficiency of a gas turbine can be improved by increasing the OPR, higher pressure ratios have an adverse effect on gas turbine cooling; as the OPR increases, the temperature of the cooling air from the high pressure (HP) compressor is also raised to a higher level. (The cooling air from the HP compressor will be ~ 1050K with an OPR of 50, on an ISA+15ºC day (Saravanamuttoo, 2009).

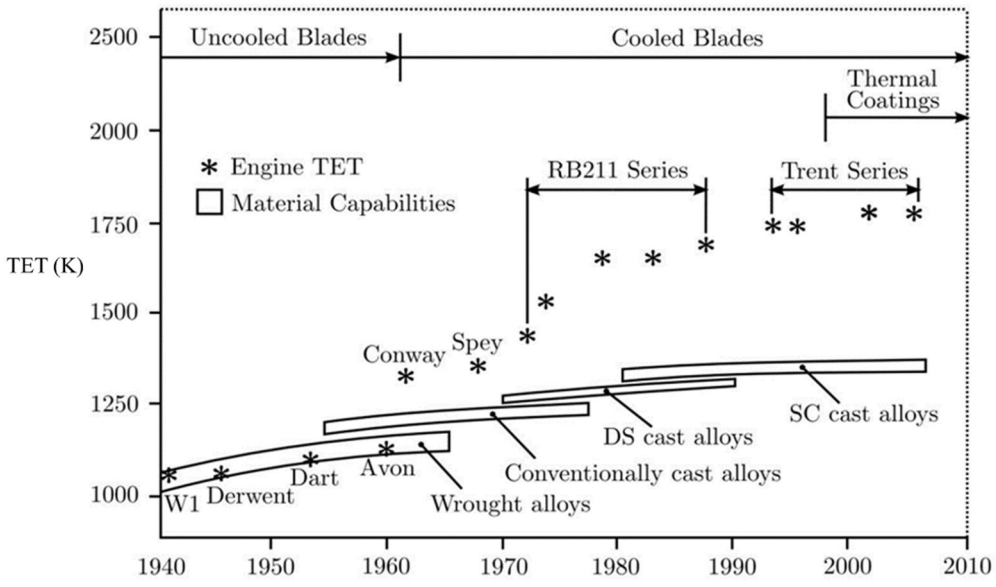

Figure 1.11 Improvement in the TET and material capabilities of Rolls Royce gas turbines (Cumpsty, 2003)

The continuous improvement in the TET of Rolls-Royce aero gas turbines is shown in Fig. 1.11 and it can be seen that this increased remarkably in 1961 when cooled blades were first introduced to the Conway engine (Saravanamuttoo, 2009). Since then, thanks to turbine cooling technologies, the TET has been increased beyond turbine material capabilities. State of the art single crystal turbine blades are designed to be operated at around 1800K, which is approximately 200K above their meting point and if today's turbine blade cooling technology were applied to an ice cube, it would be possible to prevent it from melting in a domestic oven (Rolls-Royce, 2011). In addition, even with the TET of the modern gas turbine being over 800K higher than that of the early ones, the turbines of modern civil aero engines are able to be operated in service for more than 20,000 hours (Cumpsty, 2003), which is a dramatic improvement compared to that of the world first production jet Jumo-004B engine's 50 hours (Meher-Homji, 1997).

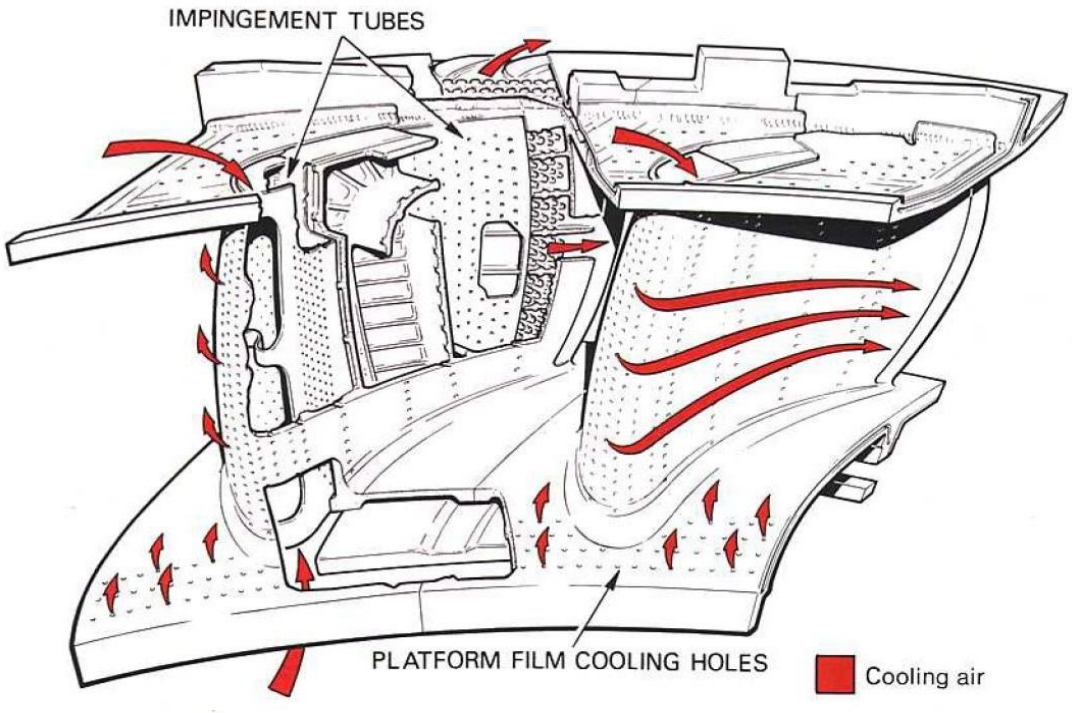

Figure 1.12 High pressure nozzle guide vane construction and cooling (Rolls-Royce., 1996)

As described above, the rising TET is closely related to the developments of turbine cooling technology; owing to this it has been possible for it to be increased from approximately 1000K to 1800K over the last 70 years. In order to increase TET

to such a high level, modern gas turbines have become far more complex than Whittle and Von Ohain's early gas turbines. For example, the first stage nozzle guide vane (NGV) and turbine blades, which are exposed to the highest cycle temperature, have complex internal cooling passages and structures (Figs. 1.12 and 1.13). In order to improve the cooling performance of the vanes and blades, a number of cooling techniques have been introduced. This includes film cooling, convection cooling and thermal barrier coating.

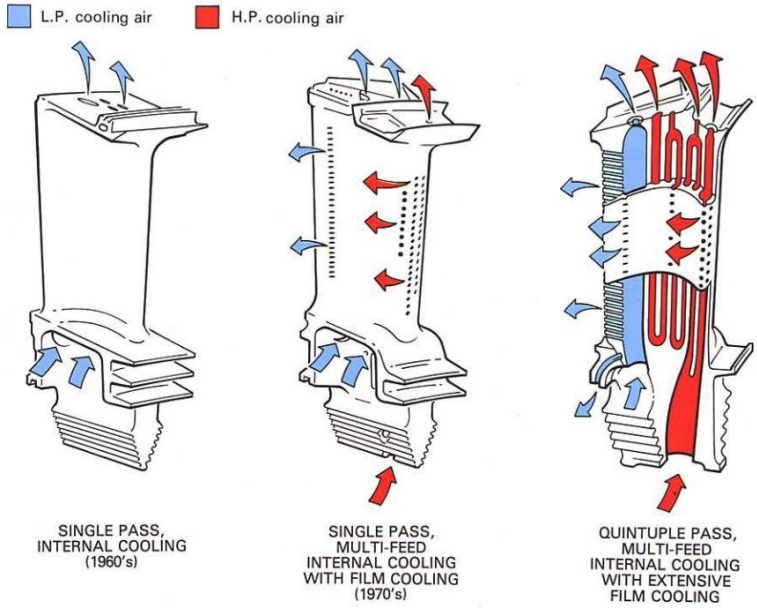

Figure 1.13 Development of high pressure turbine blade cooling (Rolls-Royce., 1996)

1.4 Introduction to hot gas ingress

Fig. 1.14 shows a typical high pressure turbine stage, which consists of nozzle guide vanes (NGVs), turbine blades, a stator disc, a rotor disc, rim seal and wheel-space. Hot mainstream gas can cause overheating problems, not only to the NGVs and turbine blades, but also to the stator and rotor discs which support these components. For example, hot mainstream gas can flow through the clearance gap between the two discs and enter the wheel-space. In gas turbines, ingress of mainstream gas to the wheel-space is predominantly caused by the non-axisymmetric pressure variation in the mainstream flow, which is known as externally-induced (EI) ingress and it is discussed in more detail in subsection 2.2.2.

The rotating components are highly stressed due to centrifugal forces and damage due to overheating is a serious issue. In order to reduce or prevent hot gas ingestion (ingress) from the mainstream annulus to the wheel-space between the stator and rotor discs, these discs of a turbine stage are separated by a non-contact rim seal. In addition, compressed air taken from the last stage of the HP compressor is used to pressurise the wheel-space.

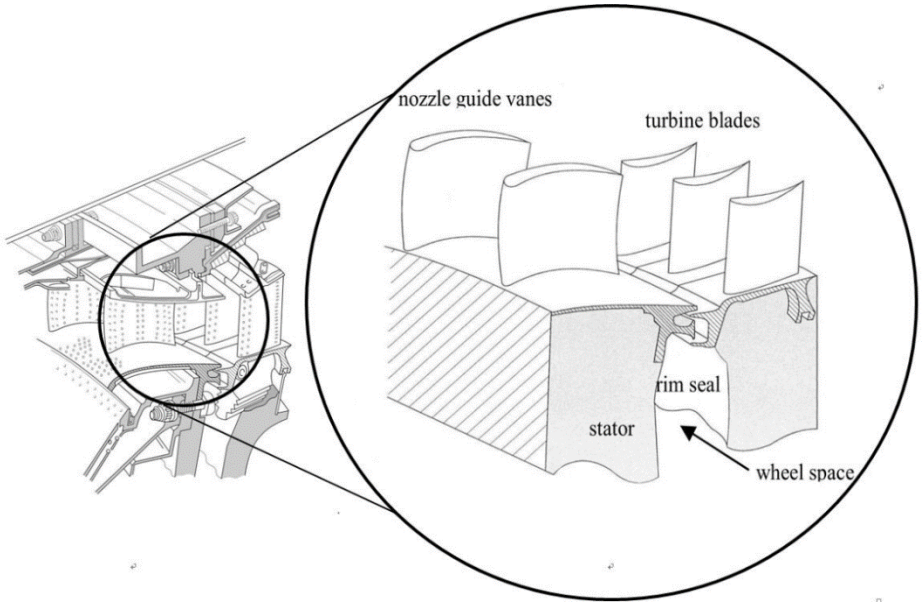

Figure 1.14 Turbine stage and schematic of rim seal and wheel-space (Owen *et al.*, 2010)

As the sealing and cooling air originated from the compressor, the amount of diverted air has an adverse effect on the efficiency of the gas turbine. A modern gas turbine engine experiences a 6 % penalty in terms of SFC in order to prevent hot gas ingestion into the wheel-space (Bohn *et al.*, 2006). However, if insufficient coolant flow is provided, a catastrophic failure could be triggered due to the thermal damage of the turbine components caused by overheating of the wheel-space. Consequently, the amount of sealing and cooling air needs to be optimised (balanced) to improve the thermal efficiency of the gas turbine, while ensuring its safety. Hence, the engine designer needs to know the following: What is the most effective seal geometry? How much sealing air is required to limit ingress to an acceptable level? When does ingress occur? How much hot gas enters the wheel-space and how far does it penetrate? How does this ingested fluid affect the temperature of the turbine disc?

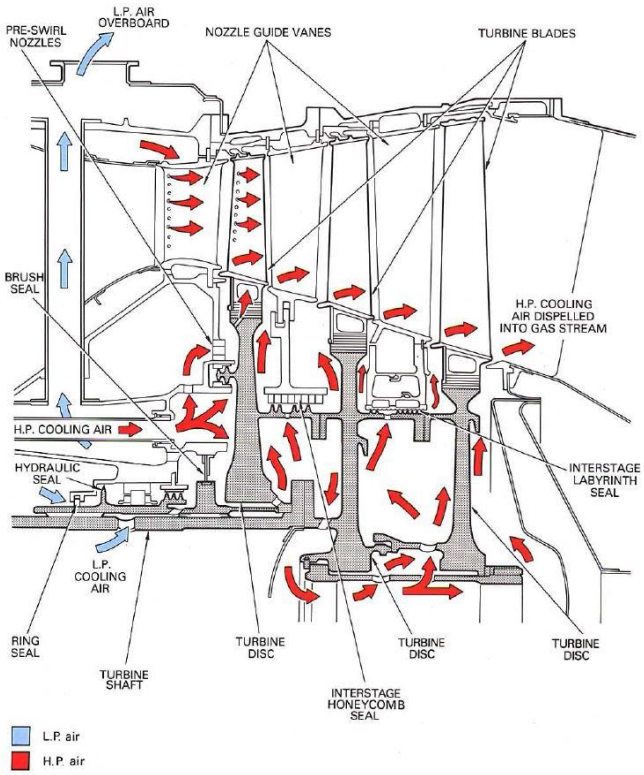

Figure 1.15 Internal air system arrangement of a gas turbine (Rolls-Royce., 1996)

Considerable research has been conducted on all but the last question. That is, the stator sealing effectiveness of various rim seal geometries has been measured by many research groups including the Gas Turbine Research Unit (GTRU) of the University of Bath. However, although gas concentration measurement techniques are well established and have been widely used, it is not practical to apply them to rotor sealing effectiveness, which thus remains a research challenge.

1.5 Thesis aims

The aim of this PhD research is to investigate the effect of hot gas ingress to the rotor disc of a turbine stage by determining the adiabatic rotor effectiveness for a series of generic rim-seal geometries in the Bath one-stage ingress test facility. It will provide fundamental insight into the ingress problem and help gas turbine design engineers improve rim seal design.

The University of Bath measured and showed, for the first time, the thermal effects of ingress on the rotor in the wheel-space for a datum seal (axial-clearance

seal) using TLC. The TLC technique is prone to large uncertainties mainly due to the limited number of temperature data which could be acquired using TLC. Therefore, the first objective was to develop a non-intrusive temperature measurement technique which can provide a full temperature history of the rotor surface in a transient experiment. This required modifications of the Bath one-stage ingestion test facility.

The second objective was to develop a data analysis method appropriate for transient experiments using the non-intrusive temperature measurement technique. The method should be developed to calculate h, the heat transfer coefficient, and T_{ad}, the adiabatic surface temperature accurately, based on the full temperature history. A series of numerical experiments were carried out to develop the analysis method and the numerical experiments were used to design the new heat transfer experiments in both the 1 and 1.5 stage ingestion rigs of the University of Bath.

The third and main experimental objective of this thesis was to measure the adiabatic rotor effectiveness of a series of generic rim-seal geometries, which will help engine design engineers improve rim seal configurations. The experimental data will also be used to develop and validate a 'thermal buffer ratio hypothesis', which will allow these designers to estimate the effect of ingress on the rotor based only on stator concentration experimental data without conducting extensive experimental heat transfer research.

1.6 Thesis Overview

Chapter 1 has contained an overview of the historical development of industrial gas turbines, fundamental gas turbine theory and cooling technologies. Also, the aims of this PhD thesis and a list of publications produced over the course of this research have been provided.

Chapter 2 provides an overview of infrared temperature measurement techniques. Also, a comprehensive literature review on flow and heat transfer in rotor-stator systems, especially ingress through gas turbine rim seals, is presented.

Chapter 3 describes the development of the non-intrusive temperature measurement technique, which is suitable for providing a full temperature history of the rotor surface in a transient heat transfer experiment. Calibration test results of the new temperature measurement technique are also presented.

Chapter 4 explains a numerical solution of Fourier's heat equation for determining the heat transfer coefficient and adiabatic surface temperature from temperature data measured by the new non-intrusive temperature measurement technique.

Chapter 5 describes the experimental facility, which simulates hot gas ingress into the wheel-space of an axial turbine stage. Concentration sealing effectiveness data were measured on the stator disc of the test facility for four generic rim seal geometries so as to determine the variation of the concentration sealing effectiveness with sealing flow rate and the radial variation of the concentration effectiveness.

Chapter 6 describes the modification of Bath one-stage ingestion test facility to improve its performance so as to allow for more accurate investigation into the heat transfer characteristic of ingress. In addition, heat transfer experimental data on the rotor of the Bath one-stage gas turbine ingestion test facility are presented for four generic rim-seals: two single and two double-clearance ones. An adiabatic effectiveness is defined and used to determine the effects of hot gas ingestion on the rotor and to compare the performances of these four seals. The concentration effectiveness data and the adiabatic effectiveness data of each seal, which were respectively acquired in Chapter 5 and 6, were compared to show the thermal buffering effect.

Chapter 7 presents a theoretical model to determine sealing effectiveness based on pressure measurements in an engine, which was developed by modifying the orifice model constructed by Professor J.M. Owen.

Chapter 8 presents the conclusions of this thesis and recommends some potentially beneficial future research directions.

1.7 Publications

The following publications were produced over the course of this thesis:

Journal publications:

1. Pountney, O.J., **Cho, G**., Lock, G.D. and Owen, J.M., 2012, "Solutions of Fourier's equation appropriate for experiments using thermochromic liquid crystal," *Int. J. Heat Mass Transfer*, 55(21-22), pp. 5908-5915.

2. Owen, J.M., Kang, W., Scobie, J.A., **Cho, G**., Sangan, C.M. and Lock, G.D., 2014, "Use of pressure measurements to determine effectiveness of turbine rim seals," ASME Paper GTP-14-1417. *ASME J. Eng. Gas Turbines Power*.

3. **Cho, G.**, Sangan, C.M., Owen, J.M. and Lock, G.D., 2015, "Effect of ingress on turbine discs," Manuscript is submitted for publication. ASME Paper GT2015-42324.

It is also expected that the contents of Chapter 3 and 4 will form the basis for future journal publications.

Chapter 2: Literature Review

This chapter provides an introduction to ingress of mainstream gas into the wheel-space. Fundamental fluid dynamics for rotor-stator systems are discussed and previous fluid dynamics and heat transfer studies for ingress through gas turbine rim seals are briefly explained. Recent theoretical and experimental researches conducted at the University of Bath are also covered, and lastly a brief overview of infrared temperature measurements technique for use in transient heat transfer experimental studies is provided.

2.1 Non-Dimensional variables

A set of fluid dynamic non-dimensional variables, which are commonly used for describing rotor-stator systems, will be defined in this section, these being:

$$\text{Rotational Reynolds number, } \quad Re_{\phi} = \frac{\rho \Omega b^2}{\mu} \tag{2.1}$$

$$\text{Axial Reynolds number, } \quad Re_{w} = \frac{\rho W b}{\mu} \tag{2.2}$$

$$\text{Non-dimensional flow rate, } \quad C_w = \frac{\dot{m}}{\mu b} \tag{2.3}$$

$$\text{Turbulent flow parameter, } \quad \lambda_T = \frac{C_w}{Re_{\phi}^{0.8}} \tag{2.4}$$

$$\text{Swirl ratio, } \quad \beta = \frac{u_{\phi}}{\Omega r} \tag{2.5}$$

where, ρ is the density, b is the radius of the seal, μ is the dynamic viscosity, W is the axial velocity of the fluid in the mainstream annulus, $\dot{m}$ is the mass flow rate of the fluid and r is the local radius.

These variables have a significant influence on the flow structure within rotor-stator systems.

2.2 Rotor-Stator systems

There are three main types of flow associated with a rotating disc, free disc, rotor-stator systems and rotating cavities, which respectively refer to, disc rotating in a stationary fluid, disc rotating close to stationary surfaces and disc rotating close to another rotating disc. As the test section of the Bath one-stage ingress test facility consists of a rotating and a stationary disc, a brief review on rotor-stator systems is provided here along with two simple cases, a free-disc in a stationary fluid and a stationary disc in a rotating flow.

2.2.1 The Free Disc

A single disc spinning in initially stationary fluid is one of the simplest rotational flow cases, which is often referred to as the free-disc. It has been studied by many researchers, including Schlichting (1979) and Owen and Rogers (1989). The flow structure and associated boundary layers near the rotating disc of this case are shown in Fig. 2.1. As the no-slip condition in the rotor boundary layer must be satisfied, the tangential velocity, where $u_\phi=\Omega r$ is the velocity component in the tangential direction (m/s), Ω is the angular velocity of the disc about the z-axis (rad/s) and r (m) is the local radius, of the fluid at the surface of the rotating disc must be the maximum, i.e. the same as the disc and be zero at the free stream (outside the boundary layer). The centrifugal forces are also acting on the fluid and cause a radial outflow, u_r, in the boundary layer. The flow is often referred to as the 'disc pumping effect'. In addition, as the fluid flows radially outward in the boundary layer, fluid outside of the rotating boundary layer needs to be entrained axially, u_z, into the boundary layer so as to satisfy the conservation of mass.

Similar to a non-rotating flow, there are three types of fluid flow near the rotating disc: laminar, transition and turbulent. The flow near the axis of rotation tends to be laminar since the determining parameter, the local rotational Reynolds number, is proportional to square of the local radius, as shown in Eq. 2.6. It can also be seen from the equation that turbulent flow can be achieved at low radius for large values of angular velocity.

$$Re_{\phi,r} = \frac{\rho\Omega\, r^2}{\mu} = \left(\frac{r}{b}\right)^2 \frac{\rho\Omega\, b^2}{\mu} \tag{2.6}$$

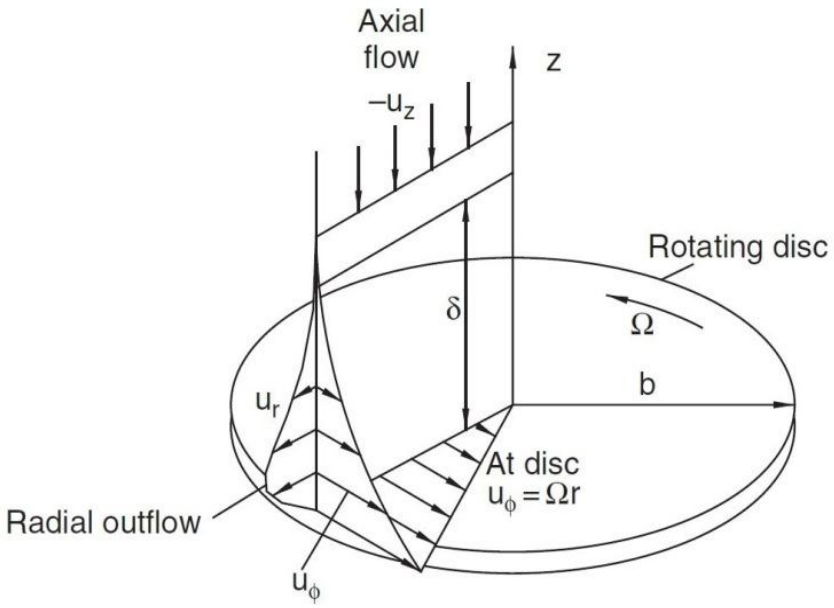

Figure 2.1 The radial and tangential boundary layers and associated inflow and outflow induced by a rotating disc in a stationary fluid, i.e. free-disc (Childs, 2011)

2.2.2 Stationary disc in a rotating fluid

A stationary disc in a rotating fluid and associated boundary layers as well as the velocity components are shown in Fig. 2.2; a stator disc of a turbine stage in a gas turbine is a typical example of this flow. This type of flow has been studied by many researchers, including Schlichting (1979) and Owen and Rogers (1989). As the tangential velocity (u_ϕ) in the boundary layer near the stationary disc is slower than that of the rotating fluid, the centripetal force of the fluid in the boundary layer is smaller than that of the free-stream rotating fluid. Consequently, due to the centripetal pressure difference, the fluid near the stationary surface flows radially inwards (u_r). Hence, in order to satisfy the conservation of mass, fluid in the rotating boundary layer near the surface flows axially (u_z) away from it.

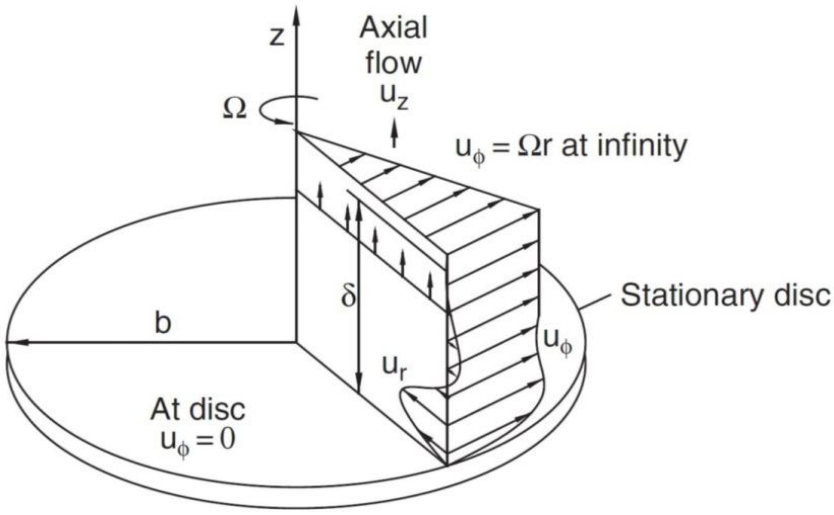

Figure 2.2 The radial and tangential boundary layers and associated inflow and outflow induced by a rotating fluid adjacent to a stationary disc (Childs, 2011)

2.2.3 Rotor-Stator systems

A rotor-stator system comprises a rotating disc and an adjacent stationary disc, which are coaxially aligned with an axial gap between the two. The two discs form a cavity between them that is known as the wheel-space (or rotor-stator cavity). Typical examples of rotor-stator systems, with various geometrical configurations that have significant influence on the fluid dynamics within the rotor-stator system, are shown in Fig. 2.3. The geometrical configurations include the gap between the discs, the presence of a stationary or rotating shroud and the supply of any superposed flow.

At the very early stage of the research on rotor-stator systems, Batchelor (1951) proposed a model that consisted of separate stator and rotor boundary layers with an inviscid core of fluid between the two. More specifically, under this theory the inviscid core is confined between the rotor and stator boundary layers and rotated at an angular velocity with a value somewhere between that of the stator and rotor. According to the model, fluid flows radially inward and outward in the stator and rotor boundary layers, respectively. Hence, in order to satisfy the conservation of mass, fluid moves axially across the core from the stator boundary layer to the rotor boundary layer, i.e. the mass of fluid entrained into the rotor boundary layer is balanced with that of fluid leaving the stator boundary layer. This theory can be

applied to a rotor-stator system when the superposed flow rate is less than the free-disc entrainment rate.

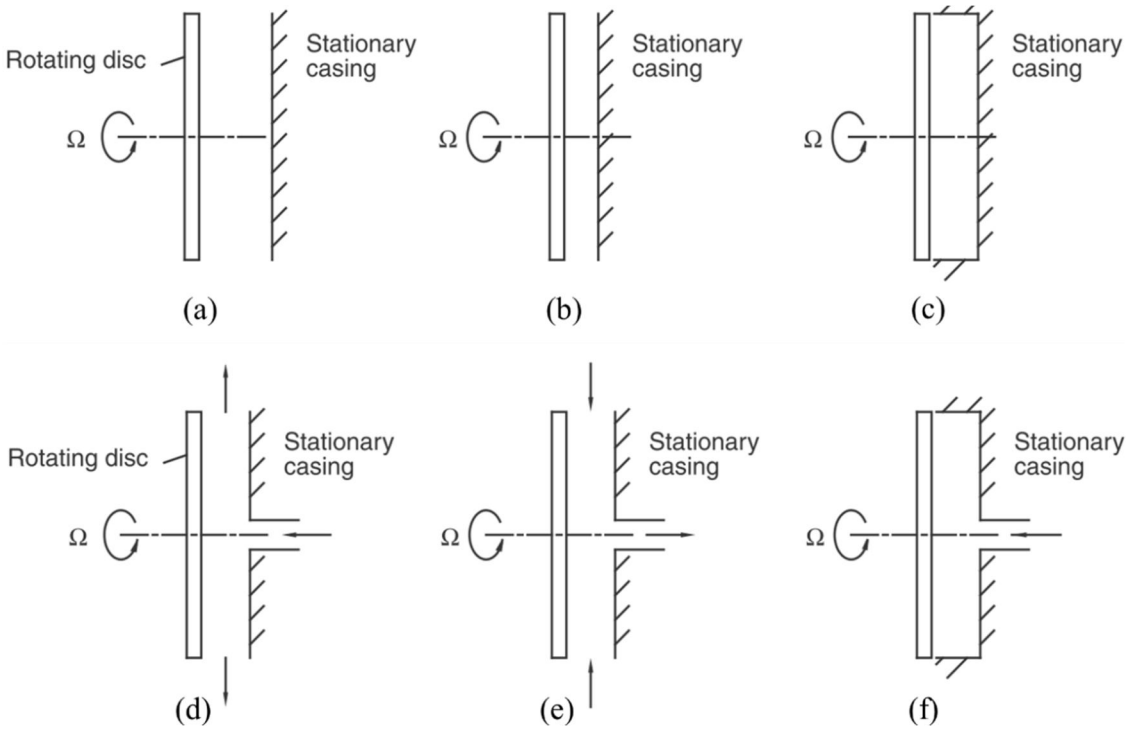

Figure 2.3 Selected flow configurations: (a) Rotor-stator disc wheel-space with a large gap, (b) Rotor-stator disc wheel-space with a narrow gap, (c) Enclosed rotor-stator disc wheel-space, (d) Rotor-stator disc wheel-space with radial outflow, (e) Rotor-stator disc wheel-space with radial inflow and (f) Rotor-stator disc wheel-space with stationary shroud and radial outflow (ESDU, cited in Childs 2011).

On the other hand, when the superposed flow rate is higher than the free-disc entrainment rate, the inviscid core is suppressed and the fluid in the rotor-stator system will follow the model proposed by Stewartson (1953). As no core rotation exists for this model, the tangential velocity (u_ϕ) reduces from the rotor disc speed, Ωr, at the rotor surface to zero outside the rotor boundary layer; the radial velocity (u_r) is positive, i.e. fluid flows radially outward, across the wheel-space; and the axial velocity (u_z) is positive, i.e. the fluid flows from the stator boundary layer to the rotor boundary layer. The velocity profiles for Batchelor and Stewartson flows are shown in Fig. 2.4 (a) to (c) and Fig. 2.4 (d) to (f), respectively.

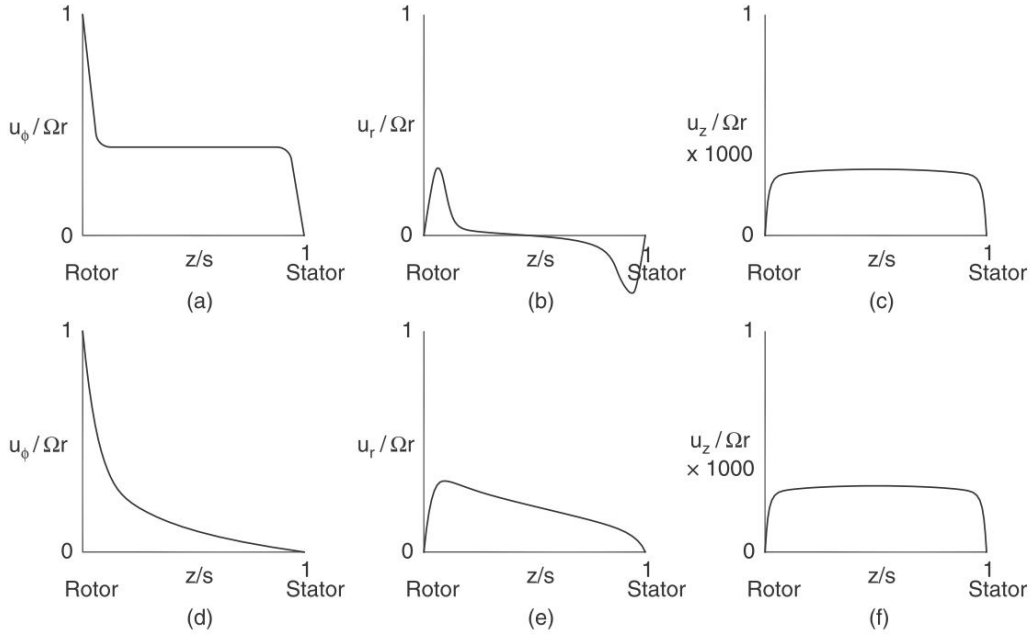

Figure 2.4 Characteristic velocity profiles in a rotor-stator system: (a) and (d) tangential velocity, (b) and (e) radial velocity and (c) and (f) axial velocity (Childs, 2011).

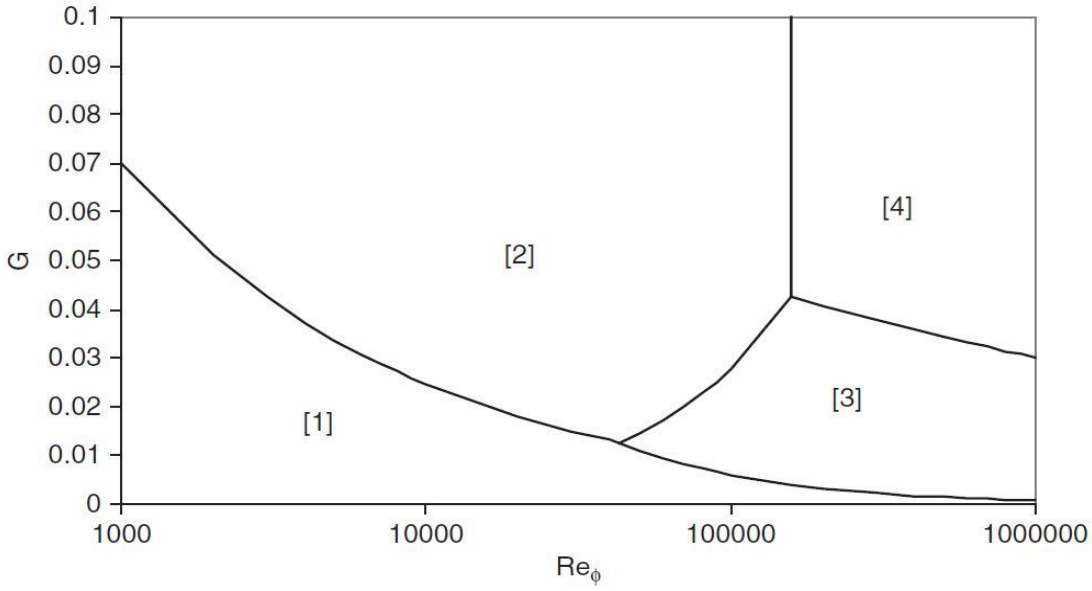

Figure 2.5 Flow regimes for an enclosed rotor-stator wheel-space **(**Daily and Nece, 1960)

Experimental and theoretical studies were carried out by Daily and Nece (1960) and the fluid flow in an enclosed rotor-stator wheel-space was categorised, shown in Fig. 2.5 as a function of the gap ratio (G) and the rotational Reynolds number (Re_ϕ)

based on the researches. The four flow regimes categorised by the authors, for a range of $0.0127 < G < 0.217$ and $1x10^3 < Re_\phi < 1x10^7$, are as follows:

Regime 1: Laminar flow, small clearance with merged rotor-stator boundary layers

Regime 2: Laminar flow, large clearance with separate rotor-stator boundary layers

Regime 3: Turbulent flow, small clearance with merged rotor and stator boundary layers

Regime 4: Turbulent flow, large clearance with separate rotor-stator boundary layers

The measurements of the swirl ratio (β) in the core of an enclosed rotor-stator system were made by Daily *et al.* (1964) for three values of the gap ratio (G). The following empirical correlations were determined between β and G.

$$\beta = 0.49 - 0.57G \tag{2.7}$$

The work carried out by Daily and Nece (1960) and Daily *et al.* (1964) are useful for predicting and understanding the flow structure in the wheel-space of rotor-stator systems.

2.3 Ingress

2.3.1 Rotationally-induced (RI) ingress

The so-called 'disc-pumping effect' causes a radial outflow of fluid, or egress, near the rotating disc through the rim seal, and consequently a radial pressure gradient is created in the wheel-space; the resulting pressure in the wheel-space increases with increasing radius. This radial pressure difference creates ingress of external fluid through the seal clearance. This type of ingestion is referred to here as rotationally-induced (RI) ingress and because this is completely caused by the 'disc-pumping effect', it can occur when there is no mainstream flow.

At the very early stage of ingestion research, Bayley and Owen (1970) conducted experiments in a test rig that consisted of a shrouded stator that was axially separated

from a rotor disc without an external annulus, i.e. there was no external flow. A superposed flow was supplied to the system at the centre of the stator disc and flowed radially outward. The experimental setup had a similar configuration to the one shown in Fig. 2.3 (f). They showed ingress of external flow into the wheel-space by measuring static pressure on the stator wall; the pressure inside the wheel-space increased with increasing the sealant flow rate and in turn, reduced the amount of ingress air. They also showed that ingress could be prevented with a sufficiently high sealant flow rate, i.e. when $C_{w,0} \geq C_{w,min}$, where $C_{w,0}$ is the non-dimensional sealing flow rate and $C_{w,min}$ is the minimum value of $C_{w,0}$ to prevent ingress. The authors also showed that $C_{w,min}$ was proportional to Re_ϕ and G_c and proposed the following empirical relationship:

$$C_{w,min} = 0.61 G_c \, Re_\phi \tag{2.8}$$

Phadke and Owen (1983) carried out further research on RI ingress with five different radially spaced shroud geometries. Pressure measurements and a flow visualisation technique were used for the research and it was shown that $C_{w,min}$ for radial-clearance seals is generally lower than that of axial-clearance seals with the same clearance gap. It was also discovered that the sealing performance of the radial seals is proportional to the length of the overlap, whereby pressure in the wheel-space increases with increasing rotating speed; this phenomenon was termed the pressure-inversion effect.

Graber *et al.* (1987) measured sealing effectiveness for a rotating-disc rig using the gas concentration measurement technique for the first time. The rig consisted of a shroudless stator disc and a shrouded rotor, and a series of experiments with four rim seal geometries that were conducted for two different swirl ratios. The coolant flow was seeded with CO_2 gas and the concentrations of this were measured in the annulus, on the stator wall and in the coolant pipe. The cooling effectiveness parameter (ε_c) based on the concentration measurements was defined as:

$$\varepsilon_c = \frac{c_s - c_a}{c_0 - c_a} \tag{2.9}$$

Where, c_s is the mean value of the concentration of CO_2 gas measured on stator wall at multiple radial locations, c_a is the concentration of the gas measured in the annulus and c_0 is the concentration measured in the coolant flow.

The typical variation of the cooling effectiveness parameter with the coolant flow rate is shown in Fig. 2.6 and it can be seen that the rate of change in this parameter decreases as flow rate increases. The authors suggested that a large amount of coolant flow can be saved, if the rotor and stator discs are designed to withstand some level of ingress, such as a cooling effectiveness of 0.8. It was also shown that the level of swirl in the mainstream annulus has little effect on the cooling effectiveness parameter.

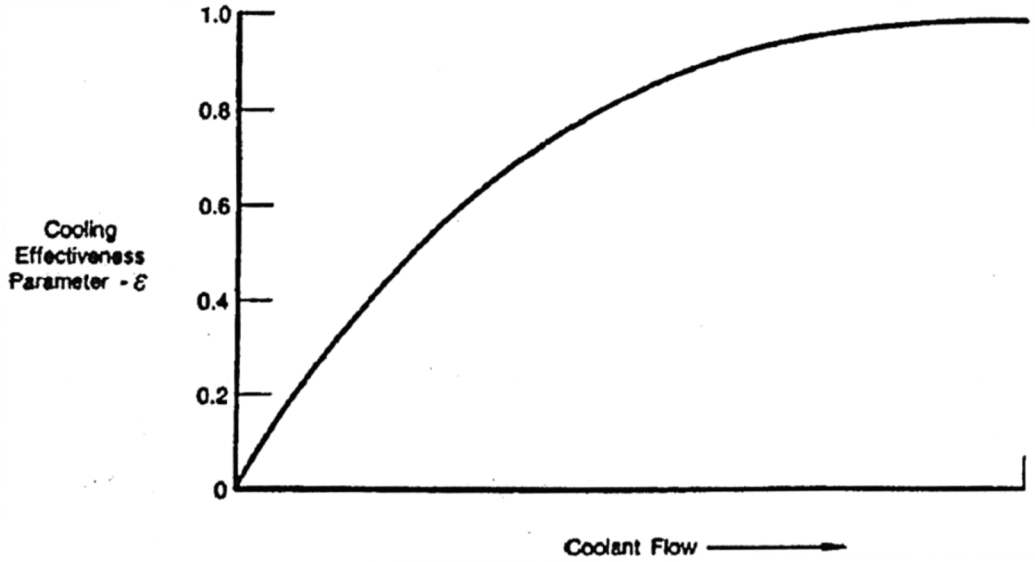

Figure 2.6 Typical variation of the cooling effectiveness parameter with the coolant flow rate (Graber *et al.* (1987))

Phadke and Owen (1988a) made CO_2 gas concentration measurements using the same setup that was used for their previous experiments (Phadke and Owen, 1983), i.e. an ingress study on a rotor-stator system without an annulus. Using a flow visualisation technique, it was found that the previously discovered pressure-inversion effect was caused by an impingement of sealant air that flows radially outwards in the rotor boundary layer, which forms a 'fluid-curtain' that helps to reduce the amount of ingress flow.

2.3.2 Externally-induced (EI) ingress

The dominant type of ingress through turbine rim seal is caused by the circumferential pressure variation in the mainstream annulus, which is created by the mainstream flow passing over the nozzle guide vanes and turbine blades. Ingress and egress occur when the pressure in the external flow (mainstream flow) is higher and lower than that in the wheel-space. This type of ingress is termed externally-induced (EI) ingress (Owen, 2011b) and Fig. 2.7 shows how this occurs.

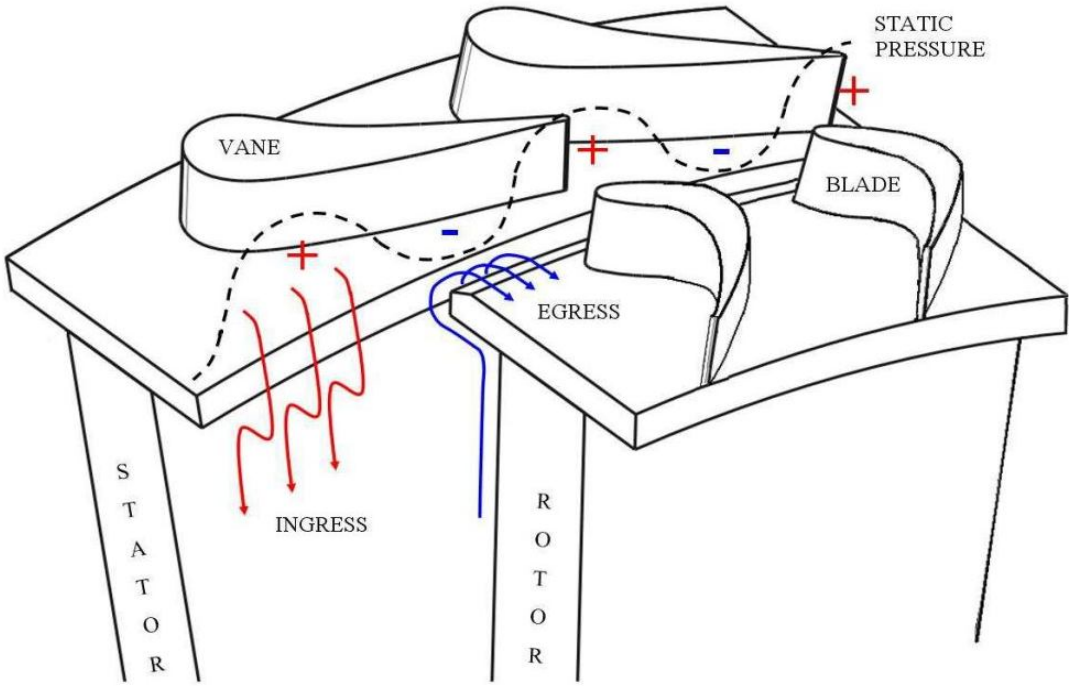

Figure 2.7 Variation of static pressure in a turbine annulus. Ingress and egress occur where the external pressure (mainstream pressure) is higher (marked +) and lower (marked -), respectively, than that in the wheel-space (Sangan *et al.*, 2013a).

Abe *et al.* (1979) conducted the first experiments that showed ingress could be dominated by the mainstream flow in the annulus rather than the 'disc-pumping effect' caused by the rotation of the disc. A stator with 27 nozzle guide vanes and a bladeless rotor were used for the research to create the circumferential pressure asymmetries in the annulus and the density of propane gas was measured at multiple radial locations on the stator wall to determine the amount of ingested mainstream fluid into the wheel-space. From the experiments conducted with several engine

representative rim-seal geometries, it was shown that the sealing flow rate required to prevent ingress increases as the mainstream flow rate increases for a given geometry.

Phadke Owen (1988b, c) investigated ingress of mainstream flow into the wheel-space with quasi-axisymmetric and asymmetric mainstream annular flow. In order to achieve asymmetric annular flow, honeycomb sections attached to wire mesh were used instead of nozzle guide vanes and rotor blades. The sealant flow was supplied to the wheel-space through the pipe connected to the centre of the stator disc and the tests were conducted for a range of Re_ϕ and Re_w up to 1.2×10^6. The following three experimental techniques were used for the experiments:

- Static pressure measurement: $C_{w,min}$ was determined by comparing the static pressure value measured inside the wheel-space to that measured outside.

- Flow visualisation: the mainstream flow was seeded with smoke particles and the level of these flowing into the wheel-space was monitored to determine $C_{w,min}$.

- Nitrous oxide, N_2O, concentration measurement: concentration measurements were made at a fixed point on the stator wall to determine $C_{w,min}$.

The effect of external flow on ingress was investigated by Phadke and Owen (1988b) using quasi-axisymmetric external flow for two axial- and one radial-clearance seals; one of the two axial-clearance seals having clearance on the stator-side and the other on the rotor-side. The two flow regimes, one rotation-dominated and the other external flow-dominated, were identified for small and large values of Re_w/Re_ϕ, respectively and the following conclusions were made (these conclusions can be seen in Fig. 2.8.)

- $C_{w,min}$ is proportional to Re_ϕ, when Re_w is zero.

- $C_{w,min}$ decreases as Re_w increases for a small value of Re_w/Re_ϕ, for a given value of Re_ϕ.

- $C_{w,min}$ is proportional to Re_w and the effect of Re_ϕ is negligible for large values of Re_w/Re_ϕ.

It was also concluded that $C_{w,min}$ increases with increasing clearance ratio, G_c, for all seals tested in the two regimes.

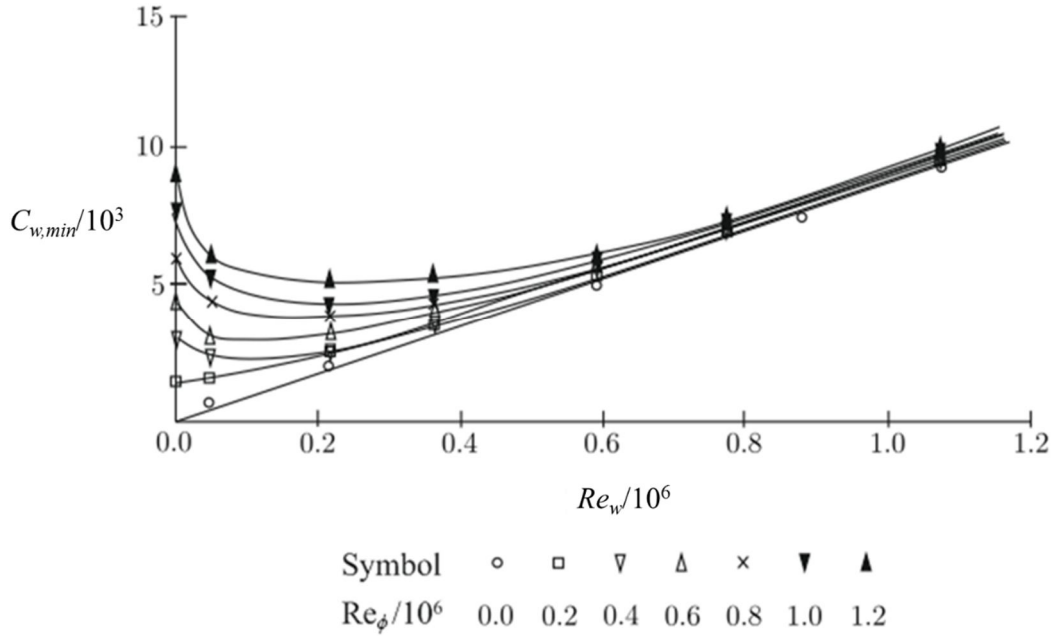

Figure 2.8 Effect of Re_ϕ on the variation of $C_{w,min}$ with Re_w for quasi-axisymmetric external flow for an axial clearance-seal with clearance on the stator-side (Phadke and Owen, 1988b)

Phadke and Owen (1988c) conducted research on the effect of a non-axisymmetric external flow on the sealing performance using static pressure measurements and flow visualisation. Four seal geometries were tested including the three seals tested in Phadke and Owen (1988b) and a double-shrouded radial-clearance seal. In order to separate the effects of the external flow rate and pressure asymmetry, experiments with six different circumferential distributions of static pressure in the annular flow were conducted. The variation of $C_{w,min}$ with Re_w was measured for the six levels of pressure asymmetry when Re_ϕ = 0, i.e. the rotor disc was kept stationary, as shown in Fig. 2.9.

It was found from the experiments that the variation of $C_{w,min}$ with Re_w and the pressure coefficient ($C_{p,max}$) for asymmetric external flow conditions, i.e. in EI ingress conditions, show a similar relationship to that for the quasi-axisymmetric condition for the same seal (axial clearance-seal with clearance on stator-side): $C_{p,max}$ is defined as $C_{p,max} = \Delta P_{max} / \frac{1}{2}\rho\overline{W}^2$, where P_{max} is defined in Eq. 2.11 and $\overline{W}$ is the

uniform value of the axial component of velocity in the external-flow. The variation of $C_{w,min}$ with Re_w for the asymmetric external flow condition, i.e. the EI ingress condition, is shown in Fig. 2.10 and the variation of $C_{w,min}$ with Re_w for the quasi-axisymmetric case with Re_ϕ= 0 is also shown in the graph for comparison.

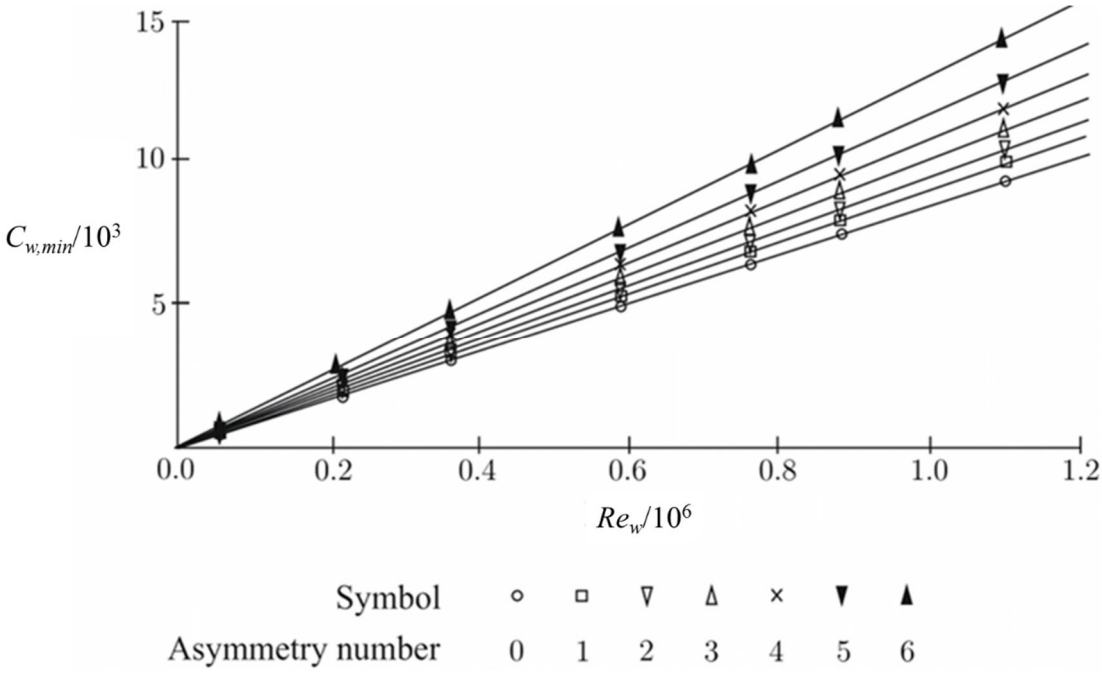

Figure 2.9 The variation of $C_{w,min}$ with Re_w for the six different pressure asymmetries in the annular flow when G_c=0.01 and Re_ϕ=0 (Phadke and Owen, 1988c).

The following empirical correlation between $C_{w,min}$, G_c and P_{max} was obtained by flow visualisation for all the seal geometries tested at G_c = 0.005, 0.01 and 0.02 for $Re_w \leq 1.1\times10^6$:

$$C_{w,min} = 2\pi G_c K P_{max}^{1/2} \tag{2.10}$$

$$P_{max} = \frac{1}{2} C_{p,max} Re_w^2 \tag{2.11}$$

where, K is an empirical constant, which was found to be 0.6 as shown in Fig. 2.11.

It was also pointed out that a double-shrouded radial-clearance seal would have better performance than other seal geometries in improving sealing performance.

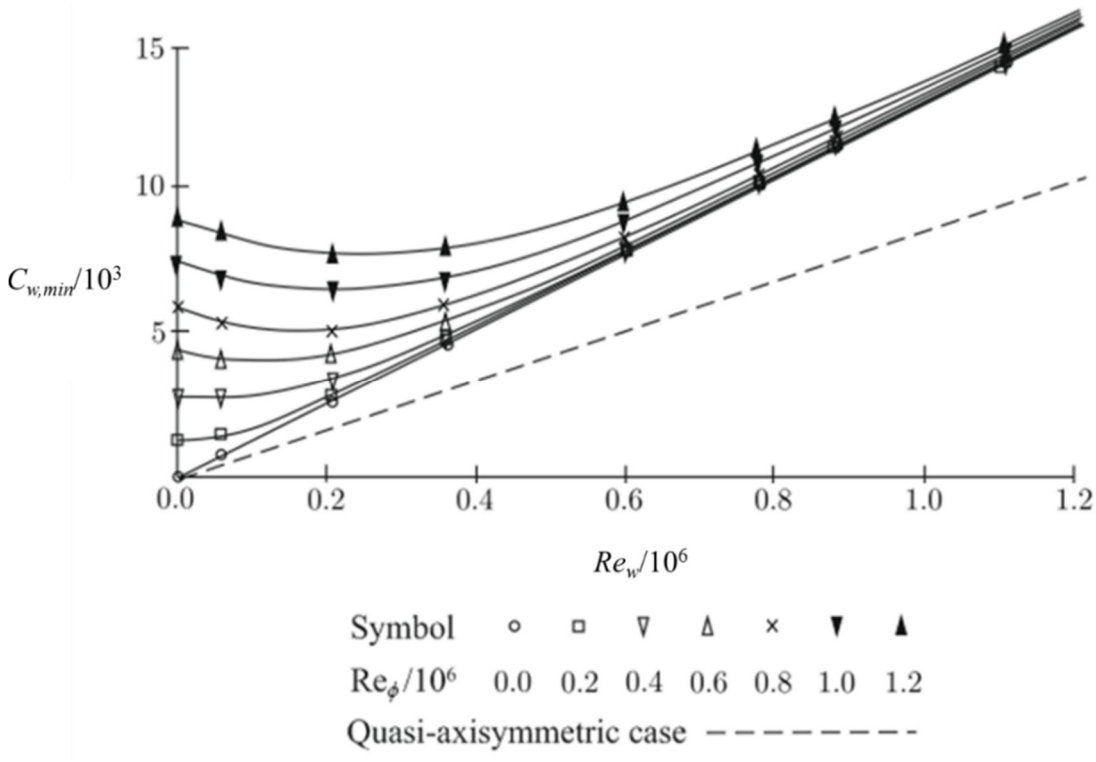

Figure 2.10 Effect of Re_ϕ on the variation of $C_{w,min}$ with Re_w for asymmetric external flow ($C_{p,max}$ =0.48) for an axial clearance-seal with clearance on the stator-side (Phadke and Owen, 1988c).

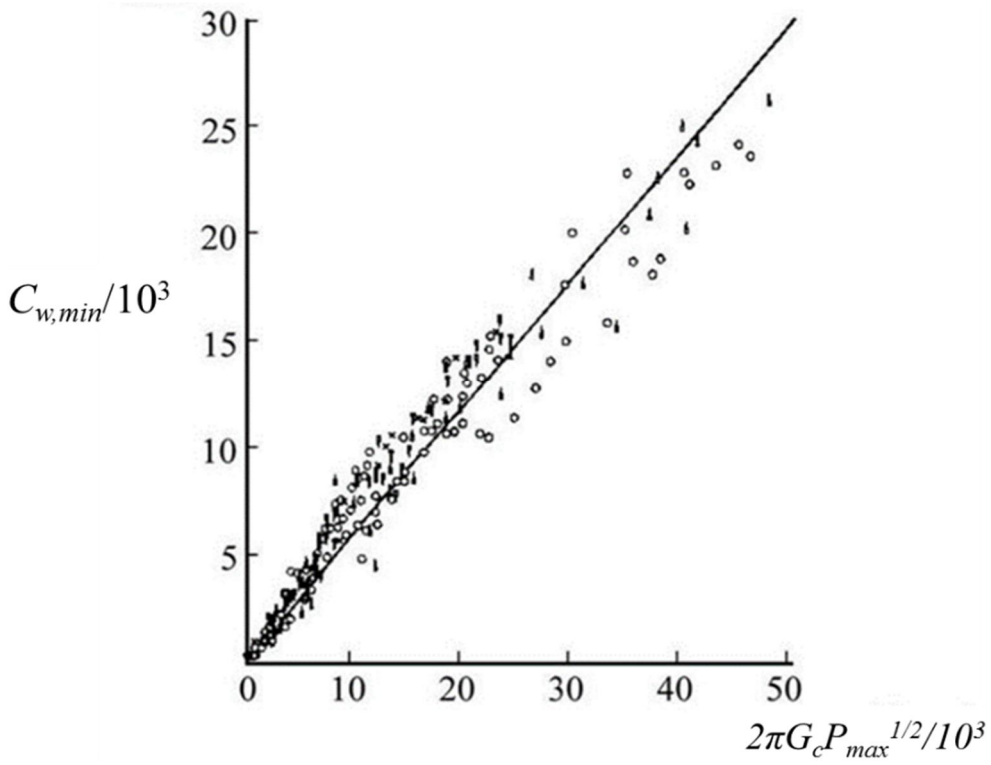

Figure 2.11 Variation of $C_{w,min}$ with $2\pi G_c P_{max}^{1/2}$ (Phadke and Owen, 1988c).

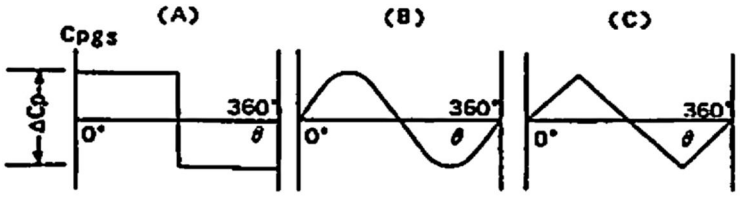

Figure 2.12 The three simplified circumferential pressure variation profiles used for the model (Hamade and Ishida, 1992).

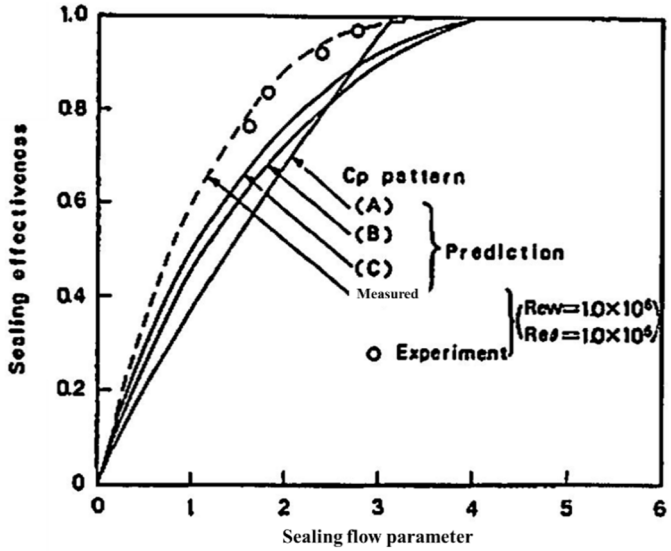

Figure 2.13 Variation of sealing effectiveness with the sealing flow parameter comparing the predicted variations with experimental values (Hamada and Ishida, 1992).

Hamabe and Ishida (1992) carried out experiments with a concentration measurement technique to examine the simplified model that was previously developed by the authors to predict the variation of effectiveness with sealing flow rate. The model was solved for three simplified circumferential pressure variation profiles (shown in Fig 2.12) and the measured pressure distribution, which was acquired from the 24 pressure taps on the outside wall of the annulus at 30mm downstream of the nozzle guide vanes. As shown in Fig. 2.13, the model with the measured pressure distribution provided the best prediction, however, that with all three simplified pressure profiles showed under-predicted sealing effectiveness. It was, therefore, concluded that the shape of the circumferential pressure variation profile has considerable effects on the predicted sealing effectiveness and that actual pressure distribution in the annulus is necessary to predict the sealing effectiveness accurately.

Dadkhah *et al.* (1992) conducted research on EI ingress in a test facility with reversible disc assemblies that allowed experiments with both upstream and downstream wheel-space configurations. Gas concentration measurements were made to determine the level of ingestion at four radial locations and axial distribution of gas concentration measurements were also made at seven axial locations per each radial location in the wheel-space. From the axial variation of the concentration measurements, it was shown that the ingested external flow travelled radially downward on the stator side and then flowed across the fluid core to be entrained into the rotor boundary layer. As a result, the rotor surface showed the 'least contamination' by the ingested external flow. The authors also concluded that if stator and rotor discs are designed to sustain a sealing effectiveness value of 0.95, then approximately 35% of sealing flow could be saved compared to a fully sealed system, which agrees with a conclusion made by Graber *et al.* (1987). However, as no vanes and blades were installed in the test facility, the external flow had a low circumferential pressure asymmetry in the annular flow, i.e. a quasi-axisymmetric flow.

Green and Turner (1994) conducted experiments in a single-stage gas turbine test facility with bladeless rotor using N_2O gas concentration measurements. The test rig was modified for experiments with and without rotor blades and the same measurement techniques as Chew *et al.* (1994), including N_2O concentration measurements, were used. Surprisingly, it was shown that the amount of ingress into the wheel-space was reduced by adding rotor blades. The authors concluded that rotor blades, together with nozzle guide vanes, play an important role on ingress and therefore, experimental rigs should be designed to have engine-representative configurations to obtain meaningful results.

Bohn *et al.* (1995) investigated EI ingress using Laser Doppler Velocimetry (LDV) in a one-stage ingress test rig with 30 vanes and no blades. Static pressure measurements in the annulus were made across two vane pitches at three axial locations downstream of the vane trailing edge. It was shown that the magnitude of peak-to-trough pressure difference over the two vane pitches decayed with distance from the vane trailing edge. Consequently, the level of ingress, increased as the vanes were moved closer to the rim seal. In addition, pressure criteria, which

compared the radial static pressure distribution in the wheel-space to the average vane pitch pressure in the annulus, were used to determine if ingress occurs, i.e. if the pressure in the wheel-space is less than in the mainstream flow, it can be assumed that hot gas ingress occurs.

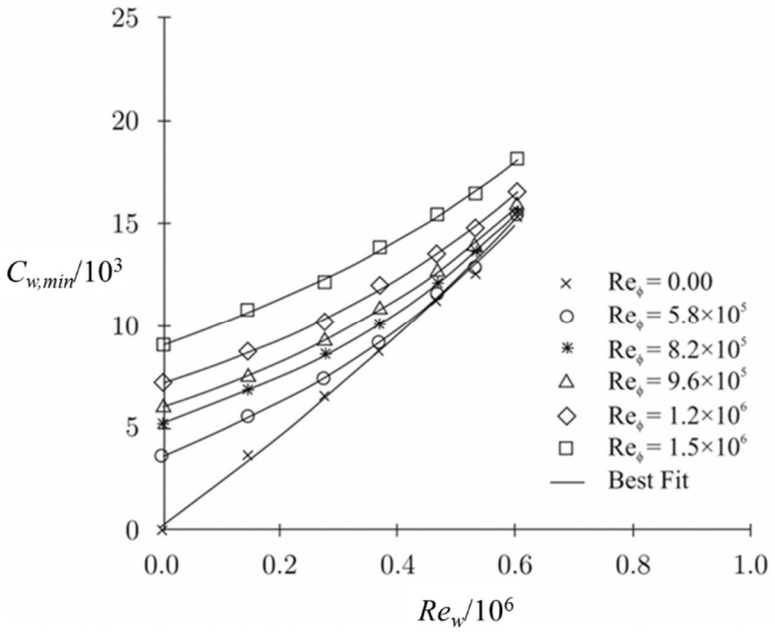

Figure 2.14 Variation of $C_{w,min}$ with Re_w and Re_ϕ for an engine representative axial-clearance seal (Khilnani and Bhavnani, 2001).

Khilnani and Bhavnani (2001) investigated the sealing performance of an engine-representative axial-clearance seal in a gas turbine test facility without vanes and blades. Concentration and pressure measurements were made to determine $C_{w,min}$ for a range of Re_ϕ and Re_w values and the variation of $C_{w,min}$ with Re_w for six different Re_ϕ values are shown in Fig. 2.15. The experimental results showed a good agreement with those of Phadke and Owen (1988c) for asymmetric external flow, which is shown in Fig. 2.10. However, as the maximum Re_w/Re_ϕ value used for Khilnani and Bhavnani (2001) was approximately half that for Phadke and Owen, the $C_{w,min}$ values were still affected by Re_ϕ even at the highest value of Re_w tested. That is, the experiments were conducted in a combined ingress regime, where the effects of both rotational speed and external flow are significant.

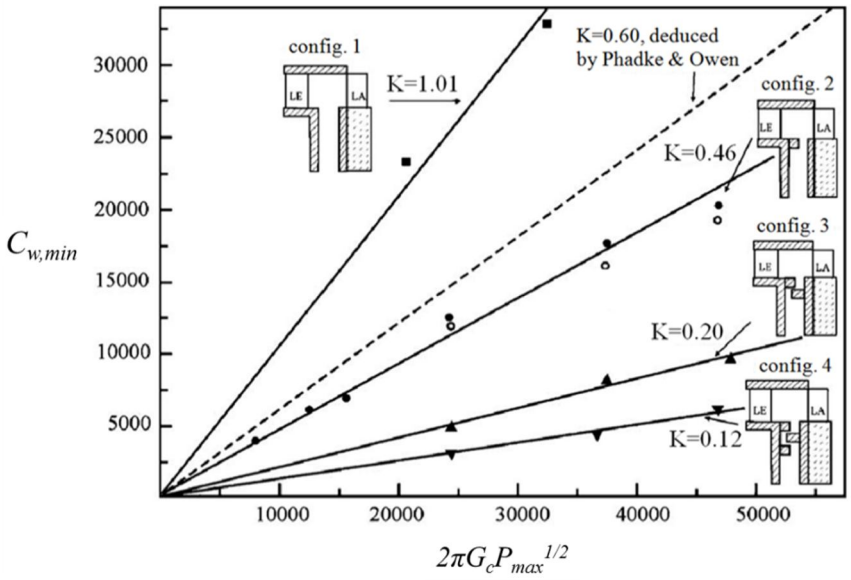

Figure 2.15 Variation of $C_{w,min}$ with $2\pi G_c P_{max}^{1/2}$ for four seal geometries (Bohn and Wolff, 2003).

Bohn and Wolff (2003) carried out an experimental study on EI ingress in a 1.5-stage ingress test facility for four rim seal geometries. CO_2 concentration measurement was used to determine $C_{w,min}$ and steady pressure measurements were also made on both the vane hub and stator wall. Correlations between $C_{w,min}$, G_c, and P_{max} were made based on the experimental measurements taken for the four rim seal geometries. The value of an empirical constant, K, was determined for each seal geometry to have the least squares error when fitted to the experimental data. Fig. 2.15 shows experimental data and K values for each seal tested. It was suggested that the value of K = 0.6 used by Phadke and Owen (1988c) gives a very conservative estimation of $C_{w,min}$ for three rim seal configurations, i.e. config. 2, 3 and 4 in Fig. 2.15.

Roy *et al.* (2007) conducted an experimental and computational study on EI ingress. The experiments were carried out in a single-stage turbine test facility using static pressure, CO_2 concentration and Particle Image Velocimetry (PIV) measurements. The time-resolved velocity maps obtained by PIV measurements showed ingress and egress occurring simultaneously, with the tangential velocity being respectively high and low in the wheel-space.

Zhou *et al.* (2011a) investigated the effect of rim seal geometry on EI ingress with three rim seal geometries including a double seal. CO_2 concentration and the PIV

technique were used to measure the level of ingestion and the instantaneous velocity in the wheel-space, respectively. At low sealant flow rate, the tangential and radial velocity distribution near the rim seal, acquired by PIV, were used to identify the locations where ingress and egress occurred.

Tian *et al.* (2014) conducted a computational study on the effects of ingress on the flow structure and heat transfer in the wheel-space. In particular, the thermal buffering effect, where the effect of ingress on the rotor is less than that measured on the stator, was shown, with the thermal buffer ratio (μ) being defined as the ratio of the stator sealing effectiveness to the rotor sealing effectiveness. Moreover, it was shown that the radial variation of μ is virtually independent of the sealing flow rate, and increases as the sealing flow rate increases.

2.4 Heat transfer in rotor-stator systems

2.4.1 The free disc

Convective heat transfer on a free rotating disc in a stationary fluid has been studied experimentally/theoretically by many researchers. The relationship between the local (Eq. 2.12)/mean (Eq. 2.13) Nusselt number and rotational Reynolds number has usually been provided as follows:

$$Nu_r = A Re_{\phi,r}^{\ B} \tag{2.12}$$

$$Nu_{av} = C Re_{\phi}^{\ D} \tag{2.13}$$

Where, A and C are empirical constants that depend on the flow regime, the Prandtl number and the radial temperature distribution of the disc, and B and D are exponents that depend on the flow regime, whilst $Re_{\phi,r}$ is the local rotational Reynolds number.

One example of such research is the study conducted by Owen and Rogers (1989). Assuming a power law temperature distribution on a rotating disc surface, the

boundary layer equations for turbulent flow over the free disc were solved. The correlation for the local Nusselt number was proposed as:

$$Nu_r = 0.0267\left(\frac{n+2.6}{4.6}\right)^{0.2} Pr^{0.6}[(r/b)^2 Re_{\phi,r}]^{0.8} \tag{2.14}$$

where, n is the power term obtained from the power law temperature distribution of the rotor disc surface; n = 0 for an isothermal disc. Hence, for an isothermal disc rotating in air (where $Pr \approx 0.71$), Eq. 2.14 can be reduced to:

$$Nu_r = 0.0194[(r/b)^2 Re_{\phi,r}]^{0.8} \tag{2.15}$$

2.4.2 Rotor-stator systems

As discussed in subsection 2.2.3, Daily and Nece (1960) categorised the fluid flow in an enclosed rotor-stator wheel-space as a function of G and Re_ϕ. Dofman (1963) proposed correlations between the Nu_r and Re_ϕ for the two regimes with high gap ratio, i.e. regime II and IV, as follows: (*Note*: The gap ratio G does not appear in these correlations because experiments were conducted for a single value of G.)

$$Nu_{r,II} = 0.922 Re_{\phi,r}^{0.5} \tag{2.16}$$

$$Nu_{r,IV} = 0.025 Re_{\phi,r}^{0.8} \tag{2.17}$$

Owen and Rogers (1989) proposed a correlation between the local and mean Nusselt number on the rotating disc and the gap ratio for regime I as follows:

$$Nu_{r,I} = \frac{1}{G}\frac{r}{R} \tag{2.18}$$

$$\overline{Nu_{r,I}} = \frac{1}{G} \tag{2.19}$$

where, R is the radius of the disc. It can be seen from Eq. 2.18 (2.19) that the local (mean) Nusselt number on the rotating disc is independent of the rotational speed and proportionally increases with a decrease in *G*.

Owen and Rogers also proposed a correlation for regime III, which has a low *G* and a high Re_ϕ, as follows:

$$Nu_{r,III} = 0.01176 \left(\frac{r}{R}\right)^{\frac{7}{4}} G^{-\frac{1}{4}} Re_\phi^{\frac{3}{4}} \tag{2.20}$$

$$\overline{Nu}_{r,III} = \frac{0.0308}{\pi} G^{-\frac{1}{4}} Re_\phi^{\frac{3}{4}} \tag{2.21}$$

Metzger *et al.* (1991) pioneered the use of TLC to measure surface temperature for heat transfer experiments in a rotor-stator system. A solution with semi-infinite and step-change assumptions was used to determine the variation of the local Nusselt number with the non-dimensional radius (*r/b*) on a rotor disc. A coolant air jet was provided normal to the rotor surface through a nozzle on the stator disc and the step change in the jet temperature was achieved using a variac electric heater and a ball diverter valve, i.e. the air was heated first by the electric heater until stabilised and then rapidly directed to the nozzle by the diverter valve. The variation of heat transfer to the rotor with the location of the coolant jet was investigated and it was concluded that the highest average Nusselt number was observed when the jet was impinged at the centre of the rotor disc.

Bunker *et al.* (1992a, b) investigated the effect of the gap ratio of the wheel-space on the heat transfer to the rotor for a rotor-stator system with a coolant air injection. The same experimental set up and temperature measurement technique as Metzger *et al.* (1991) were used with four radial locations of coolant injection: *r/b* = 0, 0.2, 0.4 and 0.8. The variation of Nu_r with *r/b* was determined using a solution with semi-infinite and step-change assumptions. In part 1 of the two papers, the case of hub (i.e. *r/b* = 0) injection of coolant was studied (Bunker *et al.* 1992a). It was shown by the local variation in the rotor heat transfer coefficient that heat transfer was dominated by the impingement of coolant air and the rotational speed of rotor at low and high radii, respectively, with a region of a low heat transfer coefficient situated between

these. It was also shown that the radial extent of these regions was dependent on the experimental configuration, including the mass flow rate of the air jet, the gap ratio of the wheel-space (G) and Re_ϕ. It was also found that the overall heat transfer to the rotor was optimised by median (i.e. $0.4 < r/b < 0.6$) and hub (i.e. $r/b = 0$) injection depending on the rotational speeds, coolant mass flow rates and the gap ratio of the wheel-space; higher overall heat transfer to the rotor resulted from the median injection for close spacings (i.e. $G \leq 0.1$), high rotational speeds and high mass flow rates. The authors also showed that the radial heat transfer distribution on the rotor disc was significantly affected by even small changes in its geometry.

Chew *et al.* (1994) conducted experiments in a single-stage gas turbine test facility with a bladeless rotor using N_2O gas concentration measurements. A simple axial-clearance seal was tested with a clearance on the rotor side of $G_c = 0.01$. The variation of the ingress and egress discharge coefficients, $C_{d,i}$ and $C_{d,e}$ respectively, with the annulus-to-seal mean velocity ratio (u_e/u_m), where u_e is the average axial velocity for annulus flow and u_m is the average radial velocity through the rim seal, was derived using the continuity equation. The authors' CFD model provided some encouraging agreement with experimental measurements, especially for the value measured at a lower sealing flow rate (with ingress), and enabled the investigation of the effect of ingress on the rotor disc. Fig. 2.16 shows the variation of the sealing effectiveness on the rotor disc with the radius, which is obtained from the CFD model. The CFD and experimental data for the stator disc are also provided in the graph for comparison. It can be clearly seen that the rotor sealing effectiveness is higher than that of the stator disc, i.e. the effect of ingress on the rotor is smaller than that on the stator.

Chen *et al.* (1996) carried out experiments to measure velocity and Nusselt number for a rotor-stator system that is open to the atmosphere through an axial-clearance rim seal, i.e. rotationally-induced ingress. Laser Doppler Anemometry (LDA) measurements were made at various radial locations in the wheel-space and temperature measurements were made using heat flux meters and thermocouples for steady-state heat transfer experiments conducted on the heated rotor. It was found that the flow in the wheel-space comprised a radial inflow and outflow in the stator and rotor boundary layer, respectively, and a rotating core between the two boundary

layers. That is, the flow structure in the wheel-space was similar to that of Batchelor (1951). The steady-state heat transfer experiments were conducted by keeping the heat flux through the rotor constant and ambient sealant flow was used; the constant heat flux was achieved by heating the back-face of the rotor with radiant heaters. It was found that the Nusselt numbers increased with $C_{w,0}$ and those obtained for the largest value of λ_T tested, approached the free-disc levels.

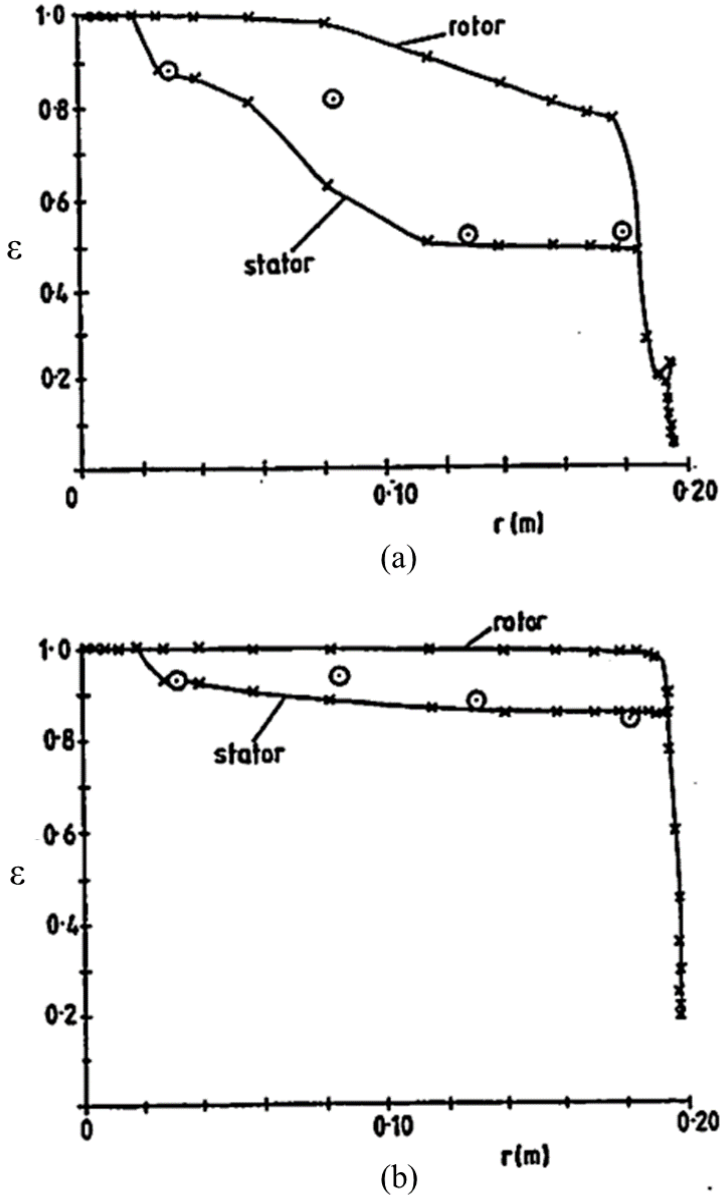

Figure 2.16 Variation of calculated sealing effectiveness with radius on rotor and stator discs for two cases with different level of ingress, open circles are measured values; (a) u_m/u_e = 0.064, (b) u_m/u_e = 0.194 (Chew e*t al.*, 1994).

Roy *et al.* (2001) conducted heat transfer experiments in a rotor-stator system with a radial-clearance rim seal to investigate the effect of varying Re_ϕ and $C_{w,0}$ on the distribution of the convective heat transfer to the rotor. The experiments were carried out under the EI ingress condition and TLC, with thermocouples and embedded resistance temperature detectors (RTDs) being used to acquire temperature data. The experiments were conducted for $1504 < C_{w,0} < 7520$ and $4.6 \times 10^5 < Re_{\phi,r}$ (local rotational Reynolds number) $< 8.6 \times 10^5$ and $Re_w = 5 \times 10^5$ and the results showed that the convective heat transfer coefficient on the rotor disc was significantly affected by ingested mainstream air as well as the rotor disc speed in the core region of the wheel-space. Based on the experimental data (Fig. 2.17), a correlation between the local Nusselt number on the rotor disc and the relative local rotational Reynolds was proposed as follows:

$$Nu_r = 0.0074 \left[(1-\beta) Re_{\phi,r}\right]^{0.89} \tag{2.22}$$

where, β is the swirl ratio (the core fluid rotation ratio).

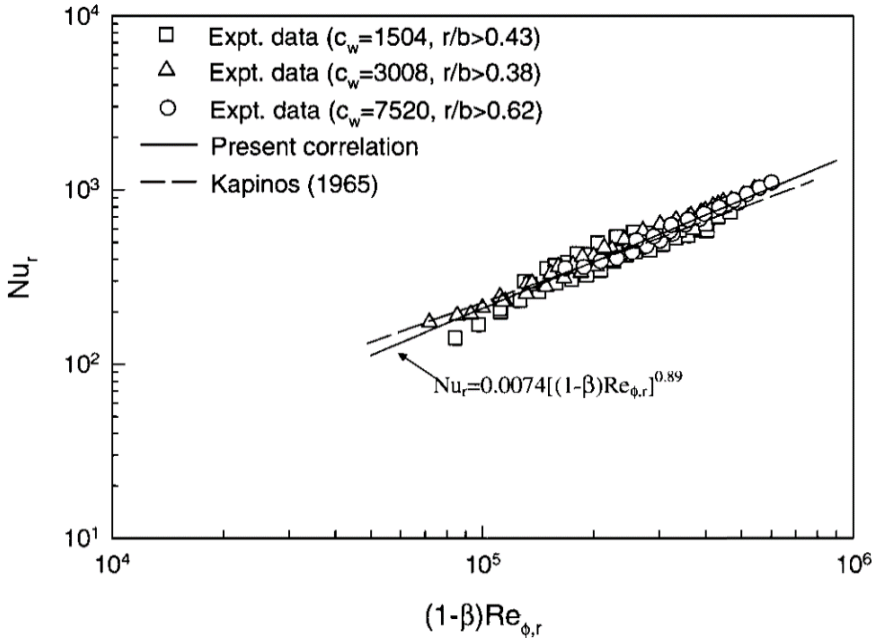

Figure 2.17 Variation of the local Nusselt number with the local relative rotational Reynolds number with empirical correlation (Roy *et al.* 2001).

Boutarfa and Harmand (2005) carried out heat transfer experiments in a shroudless rotor-stator system with a central opening in the stator without supplying

sealant flow. Embedded thermocouples with a slip-ring system and an infrared camera were used for to measure temperature of rotor disc in order to determine the local heat transfer coefficients on it. From the experimental results, the correlation between the local Nusselt number (Nu_r) on the rotor and the local rotational Reynolds number ($Re_{\phi,r}$) was proposed for the four flow regimes identified by Daily and Nece (1960) as follows:

$$Nu_r = CXRe_{\phi,r}^{\ m} \tag{2.23}$$

where, C and m are empirical constant and X is a function of the gap ratio, G.

Although the correlation was only applicable for an isothermal system with a range of $0.01 < G < 0.17$ and $5.67\times10^4 < Re_\phi < 1.4\times10^6$ and the experiments were not conducted in an engine representative setup, the importance of the flow structure in the wheel-space on the heat transfer to the rotor was demonstrated.

Pellé and Harmand (2007) conducted extensive heat transfer experiments in a rotor-stator system with an open end air gap for a range of $0.01 < G < 0.16$ and $1.29\times10^5 < Re_{\phi,r} < 6.45\times10^5$. Based on the experimental results, the authors proposed four heat transfer regimes as a function of the gap ratio and the local rotational Reynolds number, as shown in Fig. 2.18. All four heat transfer regimes shown in the figure are corresponding to the flow regimes shown in Fig. 2.5.

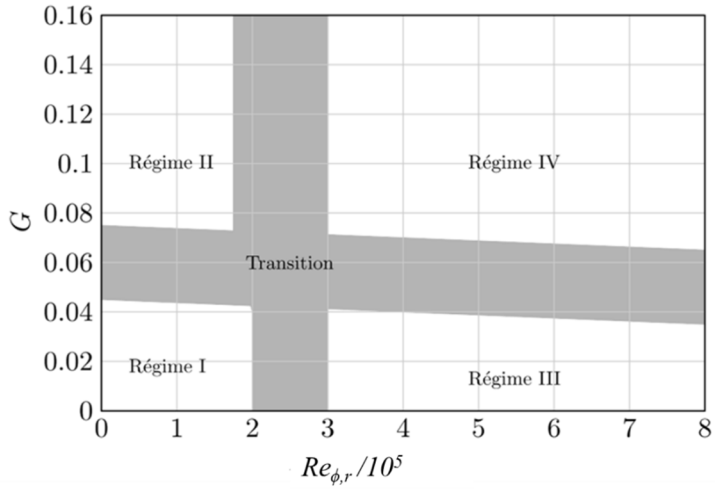

Figure 2.18 The four heat transfer regimes categorised as a function of G and $Re_{\phi,r}$ (Pellé and Harmand, 2007).

The local Nusselt numbers were correlated with the gap ratio and local rotational Reynolds number for regimes I, II and IV as follows:

$$Nu_{r,I} = 70\left(1+e^{-140G}\right)Re_{\phi}^{-0.456}\,Re_{\phi,r}^{0.478} \tag{2.24}$$

$$Nu_{r,II} = 0.463\left(1-e^{-40G}\right)\left(1-e^{-120000\,Re_{\phi}}\right)Re_{\phi,r}^{-0.456} \tag{2.25}$$

$$Nu_{r,IV} = 0.035\left(1-e^{-40G}\right)\left(1-e^{-420000\,Re_{\phi}}\right)Re_{\phi,r}^{-0.456} \tag{2.26}$$

2.5 Ingestion research at the University of Bath

Owen (2011a, b) created an orifice model to predict ingress through the seal clearance for both RI and EI ingress. The orifice models were derived for compressible and incompressible inviscid swirling flows and the seal clearance was treated as an orifice ring, where ingress and egress occur through the elemental areas δA_i and δA_e respectively, as shown in Fig. 2.19; the summation of the two areas is equal to the axial-clearance area, δA_c. Although the equations were derived for inviscid flow, in order to account for viscous losses, two discharge coefficients were introduced for ingress and egress, $C_{d,i}$ and $C_{d,e}$, respectively. These two coefficients were the only two parameters for the orifice model that needed to be determined empirically based on the measured values of the non-dimensional sealing parameter (Φ_0) and the sealing effectiveness (ε), which are defined as follows:

$$\Phi_0 = \frac{C_{w,0}}{2\pi G_c\, Re_{\phi}} = \frac{U}{\Omega b} \tag{2.27}$$

$$\varepsilon = 1 - \frac{\Phi_i}{\Phi_e} = \frac{\Phi_0}{\Phi_e} = \frac{\Phi_0}{\Phi_0 + \Phi_i} \quad \text{(when } \Phi_0 < \Phi_{min}\text{)} \tag{2.28}$$

The RI orifice model was then extended by Owen (2011b) for EI and combined-ingress (CI) cases. By assuming the circumferential pressure variation in the annulus had a 'saw-tooth' profile, the EI and CI orifice equations were solved for incompressible inviscid swirling flow. Under the assumption that both the discharge coefficients were equal (i.e. $\Gamma_c = C_{d,i}/C_{d,e} = 1$), the EI orifice model was validated by applying it to the experimental data published by Johnson *et al.* (2008) and showed

good agreement. However, the orifice model for the CI case was not validated due to a lack of published data for the condition.

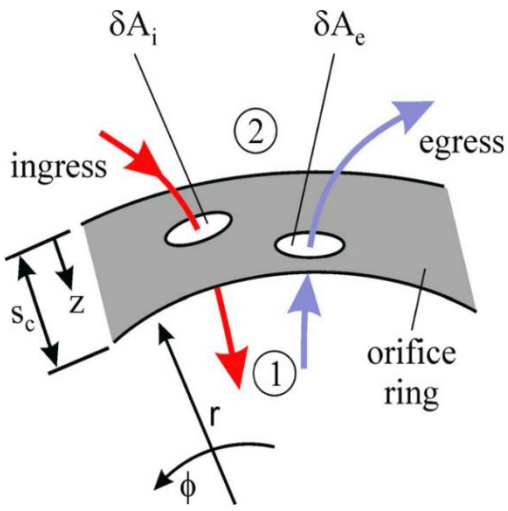

Figure 2.19 Orifice model (Owen, 2011a)

Owen (2011a) solved the RI orifice equation for incompressible flow and applied it to the experimental data of Graber *et al.* (1987). It was found that the prediction of ε determined with the RI orifice model provided a good agreement with the experimental data.

Sangan *et al.* (2013a) conducted an experimental study on EI ingress in the Bath one-stage test facility that was also used for the research presented in this PhD thesis. Static pressure measurements were made in the annulus, downstream of vane trailing edges, to determine the variation of the non-dimensional peak-to-trough pressure difference, ΔC_p. In addition, CO_2 gas concentration measurements were made to assess the performance of two generic (though engine-representative) rim seal geometries at design operating conditions. The experiments were carried out for three different Re_ϕ values to show their effect on the variation of ε with Φ_0.

Based on the implicit equations for EI effectiveness derived by Owen (2011b), the authors derived an equation, which was referred to as the 'EI effectiveness equation', which provides an explicit relationship between ε and Φ_0 as follows:

$$\frac{\Phi_0}{\Phi_{min,EI}} = \frac{\varepsilon}{\left[1+\Gamma_C{}^{-2/3}\left(1-\varepsilon\right)^{2/3}\right]^{3/2}} \tag{2.29}$$

where, Γ_c is the ratio of the discharge coefficients ($\Gamma_c = \frac{C_{d,i}}{C_{d,e}}$).

The non-dimensional ingress flow into the wheel-space, Φ_i, was determined from the experimental variation of ε with Φ_0, by:

$$\Phi_i = \Phi_0\left(\varepsilon^{-1} - 1\right) \tag{2.30}$$

By combining Eq. 2.29 and 2.30:

$$\frac{\Phi_i}{\Phi_{min,EI}} = \frac{1-\varepsilon}{\left[1+\Gamma_C{}^{-2/3}\left(1-\varepsilon\right)^{2/3}\right]^{3/2}} \tag{2.31}$$

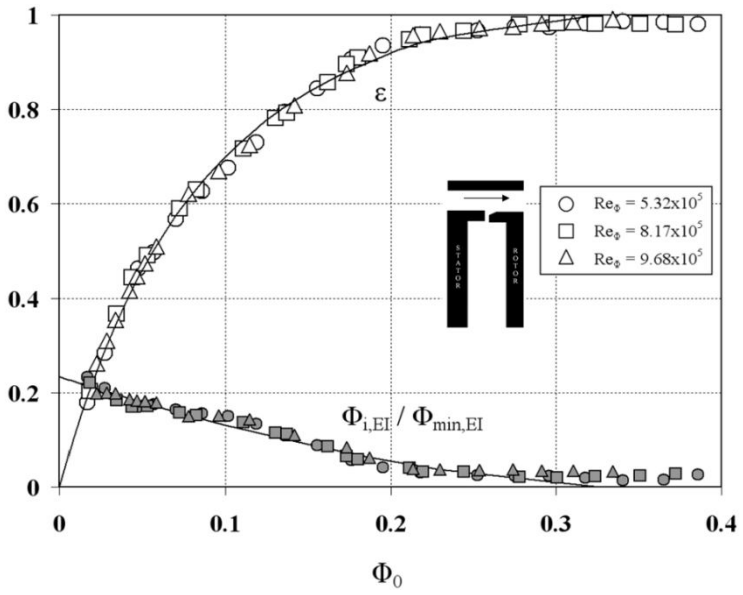

Figure 2.20 Comparison between theoretical effectiveness curves and experimental data for an axial-clearance seal with EI ingress at design condition (Open symbols denote ε data; closed symbols denote $\Phi_{i,EI}/\Phi_{min,EI}$ data; solid lines are theoretical curves) (Sangan *et al.* 2013a)

It can be seen from Eq. 2.29 that the variation of ε with Φ_0 depends on two parameters, $\Phi_{min,EI}$ and Γ_c. In order to determine the two empirical values from the experimental data of ε and Φ_0, the fit between the effectiveness equation and the experimental variation of ε with Φ_0 was made by using the statistical model developed by Zhou *et al.* (2013), which optimises the fitting in terms of $\Phi_{min,EI}$ and

Γ_c. The experimental variation of effectiveness and the theoretical variation of it, which was obtained using the statistical method for an axial-clearance seal, are provided in Fig. 2.20. A good agreement between the theoretical variation of effectiveness and the experimental data were observed for both axial- and radial-clearance seal data and the best $\Phi_{min,EI}$ and Γ_c values for each seal were determined. It was found from the estimated $\Phi_{min,EI}$ values for the two seals that the radial-clearance seal requires approximately 26% that of the sealing flow rate for the axial-clearance seal to protect the wheel-space fully from ingested mainstream flow.

Sangan *et al.* (2013b) conducted an experimental study on RI ingress at design operating conditions for the same rim seal geometries as used for Sangan *et al.* (2013a). The experiments were carried out for three different Re_ϕ values to show their effect on the variation of ε with Φ_0. Similar to the EI ingress case, the authors derived an explicit equation, the 'RI effectiveness equation', based on the implicit equations for EI effectiveness created by Owen (2011a):

$$\frac{\Phi_0}{\Phi_{minRI}} = \frac{\varepsilon}{\left[1+(1-\varepsilon)^{1/2}\right]\left[1+\Gamma_c^{-2}(1-\varepsilon)\right]^{1/2}} \tag{2.32}$$

and

$$\frac{\Phi_i}{\Phi_{minRI}} = \frac{1-\varepsilon}{\left[1+(1-\varepsilon)^{1/2}\right]\left[1+\Gamma_c^{-2}(1-\varepsilon)\right]^{1/2}} \tag{2.33}$$

It can be seen from Eq. 2.32 that the variation of ε with Φ_0 depends on the two parameters, $\Phi_{min,RI}$ and Γ_c. As for the EI ingress case, the optimum values of $\Phi_{min,RI}$ and Γ_c were estimated by using the statistical model developed by Zhou *et al.* (2013). The experimental and theoretical variation of ε with Φ_0 for the two rim seals tested are shown in Fig. 2.21. It can be seen that this variation is independent of Φ_0 for both the RI and EI ingress of the two seals. In addition, the theoretical fits provide good agreements with the experimental data and the radial-clearance seal shows approximately three times better performance than the axial-clearance seal in terms of $\Phi_{min,EI}$, the values being 0.0915 and 0.326, respectively.

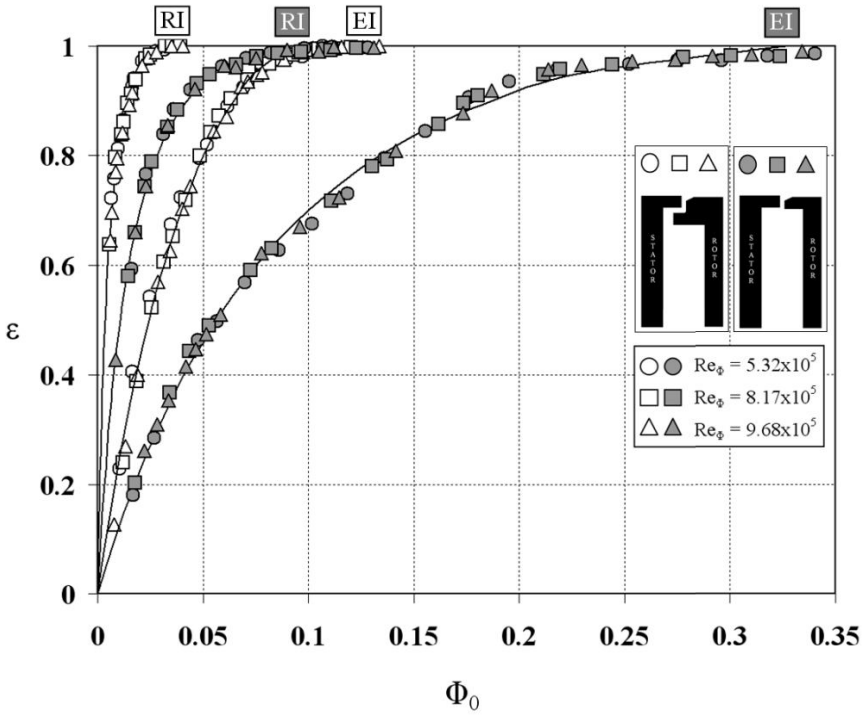

Figure 2.21 Comparison of sealing effectiveness of an axial- and a radial-clearance seal for EI and RI ingress (Symbols denote data; lines are theoretical curves) (Sangan *et al.*, 2011b).

As shown in Fig. 2.21, the value of $\Phi_{min,EI}$ is much higher than that of the $\Phi_{min,RI}$ for both seals, i.e. the ratios of $\Phi_{min,EI}$ to $\Phi_{min,RI}$ for the axial- and radial-clearance seals are 3.9 and 2.9, respectively.

Owen *et al.* (2012a) compared sealing effectiveness values determined from the saw-tooth model for EI ingress with published experimental data (Johnson *et al.*, 2006) and with 3D steady compressible CFD at several values of sealing flow rate. The CFD simulation showed how the value of ΔC_p varied in the annulus and a 'consistency criterion' was proposed to determine the value of ΔC_p that ensured consistency between pressure-and concentration-based effectiveness. The contours of ΔC_p computed near seal clearance for $\Phi_0 = 0$ are shown in Fig. 2.22 and it can be seen that the locations in the annulus where the consistency criterion is satisfied exist near the upstream and downstream edge of the seal clearance.

Owen *et al.* (2012b) solved the orifice equation for combined ingress (CI) and validated it using the experimental measurements made by Phadke and Owen (1988c). It was shown that the agreement between the theoretical value from the

orifice model and the experimental results was good. The authors suggested that EI ingress occurs when $C_{w,min,CI}/C_{w,min,RI} = \Phi_{min,CI}/\Phi_{min,RI} > 2$, i.e. if the $C_{w,min,CI}/C_{w,min,RI} = \Phi_{min,CI}/\Phi_{min,RI} < 2$ effect of rotation on ingress cannot be ignored.

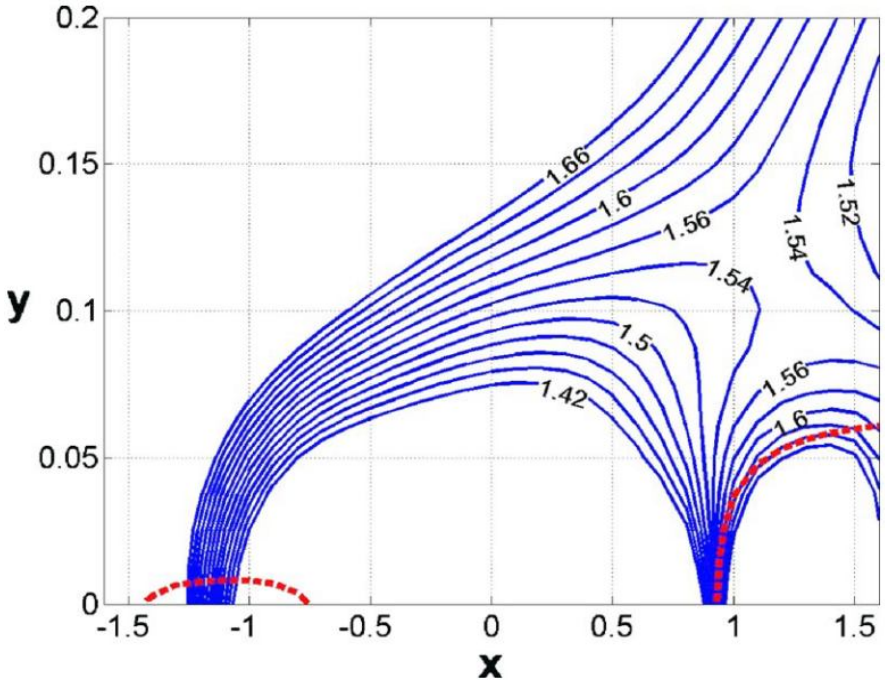

Figure 2.22 Close up of contours of ΔC_p computed near seal clearance, with the red dotted line corresponding to the locus where the consistency criterion is satisfied. (x is the non-dimensional axial distance ($=2z/S_c$), y is the non-dimensional radial distance ($=(r-r_{inner})/(r_{outer}-r_{inner})$), z is the axial distance from the centre of seal clearance, S_c is the r_{inner} is the inner radius of annulus and r_{outer} is the outer radius of the radius) (Owen *et al.*, 2012a).

Sangan *et al.* (2013c) extended previous experiments (Sangan *et al.* 2013a, b) on the effect of seal geometries on ingress for six rim seal geometries including two double-clearance seals. The performance of the seals was measured using the CO_2 gas concentration technique and theoretical curves were obtained using the statistical method of Zhou *et al.* (2013). It was shown that the sealing effectiveness for RI ingress is considerably higher than that for the EI ingress case and the benefit of using double-clearance seals was also reported. The seal performance ranking shown in order of magnitude of Φ_{min} for all seal configurations tested is presented in Chapter 5 (subsection 5.5, Fig. 5.15).

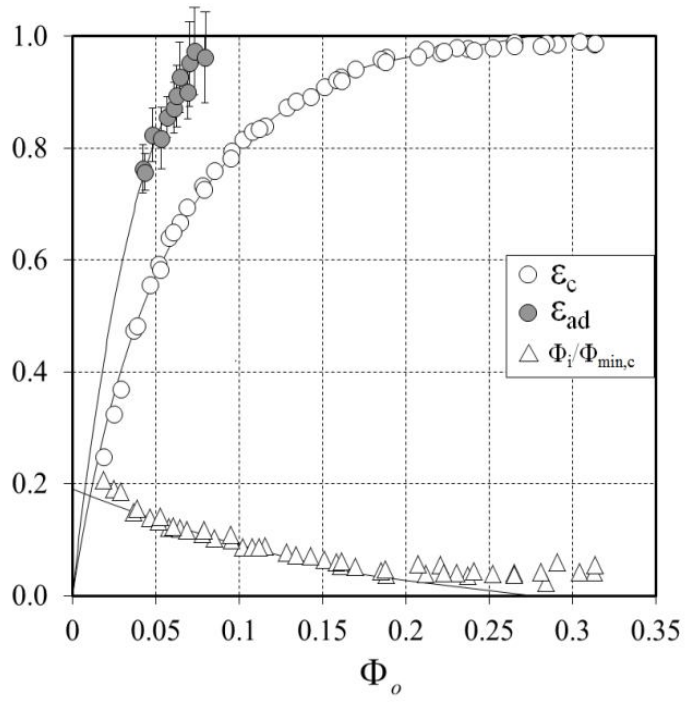

Figure 2. 23 Variation of adiabatic and concentration effectiveness with Φ_0 for the design condition. (Pountney *et al.* 2013)

Pountney *et al.* (2013) investigated the effect of ingestion on the temperature of turbine discs by transient heat transfer experiments using thermochromic liquid crystal (TLC). It was the first published experimental data that showed the variation of sealing effectiveness on the rotor with sealing flow rate. An adiabatic sealing effectiveness for the rotor disc was defined to show the effect of ingress on the rotor as follows:

$$\varepsilon_{ad} = \frac{T_{ad} - T_a}{T_{ad}* - T_a} \tag{2.34}$$

where, T_{ad}* is the value of T_{ad} when there is no ingress and T_a is the total temperature of the air in the annulus as measured by a fast response thermocouple located upstream of the nozzle guide vanes. The experiments were conducted for an axial-clearance seal with mitred inserts for both on-design and off-design operating conditions. A thermal buffer ratio (η) was defined as the ratio of Φ_0 required to seal the wheel-space to the value of the minimum Φ_0 so as to prevent the effect of ingress on the surface temperature of the rotor. That is, the thermal buffer ratio was defined as:

$$\eta = \frac{\Phi_{min,c}}{\Phi_{min,ad}} \tag{2.35}$$

Fig. 2.23 shows the variation of adiabatic and concentration effectiveness (ε_{ad} and ε_c) with sealing flow rate at design operating condition. It can be clearly seen that the adiabatic sealing effectiveness is significantly higher than the concentration effectiveness, when ingress occurs.

2.6 Infrared thermography

Infrared thermography has been used since the mid-1990s for research into convective heat transfer on a rotating body (disc), including work by Cardone *et al.* (1996, 1997), Pellé and Harmand (2006, 2007a, b, 2008, 2009), Mori *et al.* (2007) and Astarita and Cardone (2008). Some of these papers that used infrared thermography are briefly presented in this section. (The basic fundamentals of infrared thermography, which are required to ensure accurate temperature measurements using infrared thermography, are provided in Chapter 3, (section 3.1.))

Infrared thermography has been widely used for convective heat transfer measurements in various applications since the late 1960s; the first measurement of a heat transfer coefficient was made by Thomann and Frisk (1968). As an infrared camera can provide two-dimensional temperature data, a temperature map of a surface where a high spatial temperature gradient is expected can be measured accurately. In addition, it is relatively easy to evaluate error caused by radiation and lateral conduction. Modern infrared cameras typically have high sensitivity (as low as 20mK) and fast response-time (as fast as 20μs), thus, allowing for non-intrusive temperature measurements. Therefore, infrared cameras can be effectively employed for transient heat transfer studies over a wide range of applications (Carlomagno and Cardone, 2010).

Pellé and Harmand (2006, 2007a, b, 2008, 2009) conducted a series of heat transfer experimental studies in rotor-stator systems using infrared thermography. As shown in Fig. 2.24, surface temperature of the rotor disc was measured using an infrared camera, FLIR AGEMA 900, through a fluorspar infrared window on the

stator. In order to increase the infrared radiative flux emitted by the rotor disc, its surface was painted with a high emissivity black paint (ε = 0.93±0.01). The surface temperature of the disc was measured at the rate of 35Hz and the estimated uncertainty of the temperature measurement was 1K.

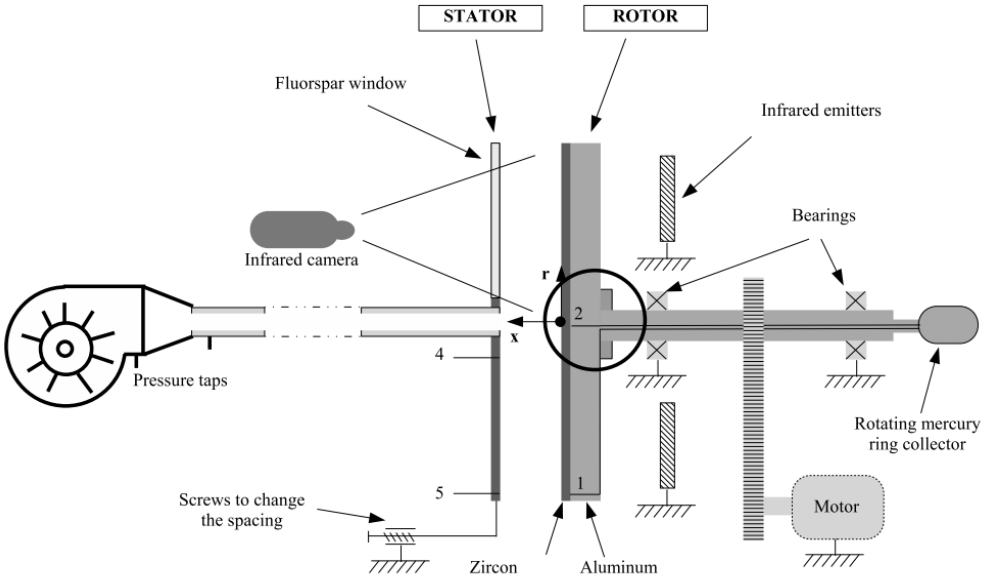

Figure 2.24 Experimental setup used by Pellé and Harmand (2008, 2009).

Mori *et al.* (2007) carried out steady state heat transfer experiments on a rotating blade using infrared thermography. The heat transfer study was conducted on the pressure side of a rotor blade with a cold mainstream and heated secondary air flow configuration. The Thermosensorik CMT 384 SM IR camera was used to measure surface temperature of the rotor blade, which was installed normal to the target surface. The infrared radiation from the rotor blade surface was measured at a rate of 150Hz and the thermal sensitivity, the noise equivalent temperature difference (NETD), of the camera was 0.02K. The infrared camera was calibrated in an oil bath, as shown in Fig. 2.25., which was thermally insulated and the aluminium plate was coated with the same black paint used for the rotor blade. The surface temperature of the aluminium surface was monitored by several Pt100 RTDs. The calibration was performed under steady-state condition and the temperature of aluminium plated was recorded simultaneously by both the infrared camera and Pt100 RTDs. The camera was calibrated to have uncertainty in the range of 1~3% of measured full scale.

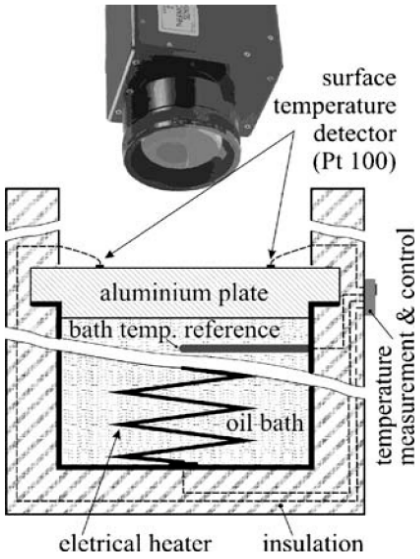

Figure 2.25 Infrared camera calibration setup used by Mori *et al.* (2007)

Astarita and Cardone (2008) conducted an experimental study on convective heat transfer on a rotating disc with a centred impinging round jet. A FLIR AGEMA thermovision 900 infrared camera was used for both flow visualisation and heat transfer measurements on a rotating disc having a maximum rotational speed of 4400 rpm. The rotor disc surface was coated with a thin layer of black paint which had an emissivity of ε=0.95 in the infrared bandwidth used for the temperature measurements, 8~12 μm. The thermal sensitivity of the IR camera was 0.07K when expressed by the noise equivalent temperature difference (NETD).

Chapter 3: Development of infrared temperature measurement technique

This chapter describes the development of a non-intrusive temperature measurement technique, based on infrared thermography, which is suitable for measuring rotor surface temperature history and has been employed in a transient heat transfer experiment in the Bath one-stage ingestion test facility.

The TLC temperature measurement technique was successfully applied to the ingress test facility in previous research and provided temperature data, which was then used to determine the world's first rotor sealing effectiveness data (Pountney *et al.*, 2013). However, this technique has the following drawbacks. First of all, only a limited range of temperature can be measured with a specific TLC. In addition, the TLC has to be re-sprayed after a certain number of experiments due to an ageing effect; in order to do so the experimental setup needs to be dismantled. Post processing work is also required to extract the temperature. Image processing, which takes a substantial amount of computing time, is required to convert the recorded colour data of the TLC into the surface temperature. Furthermore, optical access and an illumination source are required to record colour change of the crystal using a colour video camera with 3 CCDs (Charge-Coupled Devices), and making such measurements can be difficult when the target is an enclosed internal surface. Most importantly experimental data collected using a mixture of narrowband TLCs can only be analysed with a method based on the 1-D Fourier's heat equation with some simplifying assumptions: semi-infinite solid assumption, step change in the driving temperature, a constant heat transfer coefficient and constant adiabatic wall temperature during an experiment. These assumptions increase the uncertainty amplification factors, which are explained in detail later in section 4.1, and limit the time during which an experiment can be conducted (Yan and Owen, 2002). Consequently, the rotor sealing effectiveness of rim seals with a complex geometry cannot be practically determined with the TLC temperature measurement technique. In order to overcome the above described limitations, the GTRU decided to replace the TLC temperature measurement technique with a non-intrusive surface temperature measurement technique based on infrared thermography.

An infrared sensor is a useful advancement on the TLC method for the test facility. Here the surface temperature field is axis-symmetric. There are other fluid dynamic situation, where the rotor temperature field is not axis-symmetric and the TLC method has the advantage of providing local spatial variations in temperature, e.g. (Kakade *et al*., 2009).

3.1 Infrared thermography

Infrared thermography works based on a physical principle that all objects with a temperature above absolute zero, regardless of their physical states (solid, liquid or gas), emit energy in the form of electromagnetic radiation. Infrared thermography has been widely used for applications where conventional temperature sensors cannot be used. For example, those where temperature measurement of a moving object is required, or where the target temperature is too high for conventional contact temperature sensors, or where non-contact measurements are required for hazardous reasons.

3.1.1 Fundamentals of infrared thermography

Fundamentals of thermal radiation

Thermal radiation is a physical phenomenon, whereby energy is emitted from the surface of all objects with a temperature above the absolute zero, in the form of electromagnetic radiation. By definition, thermal radiation is an electromagnetic radiation occurring in the wavelength (λ) range of $0.1 < \lambda < 100\mu m$, which includes the visible, infrared and a part of the ultraviolet spectrum, as shown in Fig 3.1. For solids, it is known that thermal radiation occurs within approximately $1\mu m$ of its surface. In other words, thermal radiation properties, such as emissivity (ε), are mainly dependent on the surface properties rather than the materials from which it is made (Long, 1999).

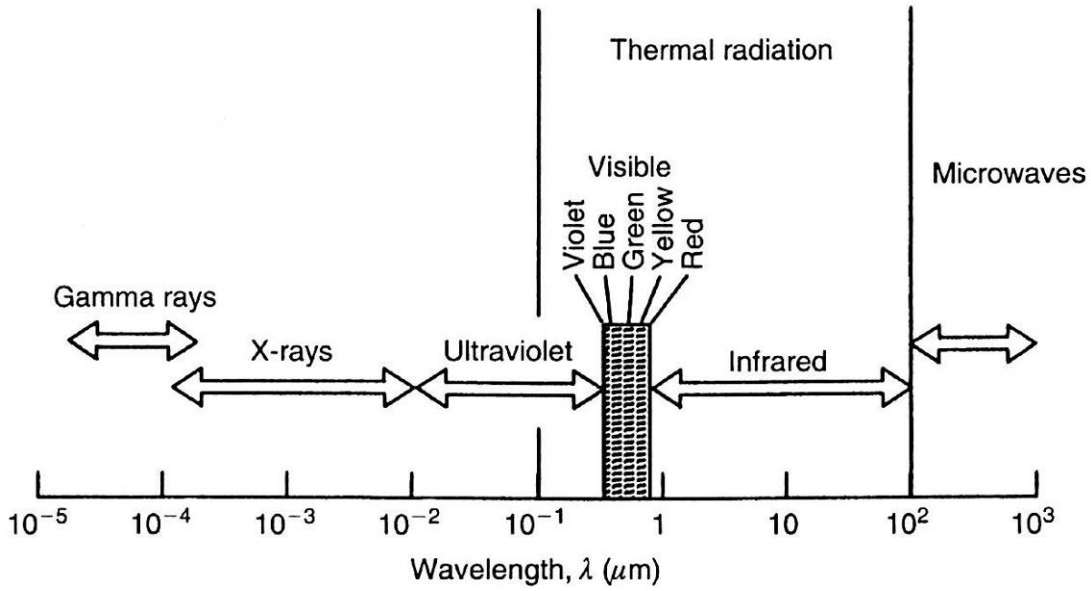

Figure 3.1 The electromagnetic spectrum for $10^{-5} < \lambda < 10^{3} \mu m$ (Long, 1999)

- **Planck's law**

The physical principle of the electromagnetic radiation, which is the basis of infrared thermography, was first explained by Max Planck. He formulated, for the first time, the energy distribution over the electromagnetic spectrum for a given temperature, which is known as the Planck's law (Eq 3.1). The intensity of thermal radiation is a function of only temperature and wavelength (Incropera, 2007).

$$I_{\lambda,b} = \frac{2hc^2}{\lambda^5 \left[exp(hc / \lambda kT) - 1 \right]} \tag{3.1}$$

where, $I_{\lambda,b}$ is the intensity of the black body radiation for a given wavelength, λ

T is the absolute temperature (K)

h is Planck's constant (6.6256×10^{-34}Js)

c is the velocity of electromagnetic radiation (2.998×10^{8} m/s)

k is the Boltzmann constant (1.3806×10^{-23}J/K).

The spectral emissive power (Eq 3.2) can be derived from Eq 3.1. The derivation process can be found in most heat transfer texts, e.g. (Incropera, 2007).

$$E_{\lambda,b} = \pi \cdot I_{\lambda,b} = \frac{2\pi hc^2}{\lambda^5 \left[exp(hc / \lambda kT) - 1 \right]} \tag{3.2}$$

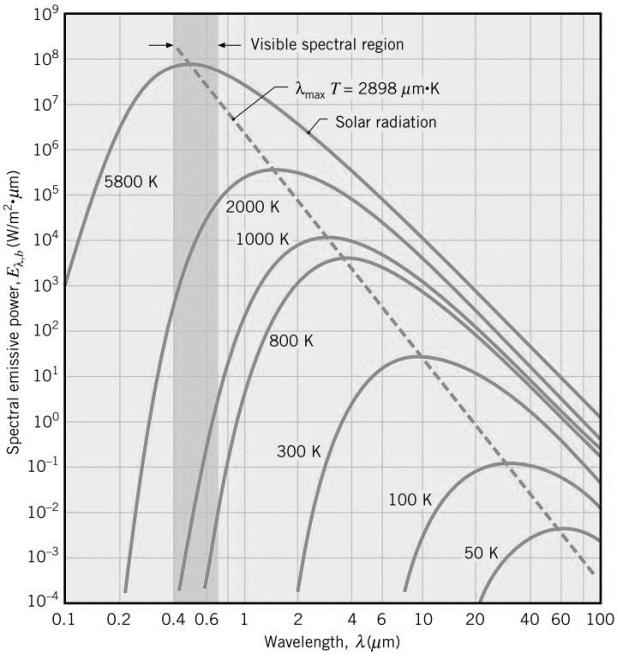

Figure 3.2 The Planck distribution of a black body for seven different temperatures (Incropera, 2007)

The variations of spectral radiative power emitted by a black body, $E_{\lambda,b}$, with wavelengths of a number of different absolute temperatures are shown in Fig 3.2. It can be observed from the graph that the spectral emissive power is a function of wavelength and temperature; like $I_{\lambda,b}$ the magnitude of the power continuously changes with wavelength and increases as temperature increases for the whole range of wavelength. In addition, it can be seen that the wavelength, which emits the maximum power, is inversely proportional to the temperature (Eq 3.3). Fig 3.2 also shows that most of the emission at lower temperatures (like room temperature) occur in the region where the wavelength is longer than the visible spectral region and consequently are not visible to the human eye (Incropera, 2007).

$$\lambda_{max} = \frac{0.0028978}{T} \quad (m) \tag{3.3}$$

- **Emissivity**

A black body is an ideal radiative body (or surface) that absorbs all incident electromagnetic radiation and it sets a theoretical upper bound for the thermal radiation of a body. That is, no surface can emit more thermal radiation than a black

body for a given temperature and wavelength, i.e. a real surface emits radiative power which is less than or equal to that of a black body (Fig. 3.3 a)). Also, the radiative energy which is emitted by a real surface can be non-isotropic, as shown in Fig. 3.3 b). The emissivity, ε, is defined as the ratio of radiation emitted by a grey body (real surface) to that of a black body at the same temperature (Eq. 3.4) and consequently, by definition, that of a black body is 1 while that of any grey one is less than 1.

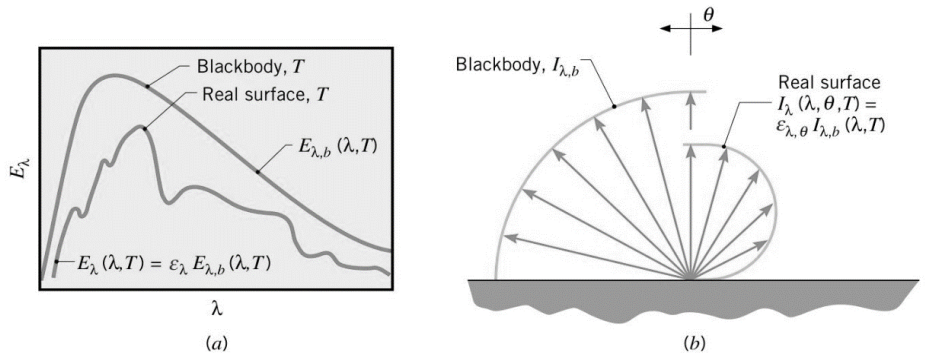

Figure 3.3 Black body and grey body behaviour: (a) spectral and (b) directional dependence (Incropera, 2007)

$$\varepsilon = \frac{E}{E_b} \tag{3.4}$$

where E = emissive power for a grey body (real surface) (W/m^2)

E_b = emissive power for a black body (W/m^2)

Considerations required for infrared thermography

Infrared thermography is a good alternative method for measuring temperature under circumstances where contact type temperature sensors, such as a thermocouple, are not applicable. However, due to the complexity of the radiant heat transfer process, many careful considerations need to be made for selecting an infrared temperature measurement system, including: temperature range of the target, field of view, ambient temperature conditions, range of wavelength that the infrared thermometer measures, response time (measurement frequency), accuracy of measurement, overall dimensions and cost. It is also known that a large number of

potential sources of errors are associated with infrared thermography, which should be carefully taken into account with the following considerations in order to achieve good measurements (Childs, 2001).

- Estimate the emissivity of the target surface by identifying the surface conditions and materials.

- Fill the field of view with the target surface in the case when an infrared sensor is used. This is due to the fact that the sensor does not absorb infrared radiation from a single point, but measures average temperature of a conical region, field of view or spot size, which is normally larger than a few millimetres in diameter. Therefore, if the field of view is not filled with the target surface, the temperature sensor will measure thermal radiation not just from the target, but also from a non-target surface and/or background.

- If possible, make sure that there are no windows in the field of view between the temperature sensor and the target surface. If special infrared windows are indispensable, then the infrared sensor should be calibrated after taking into consideration the temperature of window.

- Inspect carefully to ensure the absence of additional radiation in the field of view of a hemisphere from which the infrared sensor can receive radiant energy, such as from incandescent lamps or sunlight.

- Inspect the optics regularly to ensure they are clean, for otherwise, the infrared radiant energy absorbed by the sensor would be reduced, which in turn would lower the temperature readings.

- Calibrate the infrared thermometer regularly, like other temperature sensing devices, to ensure an accurate reading.

3.1.2 Comparison of an infrared sensor and infrared camera

Infrared sensors and infrared cameras are the two most widely used infrared temperature measurement devices. Examples of the devices are shown in Fig 3.4: an

infrared sensor, Melexis MLX90614ESF-DCI, and an infrared camera, FLIR SC7000. Infrared sensors have two key advantages over the infrared camera for the Bath one-stage ingestion test facility application. First of all, typical infrared sensors have much smaller external dimensions than infrared cameras, i.e. many sensors with a diameter smaller than 10mm are commercially available and consequently, only minor modifications to the existing ingestion test facility are required to install the infrared sensors. By contrast, most infrared cameras with decent accuracy have dimensions of a few hundred millimetres, as shown in Fig 3.4. It would be infeasible to flush-mount an infrared camera to the stator wall and so a window made of infrared transparent material, such as germanium, would be required; this would inevitably increase the uncertainty of the temperature measurement and complexity of the experimental setup. The unit price of a typical infrared sensor is normally less than £300, whereas that of an infrared camera is well over £50,000.

However, infrared cameras do hold an advantage over infrared sensors in terms of spatial resolution. This is because the latter measure average temperature of a certain surface area, which is normally larger than a few millimetres. In general, the size of the measurement area (spot size) varies with field of view and the distance between the sensor and target surface. An infrared camera can detect the temperature difference with good resolution. For example, the resolution of a FLIR SC7600 infrared camera is 640×480 pixels (FLIR), which means the spatial resolution of the camera is 1 mm by 1 mm, if an infrared image of area 640 mm by 480 mm area is recorded. The spatial resolution of the infrared sensor is determined by the 'spot size' as described in section 3.2. For the experimental setup in the Bath one-stage rig the spot size has a diameter of 5.9 mm.

An IR camera has the great advantage that it produces a temperature map, rather than the temperature averaged over a single spatial location. However, in the application describes here the flow and temperature field is axisymmetric, i.e. only a function of radius with no circumferential variation.

After considering all the advantages and disadvantages of each type of infrared device, in order to minimise the project cost and required rig modifications, it was

decided to use infrared sensor type devices for the heat transfer test in the Bath one-stage ingestion test facility.

a) b)

Figure 3.4 Example of infrared temperature measurement devices a) infrared sensor, b) infrared camera (MELEXIS, n.d., FLIR, n.d.)

3.1.3 Thermopile-based infrared thermography

The thermopile-based infrared sensor is one of the most widely used infrared temperature measurement devices, which utilises several thermocouples that are usually connected in series, for measuring temperature. Thermopiles generate a voltage output proportional to a temperature difference between each pair of cold and hot junctions. In order to minimise the effect of electromagnetic radiation incident on the cold junctions, these are kept in contact with a component with relatively large thermal inertia. In Fig 3.5 the supporting ring base is this component with large thermal mass to which the cold junctions are connected. As a result, the thermal radiation energy increases the temperature of only hot junctions and creates a temperature difference between the two junctions, which in turn, generates an output voltage, usually in tens or hundreds of millivolts (Childs, 2001, Maldague, 2001).

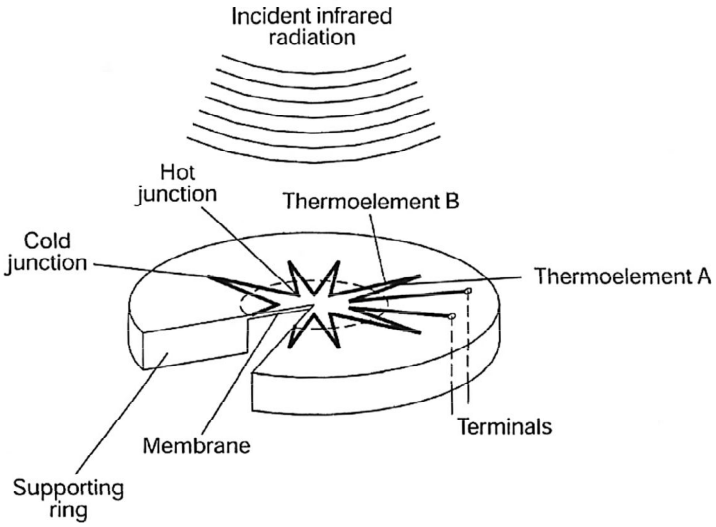

Figure 3.5 Cross sectional drawing of a thermopile sensor (Childs, 2001)

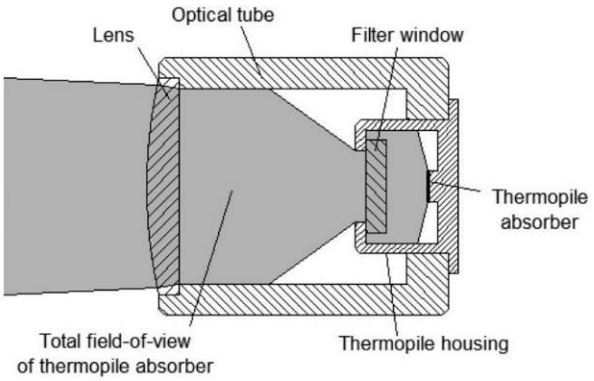

Figure 3.6 Cross section of optical assembly showing the total field of view of a thermopile absorber (Barry *et al.*, 2011)

Thermal offset voltage is one of the most significant sources of errors in temperature measurements using infrared sensors. It is associated with the temperature difference between the sensor assembly of a thermopile sensor (as described below), from where thermopile absorber can receive radiant energy, and the thermopile itself. As shown in the Fig 3.6, a thermopile sensor can receive radiant energy not just from the target object, but also from the thermopile housing, the optical tube and the lens, etc. (Barry *et al.*, 2011). Ideally, the temperature of a sensor assembly should be kept the same as that of the thermopile, otherwise it absorbs thermal energy from the assembly and hence generates additional voltage output (Graf *et al.*, 2007).

The thermal offset voltage problem is more likely to occur when a thermal gradient exists across the sensor assembly, which can be both steady state and transient (Barry *et al.*, 2011). In order to minimise this effect, many manufacturers have developed infrared sensors with a self-compensation capability, which helps improve the measurement accuracy under thermal gradient conditions. However, even infrared sensors with self-compensation are incapable of providing accurate measurements under transient temperature gradient conditions, which occurs especially when the ambient temperature around the sensor abruptly changes. Rapid changes of temperature in the wheel-space are an essential feature of the Bath one-stage test facility when conducting heat transfer experiments. Therefore, modification of infrared sensors is necessary to achieve an accurate rotor surface temperature measurement. The sudden temperature change in the wheel-space during a transient heat transfer experiment and the necessary modifications to the infrared sensor is described further in subsections 3.2.2 and 3.2.3.

3.2 New infrared temperature sensor development

3.2.1 Infrared temperature sensor selection

The following considerations were made, based on those described in 3.1.1, when selecting an infrared sensor that was appropriate for a heat transfer experiment in the Bath one-stage ingestion test facility.

- The spot size should be as small as possible.
- Target (object) temperature measurement range: the infrared sensor should have the ability to measures target temperature in the range from 10°C to 50°C.
- Ambient temperature range: the infrared sensor should have a good measurement accuracy in the ambient temperature range of 0°C to 50°C.
- Response time (measurement frequency): the shorter the response time, the better the overall experimental accuracy can be achieved. The TLC is recorded at 25Hz via CCD camera.

- Accuracy: the sensor should have its best measurement accuracy in the range 30°C to 50°C, where most of the measurements will be made and it should be better than ± 0.5°C in the whole temperature measurement range (from 10°C to 50°C).

- External dimension of the sensor: the sensor with the smallest external dimension is preferred.

- Self-compensation of ambient temperature change: the sensor should be capable of compensating for the effects of changes to the ambient temperature.

- Effect of reflection/background radiation: a minimum or negligible effect of reflection/background radiation is expected in the wheel-space of the Bath ingestion test facility, since this is virtually a darkroom.

After considering all the requirements, three infrared sensors were selected and a series of initial tests for checking repeatability and accuracy under ambient temperature change, were carried out. The key specifications of the three infrared sensors are provided in Table 3.1.

Table 3.1 Key specifications of three infrared sensors (Optris, 2012, Exergen, 2012, MELEXIS, 2012)

	Optris CSmicro 2W LT 02HS	Exergen Smart micro IRt/c.4	MELEXIS MLX90614ESF-DCI
Diameter (mm)	15	6.3	9
Spot size (mm) @ 20mm	1.2	5	6.7
Accuracy (°C)	± 1	± 0.1~0.2	± 0.2~0.5
Time constant (ms)	-	40	100
Emissivity setting	Changeable	0.9 fixed	Changeable
Ambient temperature Compensation	No	Yes	Yes
Unit price (GBP)	481	311	≈ 100

After the initial tests, the Melexis MLX90614ESF-DCI infrared sensor was selected for the Bath one-stage test facility application, since it had the best repeatability and accuracy. Drawings of the sensor are shown in Fig 3.7.

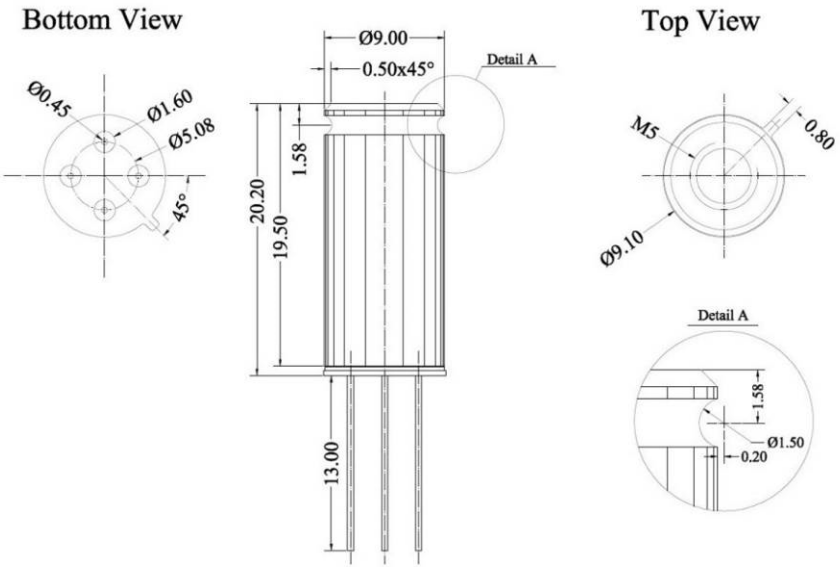

Figure 3.7 Drawings of an MLX90614DCI sensor (MELEXIS, n.d.)

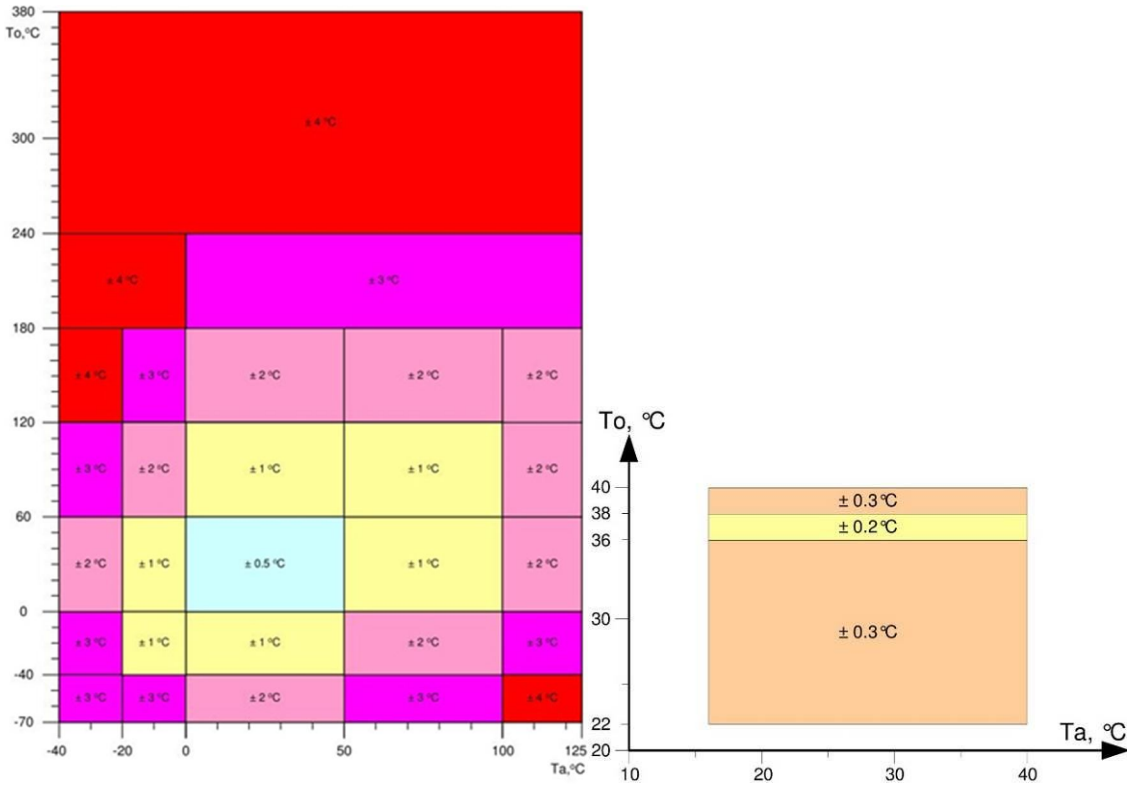

a) b)

Figure 3.8 Accuracy of an MLX90614ESF-DCI sensor (MELEXIS, n.d.)

The sensor satisfies most of the requirements except response time, which is 60ms slower than the preferred value, 40ms. However, although it is slower than that of TLC temperature measurement, it was concluded that a sufficient number of data for

good experimental accuracy could be acquired even with a response time of 100ms. For example, if a transient heat transfer experiment is carried out for 60 seconds, 600 temperature data can be acquired by the sensor, which have ± 0.5°C accuracy within the whole required target and ambient temperature range, as shown in Fig 3.8 a). Moreover, it has better accuracy in the target temperature range of 22°C and 40°C, when the ambient temperature is in the range of 16°C and 40°C, as shown in Fig 3.8 b).

3.2.2 Infrared temperature sensor assembly design for the Bath one-stage test facility application.

In the Bath one-stage ingestion test facility, heated sealing and ambient mainstream air are used for transient heat transfer tests to determine the adiabatic effectiveness of the rotor. A virtual step-change in the sealing air temperature is achieved by passing the air through a mesh heater, which converts electric power into heat. The air is heated from room temperature to approximately 45°C within 1 second from the trigger of the electric current supply to a mesh heater. The heated sealing air flows into the wheel-space through an annular-shaped inlet seal. The flush-mounted infrared sensors are exposed to an abrupt ambient temperature change that produces a thermal offset voltage, which has adverse effects on the accuracy of temperature measurements.

Two possible solutions were suggested to minimise the uncertainties caused by the thermal offset voltage: use of a material with high thermal mass to increase the thermal inertia and the use of a cooling jacket around the sensor to cool it down. Of these two, the cooling jacket method was first tried, which required either a special infrared window between the sensor optics and wheel-space or the use of cooling air through air passages around the sensor. A series of experiments were carried out, but neither method was successful in reducing the effect of an abrupt change in ambient temperature. This was because the special infrared window emitted thermal radiation as it was heated by the air in the wheel-space, which in turn, increased the uncertainty of temperature measurement. Also, the cooling air injection method needed a high accuarcy flow rate control system to control the sensor temperature accurately, which increased the complexity of the temperature measurement system.

As the cooling jacket method was not successful, the use of a high thermal mass material was tried. This involved putting a large thermal mass, such as a copper block, around the sensor housing and insulating it with a good thermal insulator, like Rohacell. The purpose of this setup was to provide slower ambient temperature changes to the infrared sensors.

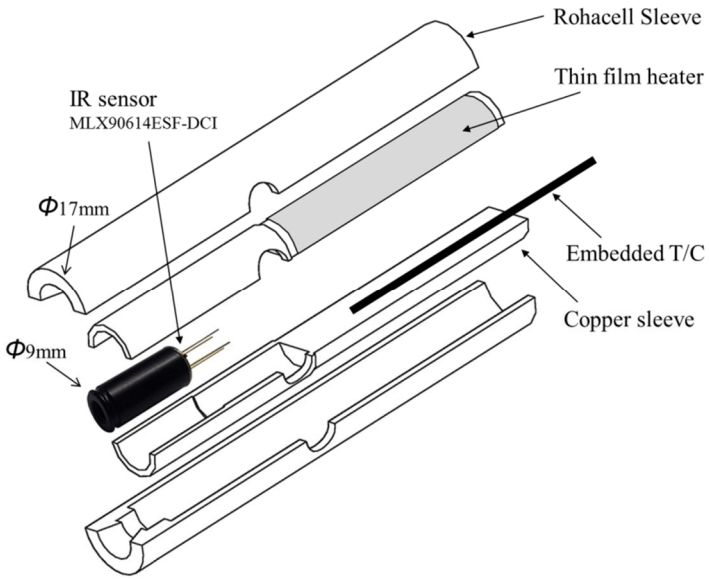

Figure 3.9 Infrared sensor assembly

The final design of the infrared sensor assembly with the large thermal mass is shown in Fig 3.9. The infrared sensor was inserted into a copper sleeve and thermal conductive grease was applied between the sensor and the sleeve to enhance heat transfer between the two. The copper sleeve was then insulated by a Rohacell sleeve, which has thermal conductivity of 0.03W/m^{2}K. A thin film heater was used to pre-heat the copper sleeve and the infrared sensor to a temperature which is close to the air temperature expected in the wheel-space around the sensor during a heat transfer experiment. The pre-heating method was used to reduce the temperature difference between the sensor and the air in the wheel-space, which in turn, reduced the thermal gradient in the sensor assembly. A K-type standard thermocouple was embedded in the copper sleeve to measure its temperature, which was then used for a feedback controller equipped with a relay switch. A photograph of the infrared sensor assembly, which shows its size relative to a 22.5mm diameter coin, is shown in the Fig 3.10.

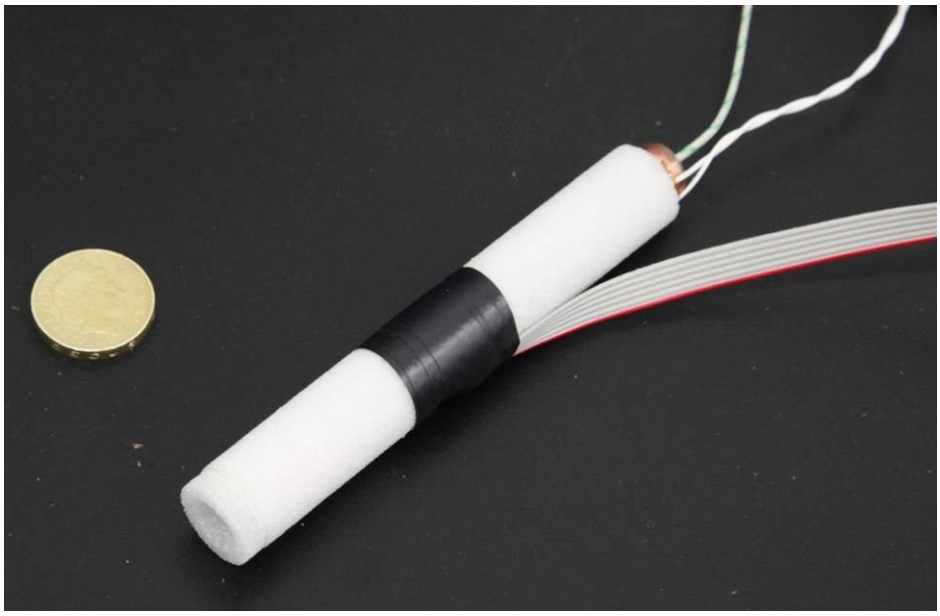

Figure 3.10 A photograph of infrared sensor assembly

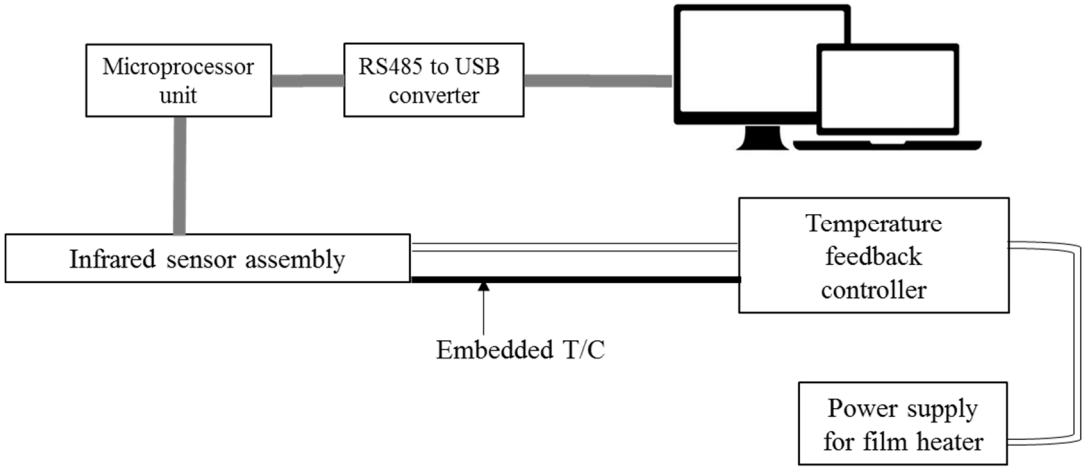

Figure 3.11 Infrared temperature measurement setup

The infrared temperature measurement setup including a temperature feedback controller and a microprocessor unit, Atmel ATmega328PU, is shown in Fig 3.11. The infrared sensor is connected to the microprocessor unit via an IIC bus and is then connected to a computer over an RS485 connection through an RS485 to a USB converter. Each infrared sensor returns two forms of data, one being the target temperature and the other the ambient temperature, i.e. the temperature of the sensor itself. A Labview code, which can monitor and record both target and sensor temperatures, was developed for the temperature measurement setup, which was

designed to accommodate up to 15 infrared sensors in parallel, with 10Hz measurement rate per sensor.

3.3 Calibration of the new infrared temperature sensor

3.3.1 Calibration test facility

This section describes the development of a new experimental facility mainly planned for the calibration of the new infrared temperature sensors, which is to be used in both the Bath 1 and 1.5-stage ingestion test rigs. The sensor is designed to be used under the condition where an abrupt change in ambient air temperature is expected; the requirement is to calibrate it in a similar environment to ensure good measurement accuracy. Therefore, the calibration facility is specifically designed to conduct the calibrations under properly controlled conditions by simulating a sudden change in the ambient air temperature. The spacing between the IR sensor and the target plate also simulates the ingestion rigs.

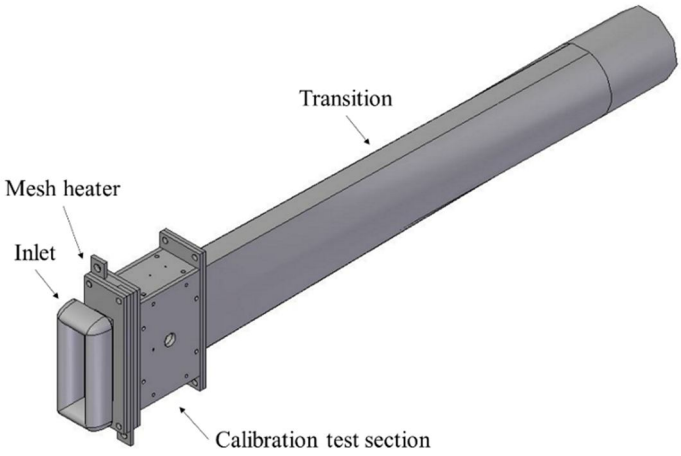

Figure 3.12 Isometric view of the calibration rig including inlet, calibration section and transition

In the conceptual phase, the calibration rig was designed to feature an inlet with a mesh heater followed by a calibration test section with rectangular cross section and a transition, which connected the calibration section and a suction pump. After the conceptual phase, a series of considerations on the channel width and length, flow velocity requirement, mesh heater specifications and design, intake design, thermal insulation for the whole test area and data acquisition systems were made. A 3D

CAD model which shows an isometric view of the calibration rig is shown in Fig 3.12.

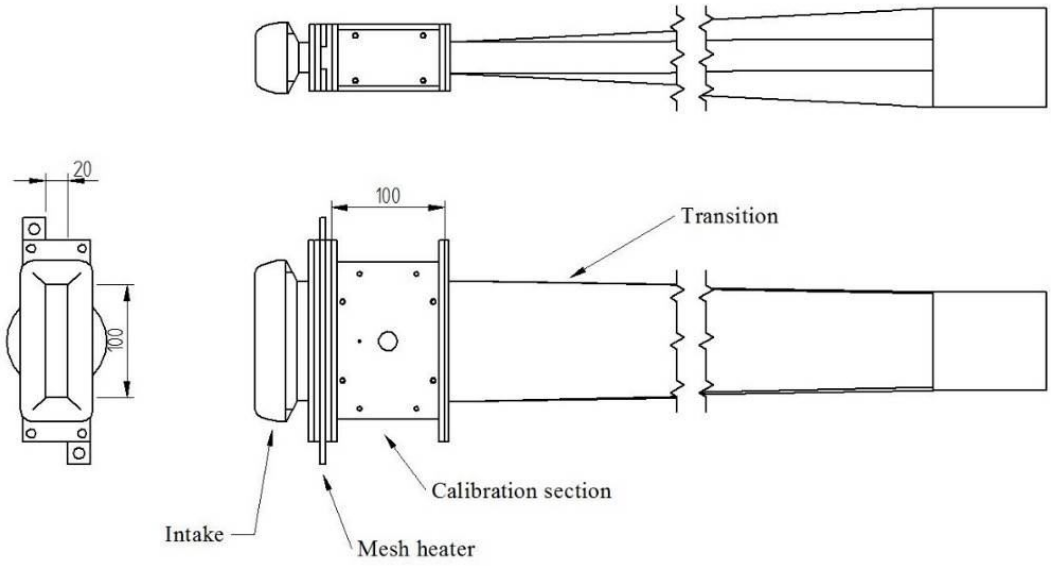

Figure 3.13 GA drawing of the calibration test rig

The channel width of the test section was set as 20mm, since the Bath one-stage ingestion test facility has a wheel-space with a 20mm axial gap between the stator and rotor disc. The channel length of the calibration test section was then chosen as 100mm (Fig 3.13) after considering the specification of the pump used, flow velocity and boundary layer growth. The intake of the test rig was designed to have a bell-mouth shape to ensure smooth air intake and the design was based on that of the British standard long radius nozzle (BSI, 2003). Due to the rectangular shape of the test area, modifications to the long radius nozzle design were made. The bell mouth intake was followed by a mesh heater, which was designed based on a patent filed by Ireland *et al.* (1996). The mesh heater converts electric energy into heat to produce a step change in air temperature for the calibration tests. A stainless steel mesh with a wire diameter and aperture of 40μm and 63μm, respectively, was used for the mesh heater. The mesh was soldered to copper bus bars on each long edge side and sandwiched in between two Tufnol plates that act as thermal and electric insulators. An exploded view of the mesh heater is illustrated in Figure 3.14.

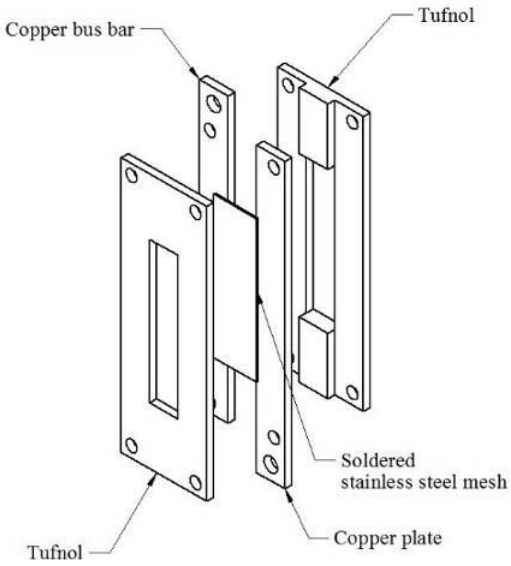

Figure 3.14 Exploded view of the mesh heater

The mesh heater is followed by the calibration test section, which is 100mm long and a cross sectional view of the calibration area, which shows its internal structure, is shown in Fig 3.15. All four internal surfaces of the calibration section were insulated by Rohacell plates to minimise the heat loss through the walls. The materials illustrated in red in Fig 3.15 are Rohacell insulators, which have a very low thermal conductivity, k, of 0.03W/m^{2}K.

A fast response thermocouple and an infrared sensor assembly were installed on the instrumentation plate of the calibration section, as shown in Fig 3.15 and 3.16. This has response time of 40ms (Lock *et al.*, 2005) and was placed approximately 25mm downstream of the mesh heater to monitor the mainstream air temperature. On the opposite side of the instrumentation plate, the calibration target plate consists of two Rohacell plates with a copper block in the middle, the surface of which was sprayed with a black paint (Hallcrest SPBB) also used on the rotor disc surface of the Bath ingestion test facility. This provided the same emissivity as the rotor disc surface of the ingestion test facility. A calibrated K-type thermocouple with a response time of 100ms was embedded in the middle of the copper block to provide a reference temperature for the calibration. The calibration section was equipped with a total and a static pressure tubes on the top wall for measuring the velocity of the mainstream air during a test, as shown in Fig 3.16.

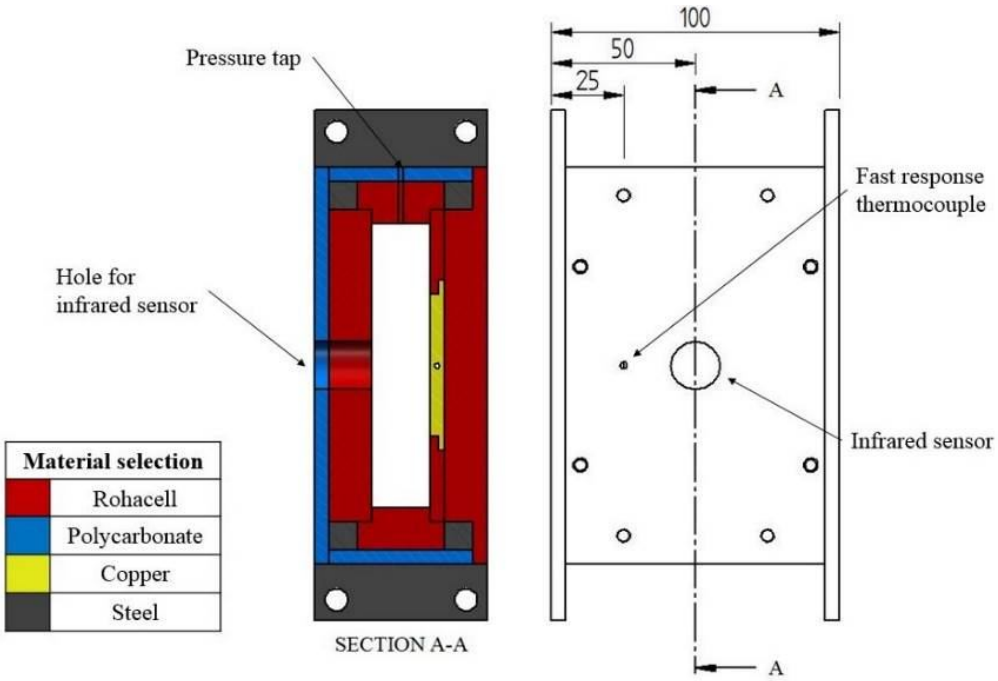

Figure 3.15 Cross sectional view of the calibration section

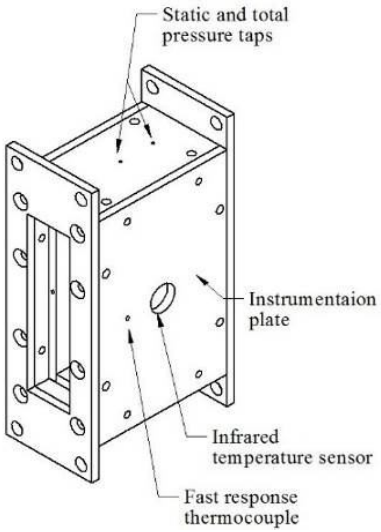

Figure 3.16 Calibration section instrumentation

The transition section was designed to provide a smooth transition from the calibration test section to the 3in. diameter diffuser to the centrifugal fan (Walsh and Fletcher, 1998). The fan is belt driven by a 1hp 3-phase AC motor. The fan was designed to give air velocity in a 3in. pipe up to approximately 40m/s (Plint, 1980). Photographs of the commissioned calibration test facility are shown in Figs 3.17 and 3.18.

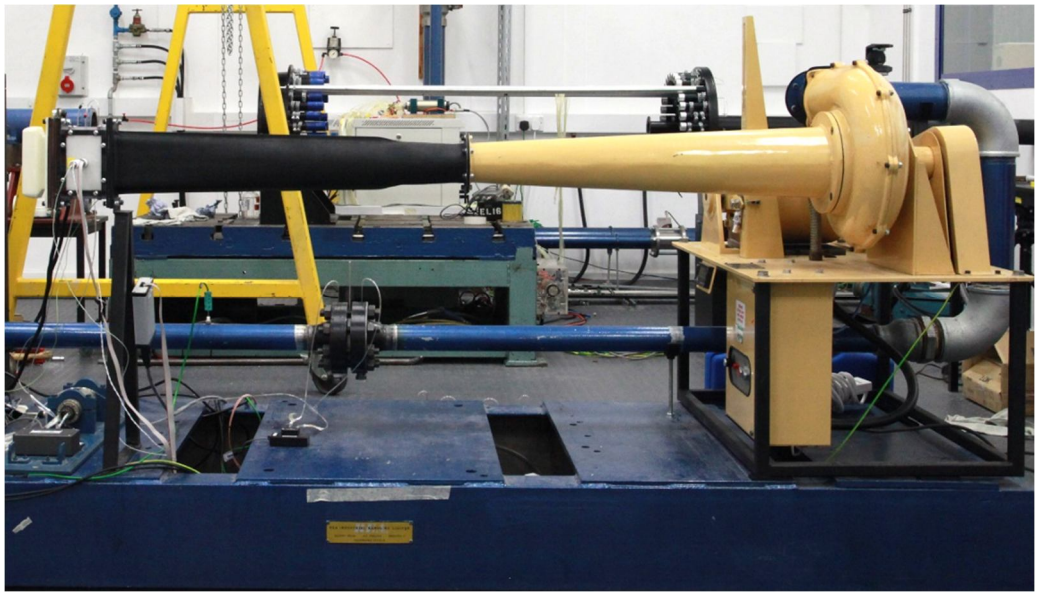

Figure 3.17 Commissioned calibration test facility

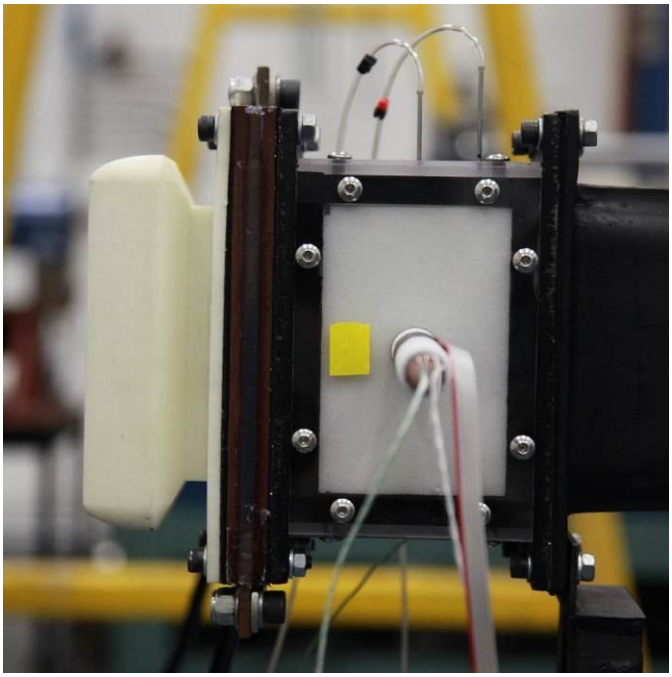

Figure 3.18 Calibration test section with instrumentation

3.3.2 Infrared temperature sensor calibration

The infrared sensor calibrations were carried out in the calibration test facility using a 50×50×5mm copper block insulated with Rohacell plates. A power supply, Magna-power electronics XR 16-375/380, which is capable of supplying 6kW

electric power, was used to increase the mainstream air temperature of the calibration with a mesh heater and the temperature of the copper block was measured with an embedded K-type thermocouple with a response time of 100ms. The embedded thermocouple was calibrated in a hot water bath and mili-voltage output from the thermocouple and reference temperature data were acquired while cooling the hot water from 70°C to ambient temperature, with a Druck P600 digital thermometer with Pt100 sensing probe being used to provide the reference temperature. The thermocouple voltages were measured with the same experimental data acquisition system as the calibration tests so as to minimise any possible bias. The calibration process was repeated five times for each thermocouple and the 95% uncertainty of the thermocouple temperature measurement was estimated to be 0.1°C.

As briefly pointed out in subsection 3.3.1, the copper block was sprayed with a mixture of 1.5ml black paint, Hallcrest SPBB, and 1.5ml water to provide the same emissivity value as the rotor disc. As explained in subsection 3.2.2, the sealing air temperature of the Bath ingestion test facility abruptly increases from room temperature to approximately 45°C in a virtual step-change in temperature. In order to minimise any thermal offset voltages caused by a temperature gradient in the infrared sensor, this was pre-heated by a thin film heater. However, as the air temperature in the wheel-space varies between 30 and 45°C depending on the amount of ingress (Pountney, 2012), it was necessary to choose a pre-heated sensor temperature that could be universally applied for the various wheel-space air temperature conditions. This 'environment temperature' was chosen as 35°C, since the average non-dimensional core temperature, Eq. 3.6, in the wheel-space found by previous research (Pountney, 2012) was approximately 0.65, i.e. equivalent to 35°C.

$$\theta_{core} = \frac{T_{core} - T_{in}}{T_0 - T_{in}} \tag{3.6}$$

where, θ_{core} is the non-dimensional core temperature in the wheel-space, T_{core} is the core temperature in the wheel-space, T_{in} is the initial temperature of the system and T_0 is the total temperature of the sealing air.

Two infrared sensor assemblies were manufactured for heat transfer tests in the Bath one-stage ingestion test facility, with the steady state calibrations of those

conducted being in the target temperature range from approximately 15℃ to 55℃. For each temperature measurement, the current from the mesh heater power supply was incrementally increased with all settings of the calibration test facility kept constant until the temperature of copper block settled down. The copper block temperature was then measured for 30 seconds by both the embedded thermocouple and the infrared sensor. The sensor temperature was carefully controlled within ±0.2℃ of the environment temperature, 35℃. The recorded temperature data was then time-averaged and plotted on the true temperature (reference temperature) vs. infrared temperature graph. The calibration curve was found to be highly linear with 95% uncertainty of 0.1℃, as shown in Fig 3.19. The steady state calibration was repeated for the other infrared sensor prepared for heat transfer experiments. The calibration curve of both infrared sensors was acquired from the steady state calibration as follows:

Sensor no. 1: $T_{true} = 1.106 \cdot T_{IR} - 3.25$

Sensor no. 2: $T_{true} = 1.108 \cdot T_{IR} - 3.30$

where T_{true} is the true temperature measured by the embedded thermocouple.

T_{IR} is the temperature measured by an infrared sensor.

Transient calibrations of the two sensor assemblies were also carried out to check the accuracy of the infrared temperature measurements, under a similar condition to the environment expected in the wheel-space of the ingestion rig during the course of a transient test. The mass flow rate of the air through the mesh heater was kept constant for a transient calibration test and a step-change between 30 and 40℃ in the air temperature was achieved by the heater and the power supply. The sensor environment temperature was carefully kept to within ±0.3℃ of 35℃. The copper block temperature change was measured by both the embedded thermocouple and the infrared sensors with measurement rates of 10Hz while the target block was heated in the transient experiment. The acquired temperature data was then plotted on a true temperature vs. infrared temperature graph and compared with the steady state calibration results. Three transient calibration tests were carried out per infrared sensor. Typical data for one sensor is shown in Fig 3.20. As can be seen, the transient

calibration curves agree well with that of the steady state calibration. The 95% uncertainty in the infrared temperature measurement for each sensor was estimated to be approximately ±0.2°C.

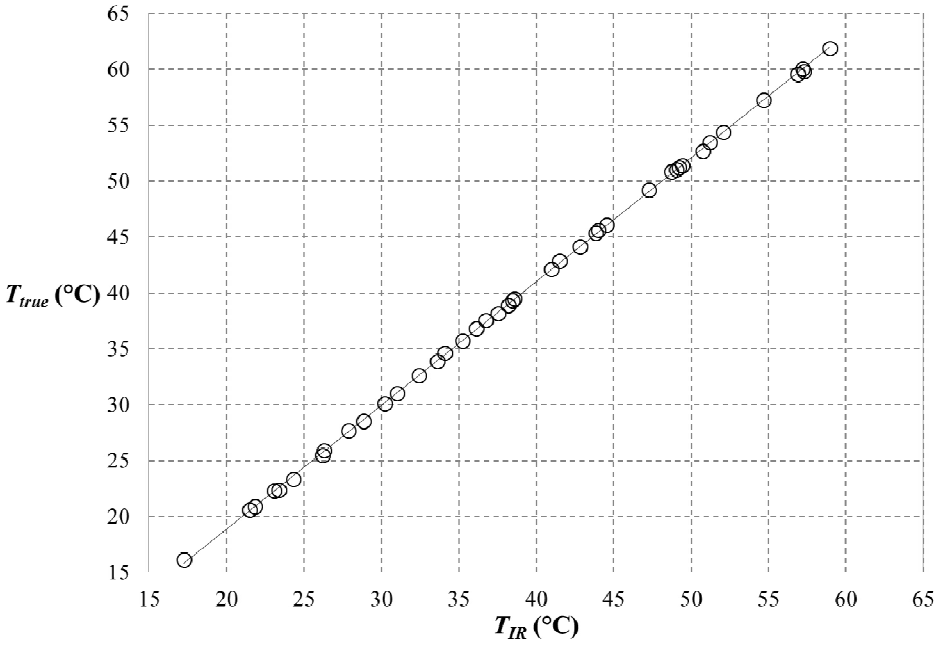

Figure 3.19 Steady state calibration result of an MLX90614ESF-DCI sensor

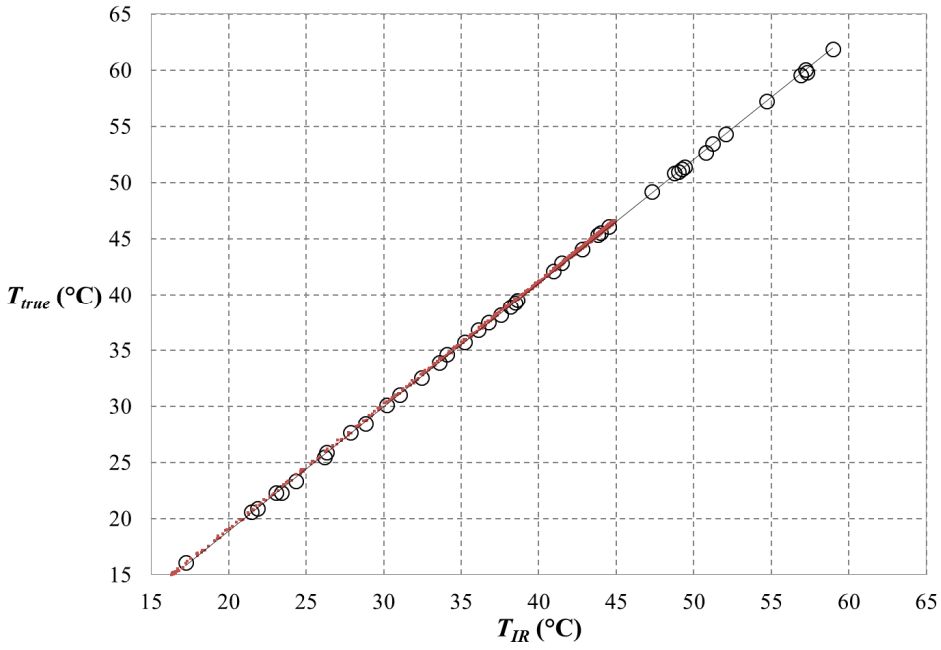

Figure 3.20 Calibration curves of an infrared sensor for both the steady state (open circle) and transient condition (shown in red)

3.4 Summary

A non-intrusive temperature measurement technique based on infrared thermography, which can be used under the conditions where abrupt ambient temperature change is expected, has been developed to measure the temperature of the rotor disc surface during a transient heat transfer experiment in the Bath one-stage ingress test facility. Taking into account the repeatability and accuracy of infrared sensors, the Melexis MLX90614ESF-DCI infrared sensor that is capable of making at 10Hz, was selected for the application. The sensor is 9mm in diameter, with 6.7mm and 5.9mm spot size diameter at 20mm and 10mm distance from the target, respectively.

As abrupt ambient temperature change, to which the infrared temperature sensor is exposed, increases uncertainties in the temperature measurement. Two solutions to minimise the adverse effect of such change were suggested: the use of a material with high thermal mass to increase thermal inertia and the use of a cooling jacket around the sensor to cool it down. After a series of tests, a method with high thermal mass was chosen, which involves putting a large thermal mass (e.g. copper) around the sensor housing and insulating it with a good thermal insulator (e.g. Rohacell). In addition, the infrared sensor was pre-heated using a thin film heater with a feedback temperature controller so as to reduce the temperature difference between the sensor and the heated air in the wheel-space, which in turn, reduces the thermal gradient in the sensor assembly.

A new calibration facility, which was specifically designed to conduct the calibrations of the new infrared temperature sensor under controlled conditions by simulating a sudden change in the ambient air temperature during the calibration, was built. The infrared temperature sensors were calibrated in the target temperature range from approximately 15°C to 55°C under steady state conditions. The accuracy of the temperature measurement in a transient condition was checked by simulating the abrupt ambient temperature change during the tests. The sensor temperature was carefully kept over the course of testing to within ±0.3°C of environmental

temperature of 35℃ and the infrared sensors were calibrated to have ±0.2℃ accuracy with 95% uncertainty level.

Chapter 4: Solutions of Fourier equation for heat transfer experiments

This chapter describes the development of an analysis method to calculate values of h and T_{ad} for a transient heat transfer experiment using TLC or IR temperature measurement sensors. The semi-infinite solution of Fourier's equation for experiments using TLC were compared with a 'quenching solution' and the limitations of the solution for accurate determination of h and T_{ad} was discussed based on the method developed by Yan and Owen (2002). The 'two temperature' and 'extrapolation' methods to determine the values of h and T_{ad} based on the semi-infinite assumption were compared and the required conditions to obtain accurate values of h and T_{ad} was discussed. It was found from this study that the value of the measured T_s needs to be maximised to achieve accurate estimation of T_{ad}, regardless of the method used for the calculation of h and T_{ad}.

In order to acquire higher T_s values, the heat transfer experiment is required to be conducted over a longer period of time. However, as time is limited for the semi-infinite solution, a numerical solution with back-face boundary condition that represents the actual experimental conditions was developed. A series of numerical experiments, to develop the numerical analysis method to determine h and T_{ad} using imperfect temperature data (with random noise), was also carried out. The method was developed based on the previous study which conducted by Owen (1979).

As the maximum achievable value of T_s is limited by the materials used in heat transfer experiments, a composite substrate was suggested to achieve higher values of T_s. It was shown that higher values of T_s could be acquired with the composite substrate, and a numerical analysis method that can be used to determine h and T_{ad} for a heat transfer experiment with composite substrate, was developed and validated.

A series of numerical experiments, to investigate the feasibility of a new method to acquire full surface temperature data using incomplete (piecewise) data based on the TLC temperature measurement technique, were also carried out. Although further numerical and experimental studies are required to develop the new method, it was

shown by the numerical experiments that the values of h and T_{ad} could be determined numerically based on the piecewise TLC temperature measurement technique.

4.1 Solutions of Fourier equation for experiments using thermochromic liquid crystal (TLC) and its limitations

The analysis of transient heat transfer experimental data, based on TLC temperature measurement technique, is usually carried out with the solution of the 1-D Fourier equation for convective heat transfer for a semi-infinite solid with a step-change in the fluid temperature; this is often called the semi-infinite solution. The limitations of the TLC temperature measurement technique and the reasons for replacing TLC with a new infrared temperature measurement technique by GTRU are previously discussed in Chapter 3. The semi-infinite solution of the 1-D Fourier equation for TLC heat transfer experiment and its limitations will be explained more in detail in this section.

Fourier's heat equation can be expressed in non-dimensional form as:

$$\frac{\partial \Theta}{\partial Fo} = \frac{\partial^2 \Theta}{\partial X^2} \tag{4.1}$$

where Θ is non-dimensional temperature difference [= $(T-T_{in})/(T_{ad}-T_{in})$]

Fo is Fourier number [= $(\alpha t/L^2)$]

Bi is Biot number [= (hL/k)]

X is non-dimensional substrate depth [= (x/L)]

T_{in} is initial temperature of the solid

T_{ad} is adiabatic surface temperature

α is thermal diffusivity of the solid

L is thickness of the solid

h is convective heat transfer coefficient

k is thermal conductivity of the solid

x is distance from front-face of the solid

4.1.1 Semi-infinite solution

The initial and boundary conditions for the semi-infinite solution in the non-dimensional form are:

$$\Theta = 0 \quad \text{for all } X \text{ when } Fo = 0$$

$$-\frac{\partial \Theta}{\partial X} = Bi\left(1-\Theta_s\right) \text{ at } X = 0 \text{ for } Fo > 0$$

$$\Theta = 0 \text{ at } X = 1 \text{ for } Fo > 0$$

The solution for a step-change in fluid temperature at the front-face of a solid of semi-infinite thickness (i.e. semi-infinite solution) can be expressed in non-dimensional form as (Incropera, 2007, Holman, 2010):

$$\Theta = erfc\left(\frac{X}{2}Fo^{-\frac{1}{2}}\right) - exp\left(XBi + Bi^2 Fo\right) erfc\left(\frac{X}{2}Fo^{-\frac{1}{2}} + BiFo^{\frac{1}{2}}\right) \tag{4.2}$$

where, *erfc* is the complementary error function, which is defined as $erfc(x)=1-erf(x)$ and $erfc(0) = 1$ and $erfc(\infty) = 0$.

As a result, the non-dimensional surface temperature, Θ_s, can be acquired by reducing Eq. 4.2:

$$\Theta_s = \frac{T_s - T_{in}}{T_{ad} - T_{in}} = 1 - exp\left(\chi^2\right) erfc\left(\chi\right) \tag{4.3}$$

where

$$\chi = BiFo^{\frac{1}{2}} = h\left(\frac{t}{\rho C_p k}\right)^{\frac{1}{2}} \tag{4.4}$$

Consequently, it can be seen that Θ_s from the semi-infinite solution is a function of χ only.

The non-dimensional back-face temperature at $X = 1$ ($x = L$) reduces to Eq. 4.5:

$$\Theta_L = \frac{T_L - T_{in}}{T_{ad} - T_{in}} = erfc\left(\frac{1}{2}\frac{1}{\sqrt{Fo}}\right) - exp\left(Bi + Bi^2 Fo\right)\left[erfc\left(\frac{1}{2}\frac{1}{\sqrt{Fo}} + BiFo^{\frac{1}{2}}\right)\right] \tag{4.5}$$

According to Schultz and Jones (1973), the errors caused by the semi-infinite solution can be treated as small, if $Fo < 0.1$. They showed that when $Fo < 0.1$, the change in back-face temperature is less than 1% of that of the front surface temperature ($\Theta_L / \Theta_S < 0.01$). It is shown in subsection 4.1.3 that the criterion suggested by Schultz and Jones is a conservative estimate.

4.1.2 Quenching solution

The quenching solution is a solution of the 1-D Fourier's equation for a solid of finite thickness $2L$ with a step change in a fluid temperature on both surfaces. Therefore, the temperature distribution in the solid can be assumed to be symmetric about its centreline, where $x = L$. As a result, an adiabatic boundary condition can be applied at $x = L$ for the quenching solution.

The initial and boundary conditions for the quenching solution in the non-dimensional form are:

$$\Theta = 0 \quad \text{for all } X \text{ when } Fo = 0$$

$$-\frac{\partial \Theta}{\partial X} = Bi\left(1 - \Theta_s\right) \text{ at } X = 0 \text{ for } Fo > 0$$

$$\frac{\partial \Theta}{\partial X} = 0 \text{ at } X = 1 \text{ for } Fo > 0$$

The quenching solution can be solved and expressed in non-dimensional form as (Incropera, 2007, Holman, 2010):

$$\Theta = 1 - 2\sum_{n=1}^{\infty} exp\left(-\beta_n^2 Fo\right)\frac{sin\ \beta_n}{\beta_n + sin\ \beta_n\ cos\ \beta_n} cos\left(\beta_n\left(1 - X\right)\right) \tag{4.6}$$

where the eigenvalue, β_n, can be found from:

$$\beta_n = Bi \cdot cot\left(\beta_n\right) \tag{4.7}$$

where

$$0 < \beta_1 < \pi/2 \text{ and } \beta_{n+1} \approx \beta_{n+1} + \pi \text{ for } n >> 1$$

β_n was calculated for this study based on the numerical method suggested by Zuoan (2012).

Bi in Eq. 4.7 can be replaced with *Fo* and χ (Eq. 4.4) and then Eq. 4.7 can be rewritten as:

$$\beta_n^2 Fo = \chi^2 \cdot cot^2(\beta_n) \tag{4.8}$$

Therefore, the non-dimensional front surface temperature (at $X = 0$), Θ_s, of the quenching solution can be expressed as:

$$\Theta_s = 1 - 2\sum_{n=1}^{\infty} exp\left(-\chi^2 cot^2 \beta_n\right) f_s(\beta_n) \tag{4.9}$$

where

$$f_s(\beta_n) = \frac{\sin \beta_n \cos \beta_n}{\beta_n + \sin \beta_n \cos \beta_n} \tag{4.10}$$

As a result, it can be seen that Θ_s from the quenching solution is a function of both χ and *Fo*.

The non-dimensional back-face temperature ($X = 1$) can be expressed by reducing Eq. 4.6 as:

$$\Theta_L = 1 - 2\sum_{n=1}^{\infty} exp(-\chi^2 cot^2 \beta_n) f_L(\beta_n) \tag{4.11}$$

where

$$f_L(\beta_n) = \frac{\sin \beta_n}{\beta_n + \sin \beta_n \cos \beta_n} \tag{4.12}$$

4.1.3 Comparison between semi-infinite and quenching solutions

The variation of χ with *Fo* for various values of Θ_s and the variation of Θ_s with *Fo* for various values of *Bi* are presented in Fig. 4.1 and 4.2, respectively. The curves for the semi-infinite and the quenching solution are plotted based on Eqs.4.3 and 4.8, respectively. The error loci of the two graphs, which shows the difference between the two solutions, were calculated by Eq. 4.13.

$$e = \frac{Bi - Bi'}{Bi} \tag{4.13}$$

where *Bi* and *Bi'* are the Biot numbers respectively correspond to the semi-infinite and quenching solutions.

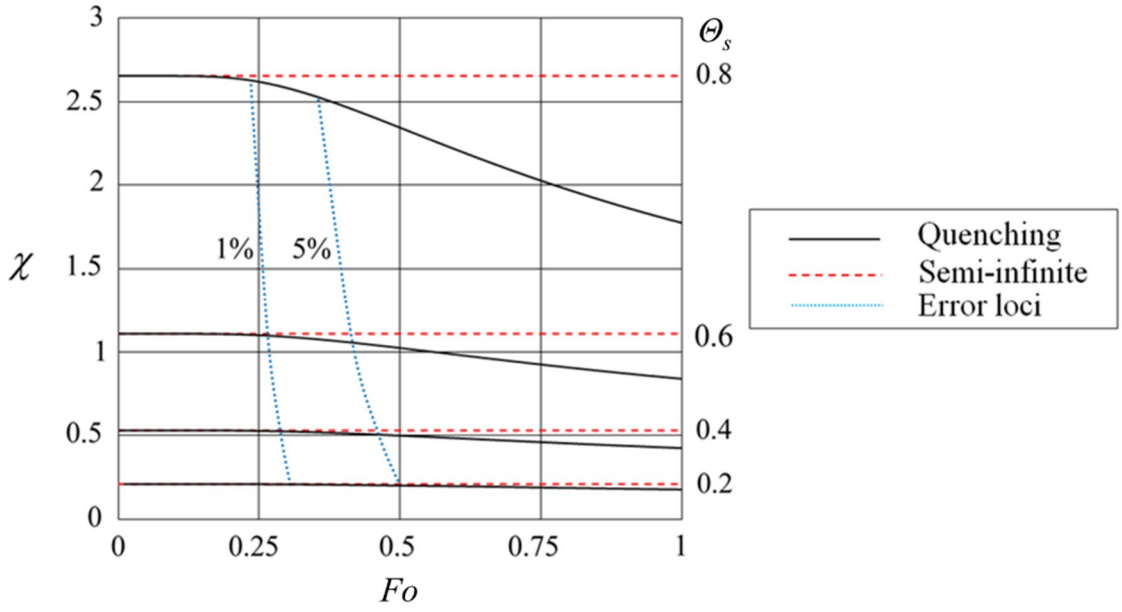

Figure 4.1 Effect of Θ_s on variation of χ with *Fo* according to the semi-infinite and quenching solutions (Pountney *et al.*, 2012)

Although, the quenching solution is only strictly applicable to the case where the back-face of the solid is perfectly insulated or when a symmetrical substrate is symmetrically heated, it is used here to check the effect of the back-face boundary condition on the accuracy of *Bi* calculated from Eq. 4.3. It can be seen from the two graphs (Fig. 4.1 and 4.2) that the differences between the two solutions increases as *Fo* increases; the semi-infinite and quenching curves diverge as *Fo* increases. It can also be found from the graphs that the limiting *Fo* for a given error loci decreases as

Θ_s increases. If a validity criterion of $e < 0.05$ is chosen for the semi-infinite solution, then the solution is valid for $Fo < 0.46$ when $\Theta_s = 0.4$ and for $Fo < 0.35$ when $\Theta_s = 0.8$. Likewise, if a validity criterion of $e < 0.01$ is selected, the semi-infinite solution is valid for $Fo < 0.29$ when $\Theta_s = 0.4$ and $Fo < 0.24$ when $\Theta_s = 0.8$. Consequently, the commonly accepted criterion suggested by Schultz and Jones (1973) appears to be overly restrictive; it can clearly be seen from the Fig. 4.1 and 4.2 that the difference between the two solutions are far smaller than 1% at $Fo = 0.1$.

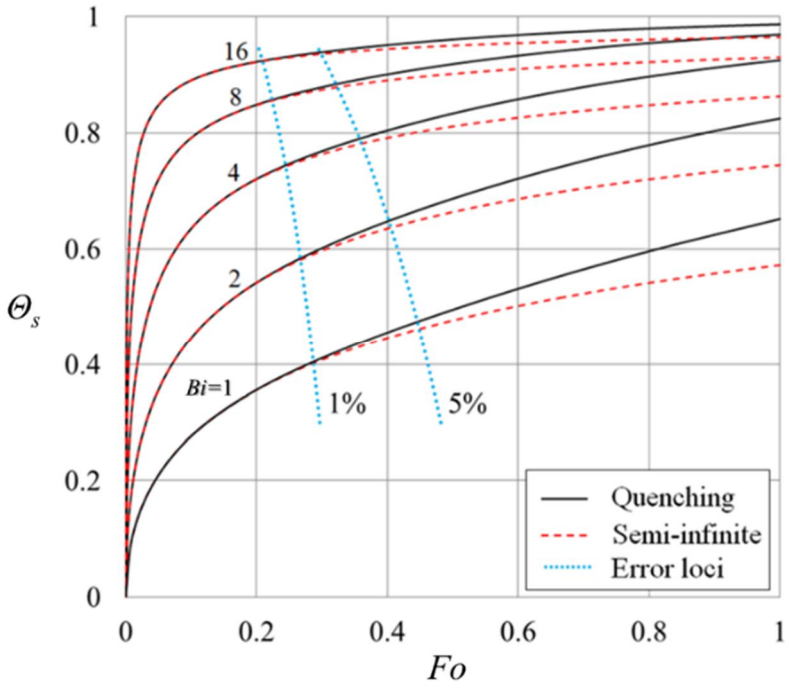

Figure 4.2 Effect of *Bi* on variation of Θ_s with *Fo* according to the semi-infinite and quenching solutions (Pountney *et al.*, 2012)

4.1.4 Effect of uncertainty in temperature measurement on calculation of h and T_{ad}

A method for evaluating the effect of uncertainty in the temperature measurement on the calculated values of h and T_{ad} for a transient heat transfer experiment was developed by Yan and Owen (2002). The authors developed the method for two different cases: uncertainty in h when T_{ad} is known and uncertainties in h and T_{ad} when both h and T_{ad} are unknown. The latter is applicable to the heat transfer experiment with TLCs in the Bath one-stage ingress test facility.

Two temperature values, $T_{s,1}$ and $T_{s,2}$, and its corresponding times, t_1 and t_2, are required to solve the semi-infinite solution, when both h and T_{ad} are unknown; it is so called two crystals method. Pountney *et al.* (2013) used two narrowband TLCs to acquire the $T_{s,1}$ and $T_{s,2}$, which can be expressed in a non-dimensional form as (note $\Theta_1 < \Theta_2$) :

$$\Theta_1 = \frac{T_{s,1} - T_{in}}{T_{ad} - T_{in}} \tag{4.14}$$

$$\Theta_2 = \frac{T_{s,2} - T_{in}}{T_{ad} - T_{in}} \tag{4.15}$$

The amplification parameters, Φ_h and Φ_{ad}, that show the ratios of the relative uncertainties in the calculated values of h and T_{ad} resulted from the uncertainties in the measured non-dimensional temperature, were defined by Yan and Owen (2002); the values of Φ_h and Φ_{ad} are closely related to the non-dimensional temperature values, Θ_1 and Θ_2.

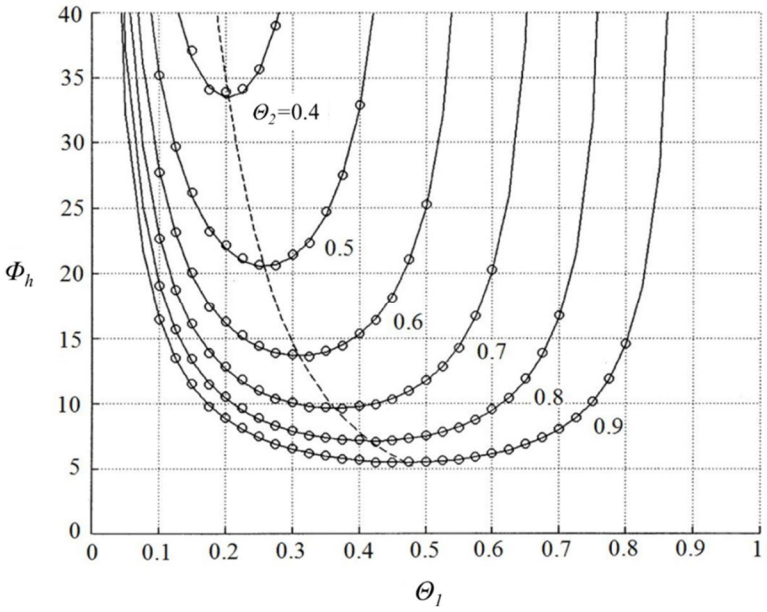

Figure 4.3Effect of Θ_2 on variation of Φ_h with Θ_1. Solid lines are theoretical curves; broken line is locus of minima; symbols are numerical values (Yan and Owen, 2002)

The effect of Θ_2 on the variation of Φ_h and Φ_{ad} with Θ_1 are shown in Fig. 4.3 and 4.4, respectively. As shown in the figures, the amplification factors can be far greater than the unity; it indicates that small uncertainties in the temperature measurements

can give rise to large uncertainties in the calculated values of h and T_{ad}. The graphs show that the amplification parameters can be minimised by carefully choosing Θ_1 and Θ_2; both Φ_h and Φ_{ad} can have minimum values when Θ_2 has the maximum possible value and $\Theta_1 \approx 0.5\ \Theta_2$.

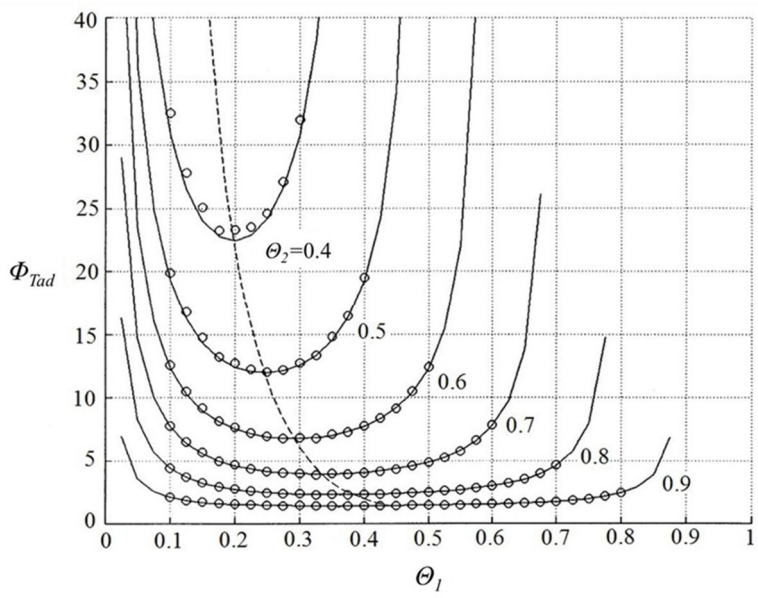

Figure 4.4 Effect of Θ_2 on variation of Φ_{Tad} with Θ_1. Solidlines are theoretical curves; broken line is locus of minima; symbols are numerical values (Yan and Owen, 2002)

The variation of Bi with Θ_s for 1 and 5% errors in the semi-infinite solution graph is shown in Fig. 4.5. The graph implies that if an experiment is conducted at values of Bi below the error loci, the errors in using the semi-infinite solution would be higher than the error indicated by the error loci. It is mainly due to the fact that the semi-infinite solution is only valid for relatively short period of the experimental time as described in section 4.1.3. Therefore, although large value of Θ_2 is required to achieve accurate estimates of h and T_{ad} with the semi-infinite solution, only a limited range of Θ_2 is achievable without violating the semi-infinite assumption; for example, the maximum achievable Θ_2 without violating the semi-infinite assumption with 5% is approximately 0.63, when Bi is 2. However, as shown in Fig. 4.3 and 4.4, when Θ_2 has a value of 0.63, the minimum achievable Φ_h and Φ_{Tad} are 13.5 and 6.6, respectively. It means that if uncertainty in the temperature measurement is 0.2°C and $T_{ad} - T_{in}$ = 40°C, then the minimum achievable errors in the calculated h and T_{ad}, under the given experimental conditions, would be 2.7% and 1.3°C, respectively.

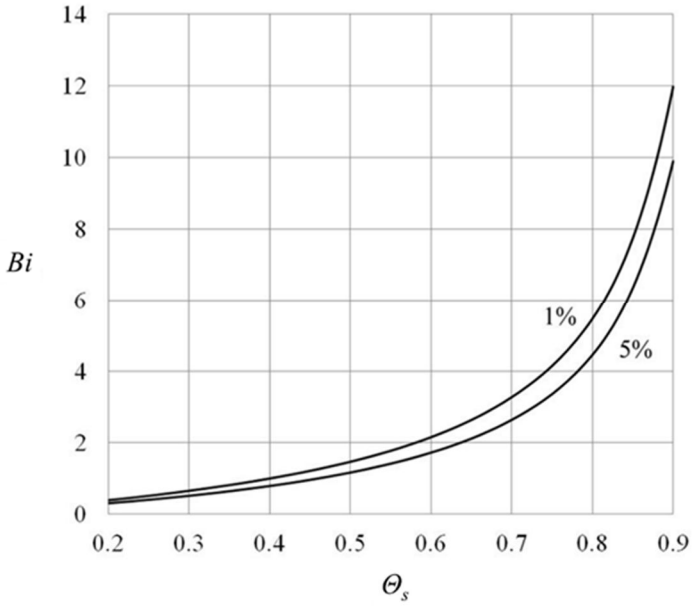

Figure 4.5 Variation of Bi with Θ_s for 1% and 5% errors in the semi-infinite solution (Yan and Owen, 2002)

Due to the aforementioned reasons, the semi-infinite solution with the two crystal method is not ideal for accurate calculation of h and T_{ad}, especially for the heat transfer experiments with low Bi, such as Bi<5. An alternative technique to the two crystal method, wide band TLC with the semi-infinite solution has been used by some research workers to determine h and T_{ad} (Wang *et al.*, 1996). For the alternative method, an extrapolation technique was used in conjunction with the semi-infinite solution to determine h and T_{ad}. In order to find h and T_{ad} with the method, the variation of the surface heat flux, q_s, was numerically determined with the semi-infinite solution based on the measured temperature history. Then, q_s vs. T_s graph was plotted, from where h and T_{ad} (if both are constant throughout an experiment) could be found by an extrapolation method based on Eq. 4.16. The value of h was acquired from the gradient of the linear regression fit and T_{ad} was found from the x-axis intercept of the graph; i.e. the value of T_s when q_s = 0. The simplified plot of the regression of q_s vs. T_s data from which h and T_{ad} can be determined is shown in Fig. 4. 6.

$$q_s = -k\left(\frac{\partial T}{\partial x}\right)_s = h\left(T_{ad} - T_s\right) \tag{4.16}$$

However, even with the alternative method, the value of the measured T_s needs to be maximised to achieve accurate estimate of T_{ad}; it is due to the fact that the uncertainty in T_{ad} increases as the difference between the centroid of the measured values of T_s and the extrapolated value increases (Chatfield, 1983). However, as both 'two crystals method' and 'extrapolation method' rely on the semi-infinite solution, the maximum achievable value of T_s is also limited by the valid experimental time.

Therefore, in order to conduct heat transfer experiment over a longer period of time without concerning the duration of valid experimental time, the back-face boundary condition that represents the actual experimental condition instead of the semi-infinite assumption is required. Hence, a numerical solution without relying on the semi-infinite assumption to analyse the heat transfer experimental data with boundary conditions that represent actual conditions of the Bath one-stage ingress test rig is developed and described below in section 4.2.

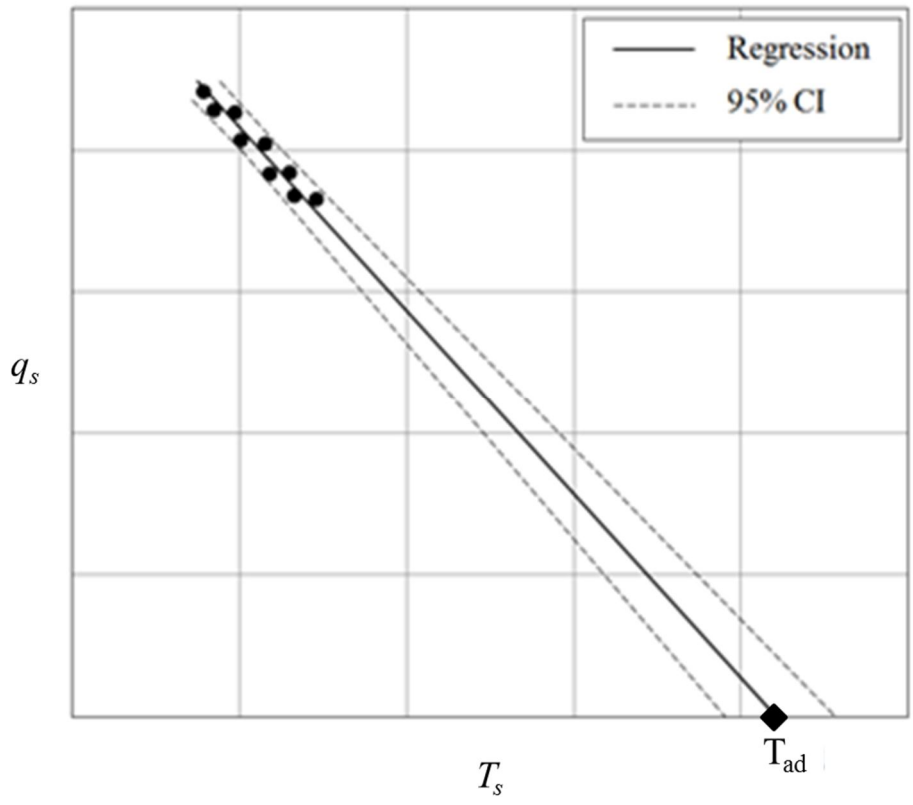

Figure 4.6 Simplified example of variation of q_s with T_s from which h and T_{ad} can be determined

4.2 Solution of Fourier equation for experiments with single substrate using IR sensor

A numerical solution of 1-D Fourier's equation was made to determine h and T_{ad} based on the temperature history acquired from heat transfer experiments in the Bath one-stage ingress test facility with the new infrared temperature measurement technique. The solution was designed to utilise the full temperature time history measured by the infrared sensor as the front-face boundary condition. The solution was firstly developed with an adiabatic back-face boundary condition for validation purpose; the solution was validated against the analytical quenching solution. The back-face boundary condition was then modified to represent the actual back-face boundary condition of the heat transfer experiment. A method to minimise the effect of imperfect (noisy) temperature measurement data was also applied to the numerical solution.

4.2.1 Solution with known convective heat transfer coefficient as front-face boundary condition

As the first step for the development of the numerical solution, a solution that simulates experiments with a single substrate under convective heat transfer at the front-face was developed. The front surface heat transfer coefficient, h_s (i.e. Bi_s), T_{in} and $T_{ad,}$ were used as input values for the simulation and the full temperature history of surfaces and internal nodes were acquired from the simulation. The purpose of this solution was to provide a simulated surface temperature history for the development of the numerical analysis method for the heat transfer experiments for the Bath one-stage rig; the simulated surface temperature history represents the measured surface temperature values acquired by the infrared temperature measurement technique. This solution will be referred to as the 'direct solution' in this thesis for convenience.

The Fourier heat equation and initial and boundary conditions used for the direct solution were expressed in non-dimensional form as:

$$\frac{\partial \Theta}{\partial Fo} = \frac{\partial^2 \Theta}{\partial X^2} \tag{4.17}$$

$$\Theta = 0 \text{ for all } X \text{ when } Fo = 0 \tag{4.18}$$

$$-\frac{\partial \Theta}{\partial X} = Bi\,(1 - \Theta_s) \text{ at } X = 0 \text{ for } Fo > 0 \tag{4.19}$$

$$\frac{\partial \Theta}{\partial X} = 0 \text{ at } X = 1 \text{ for } Fo > 0 \tag{4.20}$$

As the transient heat transfer experiments were conducted in a carefully-controlled environment, initial and boundary conditions for the numerical solution were chosen carefully to represent the actual conditions of the experiments, except for the back-face boundary condition. As the rig is required to be in thermal equilibrium prior to the conduct of the heat transfer experiment, the initial condition with uniform temperature across the rig was used for the numerical solution, Eq. 4.16. Convection and adiabatic boundary conditions were used respectively for the front and back-face boundary conditions. The convection boundary condition was used as it represents the actual experimental condition, Eq. 4.17, however the adiabatic back-face boundary condition Eq. 4.18, which does not represent the actual condition of the experiments, was used for validation purposes. The numerical solution was validated by comparison with the quenching solution. The back-face boundary condition was replaced with that representing the actual back-face experimental condition after the validation; this will be described in subsection 4.2.3.

The Crank-Nicolson method (Crank and Nicolson, 1947) was used to solve the 1-D Fourier heat equation numerically; the method has been widely used for numerically solving partial differential equations. In order to solve the heat equation numerically, the 1-D space (thickness of solid) was divided into I spatial increments, each of width L/I, and duration of heat transfer experiment (experimental time) was divided into N temporal steps. Superscripts i and n are designated for spatial and temporal increments, respectively.

The finite difference discretization of the 1-D Fourier's heat equation (Eq. 4.17) and the two boundary conditions (Eq. 4.19 and 4.20) with the Crank-Nicolson method becomes:

$$\frac{\Theta_i^{n+1}-\Theta_i^n}{\Delta Fo}=\frac{1}{2}\left[\frac{\Theta_{i-1}^{n+1}-2\Theta_i^{n+1}+\Theta_{i+1}^{n+1}}{(\Delta X)^2}+\frac{\Theta_{i-1}^{n}-2\Theta_i^{n}+\Theta_{i+1}^{n}}{(\Delta X)^2}\right] \tag{4. 21}$$

$$-\frac{\Theta_{i+1}^n-\Theta_{i-1}^n}{2\Delta X}=Bi\left(1-\Theta_i^n\right) \tag{4. 22}$$

$$-\frac{\Theta_{i+1}^n-\Theta_{i-1}^n}{2\Delta X}=0 \tag{4. 23}$$

The Eq. 4.21 was then rearranged so that the temperature at the time step of *n* and *n+1* are grouped on right and left hand side, respectively. Thus:

when, i = 1 (front surface)

$$\left(1+r+\frac{rG}{2}\right)\Theta_i^{n+1}-r\Theta_{i+1}^{n+1}=r\Theta_{i+1}^n+\left(1-r-\frac{rG}{2}\right)\Theta_i^n-rG\Theta_\infty \tag{4.24}$$

$2 \le i \le$ I-1 (internal nodes)

$$-\frac{r}{2}\Theta_{i-1}^{n+1}+(1+r)\Theta_i^{n+1}-\frac{r}{2}\Theta_{i+1}^{n+1}=\frac{r}{2}\Theta_{i-1}^n+(1-r)\Theta_i^n+\frac{r}{2}\Theta_{i+1}^n \tag{4.25}$$

i = I (back surface)

$$-r\Theta_{i-1}^{n+1}+(1+r)\Theta_i^{n+1}=r\Theta_{i-1}^n+(1-r)\Theta_i^n \tag{4.26}$$

where, $r=\dfrac{\Delta Fo}{\Delta X^2}$

$$G = 2\,Bi \cdot \Delta X$$

As shown in Fig. 4.7, the temperature values of *n=1* are known by initial conditions and *i=1* and *i=I* are known by boundary conditions. Therefore, I-2 simultaneous linear equations should be solved for every time step to obtain the temperature solution for each node. The simultaneous equations can be written in a tri-diagonal matrix system as shown in Fig. 4.8.

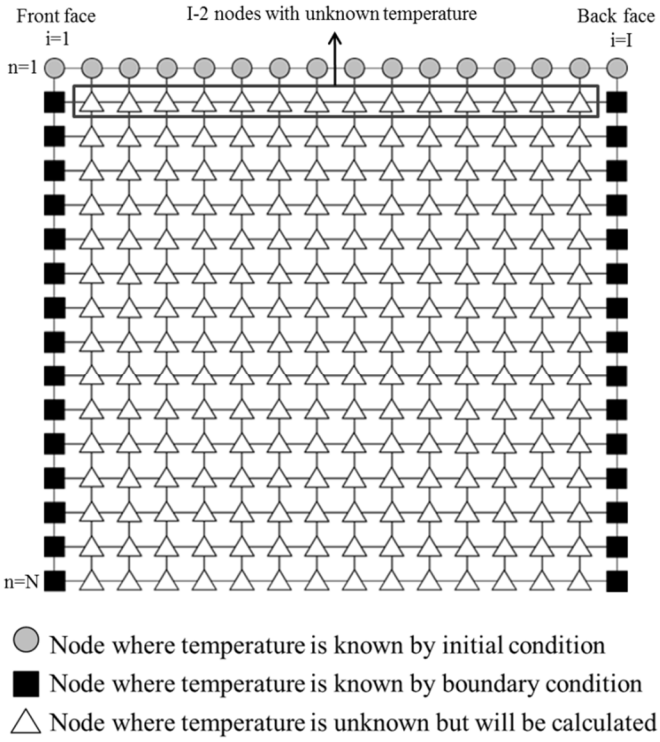

Figure 4.7 Schematic of the spatial and temporal discretisation of the direct solution

$$\begin{bmatrix} \left(1+r+\frac{rG}{2}\right) & -r & 0 & 0 & 0 & \dots & 0 & 0 \\ -\frac{r}{2} & (1+r) & -\frac{r}{2} & 0 & 0 & \dots & 0 & 0 \\ 0 & -\frac{r}{2} & (1+r) & -\frac{r}{2} & 0 & \dots & 0 & 0 \\ \dots & \dots & \dots & \dots & \dots & \dots & \dots & \dots \\ \dots & \dots & \dots & \dots & \dots & \dots & \dots & \dots \\ 0 & 0 & \dots & 0 & -\frac{r}{2} & (1+r) & -\frac{r}{2} & 0 \\ 0 & 0 & \dots & 0 & 0 & -\frac{r}{2} & (1+r) & -\frac{r}{2} \\ 0 & 0 & \dots & 0 & 0 & 0 & -r & (1+r) \end{bmatrix} \begin{bmatrix} \Theta_1^{n+1} \\ \Theta_2^{n+1} \\ \dots \\ \dots \\ \dots \\ \dots \\ \Theta_{I-1}^{n+1} \\ \Theta_I^{n+1} \end{bmatrix} = \begin{bmatrix} \left(1-r-\frac{rG}{2}\right)\Theta_1^n + r\Theta_2^n - rG\Theta_\infty \\ \frac{r}{2}\Theta_1^n + (1-r)\Theta_2^n + \frac{r}{2}\Theta_3^n \\ \dots \\ \dots \\ \dots \\ \dots \\ \frac{r}{2}\Theta_{I-2}^n + (1-r)\Theta_{I-1}^n + \frac{r}{2}\Theta_I^n \\ r\Theta_{I-1}^n + (1-r)\Theta_1^n \end{bmatrix}$$

Figure 4.8 Tri-diagonal matrix system of the direct solution

The numerical solver was validated against the analytical quenching solution. The full temperature history was acquired by solving the numerical solution with given values of Bi_s, T_{in} and T_{ad}. The temperature history of the front surface was then compared against that from the solution of the Eq. 4.6, quenching solution. The two temperature histories agree well with each other as shown in Fig. 4.9. The average difference between the numerical and the quenching solution is approximately 0.002°C, which is equivalent to a Θ value of 5×10^{-5}. Therefore, it could be concluded

that the developed numerical solution is valid and can be used to simulate the temperature history of a solid with convective front and adiabatic back-face boundary conditions.

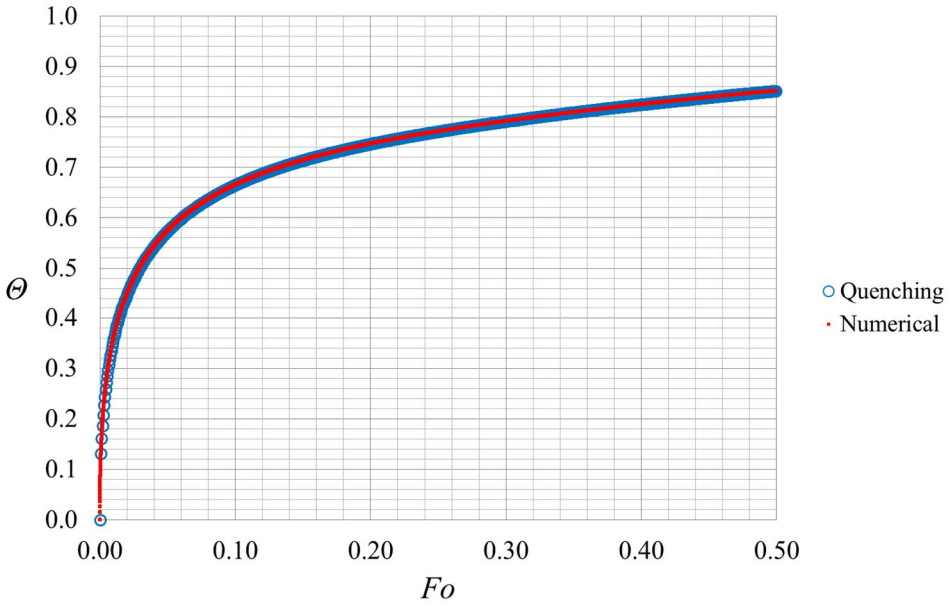

Figure 4.9 Comparison of the numerical solver against the quenching solution for validation

4.2.2 Solution with known surface temperature as front-face boundary condition

A numerical solution for a known surface temperature history as the front-face boundary condition was also developed. The purpose of this solution was to determine the unknown h_s and T_{ad} based on input values that could be acquired from a heat transfer experiment, these being the surface temperature history and the initial temperature of the system, T_{in}. This solution will be referred to as the 'inverse solution'.

The same initial and back-face boundary conditions were used for the inverse solution as the direct solution. However, known surface temperature values were used as the front-face boundary condition instead of the convection boundary condition used for the direct solution. For the back-face of the substrate, an adiabatic boundary condition was used for validation purposes; the inverse solution was validated by comparing the calculated values of h_s and T_{ad} with those used for the

direct solution as input values. The Crank-Nicolson method was also used to obtain the inverse solution and the same spatial and temporal increments were used as for the direct solution.

The following equations were acquired by rearranging the finite difference discretized form of the 1-D Fourier's heat equation, Eq. 4.21.

when, i = 1 (front surface) : temperature values of all nodes are known.

$$\Theta_1^n \text{ for } 1 \le n \le \text{N are known}$$

i = 2

$$(1+r)\Theta_i^{n+1} - \frac{r}{2}\Theta_{i+1}^{n+1} = \frac{r}{2}\left(\Theta_{i-1}^{n} + \Theta_{i-1}^{n+1}\right) + (1-r)\Theta_i^n + \frac{r}{2}\Theta_{i+1}^n \tag{4.27}$$

$3 \le i \le$ I-1 (internal nodes)

$$-\frac{r}{2}\Theta_{i-1}^{n+1} + (1+r)\Theta_i^{n+1} - \frac{r}{2}\Theta_{i+1}^{n+1} = \frac{r}{2}\Theta_{i-1}^{n} + (1-r)\Theta_i^n + \frac{r}{2}\Theta_{i+1}^n \tag{4.28}$$

i = I (back surface)

$$-r\Theta_{i-1}^{n+1} + (1+r)\Theta_i^{n+1} = r\Theta_{i-1}^{n} + (1-r)\Theta_i^n \tag{4.29}$$

where, $r = \dfrac{\Delta Fo}{\Delta X^2}$

$$G = 2\,Bi \cdot \Delta X$$

As for the direct solution, a series of simultaneous linear equations should be solved for every time step to get full temperature data of entire nodes. Therefore, the simultaneous equations was written in a tri-diagonal matrix system as shown in Fig. 4.10.

The solution was then validated against the 'direct solution'. The values of h_s and T_{ad} were determined by the 'Inverse solution' and compared against those values used as input values for the direct solution to simulate the surface temperature history.

The values of h_s and T_{ad} from the two solutions agreed well. The average difference between the calculated h_s and T_{ad} from the 'Inverse solution' and those used for the direct solution were less than 1×10^{-4}% and 1×10^{-5}°C, respectively; the average difference values were acquired from 50 numerical experiments which were carried out with different input values of T_{in}, T_{ad} and h_s. Therefore, it could be concluded that the 'Inverse solution' is valid and can be used to determine h_s and T_{ad} for heat transfer experiments based on measured surface temperature data.

$$\begin{bmatrix} (1+r) & -\frac{r}{2} & 0 & 0 & 0 & \dots & 0 & 0 \\ -\frac{r}{2} & (1+r) & -\frac{r}{2} & 0 & 0 & \dots & 0 & 0 \\ 0 & -\frac{r}{2} & (1+r) & -\frac{r}{2} & 0 & \dots & 0 & 0 \\ \dots & \dots & \dots & \dots & \dots & \dots & \dots & \dots \\ \dots & \dots & \dots & \dots & \dots & \dots & \dots & \dots \\ 0 & 0 & \dots & 0 & -\frac{r}{2} & (1+r) & -\frac{r}{2} & 0 \\ 0 & 0 & \dots & 0 & 0 & -\frac{r}{2} & (1+r) & -\frac{r}{2} \\ 0 & 0 & \dots & 0 & 0 & 0 & -r & (1+r) \end{bmatrix} \begin{bmatrix} \Theta_1^{n+1} \\ \Theta_2^{n+1} \\ \dots \\ \dots \\ \dots \\ \dots \\ \Theta_{I-1}^{n+1} \\ \Theta_I^{n+1} \end{bmatrix} = \begin{bmatrix} \frac{r}{2}\left(\Theta_1^n + \Theta_1^{n+1}\right) + (1-r)\Theta_2^n + \frac{r}{2}\Theta_3^n \\ \frac{r}{2}\Theta_2^n + (1-r)\Theta_3^n + \frac{r}{2}\Theta_4^n \\ \dots \\ \dots \\ \dots \\ \dots \\ \frac{r}{2}\Theta_{I-2}^n + (1-r)\Theta_{I-1}^n + \frac{r}{2}\Theta_I^n \\ r\Theta_{I-1}^n + (1-r)\Theta_1^n \end{bmatrix}$$

Figure 4.10 Tri-diagonal matrix system of the inverse solution

4.2.3 Numerical analysis method to compute *h* and T_{ad} using imperfect temperature data from heat transfer experiments

After the validation of the 'Inverse solution' was completed, the back-face boundary condition of the 'Inverse solution' was modified to better represent rig conditions. The 15mm thickness polycarbonate rotor disc of the Bath one-stage ingress test facility rotates at 3000rpm during heat transfer experiments. Therefore, convective heat transfer with a free disc heat transfer coefficient was chosen as the rig representative back-face boundary condition.

The relationship between local Nusselt number, Nu_r, and local rotational Reynolds number, $Re_{\phi,r}$, for turbulent flow over a free-disc rotating in a stationary fluid (i.e. β = 0) are shown by Owen and Rogers (1989) as:

$$Nu_{r,free} = 0.0267\left(\frac{n+2.6}{4.6}\right)^{0.2} Pr^{0.6}\left[(r/b)^2\, Re_{\phi,r}\right]^{0.8} \tag{4.30}$$

As the rotor can be assumed as an isothermal disc (n=0) rotating in air ($Pr \approx 0.71$), Eq. 4.30, can be reduced to:

$$Nu_{r,free} = 0.0194 \left[(r/b)^2 \, Re_{\phi,r} \right]^{0.8} \quad (4.31)$$

Therefore, the rig representative back-face boundary condition in non-dimensional form becomes:

$$-\frac{\partial \Theta}{\partial X} = Bi_b (1 - \Theta_s) \text{ at } X = 1 \text{ for } Fo > 0 \quad (4.32)$$

where Bi_b is Biot number at the back-surface (i.e. $Bi_b = h_{r,fd} \cdot L/k$)

$h_{r,fd}$ is local free-disc heat transfer coefficient ($h_{r,fd} = \frac{Nu_{r,fd} \cdot k_{air}}{r}$)

The effects of uncertainties in temperature measurement on the computation of h with the numerical solution of the 2D Fourier equation for the quenching problem were previously studied by Owen (1979). An approximate theoretical model was developed to show that small uncertainties in the 'measured temperatures' caused large uncertainties and a bias in the computed value of h. The 'amplification factor' was defined as the ratio of the relative uncertainties in the computed value of h to the relative uncertainties in the non-dimensional temperature differences. It was also shown by the research that the amplification factor could be significantly reduced by smoothing the surface temperature data. A least-squares cubic-spline fit to $\ln(T_s)$ vs. $\ln(t)$ was suggested as the most effective smoothing method that provide the smallest amplification factor.

In practice, the measured temperature data from heat transfer experiments are unlikely to be perfect. Therefore, a small error in surface temperature measurement can give rise to a large error in the calculated values of h and T_{ad}. In order to simulate the effect of random noise in calculating h and T_{ad}, a numerical experiment was carried out and the result is shown in Fig. 4.11; normally distributed pseudorandom numbers were produced by Matlab code to generate noisy data. The significantly noisy result in Fig. 4.11 a) was expected when the Fourier's heat equation was numerically solved with the inverse solution based on the non-smoothed raw temperature data with ±0.5°C of random noise. In order to develop numerical

analysis method for imperfect temperature measurement data with a random noise, the following smoothing techniques were tested.

- Least square cubic spline fit to T_s *vs.* t data

- Least square quadratic fit to T_s *vs.* t data

- Polynomial smoothing method to $\ln(T_s)$ *vs.* $\ln(t)$

- Least square cubic spline fit to $\ln(T_s)$ *vs.* $\ln(t)$

Amongst the four smoothing techniques, the least-squares cubic-spline fit to $\ln(T_s)$ *vs.* $\ln(t)$ provided the best smoothing curve and consequently the minimum error in calculated values of h and T_{ad}, as Owen (1979) reported. The 'Inverse solution' with the least-squares cubic-spline fitting method was then modified to compute h and T_{ad} based on imperfect temperature measurement data using the least square cubic spline smoothing technique. The q_s vs. T_s-T_{in} graph, from which h and T_{ad} are acquired, is shown in Fig. 4.11 b). As briefly explained in sub section 4.1.4, the value of h can be acquired from the gradient of the q vs. T_s (or T_s-T_{in}) graph and T_{ad} can be found from the x-axis intercept of the graph; i.e. the value of T_s (or T_s-T_{in}) when q_s =0.

A series of numerical experiments with four different noise levels (±0.1°C, ±0.5°C, ±1.0°C, ±3.0°C) were conducted to estimate the error expected from the numerical analysis method using the imperfect temperature data. The expected errors in the computed h and T_{ad} for the different noise levels are evaluated based on the ten numerical experiments for each noise level. The average uncertainty in calculated h and T_{ad} of each noise level are provided in Table 4.1. The expected errors in the computed h and T_{ad} increase as the uncertainty in temperature measurement increases. However, less than 0.5% and 0.05°C uncertainties in the determined h and T_{ad} are expected even with the largest uncertainty level tested. As the expected uncertainty in infrared temperature measurement is approximately ±0.2°C, it could be concluded that the effect of noisy temperature data in calculated h and T_{ad} with the new numerical analysis method, including smoothing technique, is negligible.

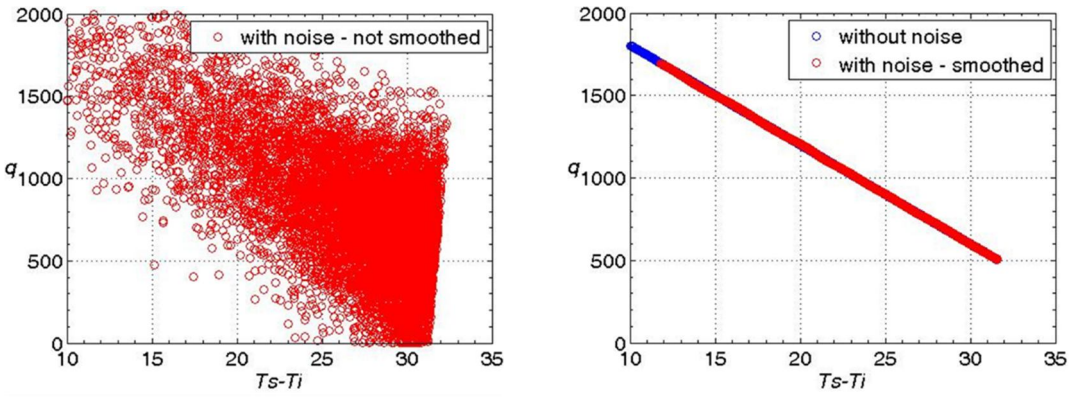

Figure 4.11 Comparison of acquired q_s vs. T_s graphs based on **a)** non-smoothed noisy temperature data without smoothing method and **b)** smoothed noisy temperature data (units of the *x* and *y*-axis: q(W/(mK)) and T_s-T_{in} (°C))

Table 4.1 The calculated h and T_{ad} of four different noise level (the true h = 60 W/m^{2}K and the true T_{ad} = 50°C)

Uncertainty in temperature measurement (with 95% confidence level)	Calculated value		Error
± 0.1°C	h (W/(m^{2}K))	60.13	**0.2 %**
	T_{ad} (°C)	49.99	**0.01 °C**
± 0.5°C	h (W/(m^{2}K))	60.13	**0.2 %**
	T_{ad} (°C)	49.97	**0.03 °C**
± 1.0°C	h (W/(m^{2}K))	60.13	**0.2 %**
	T_{ad} (°C)	49.98	**0.02 °C**
± 3.0°C	h (W/(m^{2}K))	59.7	**0.4 %**
	T_{ad} (°C)	49.97	**0.03 °C**

Only the effects of random noise are considered in this study; the effects of bias and sparseness are not considered.

4.3 Solution of Fourier equation for experiments with composite substrate using IR sensor

4.3.1 Advantages of composite substrate

As discussed in subsection 4.1.4, higher values of Θ_s from heat transfer experiment are required to acquire more accurate values of T_{ad}. Pountney *et al.* (2013) showed that a non-dimensional core temperature of up to 0.8 is achievable in the wheel-space of the Bath one-stage ingestion test facility when there is no sealing-

flow. However a core temperature higher than Θ_s of 0.8 was not achievable since the stator and rotor discs of the facility are made from polycarbonate with a thermal conductivity of 0.2W/mK; hence the system loses heat through the stator and rotor discs. The effect of the material that is used for the discs is discussed below.

The non-dimensional steady-state surface temperature, Θ_{ss}, is the maximum surface temperature that can be achieved during a heat transfer experiment. In the Bath one-stage ingress test facility, as the back-face of the rotor disc loses heat by convective heat transfer with a heat transfer coefficient value of a free-disc in a stationary fluid (h_b>100W/m^{2}K at the radius where temperature of the disc is measured), it is reasonable to assume that the back-face temperature remains unchanged from its initial temperature throughout a heat transfer experiment, i.e. Θ_b = 0 for Fo>0. Hence, the steady-state heat flux, q_{ss}, is given by

$$q_{ss} = h\left(T_{ad} - T_{ss}\right) = \frac{k}{L}\left(T_{ss} - T_i\right) \tag{4.33}$$

Therefore, it can be shown by rearranging Eq. 4.33 that

$$\Theta_{ss} = \frac{Bi}{\left(1 + Bi\right)} \tag{4.34}$$

It can be noticed from Eq. 4.34 that $\Theta_{ss} \rightarrow 1$ when Bi>>1. Therefore, for a given value L=15mm (rotor disc thickness of the Bath ingress test facility) and the maximum value of h of 60W/m^{2}K found by Pountney *et al.* (2013), the respective values of Θ_{ss} for polycarbonate (Bi=4.5) and Rohacell 51 (Bi=30) are 0.82 and 0.97 (Thermal conductivity of polycarbonate and Rohacell 51 used here are 0.2W/mK and 0.03W/mK, respectively). Therefore, Rohacell 51 could be considered as a good choice to accurately determine T_{ad}. However, due to its insufficient mechanical strength, Rohacell 51 cannot be used as the structural material for the rotor disc. In addition, the activation time would be too short to measure accurately if TLC is used for temperature measurement. Therefore, a heat transfer experiment for accurate determination of T_{ad} with a single layer of solid Rohacell is not feasible.

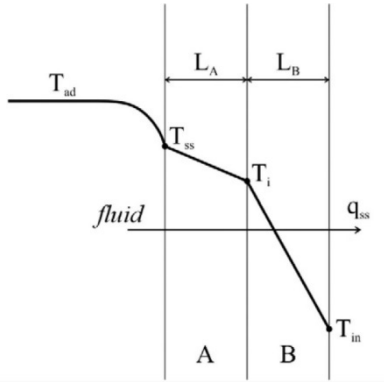

Figure 4.12 Steady state temperature distribution in composite substrate (Pountney *et al.*, 2012)

Fig. 4.12 shows an alternative solution for which an improved estimate of T_{ad} could be achieved. This is a heat transfer experiment with a composite substrate of polycarbonate and Rohacell 51. It can be shown as follows that a composite of those two materials offer a more suitable solution for accurately determining T_{ad}.

The heat flux, q_{ss}, is given by

$$q_{ss} = h(T_{ad} - T_{ss}) = \frac{k_A}{L_A}(T_{ss} - T_{int}) = \frac{k_B}{L_B}(T_{int} - T_{in}) \tag{4.35}$$

It can be shown from Eq. 4.35 that

$$\Theta_{ss} = \frac{Bi_A + Bi_B}{(1 + Bi_A + Bi_B)} \tag{4.36}$$

where, $Bi_A = \frac{hL_A}{k_A}$ and $Bi_B = \frac{hL_B}{k_B}$

T_{ss} is steady state front surface temperature

T_{int} is temperature of the interface between the materials

T_{in} is initial temperature

k_A is the thermal conductivity of polycarbonate outer layer

k_B is the thermal conductivity of Rohacell inner layer

L_A is the thickness of polycarbonate outer layer

L_B is the thickness of Rohacell inner layer

Assume $L_A = L_B = 7.5$mm and $h = 60$, then $Bi_A = 2.25$ and $Bi_B = 15$. It follows from Eq. 4.35 that $\Theta_{ss} = 0.95$, which is 0.02 lower than that of a single layer solid made of

Rohacell 51. Therefore, it is proven that composite solution could be a good alternative method to accurately determine T_{ad}.

4.3.2 Development of the numerical solution for composite substrate

The 1-D Fourier equation was solved numerically to determine *h and* T_{ad} for heat transfer experiments with a composite substrate. The solution was developed by following the same procedure for as the solution for the single substrate; i.e. the direct solution was developed to simulate the full temperature history of the surface and the inverse solution was developed to compute *h and* T_{ad} values using the simulated temperature history as the front-face boundary condition. The same initial and boundary conditions as for the inverse solution for a single substrate was used for the solution; therefore, the surface temperature history was used as the front-face boundary condition and a convective heat transfer boundary condition with heat transfer coefficient for a free-disc in a stationary fluid was used for the back-face of the Rohacell. Besides the initial and boundary conditions, additional conditions are required for the interface between the two materials; the heat flux and temperature continuity conditions as shown below (it was assumed that the two layers are in perfect thermal contact):

$$k_A\left(\frac{dT}{dx}\right)_A\Bigg|_{int} = k_B\left(\frac{dT}{dx}\right)_B\Bigg|_{int} \tag{4.37}$$

$$T_{A,int} = T_{B,int} \tag{4.38}$$

Unlike the ‘direct’ and ‘Inverse’ solutions, for convenience, a non-dimensional form was not used for the numerical solution of composite substrate.

By rearranging the finite difference discretization of the above conditions at the interface, the following equation was acquired at the interface.

when i=int (1<int<I)

$$k_A T_{i-1}^{n+1} - \left(\left(1+\frac{1}{r_A}\right)k_A + \left(1+\frac{1}{r_B}\right)k_B\right)T_i^{n+1} + k_B T_{i+1}^{n+1} = -k_A T_{i-1}^{n} - \left(\left(\frac{1}{r_A}-1\right)k_A + \left(\frac{1}{r_B}-1\right)k_B\right)T_i^{n} + k_B T_{i+1}^{n} \quad (4.39)$$

where, $r_A = \dfrac{\alpha_A t}{\Delta x_A}$ and $r_B = \dfrac{\alpha_B t}{\Delta x_B}$

Hence, the simultaneous equations for the numerical solution, including the equations for front-face, internal nodes and back-face, can be expressed in a matrix form as: $M \cdot T = R$.

where,

$$M \cdot T = \begin{bmatrix}
(1+r_A) & -\frac{r_A}{2} & 0 & 0 & \dots & 0 & 0 & 0 & \dots & 0 & 0 & 0 & 0 \\
-\frac{r_A}{2} & (1+r_A) & -\frac{r_A}{2} & 0 & \dots & 0 & 0 & 0 & \dots & 0 & 0 & 0 & 0 \\
0 & -\frac{r_A}{2} & (1+r_A) & -\frac{r_A}{2} & \dots & 0 & 0 & 0 & \dots & 0 & 0 & 0 & 0 \\
\dots & \dots & \dots & \dots & \dots & \dots & \dots & \dots & \dots & \dots & \dots & \dots & \dots \\
0 & 0 & 0 & 0 & \dots & k_A & -\left(\left(1+\frac{1}{r_A}\right)k_A + \left(1+\frac{1}{r_B}\right)k_B\right) & k_B & \dots & 0 & 0 & 0 & 0 \\
\dots & \dots & \dots & \dots & \dots & \dots & \dots & \dots & \dots & \dots & \dots & \dots & \dots \\
0 & 0 & 0 & 0 & \dots & 0 & 0 & 0 & \dots & -\frac{r_B}{2} & (1+r_B) & -\frac{r_B}{2} & 0 \\
0 & 0 & 0 & 0 & \dots & 0 & 0 & 0 & \dots & 0 & -\frac{r_B}{2} & (1+r_B) & -\frac{r_B}{2} \\
0 & 0 & 0 & 0 & \dots & 0 & 0 & 0 & \dots & 0 & 0 & -\frac{r_B}{2} & (1+r_B)
\end{bmatrix}
\begin{bmatrix} T_1^{n+1} \\ T_2^{n+1} \\ \dots \\ \dots \\ T_{int}^{n+1} \\ \dots \\ \dots \\ T_{I-1}^{n+1} \\ T_I^{n+1} \end{bmatrix}$$

$$R = \begin{bmatrix}
\frac{r_A}{2}\left(T_1^n + T_1^{n+1}\right) + (1-r_A)T_2^n + \frac{r_A}{2}T_3^n \\
\frac{r_A}{2}T_2^n + (1-r_A)T_3^n + \frac{r_A}{2}T_4^n \\
\dots \\
\dots \\
-k_A T_{i-1}^n - \left(\left(\frac{1}{r_A}-1\right)k_A + \left(\frac{1}{r_B}-1\right)k_B\right)T_i^n + k_B T_{i+1}^n \\
\dots \\
\dots \\
\frac{r_B}{2}T_{I-2}^n + (1-r_B)T_{I-1}^n + \frac{r_B}{2}T_I^n \\
r_B T_{I-1}^n + (1-r_B)T_1^n
\end{bmatrix}$$

The numerical solution for the composite substrate was validated against the analytical solution for transient heat conduction in a 1-D composite layer using the method developed by de Monte (2000). The surface temperature history of the numerical solution was compared against the analytical solution for the purpose of

validation. The temperature history from the numerical and analytical solutions agree well; numerical simulations for 10 different cases were carried out and the average difference between the numerical and the analytical solution was approximately 1×10^{-6} °C. Therefore, it could be concluded that the developed numerical solution is valid and can be used to simulate the temperature history of a composite substrate with convective heat transfer for both front and back-face boundaries. Based on the numerical solution for the composite layer, the inverse solution for a composite substrate with known surface temperature and the convective heat transfer with a free-disc heat transfer coefficient was developed to compute h and T_{ad} for a heat transfer experiment.

4.4 Solution for computing h and T_{ad} based on incomplete (piecewise) temperature data

As described in Chapter 3, it was decided to replace the previously used TLC temperature measurement technique with infrared thermography. However, the TLC technique has strong advantages over infrared pyrometer sensors where global temperature measurement data with high spatial resolution is required. Therefore, if the disadvantages of TLC could be overcome by developing a numerical method to accurately estimate full temperature history from incomplete temperature data acquired by a mixture of TLCs, TLC would be a good alternative method to infrared sensors or cameras, especially where good spatial resolution in global temperature measurement is required but infrared thermography is not a feasible option.

In principle, the full temperature history could be acquired by using a mixture of different TLCs. This can be achieved by determining temperature-hue or temperature-intensity characteristics of each crystal over its entire thermal bandwidth. If a video camera with the measurement interval of δt (typical video cameras has δt of 40ms, i.e. 25Hz measurement frequency) and the TLC with the thermal bandwidth of ΔT are used for the temperature measurement, then number of temperature data, n, that can be acquired over the time when each crystal is active, Δt, is given as:

$$n = \frac{\Delta t}{\delta t} \tag{4.40}$$

then

$$\Delta T \approx \frac{dT_s}{dt}\Delta t \tag{4.41}$$

n becomes that

$$n \approx \frac{\Delta T}{(dT_s / dt)\delta t} \tag{4.42}$$

In a transient experiment, when TLCs with the same bandwidth are used, dT_s/dt decreases and consequently *n* increases, as Θ_s increases. This implies that, in order to achieve the same accuracy of the fitted curve, the bandwidth of the TLC could be smaller at the larger values of Θ_s. It also gives an idea that wideband crystals would be required to achieve the same accuracy of the estimated temperature variation, for the small values of Θ_s, when dT_s/dt has considerably larger values.

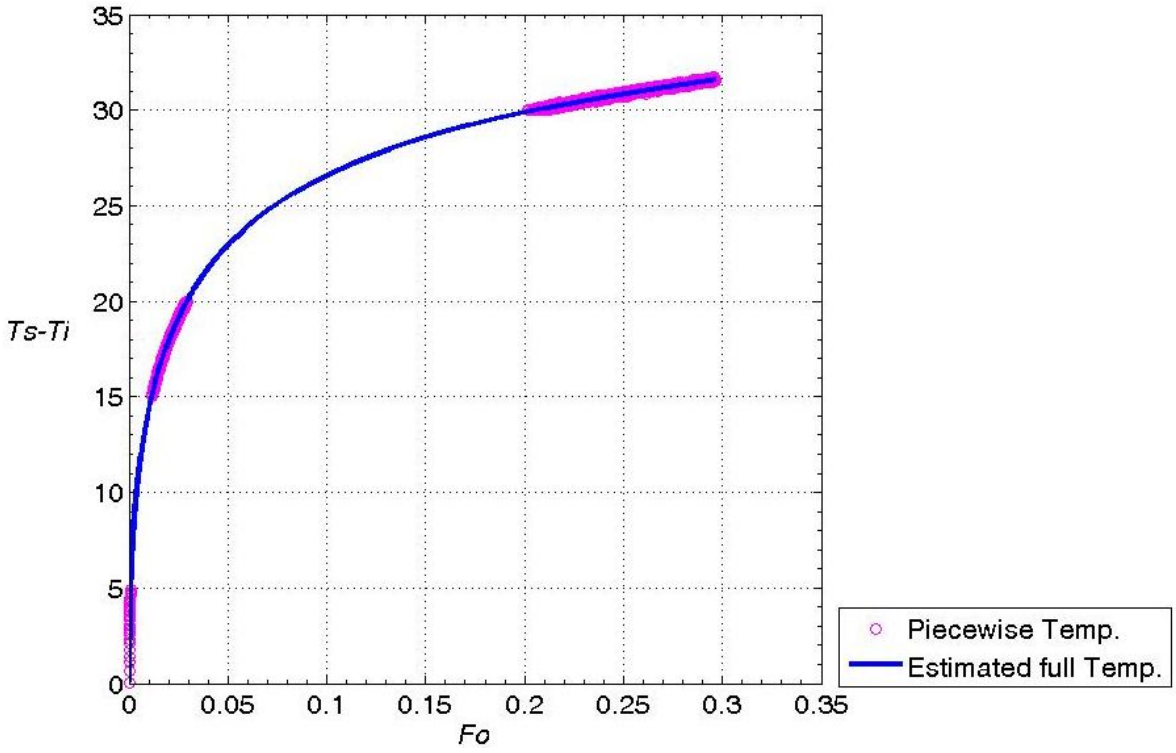

Figure 4.13 Estimation of full temperature history from piecewise data

A series of numerical experiments for computing *h* and T_{ad} using incomplete (piecewise) surface temperature data have been carried out. The purpose of these experiments was to evaluate the feasibility of accurate estimation of full temperature

history based on piecewise temperature data and compute h and T_{ad} with the estimated full temperature history. It was found from the numerical experiments that full surface temperature history could be estimated from piecewise temperature data by applying least square cubic spline fit to the piecewise temperature data ($\ln(T_s)$ *vs.* $\ln(t)$), as shown in Fig. 4.13.

As it is known that the uncertainty level of TLC is affected by its bandwidth; wideband TLCs have higher measurement uncertainty than narrowband TLCs. The uncertainty level used for simulated TLC temperature measurement was chosen based on the mixtures of TLCs used for the numerical simulation. The four different combinations of TLC mixtures were tested and corresponding uncertainty levels for the mixtures are shown in Table 4.2. The uncertainty levels were quoted from Elkins *et al.* (2001).

Table 4.2 Chosen TLC combinations and corresponding uncertainty levels

TLC combination	Uncertainty level
3 × 1°C BW (bandwidth)	± 0.1°C
1 × 5°C BW + 3 × 1°C BW	± 0.1°C
3×5°C BW	± 0.1°C
2 × 10°C BW	± 0.3°C

Table 4.3 The computed h and T_{ad} with piecewise surface temperature data from two different TLC combinations

	Full temperature history with noise (smoothed)	3 ×5°C BW		2 × 10°C BW	
		values	errors	values	errors
h (W/m^{2}K)	60.13	59.73	0.37%	58.93	1.67%
T_{ad} (°C)	49.97	50.06	0.06	50.18	0.18

The numerical experiments were repeated for ten different data sets for each TLC combinations and the averaged values of computed h and T_{ad} and corresponding errors are provided in Table 4.3. Amongst the four TLC combinations, the three 5°C

bandwidth TLCs and two 10°C bandwidth TLCs mixtures provided computed h and T_{ad} values with less than 2% and 0.2°C uncertainties. It can be concluded that values of h and T_{ad} of heat transfer experiment can be accurately determined with the numerical analysis method developed in section 4.2 based on the piecewise TLC temperature measurement technique instead of an infrared sensor. However, it has also been found that the uncertainty levels of the calculated h and T_{ad} are considerably affected by the type of TLCs (including bandwidth and activation temperature). Therefore, a combination of TLCs should be carefully considered to achieve the best result and consequently further numerical and experimental studies are required to develop the experimental method for accurate determination of h and T_{ad} based on the incomplete temperature history acquired from the TLC temperature measurement technique.

4.5 Summary

The semi-infinite solution of Fourier's equation, which is widely used for analysing data from transient experiments using TLC temperature measurement, was compared to the so-called 'quenching solution' (a solution of 1-D Fourier equation which is appropriate for tests with solids of symmetrical section). The range of Fo for which semi-infinite solutions are acceptably accurate was determined from the comparison and it was shown that the commonly accepted validity criterion for the semi-infinite solution (Schultz and Jones, 1973), $Fo<0.1$, is overly restrictive. In addition, the effect of uncertainty in temperature measurement on the calculation of h and T_{ad} was also discussed and it was concluded that accurate estimates of T_{ad} require the measured surface temperature to be as close to these as possible regardless of the analysis method used.

A numerical solution of the 1-D Fourier equation for a single-layer substrate was developed based on the Crank-Nicolson method to determine h and T_{ad}. The rig-representative initial and boundary conditions were used for the solution including the full temperature history, measured by the new infrared sensor, as the front-surface boundary condition. The developed numerical solution was then validated against the analytical solution and showed very good agreement. In addition, the

effects of uncertainties in temperature measurement on the computation of T_{ad} and h were also investigated and a numerical solution for temperature data with random noise was developed based on Owen (1979). With the numerical solution, four different levels of uncertainty in temperature measurement were tested and it was found that the effect of noisy temperature data can be virtually eliminated with this solution. However, only the effects of random noise were considered in this study, that is, the effect of bias and sparseness were not investigated.

As a higher value of surface temperature from a transient heat transfer experiment in the Bath one-stage ingress test rig is required to achieve a more accurate estimation of T_{ad}, it was suggested that a two-layer composite substrate comprising be used, for example, one layer of Rohacell foam and the other of polycarbonate. In order to determine h and T_{ad} for transient heat transfer experiments with a composite substrate, a solution to numerically solve Fourier's 1-D heat equation based on the Crank-Nicolson method was developed. The rig-representative initial and boundary conditions were used for the solution and it was validated against the analytical solution for transient heat conduction in a one-dimensional composite layer and showed a very good agreement.

A series of numerical experiments to evaluate the feasibility of accurate estimation of full temperature history based on piecewise temperature data (measured by a mixture of TLCs) and to compute h and T_{ad} with the temperature data, were carried out. It was suggested that the full temperature history could be estimated from the piecewise temperature data by applying a least squares cubic-spline fit to a $\ln(T_s)$ vs. $\ln(t)$ plot. The numerical simulations showed that it is possible to estimate h and T_{ad} values of a transient heat transfer experiment accurately based on the piecewise temperature data acquired with a mixture of TLCs. However, at the same time, it was also shown that the uncertainty levels of the calculated h and T_{ad} are considerably affected by the type of TLCs, in particular, regarding their bandwidth and activation temperature. Hence, further numerical and experimental studies are required to develop the method to estimate full temperature history accurately based on the piecewise temperature data acquired by TLC temperature measurement.

Chapter 5: Concentration sealing effectiveness measurements on the stator

This chapter presents experimentally measured concentration sealing effectiveness data that were acquired using CO_2 as a tracer gas in the Bath one-stage ingress test facility. An overview of the test facility, which experimentally simulates hot gas ingress into the wheel-space of an axial turbine stage, is provided in this chapter. This includes the configurations of the test section, design point of the turbine stage and the instrumentation used. Geometries of the four seals tested are also described in detail including the polycarbonate inserts that were attached to the inner surfaces of the aluminium platforms to reduce the heat loss through the aluminium shroud. In order to achieve a more accurate determination of the adiabatic disc temperature, a cover-plate with 5mm thickness, made of Rohacell, was attached on both the stator and rotor discs. The concentration and heat transfer measurements respectively described in Chapter 5 and Chapter 6 were conducted in the wheel-space with 10mm axial spacing between stator and rotor; all other experimental measurements made in the Bath one-stage rig so far have been achieved using a wheel-space with 20mm axial spacing. (*Note*: details of the modifications are discussed in subsection 6.1.1.)

The variation of the concentration sealing effectiveness, ε_c, with non-dimensional sealing parameter, Φ_0, was determined for four different seal geometries. The main purpose of these measurements was to provide reference data to show thermal buffering, where the effect of ingress on the rotor is less than that measured on the stator. The measurement of adiabatic sealing effectiveness and its comparison with concentration effectiveness are described in Chapter 6. By measuring the variation of the concentration sealing effectiveness with the sealing flow rate, the performance of the four generic rim seals were assessed. In addition, a series of concentration tests, to show the radial variation of the concentration effectiveness with radius, were conducted for two sealing flow rates per rim seal. The concentration measurements were in very good agreement with the experimental data provided by Sangan *et al.* (2013c).

5.1 Experimental facility

The Bath one-stage ingress test facility was designed by Sangan *et al.* (2013a) and a full description of its design and commissioning is described in Sangan (2011). This section will provide a brief overview of the test facility.

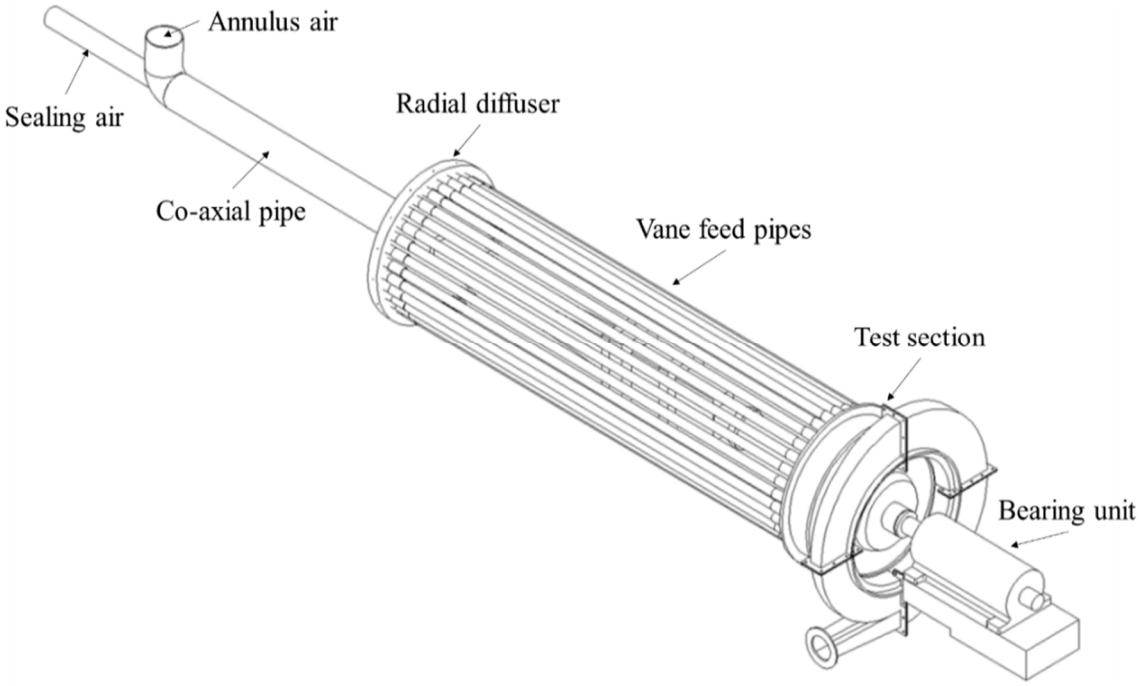

Figure 5.1 General assembly of the Bath one-stage ingress test facility (Sangan, 2011)

An isometric view of the Bath one-stage ingress test facility is shown in Fig. 5.1. The sealing and annulus air are supplied to the rig through a coaxial pipe. The mainstream air is supplied into a radial diffuser and flows through thirty two vane feed pipes and a transition section before entering the rotor-stator test section. The rotor disc of the rig can be rotated up to 4000 rpm using an electric motor, providing a maximum Re_ϕ of 1.1×10^6. Although this value is an order of magnitude lower than those of gas turbines, Re_ϕ has only a weak effect on the turbulent flow structure in the wheel-space (Owen and Rogers, 1989, Childs, 2010); the turbulent flow structure is predominantly governed by the turbulent flow parameter, λ_T. Therefore, the flow structure in the Bath one-stage test facility can be considered as being representative of that found in cooling systems of gas turbines.

5.1.1 Test section

Fig. 5.2 shows the test section of the Bath one-stage ingress rig, where the ingress of hot mainstream gas of a gas turbine is simulated and which consists of a rotor-stator system with 32 nozzle guide vanes and 41 rotor blades. The NACA 0018 symmetrical aerofoil profile was used for the blades to prevent the turbine generating excess power so as to avoid the necessity of a dynamometer. The velocity triangle for the Bath one-stage ingress test rig at the design points is provided in Fig. 5.3. The angle and velocity that air leaves the vane are α=73.5° and *C*, respectively, and the angle of the rotor blade and the velocity of the air relative to the blade were β_0=56.7° and V_o, respectively. The flow coefficient of the test facility at the design point was found to be $C_F=Re_w/Re_\phi=0.538$ using Eq. 5.1. (Saravanamuttoo, 2009).

$$C_F = \frac{1}{\tan\alpha - \tan\beta_0} \tag{5.1}$$

The rotational Reynolds number, Re_ϕ, axial Reynolds number, Re_w, flow coefficient and vane exit absolute Mach number at design operating conditions for two different rotational speeds are shown in Table 5.1. All experimental data presented in this thesis, except the variation of concentration effectiveness with sealing flow rate, were collected with a rotor disc speed of 3000 rpm.

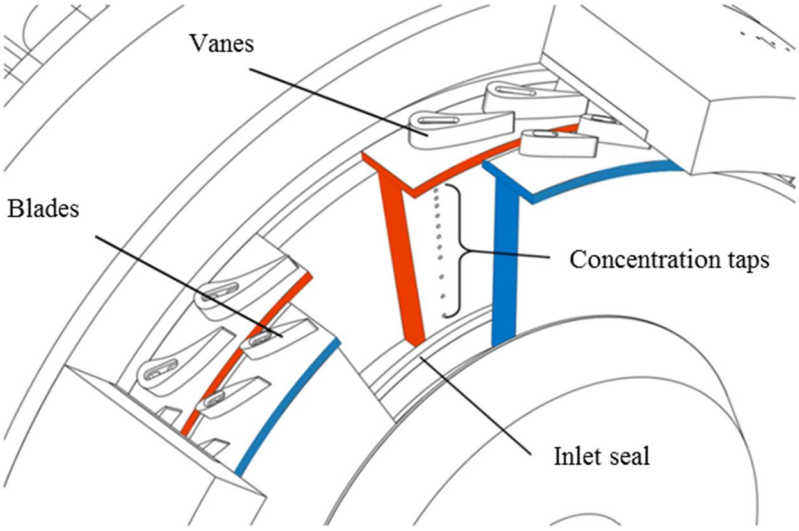

Figure 5.2 The test section of the Bath one-stage ingress rig. The stator disc is shown in red and the rotor disc in blue. (Sangan *et al.*, 2013b)

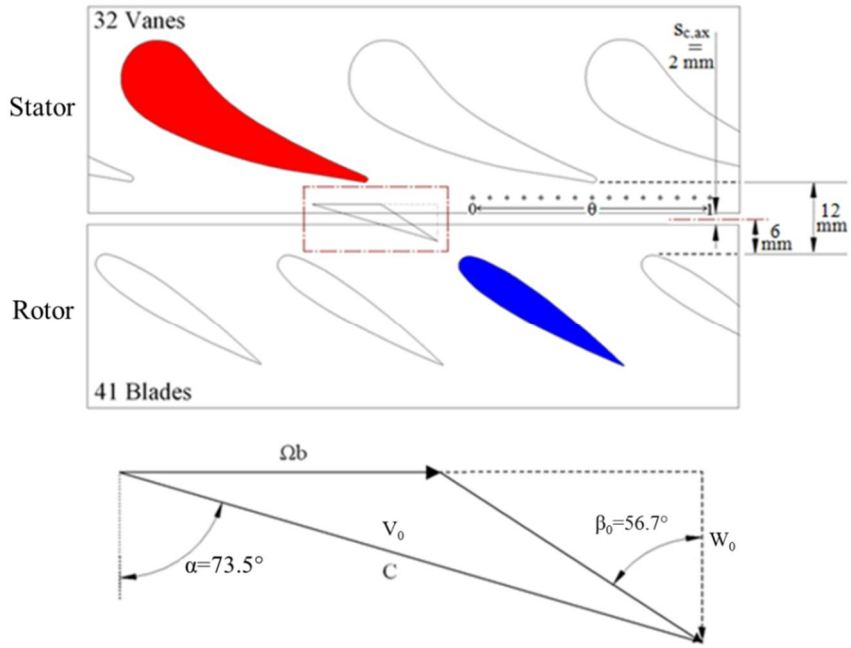

Figure 5.3 Vane and blade setup, with velocity triangles at the design point of the Bath one-stage ingress test facility (Sangan *et al.*, 2013a)

The values of the air properties and flow conditions, such as μ, M, Re_ϕ, and Re_w, were calculated based on the static pressure and temperature measured in the wheel-space on the stator at r/b=0.993. As shown in Fig 5.3, the distance from both the vane trailing edge and the blade leading edge to the mid-plane of the seal clearance were equal at 6mm, i.e. there was 2mm seal clearance, $S_{c,ax}$, and 12mm of axial distance between the vane trailing edge and the blade leading edge. In order to minimise the amount of mainstream air that is required for achieving the necessary flow velocity at the design point for the maximum rotational speed (4000 rpm), the annulus was designed to have 10mm height. It was shown by Sangan (2011) that the boundary layer thickness was estimated to be 3.5% of the total flow area through the annulus.

The rotor disc of the test facility was designed to have a 0.4mm step-down between the stator and rotor discs so as to take the radial growth of the polycarbonate rotor due to rotating into account. In addition, the rotor was machined with a 30° chamfer at the upstream edge of its shroud to prevent the impingement of the mainstream flow. The radial growth of the rotor at the maximum speed was measured with a laser transducer and found to be 0.23mm, which was smaller than

the step height of 0.4mm. The sealing air was supplied to the test section through the aforementioned sealing flow pipe, which was connected to the centre of the stator disc. The sealing air was introduced into the wheel-space through the annular-shaped inlet seal which was located at r/b=0.642, as shown in Figs. 5.2 and 5.4. The sealing air was seeded with 1% CO_2 tracer gas for the concentration tests and was heated using an electric powered mesh heater for the heat transfer tests. Detailed description of the concentration, pressure and temperature measurements is provided in subsections 5.1.2 and section 6.1 and 7.3, respectively. Calibrated orifice plates, which were built to EN ISO 5167-2 (ISO), were used to measure both the mainstream and sealing flow rate with ±3% uncertainty (Sangan, 2011).

Table 5.1 Design operating conditions for three different rotational speeds

Parameter	Disc Speed (rpm)	
	2000	3000
Re_ϕ	5.32×10^5	8.17×10^5
Re_w	2.86×10^5	4.40×10^5
$C_F=Re_w/Re_\phi$	0.538	
M	0.225	0.339

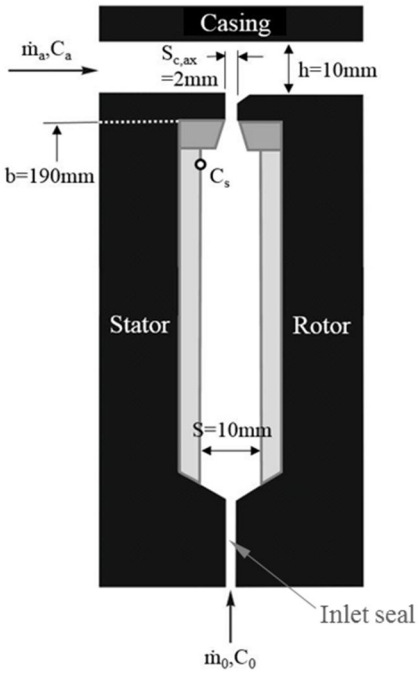

Figure 5.4 Simple axial seal geometry with key geometric parameters, mass flows and concentrations in the test section (shown in grey is a Rohacell cover-plate)

5.1.2 Concentration measurements

The sealing effectiveness of four different rim-seals, which are shown in section 5.3, were determined based on the concentration of CO_2 tracer gas on the stator disc at *r/b*=0.958 (shown as C_s in Fig. 5.4). The radial variation of sealing effectiveness was also investigated by measuring the variation of CO_2 gas concentration on the stator surface (C_s) with a radius at 13 radial locations between *r/b*=0.55 and 0.958, which are illustrated in Fig. 5.2. The CO_2 gas concentration of the air sampled from the 13 sampling taps was measured using a Signal Group 9000 MGA dual channel infrared gas analyser with ±1.5% uncertainty (Sangan, 2011). As the CO_2 gas concentration of the mainstream air (unseeded) and sealing air (1% CO_2) were different, the amount of ingress that occurred could be determined based on the CO_2 concentration levels at the sample point.

The concentration sealing effectiveness, ε_c, was defined as:

$$\varepsilon_c = \frac{c_s - c_a}{c_0 - c_a} \tag{5.2}$$

where, c_s is the concentration level on the stator wall

c_a is the concentration level of the mainstream air

c_o is the concentration level of the sealing air

The definition of ε_c satisfies the criterion that $\varepsilon_c \rightarrow 1$ (zero ingress) as $\Phi_0 \rightarrow \Phi_{min}$ and $\varepsilon_c \rightarrow 0$ (zero sealing flow) as $\Phi_0 \rightarrow 0$.

where, Φ_0 is the non-dimensional sealing flow parameter

Φ_{min} is the value of Φ_0 that is required to prevent ingress

5.2 Geometry of rim seals

Four seal geometries (two single and two double rim seals) were chosen for the concentration (Chapter 5) and heat transfer (Chapter 6) tests presented in this thesis. A Rohacell cover-plate with 5mm thickness was attached on both the stator and rotor discs, thus resulting in a wheel-space with 10mm of axial spacing. Previous tests (Pountney, 2013) were conducted with a 20mm axial spacing and polycarbonate

discs; the Rohacell boundaries in the current experiment create a near adiabatic wheel-space.

5.2.1 Single rim seals

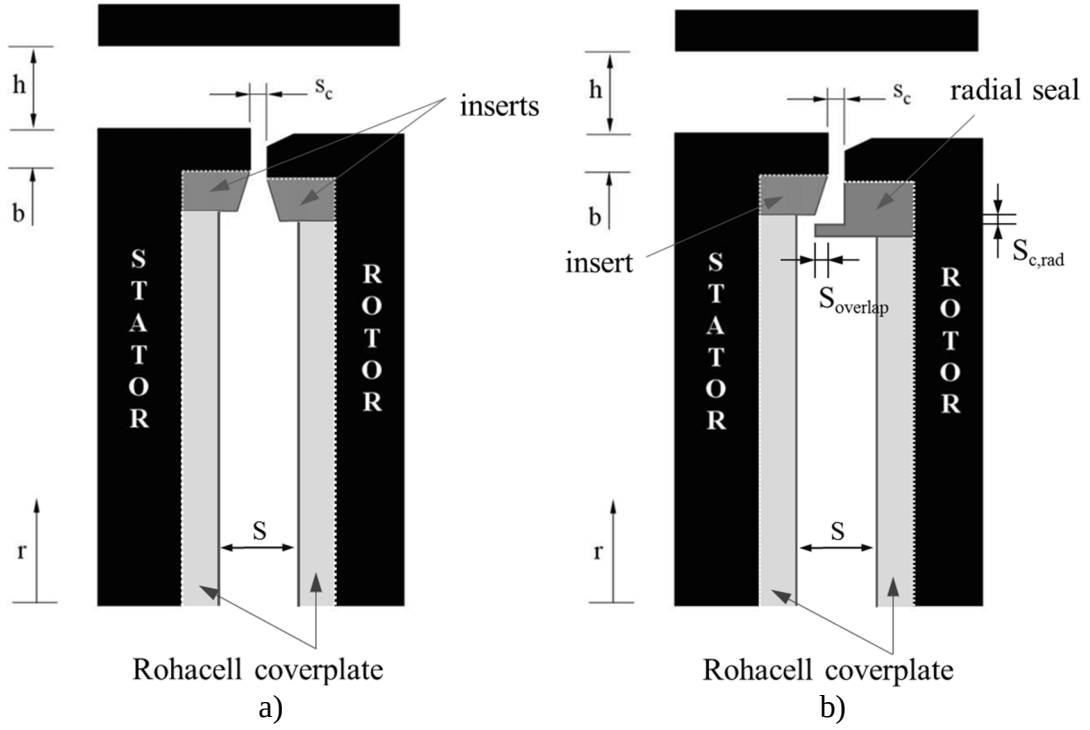

Figure 5.5 Single-clearance seal configurations: a) axial and b) radial (the parts shown in dark and light grey are made of polycarbonate and Rohacell, respectively)

The two single-clearance rim seals, an axial and a radial one, are shown in Fig. 5.5 and their static (i.e. at Ω = 0rpm) geometric details are given in Table 5.2. The vane and blade platform at the periphery of the stator and rotor form the simple axial-clearance seal used in the test. As the platforms are made of aluminium, polycarbonate inserts were attached to the inner surfaces to reduce the heat loss, as shown in Fig. 5. a). The inserts had a radial thickness of 5mm and were mitred with an angle of 15° to the radial direction. The polycarbonate insert of the rotor was replaced with a polycarbonate radial seal to form a single radial-clearance seal configuration, as shown in Fig. 5.b). The radial seal was designed to have a similar geometry to a seal tested by Sangan *et al.* (2013c), in terms of axial overlap ($S_{overlap}$) and radial-clearance ($S_{c,rad}$). The radial-clearance seal features the same geometry (polycarbonate insert) at the periphery of the stationary disc as the axial-clearance

seal, so the trench cavity of the radial-clearance seal had to be deepened to avoid interference and the radial thickness of the seal-lip was reduced from 5mm to 2mm so as to keep it away from the field of view of an infrared sensor.

Table 5.2 Static dimensions (in mm) for the two tested single-clearance rim seal configurations

Geometric Symbol	Axial-clearance seal	Radial-clearance seal
h	10.0	
b	190	
S	10.0	
$S_{c,ax}$	2.00	
$S_{c,rad}$	-	1.28
$S_{overlap}$	-	1.86

5.2.2 Double rim seals

The two double-clearance rim seals, a double axial and a double radial seal, are shown in Fig. 5.6 and their static geometric details are given in Table 5.3. The double axial-clearance seal, shown in Fig.5.6 a), was created by adding a secondary inner axial-clearance seal, made of Rohacell 51, to the single axial-clearance seal described above. The inner seal was designed to have the same axial-clearance ($s_{c,ax}$), 2mm, as the outer axial seal. The double radial-clearance seal shown in Fig. 5.6 b) was formed in a similar way to the double axial-clearance seal; the inner radial-clearance seal was created by adding an annular-shaped Rohacell piece to the each disc of the single radial seal configuration. The two double-clearance seals were designed to have the same height for the outer wheel-space (h_{buffer}).

(***Note***: A simple radial-clearance seal without polycarbonate inserts and Rohacell cover-plates was used for pressure measurements to develop the theoretical model to determine the pressure effectiveness, ε_p and its geometries are provided in section 7.1.)

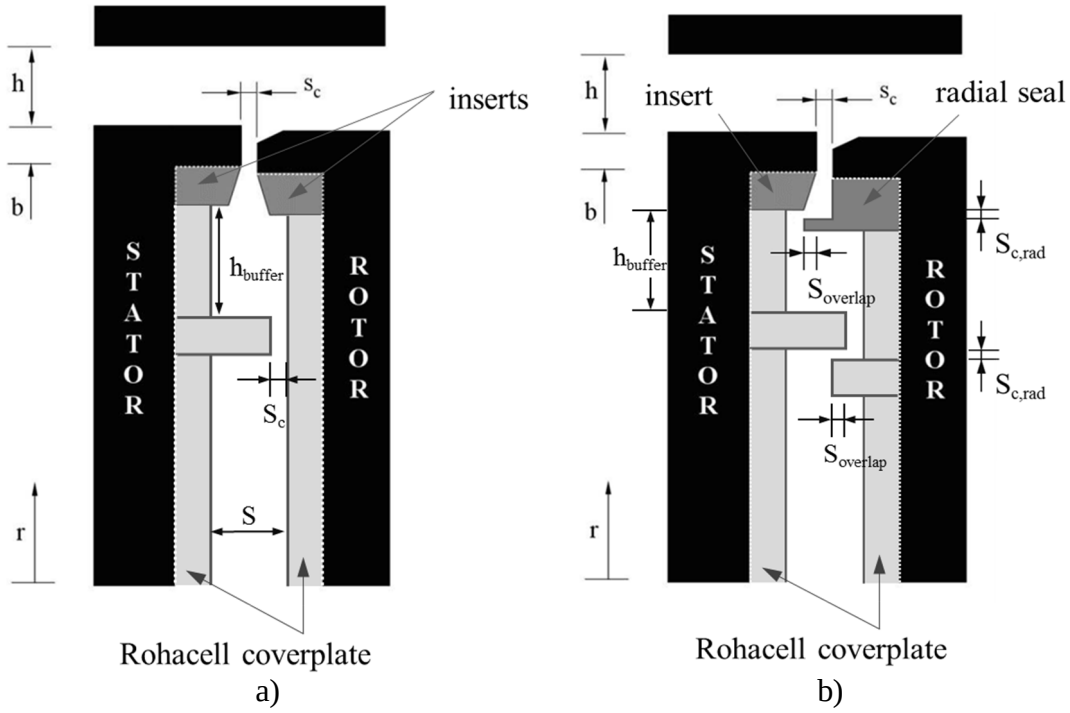

Figure 5.6 Schematic of the tested double-clearance seals: a) double axial and b) double radial (the parts shown in dark and light grey are made of polycarbonate and Rohacell, respectively)

Table 5.3 Static dimensions (in mm) for the two tested double-clearance rim seals configurations

Geometric Symbol	Double axial seal	Double radial seal
h	10.0	
b	190	
S	10.0	
$S_{c,ax}$	2.00	
$S_{c,rad}$	-	1.28
$S_{overlap}$	-	1.86
h_{buffer}	16.5	16.5

5.3 Measurements of concentration effectiveness

As this chapter is concerned only with externally-induced (EI) ingress, the subscript EI is not used below.

5.3.1 Single-clearance rim seals

The variation of ε_c with Φ_0 of the two single-clearance rim seals was measured at the non-dimensional radius, *r/b*, of 0.958 for two values of rational speed, 2000 and 3000 rpm (Re_ϕ value of 5.32×10^5 and 8.17×10^5, respectively) under design operation

conditions. It should be noted that ε_c was broadly invariant with radius for these single-clearance seals as described in subsection 5.4.1.

Axial-clearance rim seal

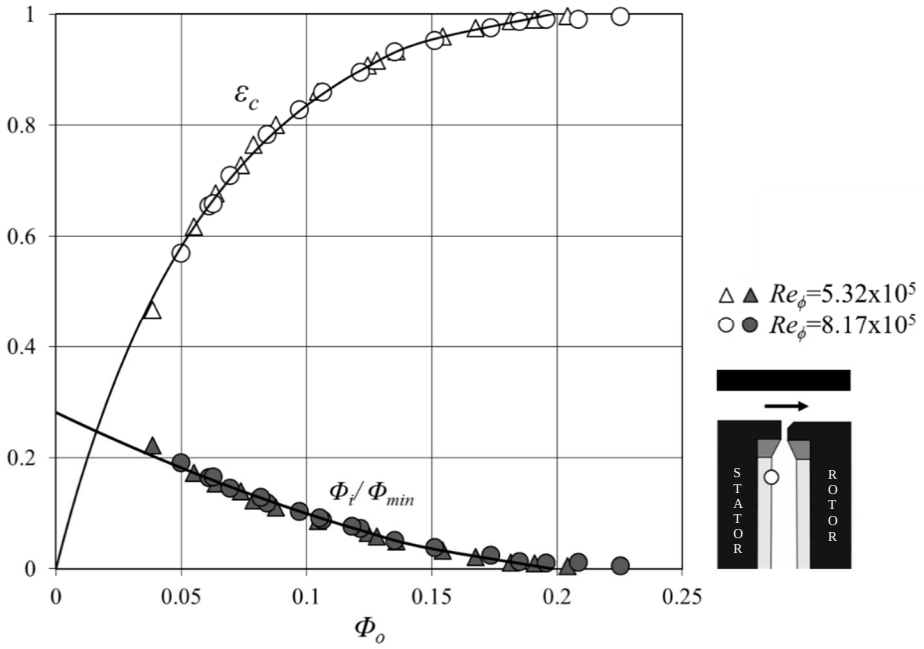

Figure 5.7 Variation of ε_c and Φ_i/Φ_{min} with Φ_0 for a single axial-clearance seal: EI ingress (Symbols denote experimental data; lines are theoretical fits)

The variation of ε_c, for the single axial-clearance seal with polycarbonate inserts, with Φ_0, is plotted in Fig. 5.7. It can be seen that the relationship between ε_c and Φ_0 is independent of Re_ϕ. In order to get a theoretical curve, the measured concentration effectiveness data were fitted according to Eq. 2.1, using the statistical technique developed by Zhou *et al.* (2013). The agreement between the fitted theoretical curve and the measured concentration data was very good and the values of Φ_{min} and Γ_c for the axial-clearance seal with polycarbonate inserts were found to be 0.198 and 0.652, respectively. Fig. 5.7 also shows the variation of the non-dimensional ingested flow rate (Φ_i/Φ_{min}) obtained from Eq. 2.31.

Radial-clearance rim seal

Similar experiments were conducted for the single radial-clearance seal and the variation of ε_c with Φ_0 for the single radial-clearance seal, compared with that of the

axial-clearance seal, is plotted in Fig. 5.8. As with the single axial-clearance seal, it can also be seen that the relationship between ε_c and Φ_0 is independent of Re_ϕ. The optimum theoretical curve was plotted using the same statistical technique used for the single axial-clearance seal data. As shown, the agreement between the fitted theoretical curve and the measured concentration data is very good and the value of Φ_{min} and Γ_c for the radial-clearance seal with polycarbonate inserts under EI conditions are found to be 0.124 and 1.601, respectively. That is, the single radial-clearance seal requires approximately 60% of the sealing air required to prevent ingress through the single axial-clearance seal.

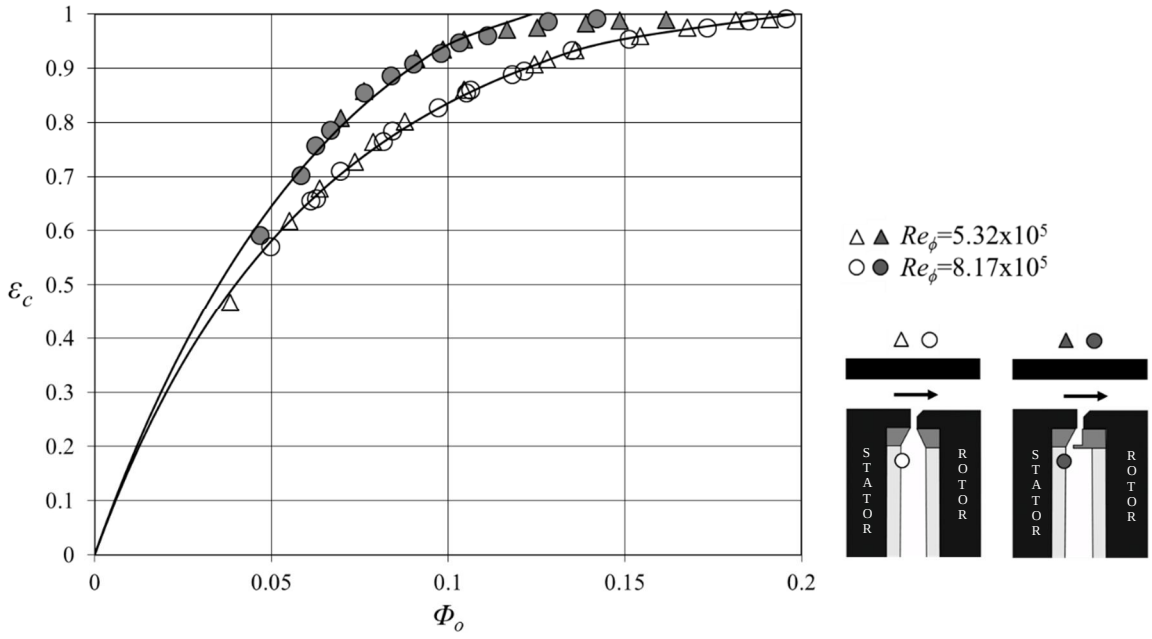

Figure 5.8 Variation of ε_c with Φ_0 for a single radial-clearance seal compared with axial-clearance seal data: EI ingress (Symbols denote experimental data; lines are theoretical fits)

5.3.2 Double-clearance rim seals

The variation of ε_c with Φ_0 for the outer (r/b > 0.913) and inner wheel-space (0.642 < r/b < 0.887) of the double axial seal were collected at r/b = 0.958 and 0.85, respectively. As with the single-clearance seals, the variation of the ε_c with Φ_0 of the double-clearance rim seals was investigated for two values of rotational speed, 2000 and 3000 rpm (Re_ϕ value of 5.32 × 10^5 and 8.17 × 10^5, respectively), with the corresponding design operation conditions shown in Table 5.1.

Double axial-clearance seal

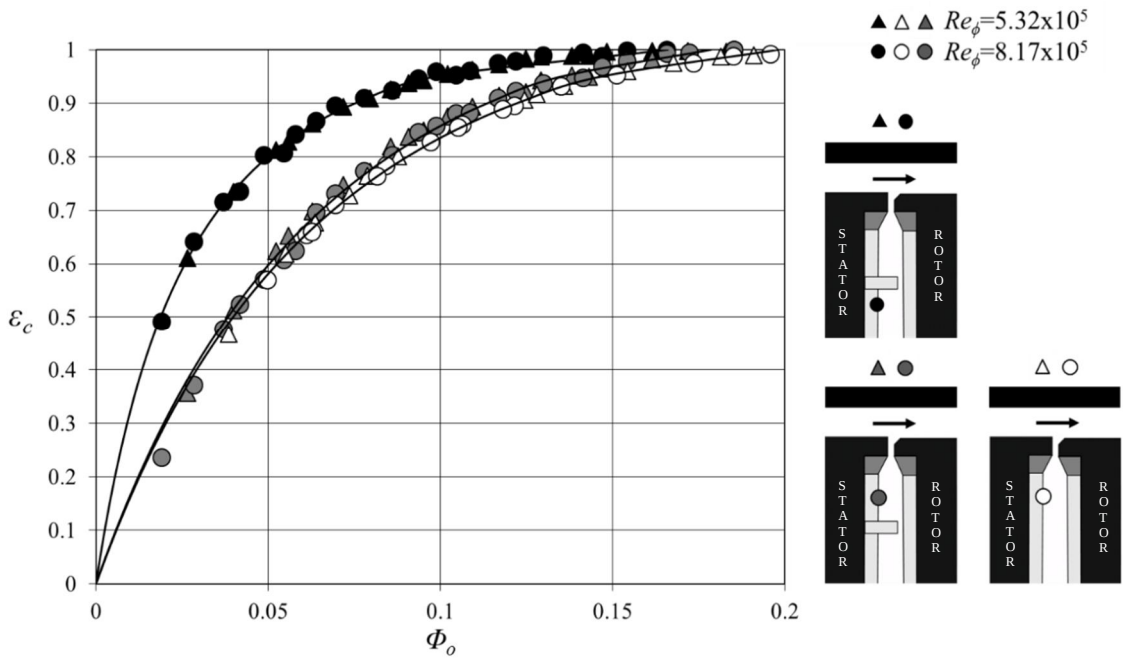

Figure 5.9 Variation of ε_c with Φ_0 for a double axial-clearance seal compared with single axial-clearance seal data: EI ingress (Symbols denote experimental data; lines are theoretical fits)

Fig. 5.9 shows the variation of ε_c with Φ_0 for the double axial-clearance seal and the single axial-clearance seal is included for comparison. For both the inner and outer wheel-space, the relationship between ε_c and Φ_0 was found to be independent of Re_ϕ, as seen in Fig 5.9. It can also be seen in the figure that the effectiveness of the outer wheel-space of the double seal is very close to that of the single axial seal. It can also be seen that the effectiveness of the inner wheel-space of the double axial seal is significantly higher than that of the outer wheel-space at the same value of Φ_0; the values of Φ_{min} for the outer and inner wheel-space are 0.179 and 0.166, respectively, and the value of Γ_c for the outer and inner wheel-space are 0.755 and 0.227, respectively. As with the single-clearance seals, the optimum theoretical curves were also plotted using the same statistical technique used for the single-clearance seals; the agreement between the fitted theoretical curve and the measured concentration data was very good for the both inner and outer wheel-spaces.

Double radial-clearance seal

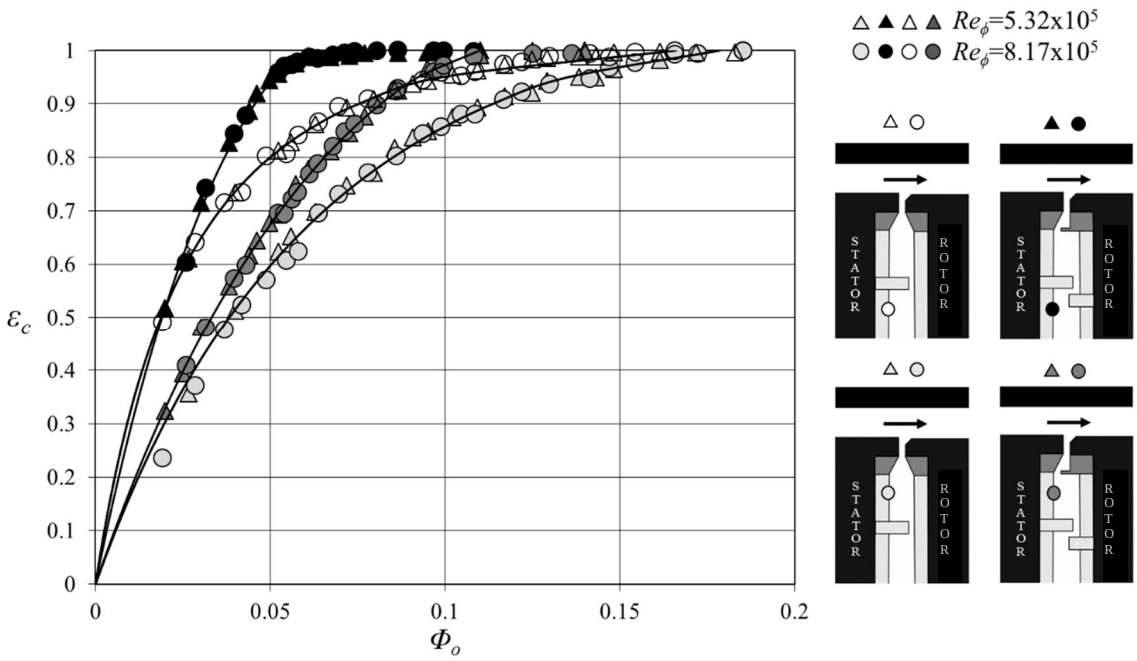

Figure 5.10 Variation of ε_c with Φ_0 for a double radial-clearance seal compared with double axial-clearance seal data: EI ingress (Symbols denote experimental data; lines are theoretical fits)

Fig. 5.10 shows the variation of ε_c with Φ_0 for the double radial-clearance seal and that of the double axial-clearance seal is included for comparison. For both the inner and outer wheel-spaces, the relationship between ε_c and Φ_0 is independent of Re_ϕ, as can be seen from Fig 5.10. It can also be seen in the figure that the double radial-clearance rim seal has significantly higher sealing effectiveness for both the inner and outer wheel-spaces than for the double axial-clearance rim seal; the values of Φ_{min} for the outer and inner wheel-space of the double radial seal are 0.11 and 0.06, respectively. That is, the inner and outer wheel-spaces of the double radial seal respectively require approximately 36% and 61% of the sealing air to prevent ingress than those of the double axial seals. As with the other seals described above, the optimum theoretical curves were also plotted; the agreement between the fitted theoretical curve and the measured concentration data was very good for the both inner and outer wheel-spaces.

5.4 Measurements of the radial variation of effectiveness

The radial variation of effectiveness for the four different rim seal geometries was measured at the design operation condition with a rotor speed of 3000 rpm (Re_ϕ value of 8.17×10^5).

5.4.1 Single-clearance rim seals

Single axial-clearance seal

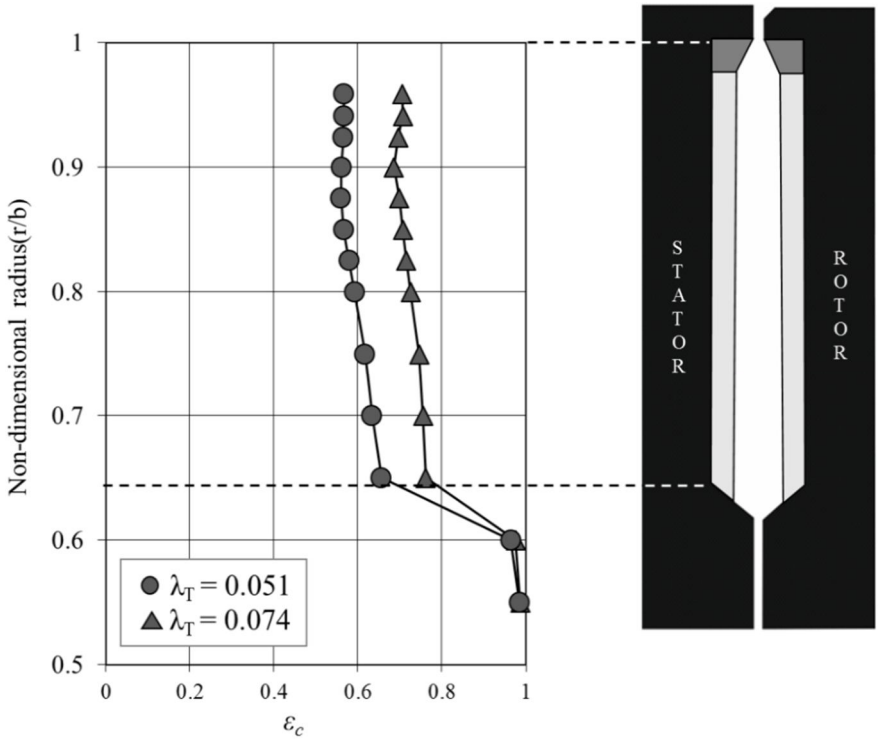

Figure 5.11 Radial variation of effectiveness on the stator surface with a single axial-clearance seal for two different turbulent flow parameters (EI ingress)

The radial variation of concentration sealing effectiveness, which was measured on the stator for a single axial-clearance seal with polycarbonate inserts, is shown in Fig. 5.11. The experiments were conducted for two values of λ_T, 0.051 and 0.074. It emerged that the effectiveness is almost invariant with the radius when the non-dimensional radius, *r/b*, is greater than 0.85, which suggests that virtually complete mixing between ingested hot gas and recirculating flow in the wheel-space occurs in a region very close to the rim seal. Although there was a small decrease in ε_c with

increasing radius when *r/b* was less than 0.85, the difference in concentration effectiveness between *r/b* = 0.81 and 0.937 was less than 0.05. The rapid increase in ε_c with decreasing radius when *r/b* was less than 0.65 was also observed, which is due to the inlet seal, as it significantly reduces the level of ingestion in the inner wheel-space.

Single radial-clearance seal

The radial variation of concentration sealing effectiveness was also measured for the single radial-clearance seal and plotted in Fig. 5.12. Similar to the axial-clearance seal, the experiments were conducted for two values of λ_T, 0.058 and 0.077. Although the value of ε_c at *r/b*=0.958 was slightly higher than those of the other radial locations, the concentration effectiveness was virtually invariant with the radius for the entire range of *r/b* in the wheel-space. A rapid increase in ε_c with decreasing radius, when *r/b* is less than 0.65, can also be observed for the radial-clearance seal and as with the single axial-clearance seal, this is caused by the inlet seal.

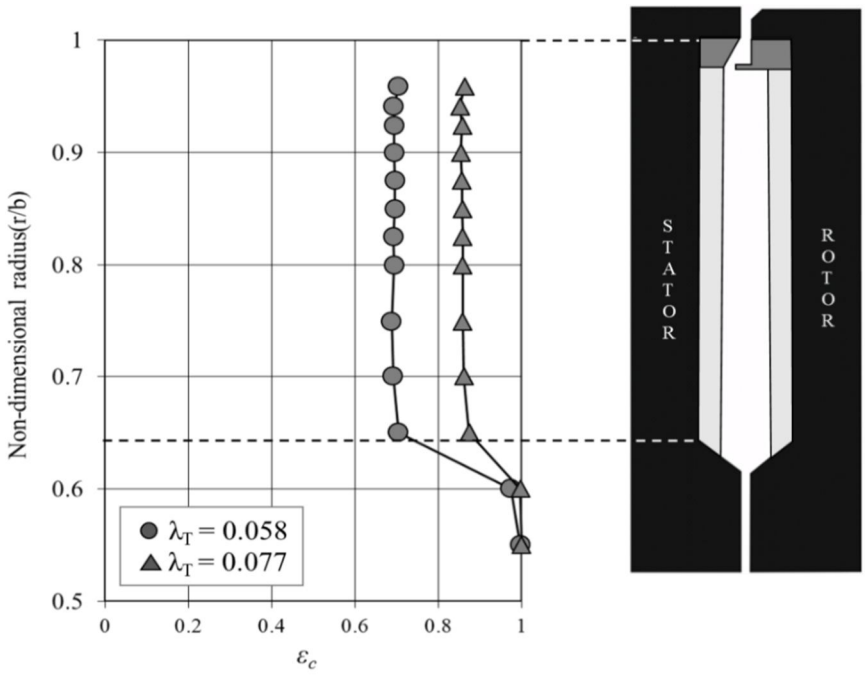

Figure 5.12 Radial variation of effectiveness on the stator surface with a single radial-clearance seal for two different turbulent flow parameters (EI ingress)

5.4.2 Double-clearance rim seals

Double axial-clearance seal

The radial variation of concentration sealing effectiveness, ε_c, for the double axial-clearance seal was plotted as shown in Fig. 5.13. The experiments were conducted for two values of λ_T, 0.05 and 0.097. As can be seen in the graph, the effectiveness of the inner wheel-space is significantly higher, approximately 20%, than that for the outer wheel-space with the same λ_T. It is also found that the concentration effectiveness in the outer wheel-space (r/b > 0.913) is almost invariant with the radius. There is a small increase in ε_c with decreasing radius in the inner wheel-space (r/b < 0.887). As with the single seals, a rapid increase in ε_c with decreasing radius, when r/b is less than 0.65, is observed.

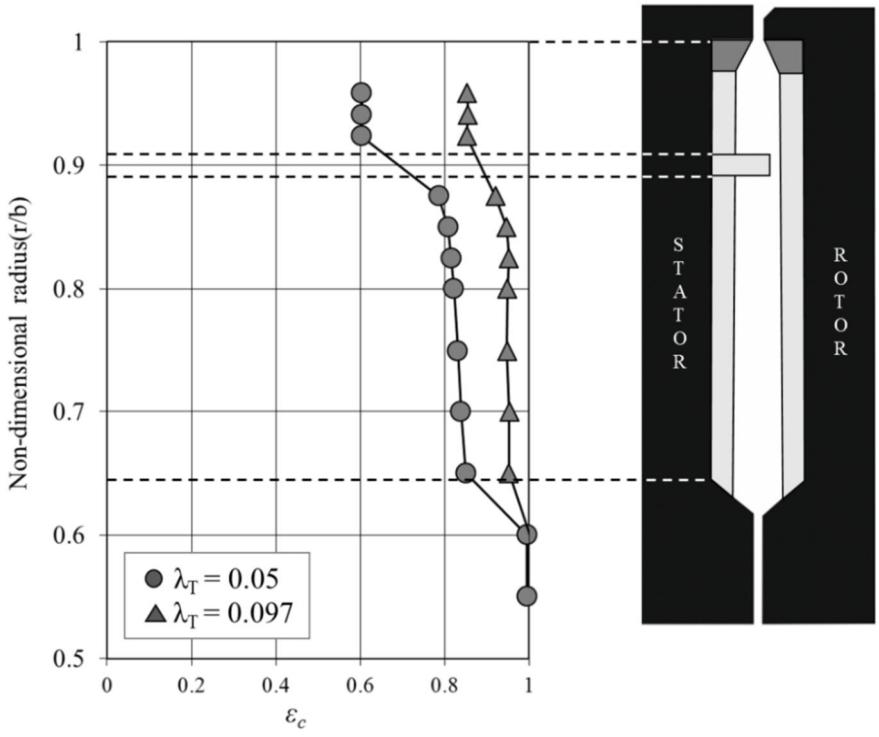

Figure 5.13 Radial variation of effectiveness on the stator surface for a double axial-clearance seal (EI ingress)

Double radial-clearance seal

The radial variation of concentration sealing effectiveness, ε_c, for the double radial-clearance seal is plotted in Fig. 5.14. The experiments were conducted for two

values of λ_T, 0.045 and 0.081. As shown, the effectiveness of the inner wheel-space is approximately 10% higher than that for the outer wheel-space with the same λ_T. It can be seen that the concentration effectiveness in the outer wheel-space ($r/b > 0.913$) increases as the radius decreases. However, the concentration effectiveness in the inner wheel-space ($r/b < 0.887$) is almost invariant with the radius. As with all the other seals, a rapid increase in ε_c with decreasing radius, when r/b is less than 0.65, is also observed for the double radial-clearance seal.

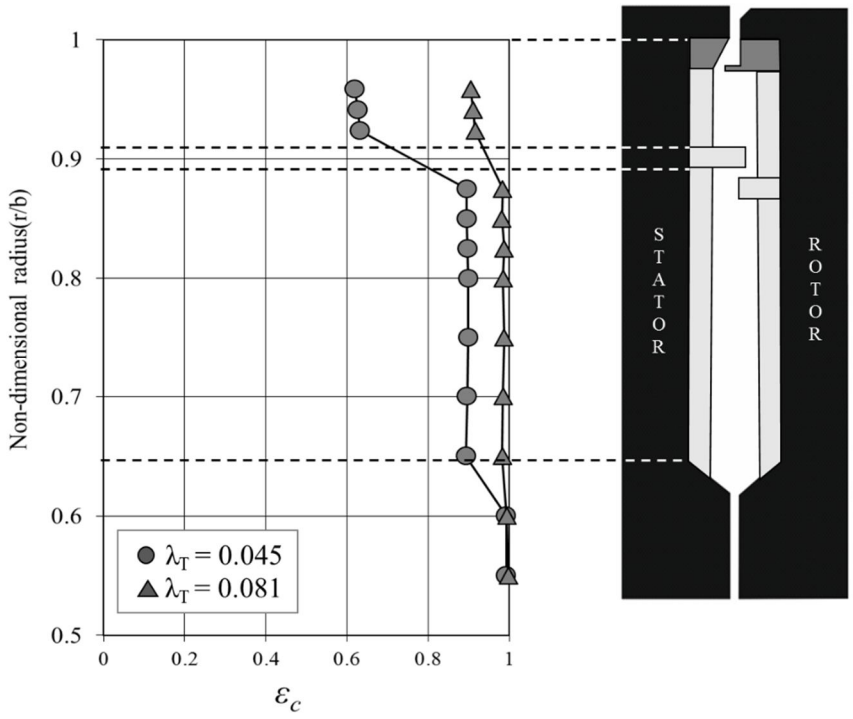

Figure 5.14 Radial variation of effectiveness on the stator surface for a double radial-clearance seal (EI ingress)

5.5 Rim seal effectiveness comparisons

Four single-clearance rim seals and two double ones were tested and the magnitudes of Φ_{min} of the seals were determined based on the concentration sealing effectiveness measurements obtained by Sangan *et al.* (2013c). The six rim seals tested were ranked based on the magnitude of Φ_{min}, as shown in Fig. 5.15. As can be seen from the bar chart, double radial seal D2 is the most effective and single axial seal S1 the least; the inner wheel-space of the double radial seal requires only

approximately a sixth of the sealing flow rate to prevent ingestion of the hot mainstream gas.

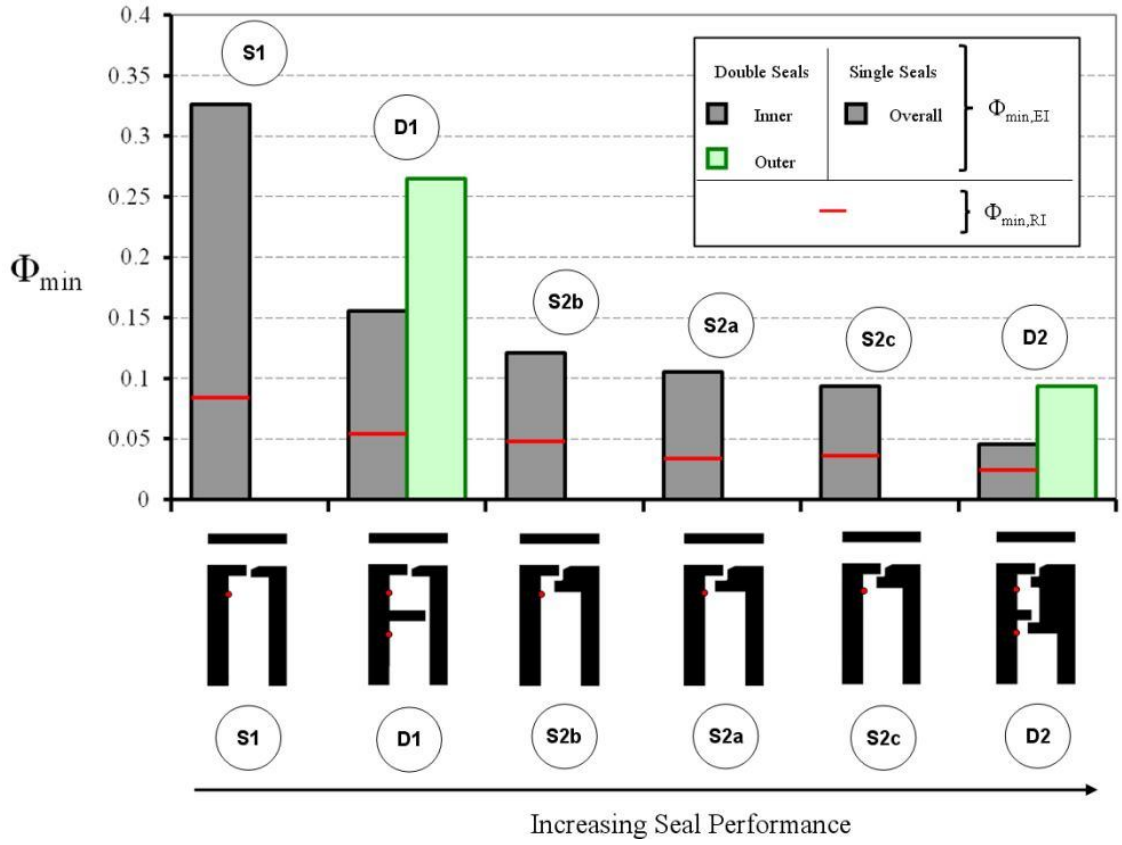

Figure 5.15 Seal performance ranking shown in order of magnitude of Φ_{min} for all seal configurations tested by Sangan *et al.* (2013c) (Φ_{min} were determined based on concentration sealing effectiveness measurements)

Although the concentration sealing effectiveness measurements for this thesis were carried out with rim seals and wheel-space that have different geometries from the ones used by Sangan *et al.* (2013c), they have provided qualitatively consistent experimental results. That is, the double radial seal and the single axial seal show the best and worst sealing performance, respectively. Similarly, the measurements of the radial variation of effectiveness, as shown in section 5.4, also show qualitatively consistent results with those provided by Sangan *et al.* (2013c). A bar chart that shows the magnitudes of Φ_{min} for all four rim seals tested is provided in Fig. 5.16; radial seal shows better performance than the double axial-clearance seal and the inner and outer seal of the double radial seal respectively require approximately 30

and 55% of sealing flow to seal the wheel-space compared to the single axial-clearance seal.

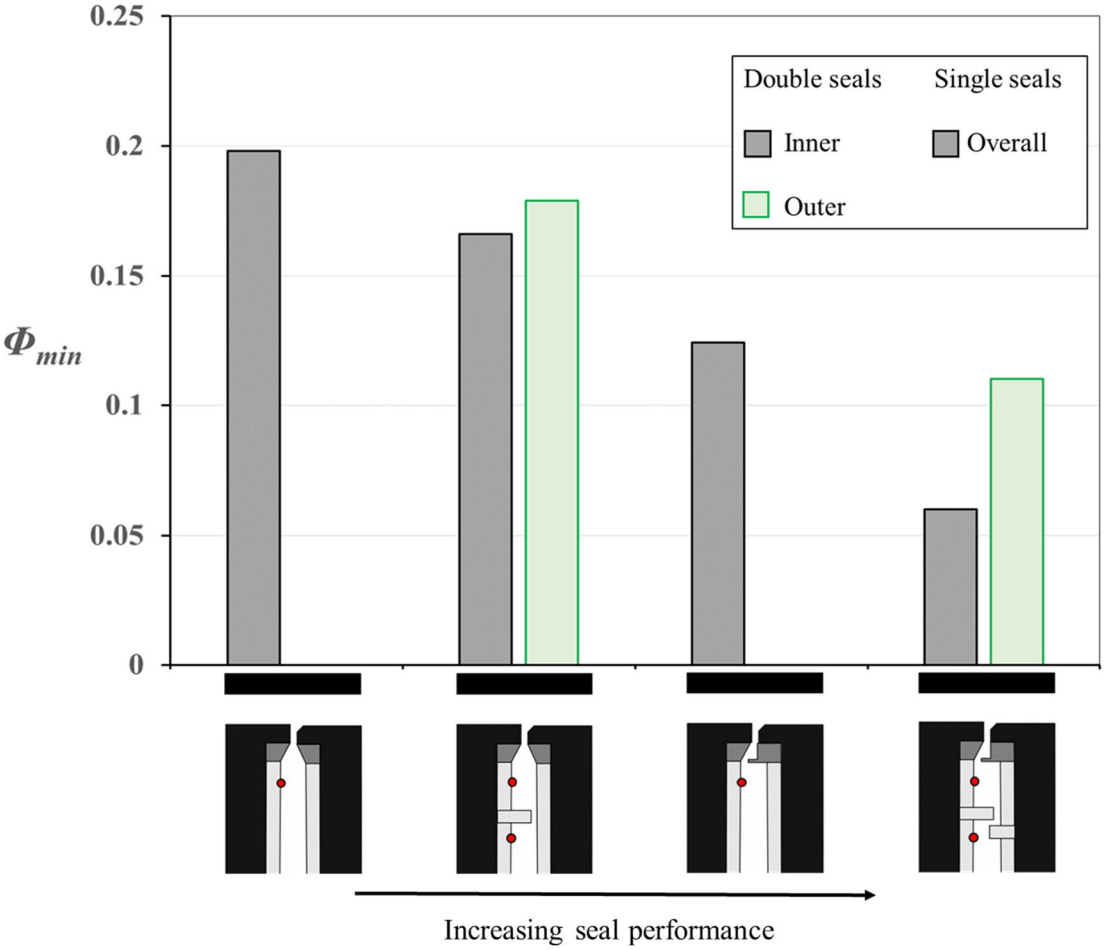

Figure 5.16 Seal performance ranking shown in order of magnitude of Φ_{min} for all seal configurations tested in this thesis (Φ_{min} were determined based on concentration sealing effectiveness measurements)

5.6 Uncertainty in concentration measurements

Uncertainty analysis method for concentration measurements is described in this section based on the method provided in Sangan *et al.* (2013c).

From Eq.5.2.

$$\varepsilon_c = \frac{c_s - c_a}{c_0 - c_a}$$

where the subscripts *a*, *o* and *s* respectively denote the air in the annulus, the sealing air at inlet, and the surface of the stator.

Let δ_ε, δ_s, δ_o, δ_a be uncertainties in ε, c_s, c_o, c_a respectively so that

$$\varepsilon \pm \delta_\varepsilon = \frac{c_s \pm \delta_s - (c_a \pm \delta_a)}{c_o \pm \delta_o - (c_a \pm \delta_a)}$$

$$= \frac{(c_s - c_a)[1 + (\pm\delta_s \pm \delta_a)/(c_s - c_a)]}{(c_o - c_a)[1 + (\pm\delta_o \pm \delta_a)/(c_o - c_a)]} \tag{5.3}$$

$$= \varepsilon \frac{[1 + (\pm\delta_s \pm \delta_a)/(c_s - c_a)]}{[1 + (\pm\delta_o \pm \delta_a)/(c_o - c_a)]} \tag{5.4}$$

If $(\pm\delta_o \pm \delta_a)/(c_o - c_a) << 1$ then

$$\varepsilon \pm |\delta_\varepsilon| \le \varepsilon \left[1 + \frac{|\delta_s| + |\delta_a|}{c_s - c_a} + \frac{|\delta_o| + |\delta_a|}{c_o - c_a} \right] \tag{5.5}$$

Hence,

$$\frac{|\delta\varepsilon|}{\varepsilon} \le \left[\frac{|\delta_s| + |\delta_a|}{c_s - c_a} + \frac{|\delta_o| + |\delta_a|}{c_o - c_a} \right] \tag{5.6}$$

If the uncertainty is a percentage of the full-scale range, which was the case in the experiments, then $\delta_s = \delta_o = \delta_a = \delta$ say, and Eq.5.6 simplifies to

$$\frac{|\delta\varepsilon|}{\varepsilon} \le 2\delta \frac{1 + \varepsilon^{-1}}{c_o - c_a} \tag{5.7}$$

or

$$\frac{|\delta\varepsilon|}{\varepsilon} \le 2\delta \frac{1 + \varepsilon}{c_o - c_a} \tag{5.8}$$

The average standard deviation, σ, in the range $0 < \varepsilon < 1$ can be calculated from Eq.5.8 by

$$\sigma = \frac{2\delta}{c_o - c_a}\sqrt{\int_0^1 (1+\varepsilon)^2\, d\varepsilon} = 3.06\,\frac{\delta}{c_o - c_a} \tag{5.9}$$

The CO_2 gas analyser had an overall uncertainty of 1.5% of each of its ranges. In the tests, where the 1% range was used, the concentration of gas in the sealing flow was close to the 1% range maximum. Hence $\delta/(c_o\text{-}c_a) \approx 0.015$, and from Eq.5.9 it follows that $\sigma \approx 0.046$. This value, which is an upper bound, exceeds the standard deviation found from the fitted $\Phi_o \sim \varepsilon$ curves.

5.7 Summary

This chapter presents concentration sealing effectiveness results of four generic (though engine-representative) rim seals. The tests were conducted, in the wheel-space with 10mm axial spacing between stator and rotor, for two values of rotational speed, 2000 and 3000 rpm, at the design operating condition, where C_F = 0.583. Concentration measurements with CO_2 tracer gas was used to determine the concentration sealing effectiveness. The variation of concentration sealing effectiveness with sealing flow rate and the radial variation of concentration sealing effectiveness were determined for the four generic rim seals.

The principal conclusions made from the experiments are listed below:

- The relationship between the sealing effectiveness and the sealing flow rate is independent of Re_ϕ.
- The agreement between the fitted theoretical curve and the measured concentration sealing effectiveness data was generally very good for the four seals tested.
- For single-clearance seals, it was found that the sealing effectiveness was generally invariant with the radius. For double-clearance seals, the sealing effectiveness of the inner wheel-space was significantly higher than that of the outer.

- A bar chart that shows the magnitude of Φ_{min}, for all four rim seals tested was plotted. Although the concentration sealing effectiveness measurements for this research were carried out with rim seals and wheel-space that have different geometries from the ones used by Sangan *et al.* (2013c), qualitatively consistent experimental results with the data presented by them.

The main purpose of these measurements was to provide reference data to show thermal buffering, where the effect of ingress on the rotor is less than that measured on the stator. The concentration sealing effectiveness data measured in this chapter will be compared to adiabatic sealing effectiveness for the same seal in Chapter 6.

Chapter 6: Adiabatic sealing effectiveness measurements on the rotor

In Chapter 5, the sealing effectiveness based upon the concentration measurement, ε_c, was defined and used to investigate its variation with the sealing flow parameter, Φ_0. Although the concentration measurement technique has been successfully used to determine the concentration effectiveness, ε_c, it is only based on the measurements made on the stator disc; it is not feasible to measure concentration of a tracer gas on the rotating disc without introducing complex slip-rings. However, sealing effectiveness data measured on the rotor disc, which is highly stressed due to high rotational speed, is essentially required so as to optimise the sealing flow rate required in turbine stages for sealing and cooling purposes. Therefore, it is necessary to investigate the effect of ingress on the rotor disc using an alternative experimental method. A transient heat transfer experiment based on the infrared temperature measurement technique was used for this study. The adiabatic surface temperature of the rotor disc was acquired by numerically analysing the temperature data measured during a transient heat transfer experiment. The adiabatic surface temperature was then used to determine the variation of the adiabatic sealing effectiveness, ε_{ad}, with Φ_0; the definition of the adiabatic sealing effectiveness is described in section 6.3.

An overview of the experimental facility, which was modified to achieve more accurate heat transfer measurement to determine the variation of ε_{ad}, with Φ_0, is provided in section 6.1. The detailed description on the modification of the Bath one-stage ingress test facility for the transient heat transfer experiments is provided in section 6.2. A discussion on the analysis method used to determine T_{ad} and h based on the temperature data acquired from a transient heat transfer experiment is briefly revisited in section 6.3, with a detailed explanation provided in Chapter 4. The variation of ε_{ad} with Φ_0 for four different rim seal geometries was determined at two different radial locations (r/b=0.81and 0.937) and this is discussed in this chapter. In order to investigate the thermal buffering effect, the variations of ε_c and ε_{ad} with Φ_0 were compared for all seal geometries tested and the performance of the seals were ranked in order of magnitude of $\Phi_{min,ad}$.

6.1 Heat transfer measurements on the rotor

The sealing effectiveness of the rotor disc, transient heat transfer experiments were carried out using the infrared temperature measurement technique described in Chapter 3. Heated sealing (hotter) and ambient mainstream (colder) flow, which is the opposite arrangement to the real gas turbine, were used due to the lack of electric power for achieving a 30 ~ 40°C step change in the mainstream flow temperature at the design points. The sealing flow was supplied to the wheel-space through the sealing flow line connected to the stator disc at the centre. As shown in Fig 6.1, two mesh heaters were fitted in series in the sealing flow line between the expansion and contraction ducts to achieve heated sealing flow for the transient heat transfer experiments. The upstream mesh heater was used to match carefully the temperature of the incoming compressed air to typically within ±0.2°C of the initial temperature, to ensure the rig was in thermal equilibrium before conducting the heat transfer experiments. The main heater was used to achieve a step-change of between 30 and 40°C in the sealant flow temperature. The mesh heaters used for the sealing flow line were based on the same design (Ireland *et al.*, 1996) as the one used for the calibration test facility described in subsection 3.3.1. The carefully-controlled electric current was supplied by MAGNA-POWER XR16-375, which provides electric power up to 6kW and the time constant for achieving the target current setting is less than 400ms. The sealing flow line, immediately downstream of the upstream mesh heater, was insulated with 5mm thickness Rohacell 51 in order to reduce the heat loss through the wall.

The initial and boundary conditions of the experiments were carefully controlled so as to achieve accurate experimental results. The air temperatures in the wheel-space, sealing flow line and annulus were measured by fast-response thermocouples in the absence of mainstream or sealing flow to achieve the thermal equilibrium condition prior to each experiment. The test facility was assumed to be in thermal equilibrium when all fast response thermocouples gave a measured temperature value within ±0.1°C.

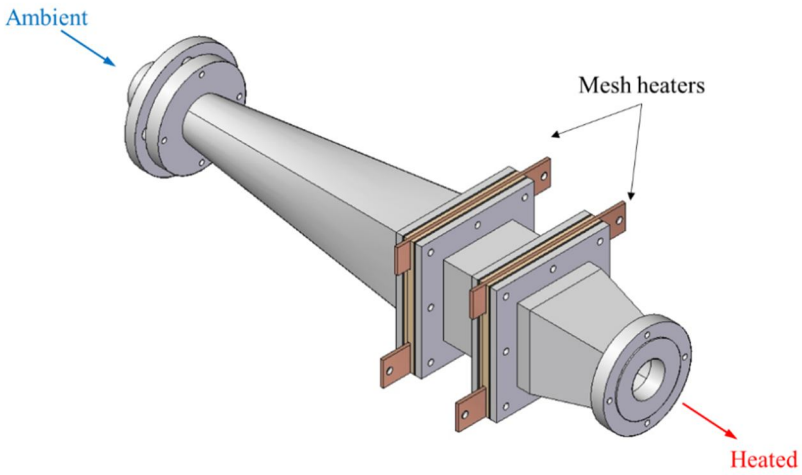

Figure 6.1 Sealing flow line showing transition sections (expansion and contraction ducts) and the two mesh heater arrangement

6.1.1 Infrared sensors

The rotor disc temperature history during each transient heat transfer experiment was measured by two infrared sensors, developed for heat transfer experiments in the Bath one-stage ingress test facility. The two sensors were flush-mounted on the stator wall to measure the rotor disc temperature at two different radial locations, r/b=0.81 and 0.937, as shown in Fig. 6.2. The two radial locations were carefully chosen to collect temperature data at comparable radial locations to those of the concentration measurements (r/b=0.85 and 0.958), without absorbing any infrared radiation from the mitred inserts and rim seals; the spot size of the infrared sensor at 10mm from the target surface was 5.9mm in diameter. Although the chosen radial locations for the temperature measurements on the rotor did not exactly match those of the concentration measurements on the stator, the sealing effectiveness based on the two measurements could be directly compared with each other. This is because the radial variations of the concentration measurements in section 5.4 show that the concentration sealing effectiveness are virtually invariant (or the variation is small enough to be ignored) with radius for both the inner and outer wheel-space.

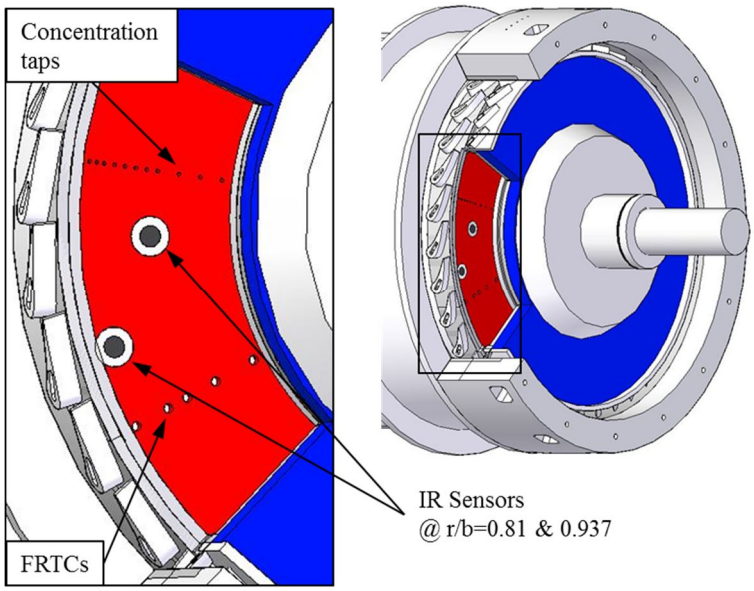

Figure 6.2 Test section showing instrumentation in the wheel-space (red, stator; blue, rotor)

In order to ensure a consistent emissivity between the rotor surface and the copper block used for calibration, the disc surface was sprayed with a black paint, Hallcrest SPBB. The rotor surface temperature change was measured by the two infrared sensors with measurement rates of 10Hz each.

6.1.2 Fast response thermocouples

Air temperatures were measured using K-type fast response thermocouples at seven different locations (see Figs. 6.3 and 6.4). The sealing flow temperature was measured in the sealant flow line just upstream of the stator disc, core temperatures in the wheel-space were measured at five different radial locations and the mainstream flow temperature was measured in the annulus just upstream of the vanes. The measurement junctions of the thermocouples in the wheel-space were located at z/S=0.5.

The fast response thermocouple shown in Fig. 6.4 was made based on the design used by Lock *et al.* (2005) using a 25μm diameter K-type bare-wire that was placed through a twin-bore ceramic tube. These were then inserted through a thin stainless steel tube to provide protection. It was recommended by Lock *et al.*(2005) that a minimum clearance of 3.5mm between the exposed bead and the tip of the ceramic

tube is required to minimise errors due to transient conduction between the bead and the ceramic tube. Thermocouple voltage data was acquired by using a National Instrument USB-9213 input module, which provides a 1200Hz measurement rate with 16 thermocouple channels and a pre-calibrated platinum resistance thermometer. According to Lock *et al.* (2005), the response time and recovery factor of the fast response thermocouple were 40ms and 0.78, respectively. Hence, the total temperature of air, T_a, was determined based on the fast response thermocouple measurements, T_{TC}, using Eq.6.1.

$$T_a = T_{TC} + R\frac{V^2}{2c_{P,air}} \tag{6. 1}$$

where, V is the velocity of the air at the measurement location and $c_{p,air}$ is the specific heat of the air at constant pressure

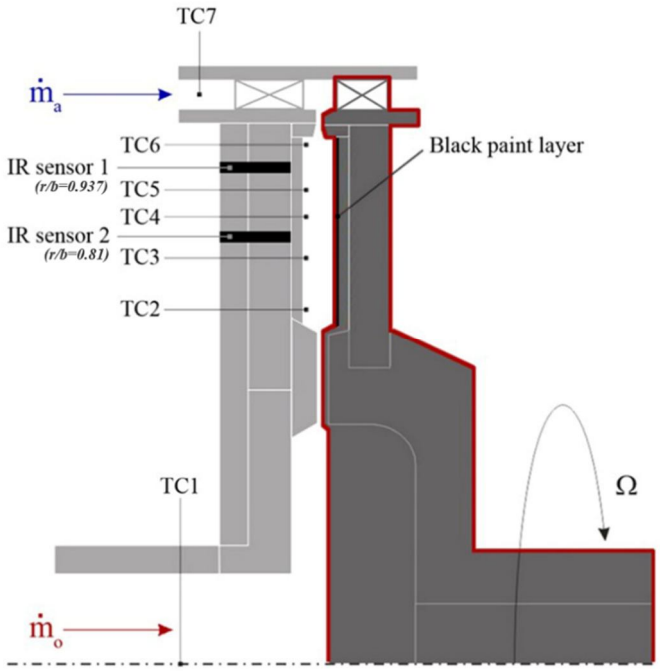

Figure 6.3 Experimental setup for fast response thermocouple (TC) and infrared pyrometer sensor (IR) measurements. The red boundary shows the rotating components, rotor disc and blades.

The fast response thermocouples were calibrated between 10°C and 70°C in a heated water bath. The voltage output of each thermocouple was recorded, while the heated water bath was slowly cooled to room temperature, with the data acquisition system of the Bath one-stage ingress test facility, using an assigned channel. The

thermocouple voltage data was then compared against the temperature of the water bath, which was measured using a pre-calibrated thermometer: a Dostmann P600 thermometer equipped with a Pt100 sensing probe. The procedure was repeated five times and each thermocouple was calibrated with an uncertainty of ±0.1°C.

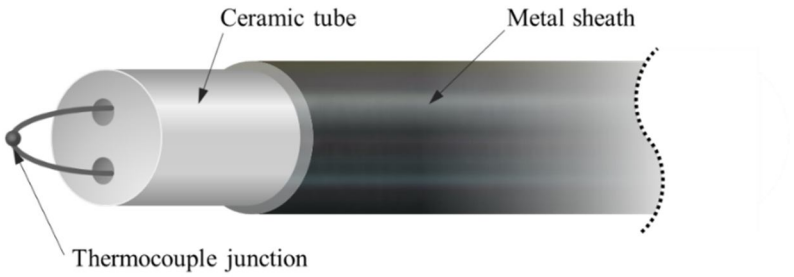

Figure 6.4 Schematic of a fast response thermocouple

6.2 Modification of the Bath one-stage ingress test facility for heat transfer experiments

The Bath one-stage ingress test facility was designed with stator and rotor discs made from optical grade polycarbonate which provided optical access to the wheel-space for temperature measurement with TLC. Both the stator and rotor shrouds were made of aerospace grade aluminium, T7075-T6. In order to reduce heat loss through the aluminium shrouds, polycarbonate inserts were attached to the inner surfaces, i.e. the wheel-space was completely enclosed by optical grade polycarbonate for the experiments performed by Pountney *et al.* (2013). However, as perfect thermal insulation cannot be provided with polycarbonate (thermal conductivity of 0.2W/mK) the test section lost a considerable amount of heat through the polycarbonate discs and inserts. It can be seen from Fig. 6.9 that the maximum achievable θ_{core} measured with this configuration was less than 0.85 (the definition of θ_{core} is provided in Eq. 6.4). Hence, it was planned to modify the wheel-space to provide an arrangement which was closer to the adiabatic core.

The modification allowed measurements of T_{ad} with less uncertainty from the transient heat transfer experiments. As previously described in subsection 4.1.4, the value of the T_s (i.e. Θ_s) measured from such an experiment needs to be maximised (or be as close as possible to the actual T_{ad}) to achieve an accurate estimation of T_{ad}.

Hence, in subsection 4.3.1, a heat transfer experiment with a composite substrate of polycarbonate and Rohacell51 was suggested for achieving a higher value of T_s.

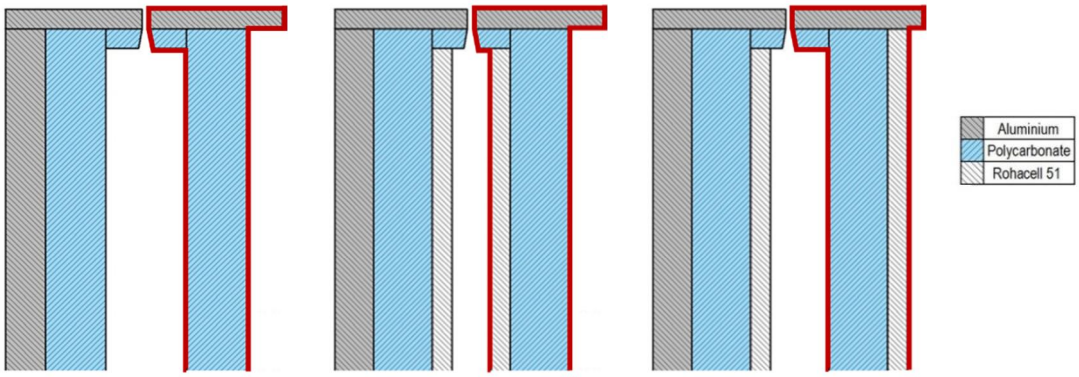

Figure 6.5 Schematics of the test section showing a) the original wheel-space configuration b) *concept1:* the modified wheel-space with Rohacell on the wet surface of the rotor disc c) *concept2:* the modified wheel-space with Rohacell on the back surface of the rotor disc (outlined in red is the rotating disc).

The following two simple modification concepts were put forward (see Figs. 6.5 (b) and (c)). A Rohacell cover-plate was attached to the stator disc so as to minimise the required modification to the existing ingress test facility. For the rotor disc, the following two concepts were suggested: Rohacell cover-plates on the wet surface for both the stator and rotor and Rohacell cover-plates on the wet surface of the stator and the back surface of the rotor. The comparative performance of the two approaches was predicted using the numerical solution for a composite substrate described in subsection 4.3.2. Numerical simulations were carried out for the rotor disc using the 1-D heat transfer analysis method with rig-representative boundary conditions.

The non-dimensional surface temperature histories on the rotor for the two concepts were simulated for four different thicknesses of Rohacell51 cover-plate and the numerical simulation results for the 5mm thickness Rohacell cover-plate are shown in Fig. 6.6. The non-dimensional surface temperature (Θ_s) is defined as:

$$\Theta_s = \frac{(T_s - T_{in})}{(T_{ad} - T_{in})} \tag{6.2}$$

where T_s is the surface temperature, T_{in} is the initial temperature of the system and T_{ad} is the adiabatic surface temperature.

It can be seen from the Fig. 6.6 that the surface temperature of concept1 (Fig. 6.5 (b)) increases much quicker than the other; it reaches Θ_s=0.9 in approximately 24 and 1500 seconds for concept1 and 2, respectively. That is, concept1 is far better than concept2 for achieving higher Θ_s (T_s) in a shorter time. This is an advantage in determining an accurate value of T_{ad}. The shorter experimental time which can be achieved using concept1 is advantageous for the following reason. Both concepts consider heat loss through the rotor when the experimental data is analysed with rig-representative initial and boundary conditions, whereas this loss through the stator is not addressed by either of them. Given these identical arrangements, the shorter time concept1 takes to reach sufficient level of T_s to achieve accurate estimation of T_{ad} means that it has lower uncertainty.

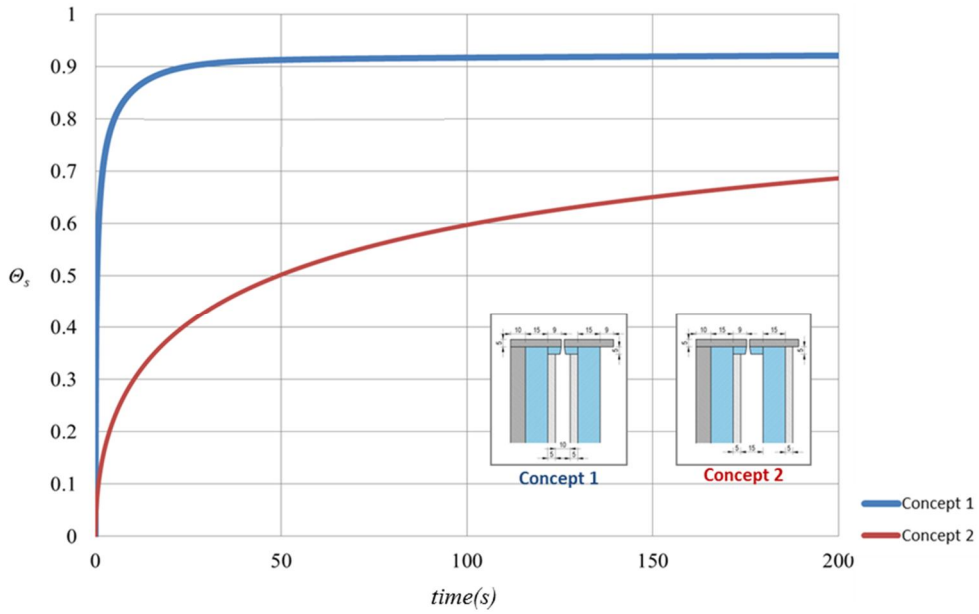

Figure 6.6. Variation of non-dimensional surface temperature with time for the two concepts considered (the conditions used for the simulation are: h=60W/m^{2}K, T_{in}=15°C and T_{ad} =60°C)

Fig 6.7 shows the variation of the non-dimensional heat loss (see Eq. 6.3) through the rotor disc with time for three configurations; a Rohacell cover-plate with 5mm thickness was used for the numerical simulations. It can be seen that concept1 loses approximately 30% of heat through the rotor disc compared to that lost through the original setup. By contrast, concept2 loses almost the same amount of heat until

approximately 600 seconds. Furthermore, concept1 was also considered to be better in terms of having a wheel-space that is symmetric to the rim seal centre line. Thus, based on the two sets of simulations, a decision was made to modify the Bath one-stage rig to have Rohacell cover-plates on the internal surfaces of the stator and rotor disc, i.e. concept 1 was selected.

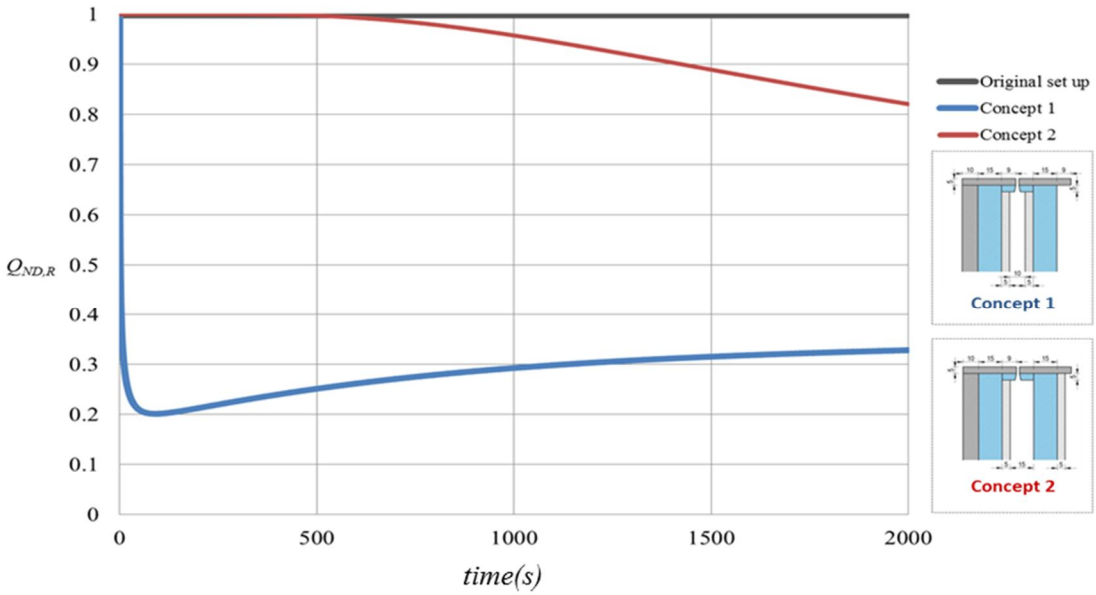

Figure 6.7 The non-dimensionalised heat loss through the rotor for each concenpt

The effects of the thickness of the Rohacell 51 cover-plates were also investigated through numerical simulation. For this simulation, five different combinations of single and double layer substrates were tested, varying the thickness of the Rohacell51 plate from 0mm to 15mm, whilst fixing the thickness of the polycarbonate plate at 15mm, which was the same as that of the stator disc. In order to show the effect of Rohacell cover-plate thickness, the non-dimensionalised heat loss through the rotor, $Q_{ND,R}$, was defined as:

$$Q_{ND,R} = \frac{The\ amount\ of\ heat\ loss\ through\ the\ rotor\ of\ each\ concept}{The\ amount\ of\ heat\ loss\ through\ the\ rotor\ with\ the\ original\ set\ up\ (without\ Rohacell)} \quad (6.3)$$

Fig. 6.8 shows that the heat loss through the substrate decreases as the thickness of the Rohacell cover-plate increases, i.e. the thicker the Rohacell, the less heat loss through the substrate. However, as the axial distance between the polycarbonate surface of the stator and rotor for the original setup was 20mm and it could not be adjusted, a decision was made to use 5mm thickness Rohacell cover-plates for both

discs so as to have at least 10mm axial spacing between them. It was estimated from the simulation that the heat loss through the rotor disc with 5mm thickness Rohacell was approximately 30% of that of the original setup.

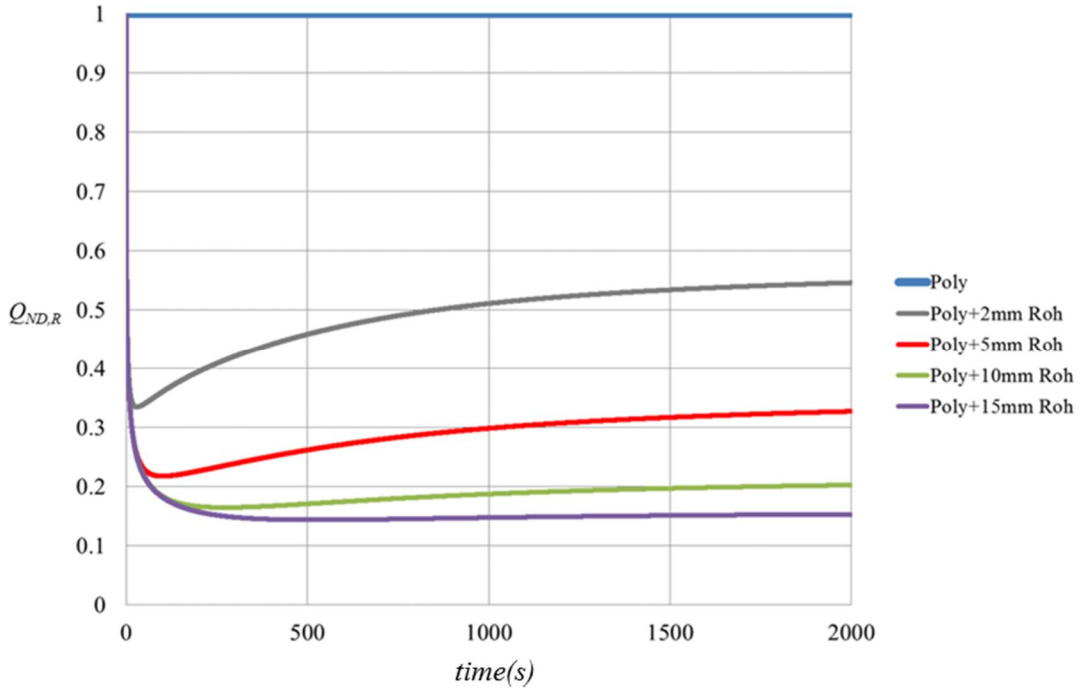

Figure 6.8 The variation of the non-dimensional heat loss through the stator disc with time for the five different combinations of the substrate, including one single and four composite ones (poly:polycarbonate (15mm thickness) and Roh:Rohacell51).

The numerical simulations, which showed that the amount of heat loss could be substantially reduced by concept1, was also supported by temperature data measured in the wheel-space core. The wheel-space core temperatures were measured by five fast response thermocouples (described in section 6.1) at five different radial locations. In order to make sure the thermocouple measured to core temperature, the thermocouples were installed so as to locate the junctions at z/S=0.5, as described in section 6.1, i.e. the junctions were considered to be outside of the stator and rotor boundary layers. A three-term exponential fitting method was applied to the core temperature histories and an extrapolation method was used to estimate the temperature data at infinity.

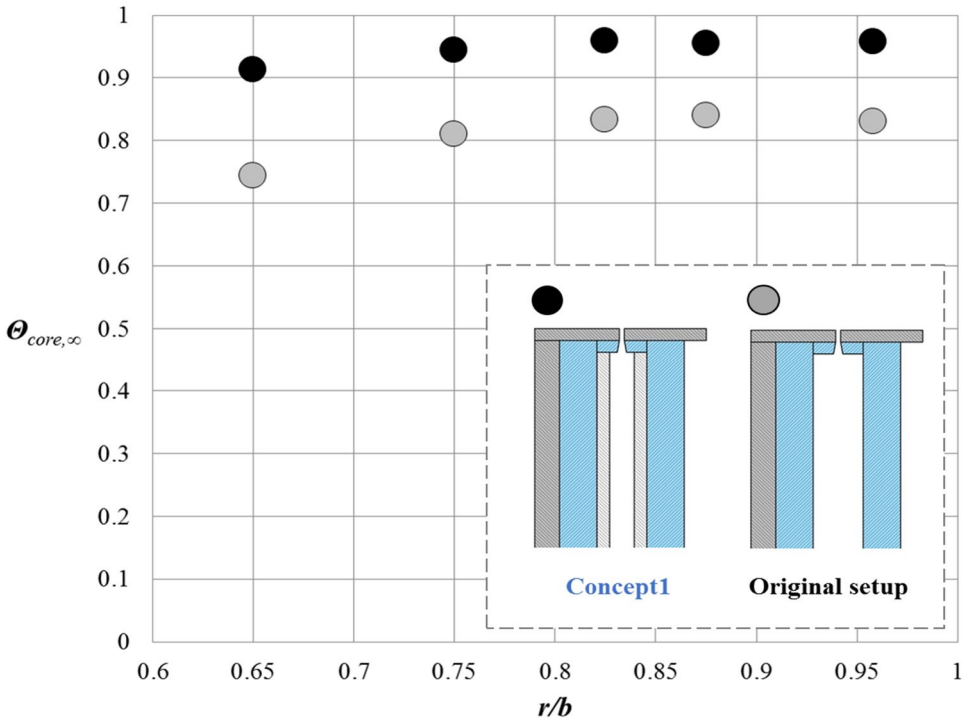

Figure 6.9 Comparison of non-dimensional core temperatures measured before and after the modifications

The variation of non-dimensional core temperature (θ_{core}) with non-dimensional radius (r/b), when the rotor-stator system was fully sealed, is shown in Fig. 6.9. The non-dimensional core temperature, θ_{core}, is defined as:

$$\theta_{core} = \frac{(T_{core} - T_{in})}{(T_o - T_{in})} \tag{6.4}$$

where, T_{core} is the measured core air temperature, T_{in} is the initial temperature of the system, T_0 is the total temperature of the sealing air after the heater has been activated and $\theta_{core,\infty}$ is the extrapolated value of θ_{core} as $t \rightarrow \infty$.

As can be seen in Fig. 6.9, the maximum achievable θ_{core} for the original set up is less than 0.85. This increases to approximately 0.95 by adding Rohacell cover-plates on both the stator and rotor discs.

The effect of the Rohacell cover-plates can also be seen from the difference between the maximum and minimum θ_{core}, which is proportional to the amount of heat loss through the stator disc. When the wheel-space is fully sealed, the sealant air flows into it through the inlet seal, is entrained into the rotor boundary layer and

pumped up the rotor disc. Once the sealant flow reaches the periphery of the rotor disc, it either flows axially from the rotor to the stator across the wheel-space or leaves it. The sealant flow that remains in the wheel-space then flows radially inward over the stationary disc. When the wheel-space is fully sealed, the stator boundary layer is entirely composed of the sealing flow and loses heat to the stator disc as it flows radially inward in the stator boundary layer. As a result, as fluid flows axially from the stator boundary layer to the core and θ_{core} decreases as *r/b* decreases.

6.3 Analysis of heat transfer data

In this section, the method used to measure the thermal properties of polycarbonate (optical grade) and Rohacell 51 is described. The measurements were made to ensure an accurate analysis of transient experimental data. An 'extrapolation' method to determine T_{ad} and h accurately, based on the temperature history determined using the solutions explained in Chapter 4, is also described and validation of the calculated estimates of these two measures is provided. The definition of adiabatic sealing effectiveness is also presented in this section.

6.3.1 Measurements of thermal properties

The thermal properties of polycarbonate and Rohacell 51 are provided by the manufacturers. Polycarbonate is a well-established material for heat transfer experiments and the manufacturer's values for these thermal properties is well established. However, as the accuracy of heat transfer data analysis is highly dependent on the thermal properties (ρ, c_p and k) used, the properties for Rohacell were measured experimentally at Bath.

The Denver instrument AA200 electronic scale was used to measure the density of both materials and the measured values are provided in Table 6.1. As special test facilities are required to measure c_p and k directly, these had to be determined from experiments in the calibration test facility described in section 3.3. The calibration section of the test facility is shown in Fig. 3.13 and the 'flat plate test section' for the thermal property measurements, is shown in Fig. 6.10.

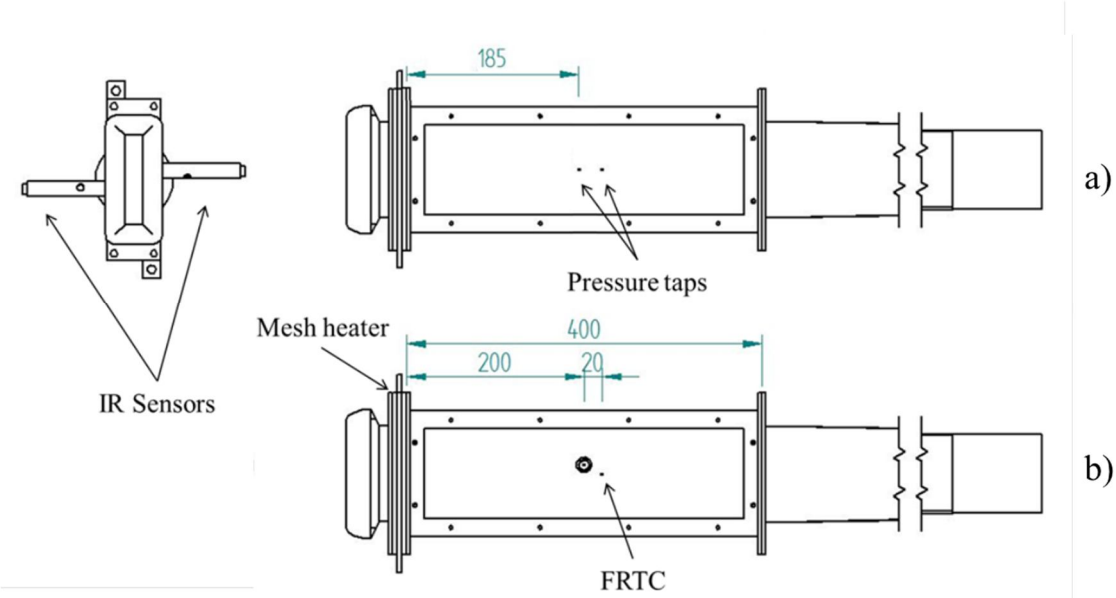

Figure 6.10 GA drawing of the calibration test rig with a flat plate test section: a) for temperature measurement, b) for velocity measurement (all dimensions in mm)

Prior to the experiments to determine c_p and k, a series of experiments were conducted to determine the heat transfer coefficient, h, and boundary layer thickness, δ, in the test facility. The variation of δ and h with Reynolds number was compared with correlation for the location. The boundary layer thickness over a vertical flat plate was measured 185mm downstream of the mesh heater. For the measurements, a smooth polycarbonate plate, which was equipped with a total and a static pressure taps, was used (Fig. 6.10 a)). The velocity of the flow across the width of the test section was measured at 0.5mm increments and the boundary layer thickness was determined based on the measurements made for a range of Reynolds numbers ($3\times10^5 < Re_x < 6\times10^5$). The measured values were then compared with the turbulent boundary layer thicknesses acquired using an empirical correlation, Eq. 6.5 (White, 1994). As shown in Fig.6.11, the measured boundary layer thicknesses agree well with the empirical correlation and consequently, it was concluded that the flow in the test section could be considered to be similar to the 'flow over a flat plate'.

$$\delta = 0.16x\,Re_x^{(-1/7)} \tag{6.5}$$

where, $Re_x = \frac{\rho x V}{\mu}$

Transient heat transfer experiments were conducted under carefully controlled initial and boundary conditions using vertical plates of polycarbonate (known thermal properties) and Rohacell 51 (unknown thermal properties), see Fig. 6.12. The mesh heater used for the infrared sensor calibration was also used to achieve a virtual step change in air temperature. Both vertical surfaces were sprayed with a black paint (Hallcrest SPBB) for the infrared temperature measurements and two staggered infrared sensors were installed (10mm vertically offset from the centre line of the plate), one on each side of the test section, at a position 200mm downstream of the mesh heater, as shown in Fig. 6.10 b). The surface temperature histories of the two plates were measured simultaneously using the two sensors. The temperature history of the entire solid was subsequently determined using the numerical solution described in Chapter 4, and the values of T_{ad} and h of each experimental case were found using the 'extrapolation method' described in subsection 6.3.2.

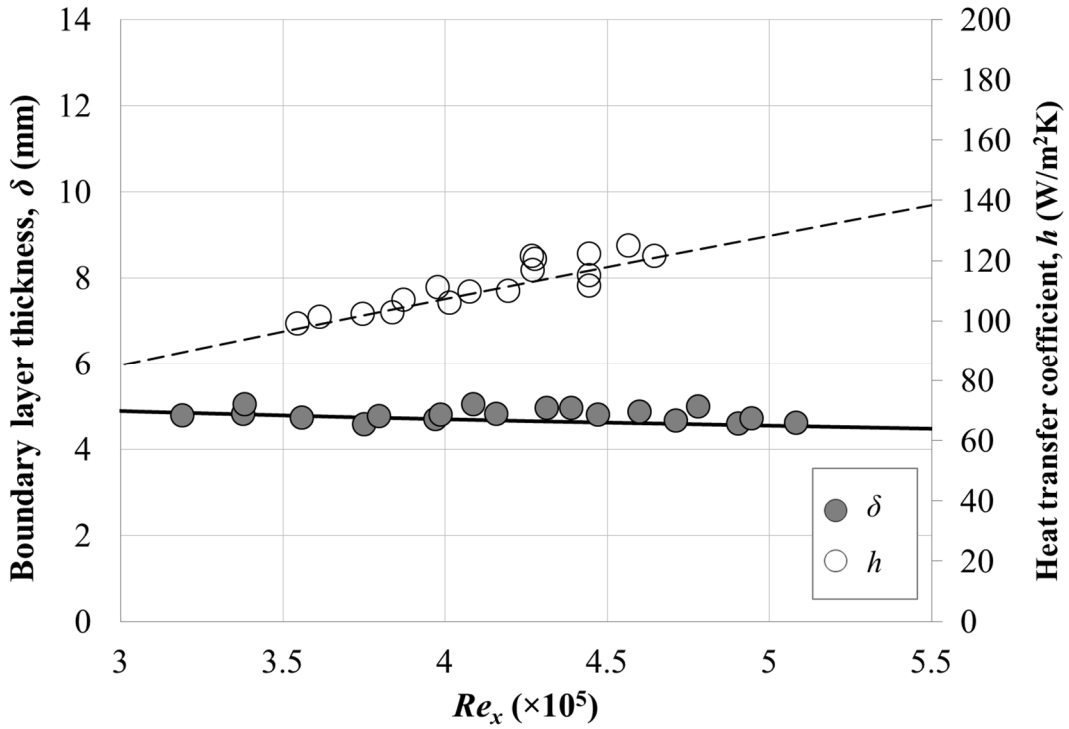

Figure 6.11 Variation of boundary layer thickness (δ) and heat transfer coefficient (h) with Reynolds number (lines are empirical correlations)

When the manufacturer's thermal properties were used for the analysis, the experimentally determined h and T_{ad} for the polycarbonate plate had a reasonable agreement with the flat plate turbulent convection correlation and the air temperature

measured by the fast response thermocouple, respectively. The 'flat plate turbulent convection correlation' was acquired using Eq.6.6 (Holman, 2010) and variation of h measured for a range of Reynolds number is shown in Fig.6.11.

$$h = \frac{0.0296}{x} k_{air} Re_x^{0.8} Pr \tag{6.6}$$

where k_{air} is the thermal conductivity of the air and Pr (≈0.72) is the Prandtl number of the air based on the air temperature.

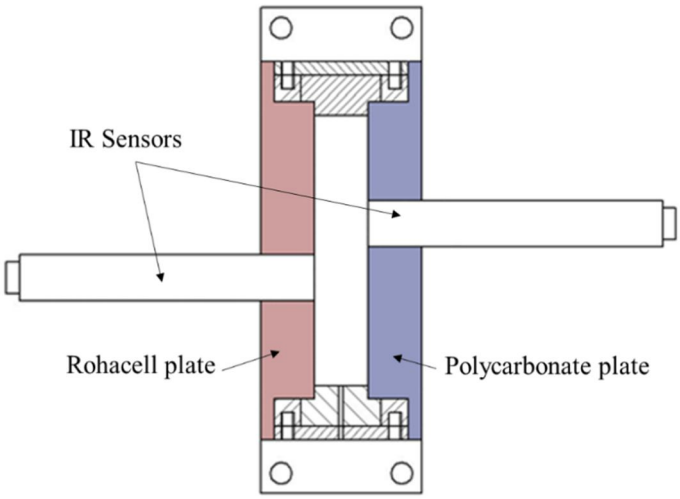

Figure 6.12 Cross sectional view of the test section

As the thermal properties of Rohacell 51 from the manufacturer were uncertain, these were determined by matching the measured h and T_{ad} with those determined for the experiments with the polycarbonate substrate. The thermal properties of Rohacell 51 found using the method are shown in Table 6.1.

Table 6. 1 Measured thermal properties of polycarbonate (optical grade) and Rohacell 51

	Polycarbonate (optical grade)	Rohacell 51
ρ (kg/m^3)	1200	52
c_p (J/kgK)	1250	3000
k (W/mK)	0.2	0.04

6.3.2 Extrapolation method to determine T_{ad} and h

A typical temperature history measured during a heat transfer experiment in the 1-stage test rig with ingress is shown in Fig. 6.13. The sealing air temperature reached 98% of the final temperature in less than 1 second from the trigger of the current supply to the mesh heater, and the core air temperature took approximately 50 seconds to stabilise. In order to calculate T_{ad} and h, Fourier's one-dimensional heat equation was numerically solved to determine the temperature history of the entire substrate. In this case the substrate was a composition of 5mm of Rohacell 51 and 15mm of Polycarbonate. The temperature histories was then used to calculate heat flux, q, at the rotor disc surface, from which the q vs. surface temperature, T_s, graph could be created.

As the relationship between q, h and T_{ad} is given by Eq.6.7, T_{ad} and h can be determined from the x-intercept and the gradient of the extrapolated graph, respectively, as shown in Fig. 6.14.

$$q = h\ \left(T_{ad} - T_s\right) \tag{6.7}$$

T_{ad} and h, determined by the extrapolation method, were then used to regenerate the surface temperature history using the 'direct solution' with the given experimental initial and boundary conditions. Subsequently, the temperature history was compared with the measured disc surface temperature history from the heat transfer experiment with the given condition. For this comparison, non-dimensionalised temperature was used, the definition of which is as follows:

$$\Theta_s{}' = \frac{T_s - T_{in}}{T_0 - T_{in}} \tag{6.8}$$

where, T_s is temperature

T_0 is the sealing air temperature measured by a fast response thermocouple

T_{in} is the initial temperature

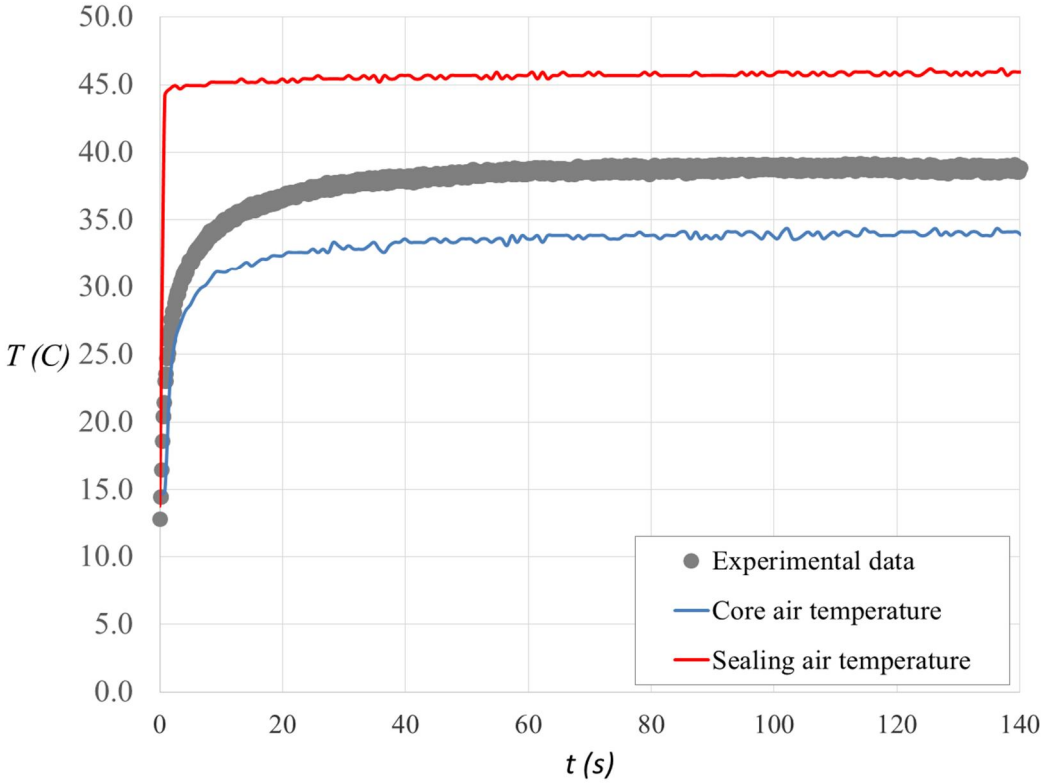

Figure 6. 13 Typical temperature history measured during a heat transfer experiment

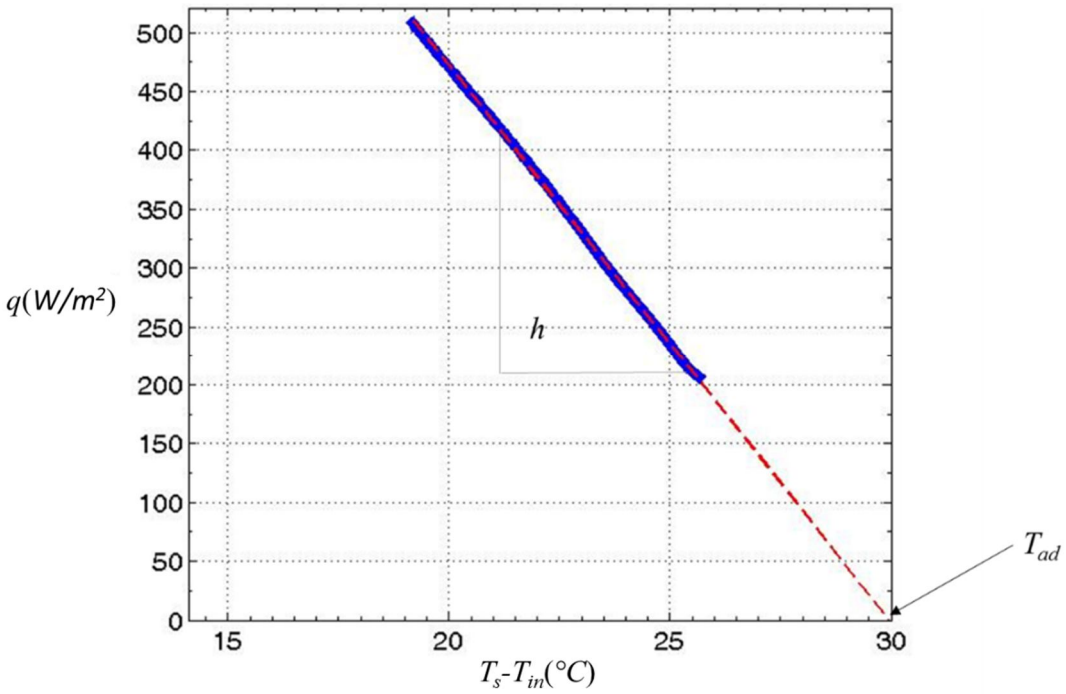

Figure 6.14 Heat flux vs. rotor disc temperature graph acquired from numerical analysis of heat transfer experiment data (The blue line are data analysed from the heat transfer experiment and the red dotted line is the extrapolation).

As shown in Fig.6.15, the regenerated surface temperature history based on the determined T_{ad} and h agrees well with the experimental data. Hence, it can be concluded that the determined T_{ad} and h are correct values.

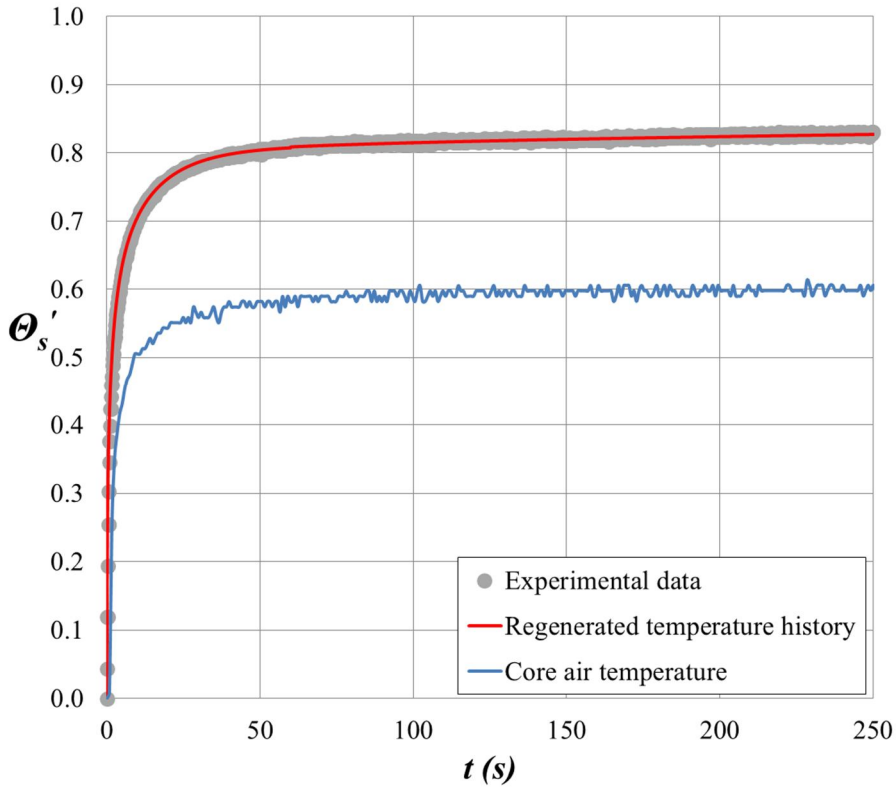

Figure 6.15 Non-dimensionalised temperature histories from a heat transfer experiment

6.3.3 Definition of adiabatic effectiveness

As explained at the beginning of this chapter, a heat transfer experiment method was chosen as an alternative to concentration measurement in order to investigate the effect of ingress on the rotor. An alternative form of effectiveness ('adiabatic effectiveness'), was defined as:

$$\varepsilon_{ad} = \frac{T_{ad} - T_a}{T_{ad}^* - T_a} \tag{6.9}$$

where, T_{ad} is the adiabatic disc temperature of the rotor

T_{ad}^* is the value of T_{ad} when there is no ingress (from a fully-sealed RI case)

T_a is the total temperature of the air in the annulus

The value of T_{ad} when there is no sealing flow is approximately equal to the sum of T_a and frictional heating at the given radial position. As the frictional heating was small for the results presented here, the definition of ε_{ad} satisfies the criterion, $\varepsilon_{ad} = 0$ when $\Phi_o = 0$ and $\varepsilon_{ad} = 1$ when $\Phi_o \geq \Phi_{min,ad}$.

6.4 Measurements of adiabatic effectiveness

6.4.1 Adiabatic temperature measurements with no ingress (fully-sealed case)

In order to determine ε_{ad}, a value of T_{ad}^* (the value of T_{ad} when there is no ingress) is required as shown in Eq. 6.9. Thus, heat transfer experiments under RI condition, i.e. with no mainstream flow (Re_w=0) in the annulus, using the infrared sensors, were carried out for fully sealed conditions ($\Phi_0 > \Phi_{min,c}$). $\Phi_{min,c}$ for the RI case was determined for each rim seal tested prior to the heat transfer experiments.

Table 6.2 Test conditions for RI heat transfer tests and acquired T_{ad}^* values for each seal

Seal	Radial location (r/b)	$\Phi_{min,c,RI}$	Φ_0 for RI heat transfer tests	ΔT(°C)	$T_{o,in}+\Delta T$(°C)	T_{ad}*(°C)
Axial	0.81	0.0741	0.085	1.1	45.2	44.5
	0.937			1.4	45.5	45.1
Radial	0.81	0.0389	0.045	1.1	47.1	46.5
	0.937			1.4	47.4	47.0
Double Axial	0.81	0.0572	0.065	1.1	44.3	43.5
	0.937	0.1	0.11	1.4	44.6	44.3
Double Radial	0.81	-	0.05	1.1	48.2	47.6
	0.937	-	0.05	1.4	48.5	48.1

As shown in Pountney *et al.* (2013), for an adiabatic system without ingress, T_{ad}^* can be expressued as:

$$T_{ad}^* < T_{0,in} + \Delta T \tag{6.10}$$

where

$$\Delta T = Pr^{1/3}\frac{\Omega^2 r^2}{2c_{p,air}} \tag{6.11}$$

The T_{ad}^* values acquired from the RI heat transfer experiments and the values of ΔT are shown in Table 6.1. The calculated T_{ad}^* is seen to satisfy the relationship given by Eq. 6.10.

6.4.2 Experimental results of single rim seals

The variation of ε_{ad} with Φ_o for the two single-clearance rim seals was determined at two radial locations (r/b=0.937 and r/b=0.81) for a rational speed of 3000 rpm ($Re_\phi = 8.17\times10^5$) at the design operation point.

Axial-clearance seal

The variation of ε_{ad}, for the single axial-clearance seal with Φ_o is plotted in Fig. 6.13. The variation of ε_c with Φ_o for the same seal geometry is also plotted for comparison. The thermal buffering effect can be seen from the graph, where $\varepsilon_{ad} \geq \varepsilon_c$, when the system is not fully sealed (i.e. when $\Phi_o<\Phi_{min,c}$). The radial variation of ε_c shown in section 5.4 (Fig. 5.11), i.e. ε_c is virtually invariant with the radius. The theoretical curve for ε_c was generated using the statistical technique developed by Zhou *et al.* (2013), as described in section 5.3 and the theoretical curve for ε_{ad} was generated by the thermal buffering model developed by Mear *et al.* (2015). As the thermal buffering model has not been published yet, the note that fully describes it is provided in Appendix A. As can be seen from Fig. 6.13, the agreement between the fitted theoretical curve and the measured data is good. The values of $\Phi_{min,ad}$ and $\Phi_{min,c}$ for the axial-clearance seal with polycarbonate inserts were found to be 0.106 and 0.198, respectively. This means that only approximately 54 % of the sealing flow is required to protect the rotor disc fully from hot gas ingress compared to that required for the stator.

It can also be seen from Fig. 6.13 that the difference between ε_{ad} and ε_c increases as Φ_0 increases. This is because when the sealing flow rate increases, the entrainment

from the core flow into the rotor boundary layer decreases and consequently, the thermal buffering effect increases.

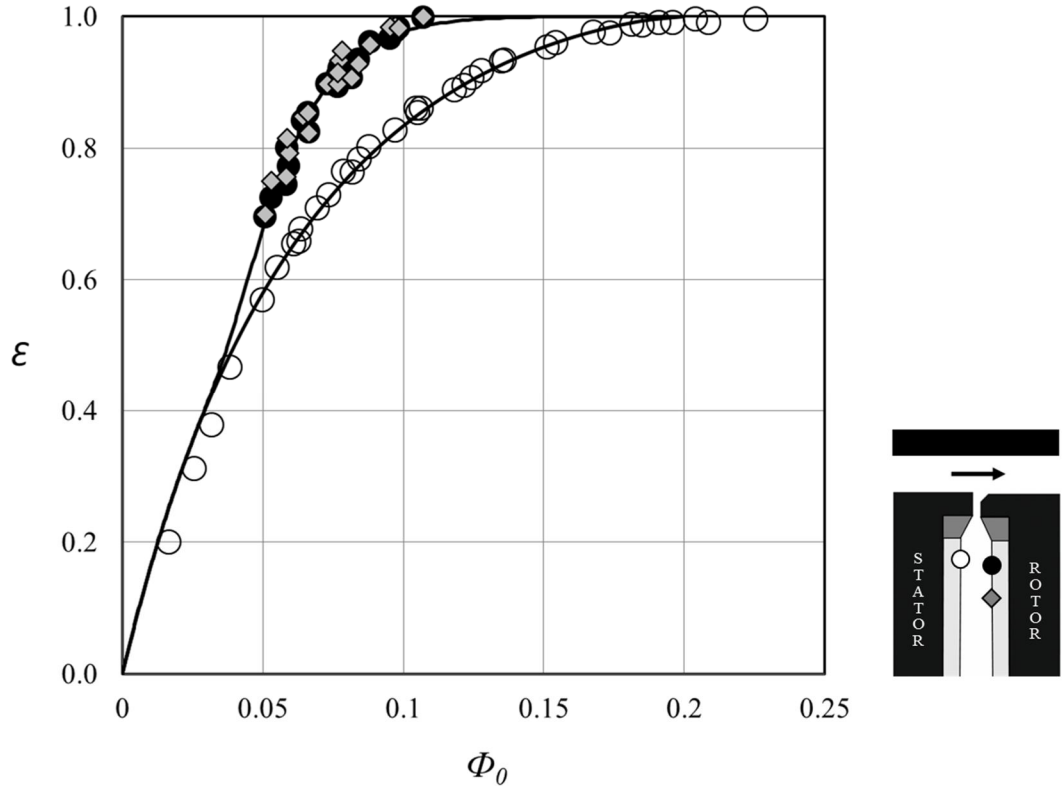

Figure 6.16 Variation of ε (ε_{ad} or ε_c) with Φ_0 for a single axial-clearance seal: Symbols denote experimental data (shown in black or gray: ε_{ad}, shown as open circles: ε_c) and lines are theoretical curves.

Radial-clearance seal

The variation of ε_{ad} for the single radial-clearance seal with Φ_o is plotted in Fig. 6.14. The variation of ε_c with Φ_o for the same seal geometry is also plotted for comparison and the thermal buffering effect can be seen. The theoretical curves for ε_c and ε_{ad} were respectively generated using the statistical technique developed by Zhou *et al.* (2013) and the thermal buffering model (see Appendix A) developed by Mear *et al.* (2015). As can be seen, the agreement between the fitted theoretical curve and the measured data is good. The values of $\Phi_{min,ad}$ and $\Phi_{min,c}$ for the radial-clearance seal with a polycarbonate insert were found, to be 0.082 and 0.127 respectively, i.e. approximately 65 % of sealing flow is required to protect the rotor disc fully from hot gas ingress compared to that for stator. As with the axial-clearance seal, it can

also be seen that the difference between ε_{ad} and ε_c increases as Φ_0 increases. This is because when the sealing flow rate increases, the entrainment from the core flow into the rotor boundary layer decreases and consequently, the thermal buffering effect increases.

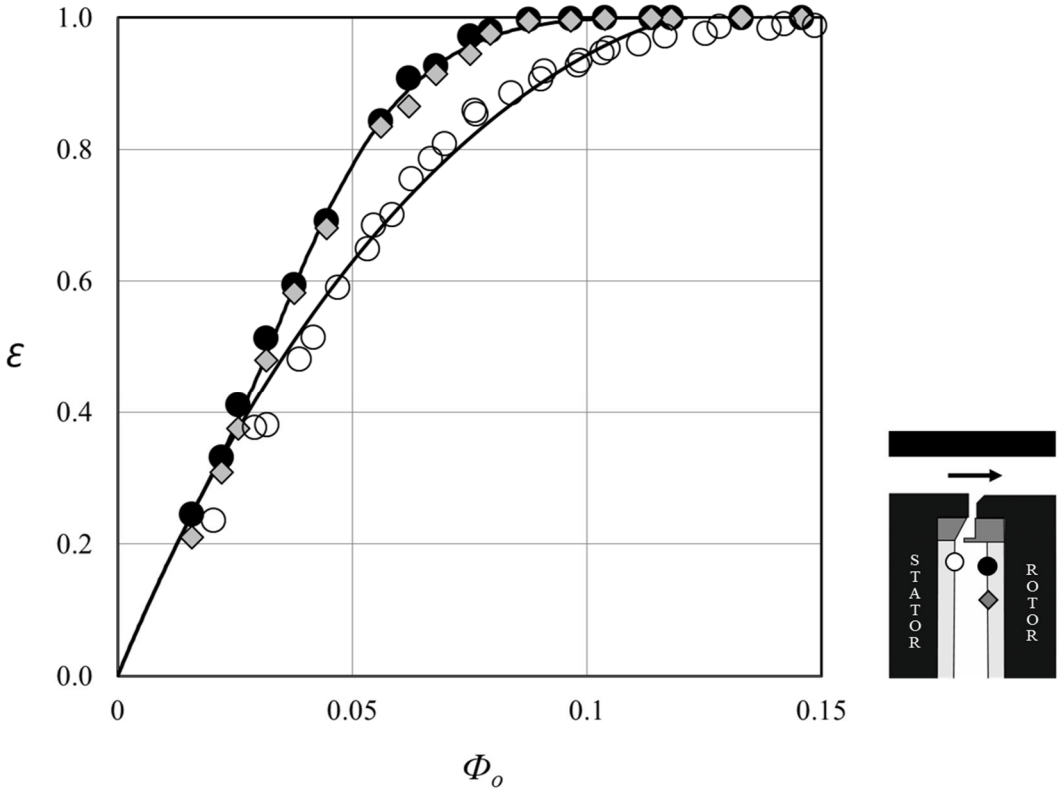

Figure 6.17 Variation of ε (ε_{ad} or ε_c) with Φ_0 for a single radial-clearance seal: Symbols denote experimental data (shown in black or gray: ε_{ad}, shown as open circles: ε_c) and lines are theoretical curves.

6.4.3 Experimental results of double rim seals

Transient experiments for the two double-clearance rim seals were conducted at a rotational speed of 3000 rpm (Re_ϕ = 8.17×10^5) at the design operation point to determine the variations of ε_{ad} with Φ_o. Two radial locations are presented; r/b = 0.81 in the inner wheel-space and r/b = 0.937 in the outer wheel-space.

Double axial-clearance seal

Fig. 6.15 shows the variations of ε_{ad} with Φ_o for the inner and outer wheel-space of the double axial-clearance seal. The variations of ε_c with Φ_o for the two wheel-spaces are also plotted for comparison. The data again shows the thermal buffering effect with $\varepsilon_{ad} > \varepsilon_c$, when the system is not fully sealed (i.e. when $\Phi_o<\Phi_{min,c}$). However, unlike the single-clearance seals, ε_{ad} in the inner radius (r/b=0.81) is significantly higher than that of the outer radius for the same Φ_0. Most of the ingested mainstream flow is confined to the outer wheel-space and only a small amount penetrates into the inner wheel-space.

As with the single-clearance seals, it can also be seen from Fig. 6.15 that the difference between ε_{ad} and ε_c increases as Φ_0 increases. This is because when the sealing flow rate increases, the entrainment from the core flow into the rotor boundary layer decreases and consequently, the thermal buffering effect increases. The theoretical curves for ε_c and ε_{ad} were generated as discussed above. As can be seen from Fig. 6.15, the agreements between the fitted theoretical curves and the measured data are generally good. The values of $\Phi_{min,ad}$ and $\Phi_{min,c}$ for the outer wheel-space of the double axial-clearance seal were found to be 0.105 and 0.173, respectively. Those for the inner wheel-space of the seal were determined to be 0.087 and 0.164, respectively.

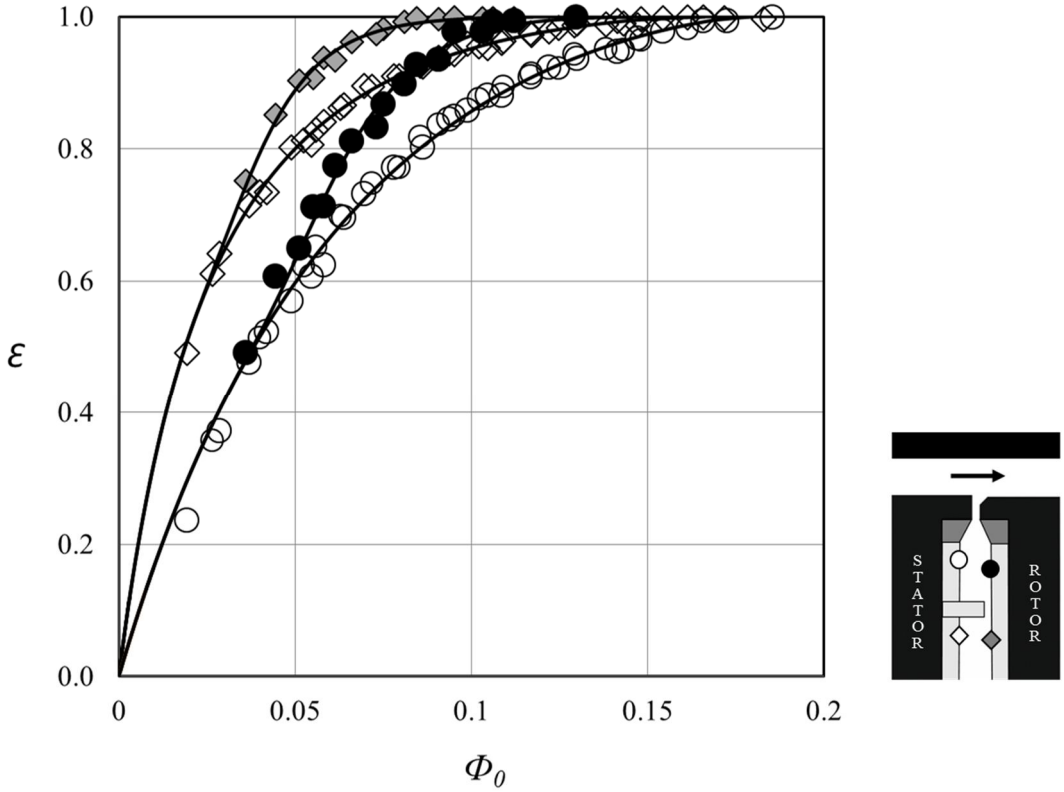

Figure 6.18 Variation of ε (ε_{ad} or ε_c) with Φ_0 for a double axial-clearance seal: Symbols denote experimental data (shown in black or gray: ε_{ad}, shown as open symbols: ε_c) and the lines are theoretical curves (unbroken lines are for ε_{ad} and broken lines are for ε_c).

The variation of the ε_{ad} with Φ_0 for the outer wheel-space of the double axial-clearance seal is compared with that of the single axial-clearance seal in Fig. 6.16. It can be seen from the graph that both seals have similar values of ε_{ad} at the outer radius (r/b=0.937) for the same Φ_0. That is, although the inner seal is an effective method to prevent or reduce ingestion into the inner wheel-space, the level of ingestion into the outer wheel-space for the double axial seal is not attenuated by the inner rim seal.

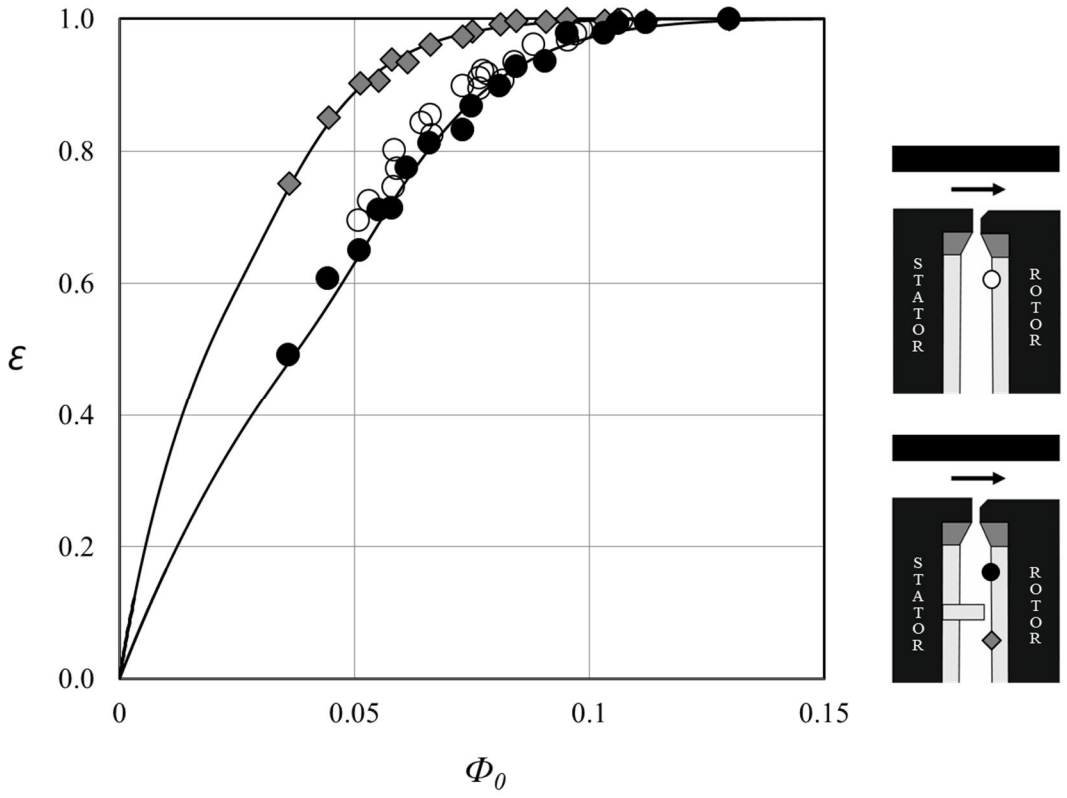

Figure 6.19 Variation of ε (ε_{ad} or ε_c) with Φ_0 for a double axial-clearance seal compared with axial-clearance seal data: Symbols denote experimental data (shown in black or gray: double axial-clearance seal, shown as open circles: single axial-clearance seal) and the lines are theoretical curves (the theoretical curve for ε_{ad} of the axial seal is not shown here).

Double Radial-clearance seal

Fig. 6.17 shows the variation of ε_{ad} and ε_c with Φ_0 in the inner and outer wheel-space of the double radial-clearance seal; the variations of ε_c with Φ_o are plotted to show the thermal buffering effect. Like the other seals, ε_{ad} is always greater than ε_c for both the inner and outer wheel-spaces, when the system is not fully sealed. The value of ε_{ad} for the inner radius (r/b=0.81) is significantly greater than that of the outer radius (r/b=0.937) for the same Φ_0. It can be concluded that the ingested mainstream flow is confined to the outer wheel-space and only a small amount of ingested mainstream air penetrates into the inner wheel-space.

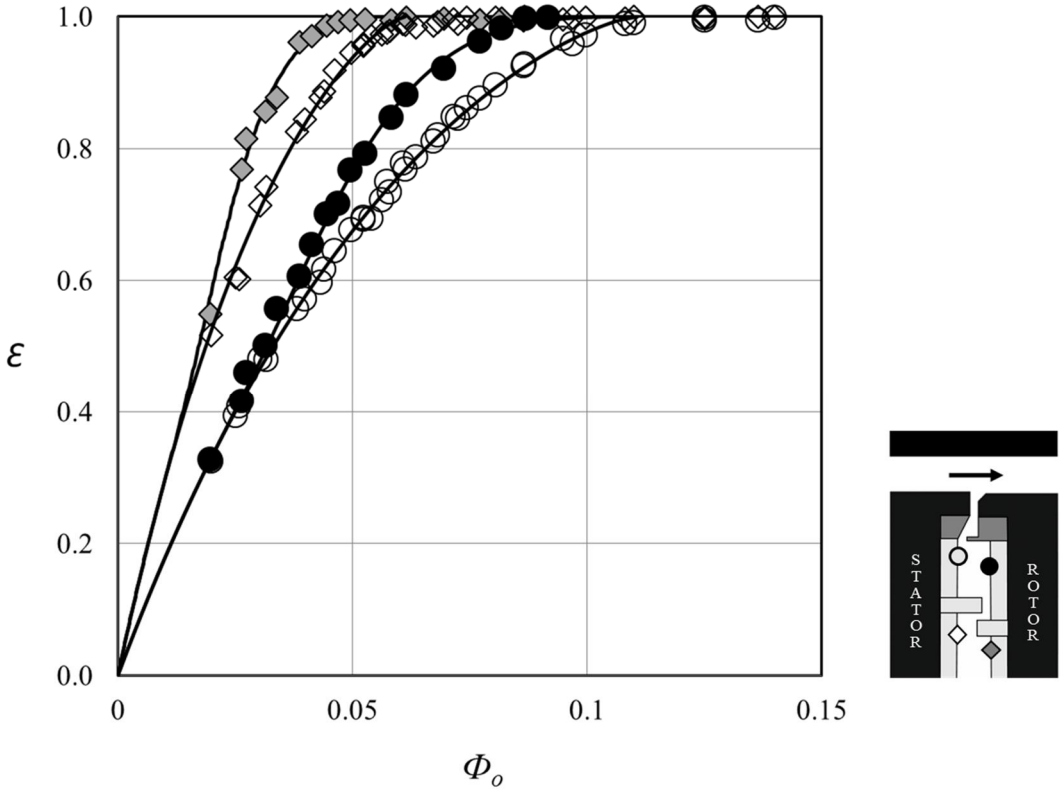

Figure 6.20 Variation of ε (ε_{ad} or ε_c) with Φ_0 for a double radial-clearance seal: Symbols denote experimental data (shown in black or gray: ε_{ad}, shown as open symbols: ε_c) and the lines are theoretical curves (unbroken lines are for ε_{ad} and broken lines are for ε_c).

The theoretical curves for ε_c and ε_{ad} are shown in Fig. 6.17 and again these fit the data well. The values of $\Phi_{min,ad}$ and $\Phi_{min,c}$ for the outer wheel-space of the double radial-clearance seal were found to be 0.057 and 0.091, respectively. Those for the inner wheel-space of the seal were determined to be 0.044 and 0.06, respectively.

A bar chart that shows the magnitudes of $\Phi_{min,c}$ and $\Phi_{min,ad}$ for all the rim seals tested is provided in Fig. 6.18. The seal performance is ranked in terms of the magnitude of $\Phi_{min,ad}$ and it shows the same ranking based on $\Phi_{min,c}$. The single axial-clearance seal shows the worst performance and the inner seal of the double radial-clearance seal has the best, for both concentration (ε_c) and adiabatic effectiveness (ε_{ad}).

6.5 Comparison of adiabatic effectiveness

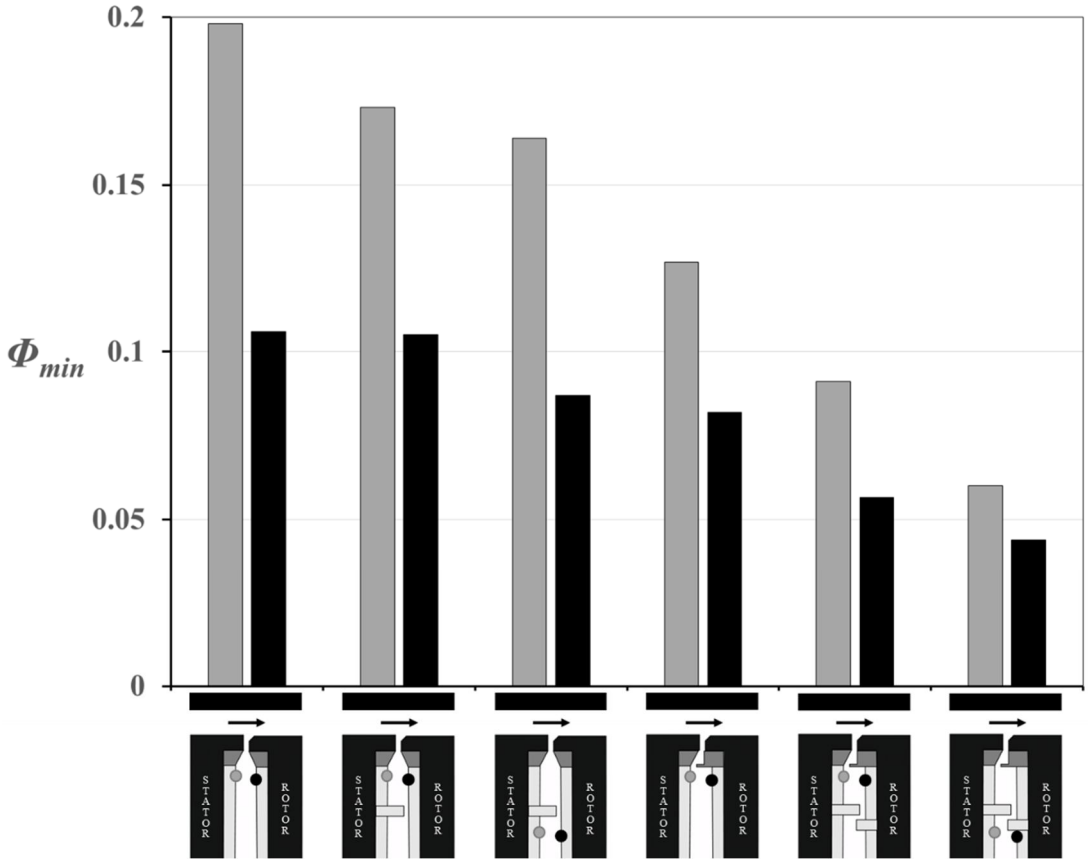

Figure 6.21 Seal performance ranking shown in order of magnitude of $\Phi_{min,c}$ and $\Phi_{min,ad}$ for all the seal configurations tested. Shown in gray is $\Phi_{min,c}$ and in black is $\Phi_{min,ad}$.

It can also be clearly seen that $\Phi_{min,c} \geq \Phi_{min,ad}$ for all cases, i.e. the thermal buffering effect is observed for all the seals tested. In addition, the difference between $\Phi_{min,c}$ and $\Phi_{min,ad}$ decreases as the performance of the seal improves; the difference is largest for the axial-clearance seal ($\Phi_{min,ad}$ ~0.54 $\Phi_{min,c}$) and smallest for the inner seal of the double radial-clearance seal ($\Phi_{min,ad}$ ~0.73 $\Phi_{min,c}$).

6.6 Summary

Transient heat transfer experiments using infrared temperature measurement sensors were carried out to investigate the effect of ingress on the rotor disc. In order to determine sealing effectiveness based on the heat transfer experiments, an adiabatic effectiveness was defined and Fourier's 1-D heat equation was solved

numerically with the appropriate initial and boundary conditions to calculate T_{ad} and h. These experiments were carried out for four generic rim seal geometries, including two single and two double rim seals. The variation of adiabatic effectiveness with sealing flow rate quantified the effect of ingress on the rotor disc.

Gas concentration of CO_2 was also measured for the four rim seal geometries and the variation of concentration effectiveness with sealing flow rate was determined. The concentration measurements were made at two different rotational speeds (2000 and 3000rpm) and the heat transfer ones were measured at 3000rpm. All experiments were conducted at the design operating points. The adiabatic effectiveness measured on the rotor and concentration effectiveness calculated on the stator were then compared to demonstrate the thermal buffering effect, where the effect of ingress on the rotor is less than that measured on the stator, i.e. the boundary layer on the rotor disc protects the disc from ingress.

It was shown that the sealing effectiveness on the rotor was significantly higher than the equivalent stator effectiveness for all four generic rim seals tested. The theoretical curves for the adiabatic effectiveness versus sealing flow rate data for each measurement location were generated by the thermal buffering model developed by Mear *et al.* (2015) and the curves generally showed a good agreement with the measured experimental data. For the two double-clearance rim seals, the adiabatic effectiveness of the inner wheel-space was significantly higher than that of the outer, i.e. the most of the ingested mainstream flow is confined in the outer wheel-space and only a small amount penetrates into the inner wheel-space.

Chapter 7: Use of pressure measurements to determine sealing effectiveness

This chapter describes a model to determine effectiveness not from concentration but pressure measurements. The author's contribution was collecting the experimental data. The results from this chapter are published in Owen *et al.* (2014).

The Bath one-stage ingress test facility has been used to determine ε_c, the sealing effectiveness, based on concentration measurements of CO_2 gas. However, as described in section 2.2, the ingress of hot gas through the rim seal of a gas turbine is driven by the pressure difference between the mainstream flow in the turbine annulus and that in the wheel-space radially inward of the rim seal. The engine design requires a sealing effectiveness based on the pressure difference across the rim seal. Although pressure measurements can be used to determine the sealing effectiveness, they are, in effect, proxy measurements, and the effectiveness determined in this way is strongly affected by the locations where the pressures are measured. Orifice models can be used to relate the amount of ingress to the pressure difference across the rim seal. However, to incorporate these models into design codes, the designer needs to know where in the turbine the pressures should be determined. More broadly, it is necessary to understand the relationship between the effectiveness measured by concentration and pressure, if the concentration measurements obtained from experimental rigs are to be used in gas turbine design methods (The symbols ε_c and ε_p are used here to denote the sealing effectiveness determined from the concentration and pressure measurements, respectively, and in general $\varepsilon_c \neq \varepsilon_p$).

In this chapter a theoretical model (developed by Professor J. M. Owen) is used to enable the 'correct' value of ε_p to be determined from pressure measurements made at any arbitrary location (referred to as location A, see Fig.7.1) on the vane platform, upstream of the seal clearance in a rig or gas turbine. The model is based on a previously published orifice model (Owen, 2011a, 2011b) and on the hypothesis that there is a unique location, referred to as the sweet spot, where the pressure distribution on the vane platform would ensure that $\varepsilon_c = \varepsilon_p$ for all sealing flow rates. Pressure and concentration measurements in the Bath one-stage ingress test rig with

a radial-clearance rim seal are used to validate the theoretical model and to determine the values of ε_c and ε_p.

As this chapter is concerned only with externally-induced (EI) ingress, the subscript EI is not used below.

7.1 Sealing effectiveness of the radial-clearance rim seal

A schematic diagram of the radial-clearance seal that was used to determine the concentration and pressure sealing effectiveness (ε_c and ε_p) experimentally is shown in Fig.7.1 with static dimensions. The seal-clearance ratio, $G_c = s_{c,ax} / b = 0.0105$, used in Eqs. 2.27 and 2.29, was based on the axial-clearance $s_{c,ax} = 2.0$ mm.

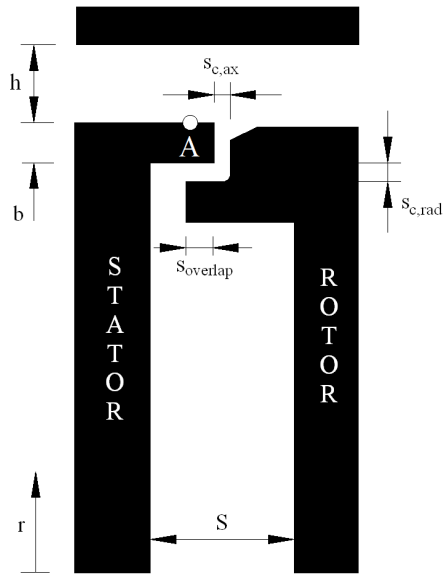

Figure 7.1. Schematic of a radial-clearance seal and annulus showing location A. Static dimensions in mm: $h = 10$; $S = 20$; $S_{c,ax} = 2.00$; $S_{c,rad} = 1.28$;$S_{overlap} = 1.86$ (Owen *et al.*, 2014).

Fig.7.2 shows comparisons between the theoretical curve, Eq.2.29, and the experimental values of ε_c based on the concentration measured on the stator at a non-dimensional radius $r/b = 0.958$. Φ_{min} and Γ_c were calculated from a statistical fit of the data (Zhou *et al.*, 2013), and their respective values were found to be 0.0915 and 1.32 for the radial-clearance seal. The experimental data, which are in good agreement with the theoretical curve, show that the rotational Reynolds number, Re_ϕ, has no significant effect on the results in the range of Re_ϕ investigated in this research.

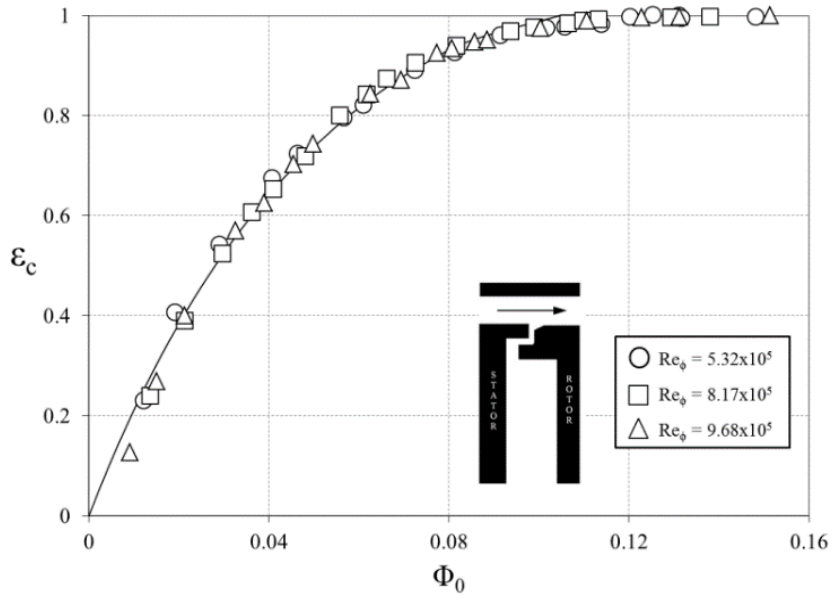

Figure 7.2 Comparison between theoretical and measured values of ε_c for a radial-clearance seal (Owen *et al.*, 2014)

7.2 Determination of sealing effectiveness from pressure measurement

7.2.1 Use of an orifice model to calculate effectiveness

The Bath orifice model derived by Owen (2011a, b) is based on pressures, and it was assumed that EI ingress is related to Δp, the peak-to-trough pressure difference in the annulus, where:

$$\Delta p = p_{2,max} - p_{2,min} \tag{7.1}$$

The sealing effectiveness in the model is related to g, the normalised pressure difference across the seal, where:

$$g = \frac{p_1 - p_{2,min}}{\Delta p} \tag{7.2}$$

The subscripts 1 and 2 refer to locations in the wheel-space and annulus, respectively, and these locations were not specified in the orifice model. By

assuming a linear saw-tooth model for the circumferential distribution of pressure in the annulus, the orifice equations were solved by Owen (2011b) to give:

$$\frac{\Phi_o}{\Phi_{min}} = g^{3/2} - \Gamma_c (1-g)^{3/2} \tag{7.3}$$

It was also shown from the orifice equations that:

$$\varepsilon_p = 1 - \Gamma_c \left[\frac{1-g}{g} \right]^{3/2} \tag{7.4}$$

As discussed above, ε_p is the sealing effectiveness based on pressure differences, and $\Gamma_c = C_{d,i}/C_{d,e}$ is the ratio of the discharge coefficients for ingress and egress through the seal clearance. In practice, g (and therefore ε_p) depends on the sealing flow rate, and it also depends on where the pressures are measured. That is, $g=g(\Phi_o,x)$, where x is that axial location in the annulus where Δp is measured. At the sweet spot (where $x = \hat{x}$, $\varepsilon_p = \hat{\varepsilon}_p = \varepsilon_c$ and $g = \hat{g}$), Eq.7.4 becomes:

$$\hat{\varepsilon}_p = \varepsilon_c = 1 - \Gamma_c \left[\frac{1-\hat{g}}{\hat{g}} \right]^{3/2} \tag{7.5}$$

Using Eq.2.29, the effectiveness equation for ε_c, it follows from Eq.7.5 that:

$$\hat{g} = \frac{1}{1 + \Gamma_c^{-2/3} (1-\varepsilon_c)^{2/3}} \tag{7.6a}$$

Defining $\hat{g}^* = \hat{g}$ when $\Phi_o = 0$, and $\varepsilon_c = 0$, it follows from Eq.7.6a that:

$$\hat{g}^* = \frac{\Gamma_c^{2/3}}{1 + \Gamma_c^{2/3}} \tag{7.6b}$$

For the radial-clearance seal, $\Gamma_c = C_{d,i}/C_{d,e} = 1.32$ and so $\hat{g}^* = 0.546$.

It is shown below in subsection 7.2.2, how $\hat{g}$ and $\hat{\varepsilon}_t$ can be determined from experimental measurements.

7.2.2 Determination of effectiveness from pressure measurements

In the model developed below, it is assumed that the sweet spot, where $g^* = \hat{g}^*$, can be found on the vane platform upstream of the clearance. This is consistent with the results of Owen (2011b), who used steady 3-D CFD based on the geometry of the Bath one-stage ingress rig (but without blades and with an axial-clearance seal) to determine the sealing effectiveness.

In the annulus, $p_{2,min}$, $p_{2,max}$ and Δp depend on both Φ_o and x, where x is the non-dimensional axial distance from the centre of the seal clearance and in the wheel-space, p_1 is invariant with x, depending only on Φ_o. To make these dependencies explicit, Eq.7.2 is rewritten as:

$$g(\Phi_o, x) = \frac{p_1(\Phi_o) - p_{2,min}(\Phi_o, x)}{\Delta p(\Phi_o, x)} \tag{7.7a}$$

Similarly, at location A, where the pressures are measured in the annulus, $x = x_A$ and:

$$g(\Phi_o, x_A) = \frac{p_1(\Phi_o) - p_{2,min}(\Phi_o, x_A)}{\Delta p(\Phi_o, x_A)} \tag{7.7b}$$

Eliminating p_1 from Eqs.7.7a and 7.7b, it follows that:

$$g(\Phi_o, x) = \frac{\Delta p(\Phi_o, x_A)}{\Delta p(\Phi_o, x)} g(\Phi_o, x_A) + \ldots \\ \ldots \frac{p_{2,min}(\Phi_o, x_A) - p_{2,min}(\Phi_o, x)}{\Delta p(\Phi_o, x)} \tag{7.8}$$

Using a ‘separation-of-variables’ approach, it is assumed that:

$$\Delta p(\Phi_o, x) = \zeta(x) \Delta p(\Phi_o, x_A) \tag{7.9a}$$

and

$$\left[p_{2,min}(\Phi_o, x) - p_{2,min}(\Phi_o, x_A)\right] = \chi(x) \Delta p(\Phi_o, x_A) \tag{7.9b}$$

where $\zeta(x)$ and $\chi(x)$ are similarity parameters that depend on x but are assumed to be invariant with Φ_o. At location A, $\zeta(x_A) = 1$ and $\chi(x_A) = 0$.

Eq.7.8 can now be written as:

$$g(\Phi_o,x)=\zeta(x)^{-1}\left[g(\Phi_o,x_A)-\chi(x)\right] \tag{7.10}$$

Consequently, at the sweet spot where $x=\hat{x}$ and $g=\hat{g}$, Eq.7.10 becomes:

$$g(\Phi_o,\hat{x})=\hat{g}(\Phi_o)=\zeta(\hat{x})^{-1}\left[g(\Phi_o,x_A)-\chi(\hat{x})\right] \tag{7.11a}$$

As $\zeta(\hat{x})$ and $\chi(\hat{x})$ are constants, Eq.7.11a can be expressed more simply as:

$$\hat{g}(\Phi_o)=B\,g(\Phi_o,x_A)+C \tag{7.11b}$$

where the constants *B* and *C* are given by:

$$B=\zeta(\hat{x})^{-1}=\frac{\Delta p(\Phi_o,x_A)}{\Delta p(\Phi_o,\hat{x})} \tag{7.12a}$$

$$C=-\frac{\chi(\hat{x})}{\zeta(\hat{x})}=-\frac{p_{2,min}(\Phi_o,\hat{x})-p_{2,min}(\Phi_o,x_A)}{\Delta p(\Phi_o,\hat{x})} \tag{7.12b}$$

As $x_A\rightarrow\hat{x}$ then $B\rightarrow 1$ and $C\rightarrow 0$.

Knowing $\hat{g}$ from Eq.7.6a, the constants *B* and *C* in Eq.7.11b can be found from linear regression of $\hat{g}$ versus the measured values of $g(\Phi_o,x_A)$, as shown in section 7.3. The sealing effectiveness $\hat{\varepsilon}_p$, which in principle could be determined from pressure measurements at the sweet spot, can be calculated from Eq.7.5, where:

$$\hat{\varepsilon}_p(\Phi_o)=1-\Gamma_c\left[\frac{1-C-Bg(\Phi_o,x_A)}{Bg(\Phi_o,x_A)+C}\right]^{3/2} \tag{7.13}$$

As shown in section 7.3, Eq.7.13 ensures that the sealing effectiveness determined from pressure measurements is equivalent to that determined from concentration ones.

7.2.3 Calculation of discharge coefficients at the sweet spot

The discharge coefficient for egress, determined from measurements at location (A), can be calculated by:

$$C_{d,e}(x_A) = \frac{3}{2}\frac{\Phi_{min}}{\left[\Delta C_p(x_A)\right]^{1/2}} \tag{7.14}$$

This value depends on where the measurements are made, and the correct value to use is the one determined at the sweet spot, where:

$$C_{d,e}(\hat{x}) = \frac{3}{2}\frac{\Phi_{min}}{\left[\Delta C_p(\hat{x})\right]^{1/2}} \tag{7.15}$$

At the sweet spot, Eq.7.12 shows that:

$$\frac{\Delta p(\Phi_o, x_A)}{\Delta p(\Phi_o, \hat{x})} = B \tag{7.16}$$

where, as described above, the constant B is found from linear regression of the pressure measurements. It follows from Eq.7.16 that:

$$\Delta C_p(\hat{x}) = B^{-1}\Delta C_p(x_A) \tag{7.17}$$

Substitution into Eq.7.15 gives:

$$C_{d,e}(\hat{x}) = B^{1/2}C_{d,e}(x_A) \tag{7.18a}$$

Similarly, for ingress:

$$C_{d,i}(\hat{x}) = B^{1/2}C_{d,i}(x_A) \tag{7.18b}$$

As shown in section 7.4, the discharge coefficients determined from measurements in an experimental rig could be used to compute the ingress through a gas turbine rim seal.

7.2.4 Computation of location of the sweet spot

CFD, which was conducted by a co-author of Owen *et al.* (2014), was used to support the experiments which validate the theoretical model. The principal object of the CFD was to determine the location of the sweet spot and to test the hypothesis that its location invariant with the sealing flow rate. Although, as shown in subsection 7.2.3, the sealing effectiveness and the discharge coefficients can be calculated without knowing the location of the sweet spot, it is needed if the experimental results are to be applied to a gas turbine rim seal. As shown below, its location can be determined computationally using Eqs.7.2 and 7.6.

Fig.7.3 shows the computed axial distribution of $g(x)$, based on Eq.7.2, for five values of Φ_o/Φ_{min}. The horizontal lines represent the five corresponding values of $\hat{g}$, which were calculated from Eq.7.6 with the values of ε_c and Γ_c, determined from the concentration measurements. The intercept of these two curves occurs at the point where $g = \hat{g}$ and consequently, where $x = \hat{x}$. The vertical line corresponds to the mean of the computed values of $_{\hat{x}}$. (The values of p_1 were computed on the stator surface at r/b = 0.958, which is the location used for the experimental measurements discussed in section 7.3)

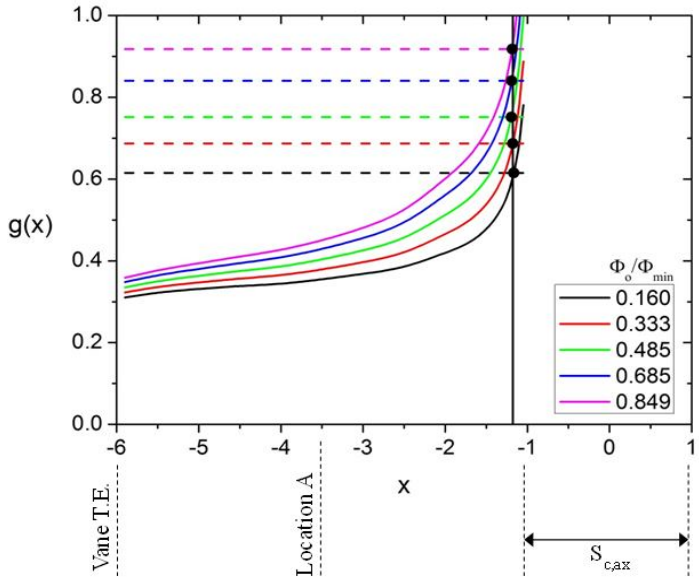

Figure 7.3 Effect of Φ_o/Φ_{min} on computed variation of g with x showing location of the sweet spot. (Horizontal broken lines show values of $\hat{g}$; solid curve shows computed variation of g(x); solid vertical line shows mean value of computed $_{\hat{x}}$.) (Owen *et al.*, 2014)

Fig.7.4 shows the computed values of $\hat{x}$ for the 22 values of Φ_o/Φ_{min} used for the pressure measurements described in section 7.3. The mean value of $\hat{x}$ for the radial-clearance seal was - 1.18, which is just 0.18 mm upstream of the seal clearance in the experimental rig. Although there is no reason to believe that this value will be the same for all seals, it is consistent with previous computations for an axial-clearance seal in the same rig (Sangan *et al.*, 2013a). The fact, that there is no significant effect of the sealing flow rate on the computed values of $\hat{x}$, provides support for the assumption that $\hat{x}$ is invariant with Φ_o.

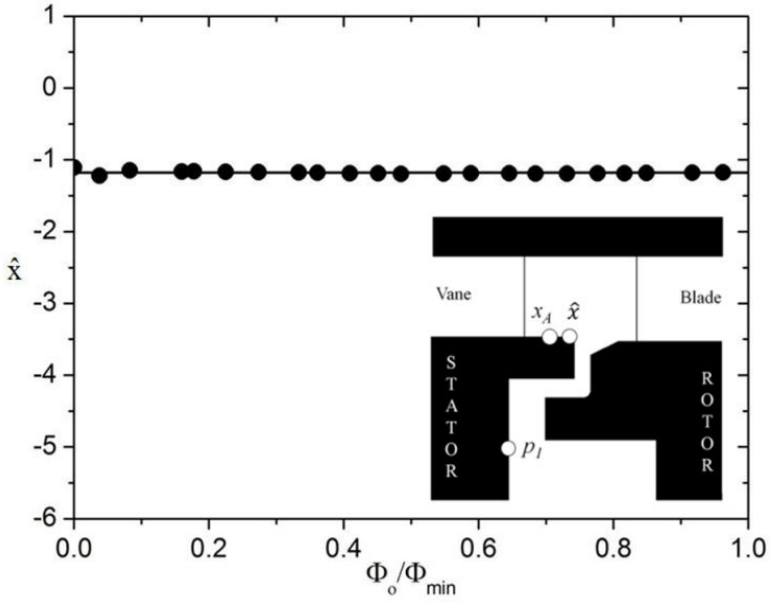

Figure 7. 4 Computed variation of $\hat{x}$ with Φ_o/Φ_{min}. (Solid line shows mean value of $\hat{x}$, with its geometric position shown in relation to the seal clearance (inset)) (Owen *et al.*, 2014)

7.3 Experimental measurements

In order to validate the theoretical model, static pressure was measured both in the annulus and wheel-space. Regarding the former, this was measured on the vane platform (stator shroud) 2.5mm axially upstream of the edge of the seal clearance, location A. For this, pressure taps were installed for four different vane pitches at 90° apart and the static pressure data were averaged over the four vane pitches, i.e. 15 equally spaced taps (each 0.5 mm in diameter) across a single vane pitch ($0 < \theta < 1$, where θ is the normalised angular location between adjacent vanes). The arrangement of the static pressure taps on the vane platform and stator wall are

shown in Fig. 7.5. The pressures were measured using a Scanivalve system, which was connected to the taps with flexible plastic tubing.

The non-dimensional pressure coefficient, C_p, and the non-dimensional pressure difference, ΔC_p, are defined as:

$$C_P = \frac{p_2 - \overline{p_2}}{0.5\rho\Omega^2 b^2} \tag{7.19}$$

$$\Delta C_p = \frac{\Delta P}{0.5\rho\Omega^2 b^2} \tag{7.20}$$

where, p_2 is the local static pressure at the measurement location

$\overline{p_2}$ is the arithmetic mean of the measured values of p_2 over one vane pitch

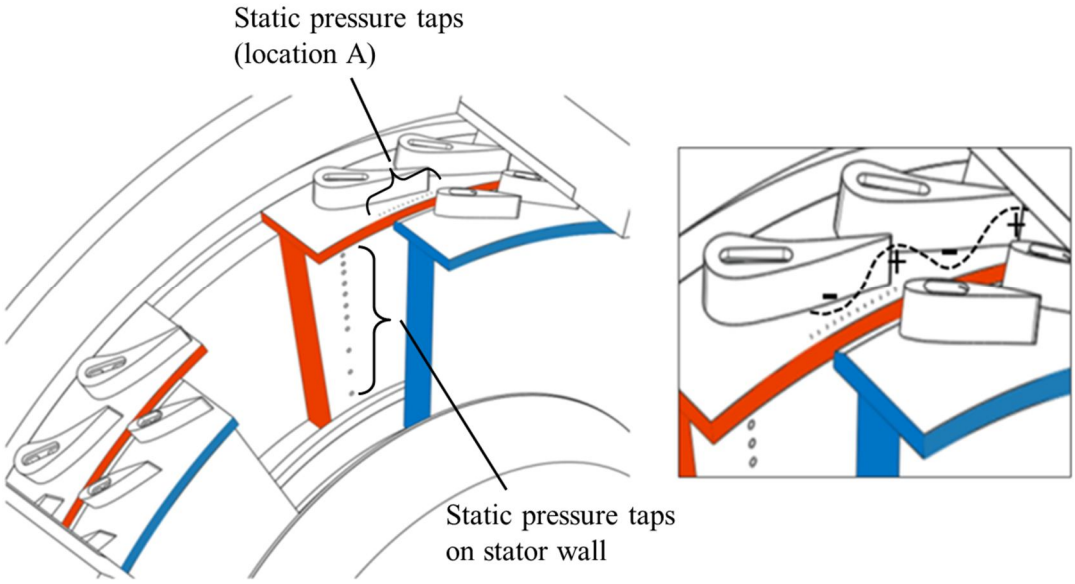

Figure 7.5 Rig test section showing the static pressure taps on the stator wall and the vane hub (location A) with typical pressure asymmetry in the annulus. The stator disc is shown in red and the rotor disc in blue (Owen *et al.*, 2014)

In the wheel-space, 14 pressure taps ($0.55 < r/b < 0.993$) were used to determine the distribution of static pressure along the stator. All pressure measurement data presented in this thesis are for the design condition, with similar annulus velocity triangles at the three operating points listed in Table 1. At the design condition, the

flow coefficient was C_F = 0.538 and the circumferential variation of C_p (Fig.7.6) were shown to be independent of Re_ϕ.

The pressure measurements were obtained for the radial-clearance rim seal with Re_ϕ=8.17×10^5 and Fig.7.7 shows the measured variation of $g(x_A)$ with Φ_o/Φ_{min}. Although the static pressure was measured at 14 different radial locations, as described above, only five of these measurements are shown in Fig. 7.7 for clarity. It can be seen that there is no location of r_1/b that ensures that $g(x_A)$ = 1 when Φ_o/Φ_{min} = 1, which confirms the fact that location A cannot be the sweet spot and consequently, these uncorrected measurements cannot be used to determine the effectiveness.

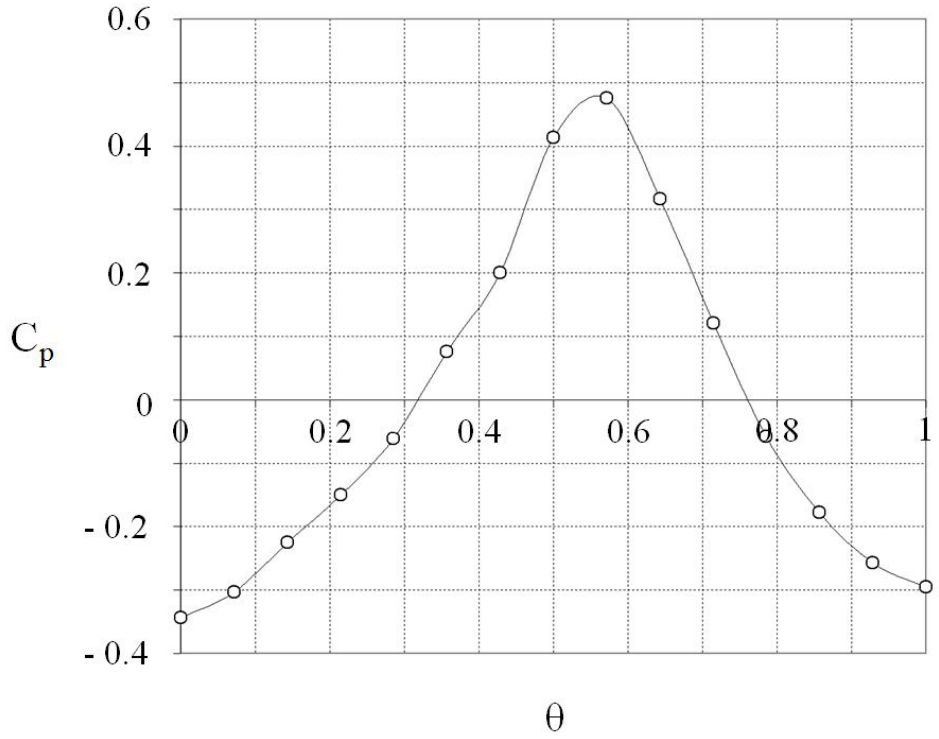

Figure 7.6 Variation of C_p with θ measured at location A for design condition (Sangan, 2011)

Although, in theory, the variation of $g(x_A)$ with Φ_o/Φ_{min} should be slightly nonlinear, the fact that the nonlinearity shown in Fig.7.7 increases as r_1/b decreases is attributed to the swirl in the wheel-space. That is, the swirl creates a nonlinear radial pressure gradient, and the difference between the pressures at the measurement radius r_1 and the seal radius b increases as r_1/b decreases.

There are two extremes to avoid in choosing a suitable location of r_1/b to measure p_1. As shown by Bohn *et al.* (1995), if the radius is too close to the seal then the pressure in the wheel-space will be non-axisymmetric; if too small, the effects of swirl will be significant. (The effect of swirl on the radial distribution of pressure in the wheel-space of the rig used here is discussed in Sangan *et al.* (2014)). A value of r_1/b = 0.958 was chosen here as a compromise, which was also the radial location used to make the concentration measurements from which ε_c was determined.

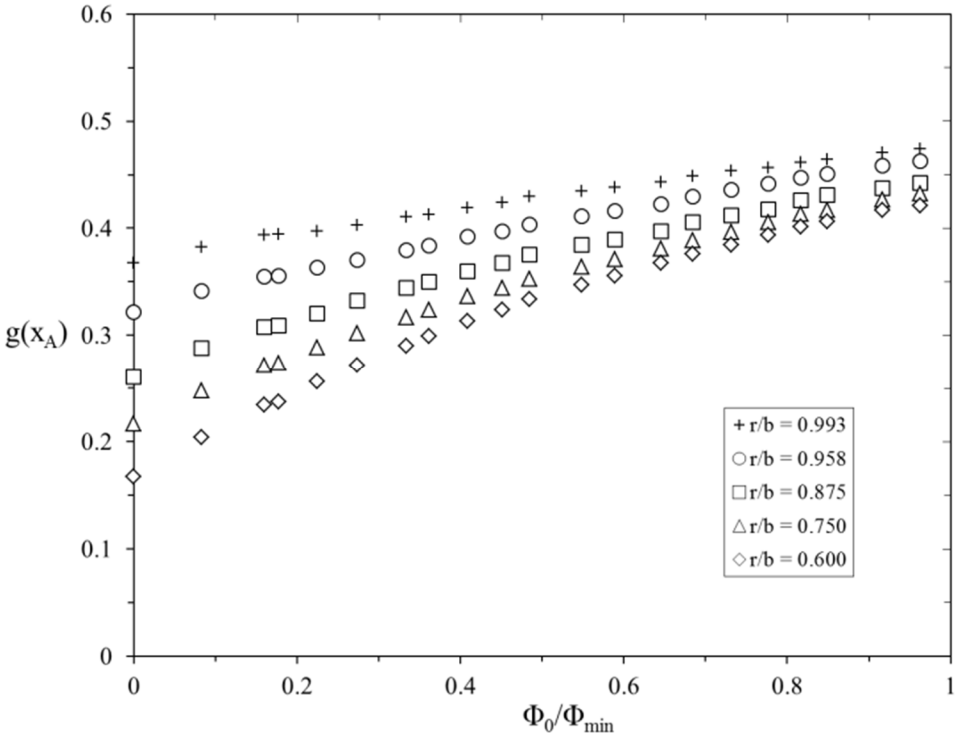

Figure 7.7 Effect of r_1/b on measured variation of $g(x_A)$ with Φ_o/Φ_{min} (Owen *et al.*, 2014)

Fig.7.8 shows the variation of $g(x_A)$, the values of which were measured at r_1/b = 0.958, versus $\hat{g}$, calculated from Eq.7.6a. Linear regression was used to determine the values of the constants, and it was found that B = 3.07 and C = - 0.472. The standard deviation between the experimental values of $g(x_A)$ and the correlation was 0.012; in section 7.5, the uncertainty in the measured value of $g(x_A)$ was estimated to be $\leq$ 0.0077. These results support the assumptions made in deriving Eq.7.12.

Fig.7.9 shows the variation of g(A) and $\hat{g}$ with Φ_o/Φ_{min}, where the curve for $\hat{g}$ is based on Eq.7.6a and the values of $g(x_A)$ are the same as those shown in Fig.7.9. For $\Phi_o = 0$, $\hat{g} = \hat{g}*$, and it follows from Eq.7.6b (with $\Gamma_c = 1.32$) that $\hat{g}* = 0.546$.

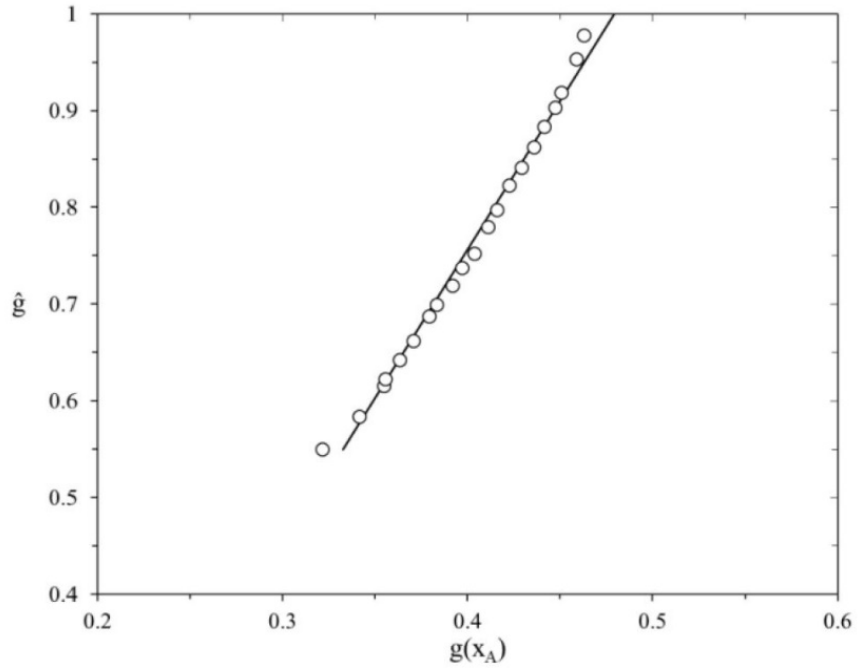

Figure 7.8 Variation of $\hat{g}$ with measured values of $g(x_A)$. (Solid line shows linear regression of the data.) (Owen *et al.*, 2014)

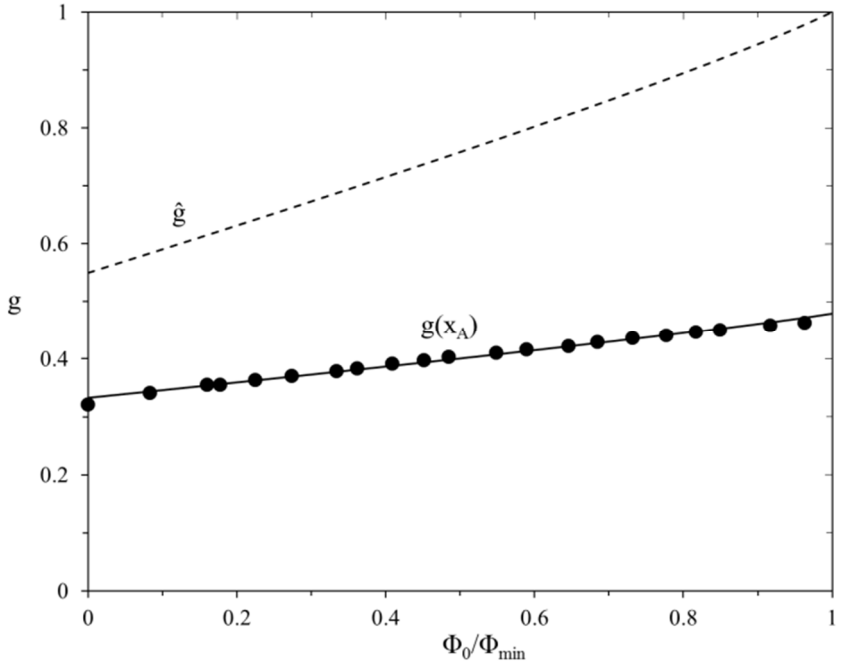

Figure 7.9 Variation of $\hat{g}$ and g (x_A) with Φ_o/Φ_{min} (Owen *et al.*, 2014)

Fig.7.10 shows the variation of sealing effectiveness with Φ_o/Φ_{min}. The values of ε_p were calculated from Eq.7.13, using the values of B and C given above and the measured values of $g(x_A)$ shown in Fig.7.9. The values of ε_c were obtained from the concentration measurements, and Eq.2.29 was used to produce the effectiveness curve. The standard deviation between the calculated values of ε_p and the effectiveness curve was 0.017, and that between the measured values of ε_c and the curve was 0.019. (Note: these standard deviations are based on the differences between the individual calculated or measured values and the theoretical curve and not on the uncertainties calculated using the method described in section 7.5.)

These results give confidence in the theoretical model used in this paper.

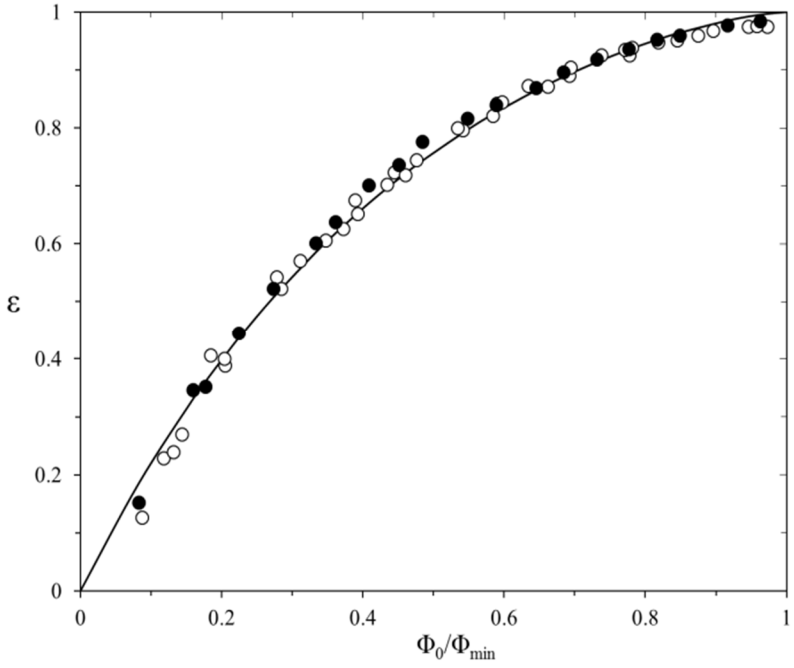

Figure 7.10 Variation of sealing effectiveness with Φ_o/Φ_{min}. (Solid symbols denote values of ε_p from pressure measurements; open symbols denote values of ε_c from concentration measurements; solid curve is based on the effectiveness equation.) (Owen *et al.*, 2014)

The values of $C_{d,e}$ and $C_{d,i}$ determined from the measurements of ΔC_p at location A are 0.177 and 0.239 respectively. Using Eq.7.20 with B = 3.07, the values of $C_{d,e}$ and $C_{d,i}$ at the sweet spot are 0.310 and 0.419, respectively.

It is shown below how the model could be used by the gas turbine designer.

7.4 Extrapolation of effectiveness data from rig to gas turbine

In principle, orifice models provide a simple method of extrapolating the experimentally-measured effectiveness of a particular rim seal to a turbine with similar seal geometry. However, the conditions – particularly the Mach number and temperatures – in gas turbines are usually significantly different from those in the experimental rig. Also, the design codes used for internal air systems usually estimate ingress from pressures rather than from the concentration measurements made in most rigs. Care and attention regarding mathematical consistency are needed if orifice models are used to extrapolate rig measurements to gas turbine conditions. In particular, the 'correct' pressures must be used in the gas turbine, and the theoretical model discussed above was developed to ensure that consistency.

The Mach number effect was considered by Teuber *et al.* (2012), who showed, theoretically and computationally for the Bath one-stage rig, that the magnitude of ΔC_p increases as the Mach number increases. They showed that by correcting ΔC_p and assuming that the discharge coefficients are unaffected by Mach number, the sealing effectiveness , ε_c , determined by concentration measurements in an experimental rig at one Mach number, could be used to compute the effectiveness in a gas turbine at another Mach number. Their suggested the correction for Φ_{min} is:

$$\frac{\Phi_{min,engine}}{\Phi_{min,rig}} = \left(\frac{\Delta C_{p,engine}}{\Delta C_{p,rig}} \right)^{1/2} \tag{7.21}$$

where the ratio on the RHS of Eq.7.21 is determined from the ratio of the Mach numbers. However, unless the location of the sweet spot is known, the effectiveness cannot be related to pressure differences in the gas turbine, which makes the method of limited use to designers.

The location of the sweet spot in the gas turbine has to be determined using CFD, as described in subsection 7.2.4. In the gas turbine, unsteady CFD would be required to account for the turbine blades, which were not included in the steady CFD used in this chapter. This is because symmetrical blades used in the test rig have little effect on ingress at the design condition (Scobie *et al.*, 2014). The mean value of $_{\hat{x}}$ could then be determined from computations made for a range of sealing flow rates. An

approximate value could be found by computing $\hat{x}$ only for the case where the sealing flow rate is zero. For this case, where $\hat{g}=\hat{g}*$, as shown in subsection 7.2.1:

$$\hat{g}* = \frac{p_1* - p_{2,min}*(\hat{x})}{\Delta p*(\hat{x})} = \frac{\Gamma_c^{2/3}}{1+\Gamma_c^{2/3}} \tag{7.22}$$

and Γ_c is known from the concentration measurements in the rig. The value of p_1* could be evaluated at any convenient radial location in the wheel-space of the gas turbine, bearing in mind the qualifications given in section 7.3. The approximate value of $\hat{x}$ could then be found by computing $p_{2,min}*(x)$ and $\Delta p*(x)$ for different values of x, on the vane platform upstream of the seal clearance, until Eq.7.22 is satisfied.

In the proposed method, it is assumed that the discharge coefficients at the sweet spot for the rim seal in the gas turbine are equal to those at that in the rig. As $C_{d,e,gas\ turbine} = C_{d,e,rig} = C_{d,e}$, it follows that:

$$\Phi_{min,engine} = \frac{2}{3} C_{d,e} \Delta C_{p,engine}^{1/2} \tag{7.23}$$

where $\Delta C_{p,gas\ turbine}$ is the time-average value determined at the sweet spot in the gas turbine. As proposed by Teuber *et al.*(2012), this relationship is assumed to apply for all Mach numbers.

For the case where $\Phi_o < \Phi_{min}$, it is necessary to calculate $\hat{g}$ for any flow rate by:

$$\hat{g} = \frac{p_1 - p_{2,min}(\hat{x})}{\Delta p(\hat{x})} \tag{7.24}$$

Knowing $\hat{g}$, the sealing effectiveness can be calculated from Eq.7.25, where:

$$\hat{\varepsilon}_p = 1 - \Gamma_c \left[\frac{1-\hat{g}}{\hat{g}} \right]^{3/2} \tag{7.25}$$

The uncertainties in $\hat{\varepsilon}_p$ depend on the uncertainties in $\hat{g}$, which, as shown in section 7.5, depend on the uncertainties in the pressures determined for the gas turbine.

The above method of extrapolation requires validation by experiments and CFD at gas turbine-representative Mach numbers and density ratios that are not achievable in the existing Bath rig. Experimental rigs like the large HGIR rig described by Palafox *et al.* (2013) and the Sussex rig used by Gentilhomme *et al.* (2002) are more suitable for this purpose. Also, a new 1.5 stage rig featuring realistic turbine blade and vane geometries, is under construction at the University of Bath. It is hoped that rigs like these will be able to provide the data necessary to test theoretical models thoroughly that could then be used with confidence by gas turbine designers.

7.5 Uncertainty in pressure measurements

From Eq.7.2:

$$g = \frac{p_1 - p_{2,min}}{p_{2,max} - p_{2,min}} = \frac{X}{Y} \tag{7.26}$$

where $X = p_1 - p_{2,min}$ and $Y = p_{2,max} - p_{2,min}$ and hence:

$$dg = \frac{\partial g}{\partial X} dX + \frac{\partial g}{\partial Y} dY \tag{7.27}$$

$$= \frac{dX}{Y} - X \frac{dY}{Y^2} \tag{7.28}$$

The magnitude of the relative uncertainty in g is then bounded by:

$$\left|\frac{\delta_g}{g}\right| \leq \left|\frac{\delta_X}{X}\right| + \left|\frac{\delta_Y}{Y}\right| \tag{7.29}$$

where $|\delta_X| = |\delta_{p1}| + |\delta_{p2,min}|$ and $|\delta_Y| = |\delta_{p2,max}| + |\delta_{p2,min}|$, and $\delta_g, \delta_{p1}, \delta_{p2,min}, \delta_{p2,max}$ are the uncertainties in $g, p_1, p_{2,min}, p_{2,max}$, respectively, and hence:

$$\frac{|\delta_g|}{g} \leq \left\{ \frac{|\delta_{p1}| + |\delta_{p2,min}|}{p_1 - p_{2,min}} + \frac{|\delta_{p2,max}| + |\delta_{p2,min}|}{p_{2,max} - p_{2,min}} \right\} \tag{7.30}$$

When the uncertainty is a percentage of the full-scale range, which was the case in the experiments, then $|\delta_{p1}| = |\delta_{p2,min}| = |\delta_{p2,max}| = \delta$, say, and Eq.(7.30) simplifies to:

$$\frac{|\delta_g|}{g} \le \frac{2\delta}{p_{2,max} - p_{2,min}}\left(1 + g^{-1}\right) \tag{7.31}$$

or

$$|\delta_g| \le \frac{2\delta}{p_{2,max} - p_{2,min}}(1 + g) \tag{7.32}$$

The Druck PDCR 22 Scanivalve pressure transducers used in the experiments had a stated uncertainty of ±0.06% (Best Straight Line) across a range of 70 mbar, which implies that δ = 0.042 mbar. In the experiments, $p_{2,max}$ - $p_{2,min} \approx$ 16.3 mbar, and $g(x_A) < 0.5$, so from Eq.7.32, $|\delta_g| \le 0.0077$.

7.6 Summary

A theoretical model which could be used to determine the effectiveness of using pressure measurements (ε_p) in a gas turbine was developed by Professor J. M. Owen. The model was developed with the aim of finding a hypothetical location on the vane platform, the 'sweet spot', where the pressure should be measured to ensure that $\varepsilon_p = \varepsilon_c$. For this model, this sweet spot was assumed to be invariant with Φ_0.

Concentration and pressure measurements were made for a radial clearance seal on the Bath single-stage turbine rig and a non-dimensional pressure difference across the seal (referred to as $g(x_A)$) was determined based on the measurements made at an arbitrary position (location A) in the annulus. It was shown that the non-dimensional pressure difference determined at the sweet spot and that measured at the location A has linear relationship for $0 < \Phi_0/\Phi_{min} < 1$. In addition, the variation of ε_p with sealing effectiveness was determined using the theoretical pressure model with two constants determined by linear regression of $\hat{g}$ versus $g(x_A)$ and this variation showed good agreement with the measured values of concentration effectiveness, ε_c. It was also shown by steady 3-D CFD that location of the sweet-spot is virtually invariant with the sealing flow rate and is very close to the upstream edge of the seal clearance. The

location of the sweet spot for the real gas turbine seal could be determined with the values of the discharge coefficients for ingress and egress using CFD. It was shown, in principle, how the theoretical model developed here could be used to determine the effectiveness of the rim seals in an engine.

Chapter 8: Conclusions

The aim of this PhD research was to investigate the effect of hot gas ingress on the rotor disc of a turbine stage by determining the adiabatic rotor effectiveness for a series of generic rim seal geometries in the Bath one-stage ingress test facility. It was anticipated that the work would provide fundamental insights into the ingress problem that would help gas turbine design engineers improve rim seal design. In order to achieve this aim, a non-intrusive temperature measurement technique and a numerical analysis method were developed for transient heat transfer experiments. The main conclusions of this PhD thesis and possible future work are presented below.

8.1 Development of the infrared temperature measurement technique

A non-intrusive temperature measurement technique based on infrared thermography, which can be used under the conditions where abrupt ambient temperature change is expected, has been developed to measure the temperature of the rotor disc surface during a transient heat transfer experiment. Taking into account the repeatability and accuracy of infrared sensors, the Melexis MLX90614ESF-DCI infrared sensor that is capable of making up to 10 measurements per second (10Hz), was selected for the application. The sensor is 9mm in diameter, with 6.7mm and 5.9mm spot size diameter at 20mm and 10mm distance from the target, respectively.

As abrupt ambient temperature change, to which the infrared temperature sensor is exposed, increases uncertainties in the temperature measurement. Two solutions to minimise the adverse effect of such change were suggested: the use of a material with high thermal mass to increase thermal inertia and the use of a cooling jacket around the sensor to cool it down. After a series of tests, a method with high thermal mass was chosen, which involves putting a large thermal mass (e.g. copper) around the sensor housing and insulating it with a good thermal insulator (e.g. Rohacell). The infrared sensor was pre-heated using a thin film heater with a feedback temperature controller so as to reduce the temperature difference between the sensor

and the heated air in the wheel-space, which in turn, reduced the thermal gradient in the sensor assembly.

A new calibration facility, which was specifically designed to conduct the calibration of the new infrared temperature sensors under controlled conditions, was built. The infrared temperature sensors were calibrated in the target temperature range from approximately 15°C to 55°C under steady state conditions. The accuracy of the transient temperature measurements was checked by simulating an abrupt ambient temperature change during the tests. The sensor temperature was carefully kept constant within ±0.3°C of 35°C and the infrared sensors were calibrated to have ±0.2°C accuracy with 95% uncertainty level.

8.2 Development of a numerical analysis method for heat transfer experiments in Bath one-stage ingress rig

The semi-infinite solution of Fourier's equation, which is widely used for analysing data from transient experiments using TLC temperature measurement, was compared to the so-called 'quenching solution' (a solution of 1-D Fourier equation which is appropriate for tests with solids of symmetrical section). The range of Fo for which semi-infinite solutions are acceptably accurate was determined from the comparison and it was shown that the commonly accepted validity criterion for the semi-infinite solution (Schultz, 1973), $Fo<0.1$, is overly restrictive. In addition, the effect of uncertainty in temperature measurement on the calculation of h and T_{ad} was also discussed and it was concluded that accurate estimates of T_{ad} require the measured surface temperature to be as close to T_{ad} as possible, regardless of the analysis method used.

A numerical solution of the 1-D Fourier equation for a single-layer substrate was developed based on the Crank-Nicolson method to determine h and T_{ad}. The rig-representative initial and boundary conditions were used for the solution including the full temperature history, measured by the new infrared sensor. The developed numerical solution was then validated against the analytical solution and showed very good agreement. In addition, the effects of uncertainties in temperature measurement on the computation of T_{ad} and h were also investigated and a numerical

solution for temperature data with random noise was developed based on Owen (1979). With the numerical solution, four different levels of uncertainty in temperature measurement were tested and it was found that the effect of noisy temperature data can be virtually eliminated with this solution.

A two-layer composite substrate comprising one layer of Rohacell foam and the other of polycarbonate was suggested. In order to determine h and T_{ad} for transient heat transfer experiments with a composite substrate, a solution to Fourier's 1-D heat equation based on the Crank-Nicolson method was developed. The rig-representative initial and boundary conditions were used for the solution and it was validated against the analytical solution for transient heat conduction in a one-dimensional composite layer and showed a very good agreement.

A series of numerical experiments to evaluate the feasibility of an accurate estimation of full temperature history based on piecewise temperature data (measured by a mixture of TLCs) and to compute h and T_{ad} with the temperature data, were carried out. It was suggested that the full temperature history could be estimated from the piecewise temperature data by applying a least squares cubic-spline fit to a $\ln(T_s)$ vs. $\ln(t)$ plot. The numerical simulations showed that it is possible to estimate h and T_{ad} from a transient heat transfer experiment accurately based on the piecewise temperature data acquired with a mixture of TLCs. It was also shown that the uncertainty levels of the calculated h and T_{ad} are considerably affected by the bandwidth and activation temperature ranges of the TLCs.

8.3 Rotor temperature and heat transfer measurements

Transient heat transfer experiments using infrared temperature measurement sensors were carried out to investigate the effect of ingress on the rotor disc. In order to determine sealing effectiveness based on the heat transfer experiments, an adiabatic effectiveness was defined and Fourier's 1-D heat equation was solved numerically with the appropriate initial and boundary conditions find T_{ad} and h. These experiments were carried out for four generic rim seal geometries, including two single and two double rim seals. The variation of adiabatic effectiveness with sealing flow rate was determined at two infrared temperature measurement locations.

Gas concentration of a CO_2 tracer gas was also measured for the four rim seal geometries and the variation of concentration effectiveness with sealing flow rate was determined. All experiments were conducted at the design operating points. The adiabatic effectiveness measured on the rotor and concentration effectiveness calculated on the stator were then compared to demonstrate the thermal buffering effect, where the effect of ingress on the rotor is less than that measured on the stator, i.e. the boundary layer on the rotor disc protects the disc from ingestion.

It was shown that the sealing effectiveness on the rotor was significantly higher than the equivalent stator effectiveness for all four generic rim seals tested. The theoretical curves for the adiabatic effectiveness versus sealing flow rate data for each measurement location were generated by the thermal buffering model developed by Mear *et al.* (2015) and the curves generally showed a good agreement with the measured experimental data. For the two double-clearance rim seals, the adiabatic effectiveness of the inner wheel-space was significantly higher than that of the outer, i.e. the most ingested mainstream flow is confined in the outer wheel-space and only a small amount penetrated into the inner wheel-space.

8.4 Effectiveness from pressure measurements

A theoretical model, which could be used to determine the effectiveness of using pressure measurements (ε_p) in a gas turbine, was developed by Professor J. M. Owen. The model was developed with the aim of finding a hypothetical location on the vane platform, the 'sweet spot', where the pressure should be measured to ensure that $\varepsilon_p = \varepsilon_c$. For this model, this sweet spot was assumed to be invariant with Φ_0.

Concentration and pressure measurements were made for a radial clearance seal on the Bath single-stage turbine rig and a non-dimensional pressure difference across the seal (referred to as $g(x_A)$) was determined based on the measurements made at an arbitrary position (location A) in the annulus. It was shown that the non-dimensional pressure difference determined at the sweet spot and that measured at the location A has linear relationship for $0<\Phi_0/\Phi_{min}<1$. In addition, the variation of ε_p with sealing effectiveness was determined using the theoretical pressure model with two constants determined by linear regression of $\hat{g}$ versus $g(x_A)$ and this variation showed good

agreement with the measured values of concentration effectiveness, ε_c. It was also shown by steady 3-D CFD that location of the sweet-spot is virtually invariant with the sealing flow rate and is very close to the upstream edge of the seal clearance. The location of the sweet spot for the real gas turbine seal could be determined with the values of the discharge coefficients for ingress and egress using CFD. It was shown, in principle, how the theoretical model developed here could be used to determine the effectiveness of the rim seals in an engine.

8.5 Future work

The results presented in this thesis have broadly widened the understanding of the effect of ingress on the rotor disc in a turbine stage, however such research could be further extended in a number of ways.

- Measurements of adiabatic sealing effectiveness on a rotor disc surface of a downstream wheel-space as well as an upstream one. This research will be carried out in the Bath 1.5-stage ingress test facility that has recently been built and commissioned. Such an endeavour would allow the effects of ingress on the rotor for upstream and downstream wheel-space to be compared. If the research were successfully carried out, it would provide the first rotor effectiveness measurements data in the downstream wheel-space, as far as this researcher is aware.

- The Bath one-stage ingress test facility, on which this research was carried out, was originally designed for heat transfer experiments with the TLC temperature measurement technique. However, only two infrared sensors could be used for temperature measurements of the rotor disc without extensive modification of the existing test facility, i.e. variations of adiabatic effectiveness with sealing flow could only be measured at two radial locations, one in outer wheel-space and the other in inner. At the time of writing this thesis, major refurbishment work was being carried out on the Bath one-stage test facility, which will allow for heat transfer experiments under better controlled conditions, for it has infrared temperature measurements at nine radial locations. In particular, this will mean that the

radial variation of adiabatic effectiveness can be determined with better spacial resolution.

- As the research presented in this thesis was concentrated on determining adiabatic effectiveness, the heat transfer coefficient on the rotor disc has not been closely investigated. It would also be interesting to study the effects of ingress on this for both upstream and downstream wheel.

- Although the variation of adiabatic effectiveness with sealing flow rate under off-design operational conditions was investigated by Pountney *et al.* (2013), it was restricted to an axial clearance-seal with polycarbonate inserts. Hence, it would be interesting to investigate the effect of ingress on the rotor disc under off-design conditions for more generic rim seal geometries, such as radial, double axial and double radial clearance seals. Such experiments could be carried out in both the Bath one-stage and 1.5-stage ingress test facilities.

References

Abe, T., Kikuchi, J. and Takeuchi, H., 1979, "An Investigation of turbine disk cooling (Experimental investigation and observation of hot gas flow into a wheel space)," *CIMAG - 13th International Congress on Combustion Engines.*

Astarita, T. and Cardone, G., 2008, "Convective heat transfer on a rotating disk with a centred impinging round jet," *Int. J. Heat Mass Tran.*, 51(7-8):1562-1572

Batchelor, G. K., 1951, "Note on the class of solutions of the Navier-Stokes equations representing steady rotationally symmetric flow," *Quarterly Journal of Applied Mathematics*, 4 (1), pp. 29-41.

Bakken, L.E., Jordal, K., Syverud, E. and Veer, T., 2004, "Centenary of the first gas turbine to give net power output: a tribute to Agidius Elling," *ASME Turbo Expo 2004. ASME*, pp. 83-88.

Balling, L., Termuehlen, H. and Baumgartner, R., 2002, "40 years of combined cycle power plants," 2002 *Internaional Joint Power Generation Conference, ASME*, pp537-548.

Barry, T., Fuller, G., Hayatleh, K., and Lidgey, J., 2011, "Self-calibrating infrared thermometer for low-temperature measurement," *IEEE Instru. Meas.*, 60, 2047-2052

Bayley, F. J. and Owen, J. M., 1970, "Fluid dynamics of a shrouded disk system with a radial outflow of coolant," *ASME J. Eng. P.*, 92(3), pp. 335-341.

Bohn, D. E., Decker, A., Ohlendorf, N. and Jakoby, R., 2006, "Influence of an axial and radial rim seal geometry on hot gas ingestion into the upstream cavity of a 1.5-stage turbine," ASME Paper GT2006-90453.

Bohn, D. E., Johann, E. and Kruger, U., 1995, “Experimental and numerical investigations of aerodynamic aspects of hot gas ingestion in rotor-stator systems with superimposed cooling mass flow,” ASME Paper 95-GT-143.

Bohn, D. E. and Wolff, M., 2003, “Improved formulation to determine minimum sealing flow - $C_{w,\ min}$ – for different sealing configurations,” ASME Paper GT2003-38465.

Boutarfa, R., and Harmand, S., 2005, “Local convective heat trasnfer for laminar and turbulent flow in a rotor-stator system,” *Exp. Fluids* 38(2):209-221

Brayton, G. B., 1872, *Improvement in gas-engines*. Google Patents.

Brooks, F. J., n.d., *GE Gas turbine performance characteristics.* GE Power Systems.

BS EN ISO 5167- 3:2003. *Measurement of fluid flow by means of pressure differential devices inserted in circular cross-section conduits running full. Nozzles and Venturi nozzles.* BSI.

Bunker, R. S., Metzger, D. E. and Wittig, S., 1992a, "Local heat transfer in turbine disk cavities: Part I- rotor and stator cooling with hub injection of coolant," *ASME J. Turbomach.*, 114(1), pp. 211-220.

Bunker, R. S., Metzger, D. E. and Wittig, S., 1992b, "Local heat transfer in turbine disk cavities: Part II- rotor cooling with radial location injection of coolant," *ASME J. Turbomach.*, 114(1), pp. 221-228.

Cardone, G., Astarita, T., and Carlomagno, GM., 1996, “Infrared heat trasnfer measurements on a rotating disk,” *Opt. Diagn. Eng.* 1(2):1-7

Cardone, G., Astarita, T., and Carlomagno, GM., 1997, “Heat trasnfser measruements on a rotating disk,” *Int. J. Rotat. Mach.* 3:1-9

Carlomagno, G. and Cardone, G., 2010, "Infrared thermography for convective heat transfer measurements," *Exp. Fluids*, 49(6), pp. 1187-1218.

Cengel, Y. A., Boles, M. A., and Kanoglu, M., 2011, *Thermodynamics : an engineering approach*, London: McGraw-Hill.

Chatfield, C., 1983, *Statistics for technology : a course in applied statistics*, London: Chapman and Hall/CRC.

Chen, J.-X., Gan, X. and Owen, J. M., 1996, "Heat transfer in an air-cooled rotor-stator system," *ASME J. Turbomach.*, 118(3), pp. 444-451.

Chew, J. W., Green, T. and Turner, A. B., 1994, "Rim sealing of rotor-stator wheelspaces in the presence of external flow," ASME Paper 94-GT-126.

Childs, P. R. N., 2001. *Practical temperature measurement*, Oxford: Butterworth-Heinemann.

Childs, P. R. N., 2011, *Rotating flow*, Oxford: Butterworth-Heinemann.

Crank, J., and Nicolson, P.A., 1947, "Practical method for numerical evaluation of solutions of partial differential equations of the heat-conduction type," *Mathematical Proceedings of the Cambridge Philosophical Society*, Cambridge Univ Press, 50-67.

Cumpsty, N., 2003, *Jet propulsion*, 2nd ed. Cambridge: Cambridge University Press

Dadkhah, S., Turner, A. B. and Chew, J. W., 1992, "Performance of radial clearance rim seals in upstream and downstream rotor-stator wheelspaces," *ASME J. Turbomach.*, 114(2), pp. 439-445.

Daily, J. W. and Nece, R. E., 1960, "Chamber dimension effects on induced flow and frictional resistance of enclosed rotating disks," *J. Basic Eng.-Trans. ASME*, 82(1), pp. 217-230.

Daily, J. W., Ernst, W. D. and Asbedian, V. V., 1964, "Enclosed rotating disks with superposed throughflow," MIT Hydrodynamics Lab. Rep. 64.

De Monte, F., 2000, “Transient heat conduction in one-dimensional composite slab. A ‘natural’ analytic approach,”, *Int. J. Heat Mass Transfer*, 43, 3607-3619.

Dorfman, L.A., 1963, *Hydrodynamic resistance and heat loss from rotating solids*, Edinburgh and London: Oliver and Boyd.

ESDU. 07004, 2007, *Flow in rotating components—discs, cylinders and cavities. ESDU fluid mechanics, internal flow series, volume 4c (flow in rotating machinery)* (Cited in Childs, 2011).

Elkins, C.J., Fessler, J., and Eaton, J.K., 2001, “A novel mini calibrator for thermochromic liquid crystals,” *J. Heat Transf.-Trans. ASME*, 123, 604-607.

Exergen, 2012, Available from: http://www.exergen.com//industrial/index.htm [Accessed 18.06 2012].

FLIR, n.d., SC6000 MWIR series datasheet.

Gentilhomme, O., Hills, N. J., Turner, A. B., and Chew, J.W., 2002, “Measurement and Analysis of Ingestion through a Rim Seal,” *ASME J. Turbomach.*, 125. pp. 505-512.

Graber, D. J., Daniels, W. A. and Johnson, B. V., 1987, “Disc pumping test, final report,” Air Force Wright Aeronautical Laboratories, Report No. AFWAL-TR-87-2050.

Graf, A., Arndt, M., Sauer, M., and Gerlach, G., 2007, “Review of micromachined thermopiles for infrared detection,”, *Meas. Sci. Technol.*, 18, R59.

Green, T. and Turner, A. B., 1994, “Ingestion into the upstream wheelspace of an axial turbine stage,” *ASME J. Turbomach.*, 116(2), pp. 327-332.

Hamabe, K. and Ishida, K., 1992, “Rim seal experiments and analysis of a rotor-stator system with nonaxisymmetric nain flow,” ASME Paper 92-GT-160.

Holman, J. P., 2010, *Heat transfer*, 10th ed. Boston: McGraw-Hill.

HüNecke, K., 1997, *Jet engines : fundamentals of theory, design, and operation*, Osceola, WI, USA: Motorbooks International.

Incropera, F. P. 2007. *Fundamentals of heat and mass transfer*, Chichester : John Wiley.

Ireland, P. T., Gillespie, D. R. H. and Wang, Z., 1996, “Heater element,” European Patent No. 0847679 B1.

ISO 5167-2: 2003. *Measurement of fluid flow by means of pressure differential devices inserted in circular-cross section conduits running full-Part*, 2. ISO.

Johnson, B. V., Wang, C. Z. and Roy, R. P., 2008, “A rim seal orifice model with two Cd's and effects of swirl in seals,” ASME Paper GT2008-50650.

Kakade, V. U., Lock, G. D., Wilson, M., Owen, J. M. and Mayhew, J. E., 2009, "Accurate heat transfer measurements using thermochromic liquid crystal. Part 2: Application to a rotating disc," *Int. J. Heat Fluid Flow*, 30(5), pp. 950-959.

Karabay, H., Wilson, M. and Owen, J. M., 2001, "Predictions of effect of swirl on flow and heat transfer in a rotating cavity," *Int. J. Heat Fluid Flow*, 22(2), pp. 143-155.

Khilnani, V. I. and Bhavnani, S. H., 2001, “Sealing of gas turbine disk cavities operating in the presence of mainstream external flow,” *Exp. Therm. Fluid. Sci.*, 25(3-4), pp. 163-173.

Langston, L. S., 2011, Powering ahead, *Mech. Eng.*, 30-33.

Langston, L. S. and Opdyke, G., 1997, Introduction to gas turbines for non-engineers. *Global Gas Turbine News,* 37.

Lock, G. D., Yan, Y., Newton, P. J., Wilson, M. and Owen, J. M., 2005, "Heat transfer measurements using liquid crystals in a preswirl rotating-disk system," *ASME J. Eng. Gas Turb. Power*, 127(2), pp. 375-382.

Long, C., 1999, *Essential heat transfer*, Harlow: Longman.

Maldague, X. P. V., 2001, *Theory and practice of infrared technology for nondestructive testing*, New York: Wiley.

Mear, L. I., Cho, G. , Owen, J. M., and Lock, G. D., 2015, "Effect of ingress on sealing effectiveness of turbine discs - part 2: Theoretical model of adiabatic effectiveness," Manuscript is submitted for publication. ASME Paper GT2015-42326.

Meher-Homji, C. B., 1997., "The development of the Junkers Jumo 004B : The world's first production turbojet," *ASME J. Eng. Gas Turbines Power*, 119**,** 783-789.

Meher-Homji, C. B., 1998, "The development of the Whittle turbojet," *ASME J. Eng. Gas Turb. Power*, 120(2), pp. 249-256.

Meher-Homji, C. B., 2000, "The historical evolution of turbomachinery,", *Proceedings of the 29th Turbomachinery Symposium, Houston, Texas,* 281-310.

Melexis. 2012. Available: http://www.melexis.com/ [Accessed 18.06 2012].

Melexis, n.d., MLX90614 family, single and dual zone infra red thermometer in TO-39.

Metzger, D. E., Bunker, R. S. and Bosch, G., 1991, "Transient liquid crystal measurement of local heat transfer on a rotating disk with jet impingement," *ASME J. Turbomach.*, 113(1), pp. 52-59.

MHI., 2014., *J-series gas turbine* [Online]. Available from: http://www.mhi.co.jp/en/products/detail/j_series_gas_turbine.html: Mitsubishi Heavy Industry. [Accessed 14 April 2014].

Mirzamoghadam, A.V., Heitland, G., Morris, M.C., Smoke, J., Malak, M. and Howe, J., 2008, "3D CFD ingestion evaluation of a high pressure turbine rim seal disk cavity" ASME paper GT2008-50531.

Mori, M., Novak, L., Sekavcnik, M., 2007, "Measurements on rotating blades using IR thermography," *Exp. Thermal Fluid Sci.*, 32(2):387-396

Optris., 2012, Available: http://www.optris.com/ [Accessed 18.06 2012].

Owen, J. M., 1979, "Computation of heat-transfer coefficients from imperfect temperature-measurements," *J. Mech. Eng. Sci.*, 21**,** 323-334.

Owen, J. M. and Rogers, R. H., 1989, *Flow and heat transfer in rotating-disc systems, Volume 1: Rotor-stator systems*, Taunton: Research Studies Press Ltd.

Owen, J. M., Lock, G. D., Sangan, C. M., Tham ,K. M., Laurello, V.P., and Lee, C. P., 2011, "Finned seal assembly for gas turbine engines," USPTO patent application, 2012P08852US.

Owen, J. M., 2011a, "Prediction of ingestion through turbine rim seals. part I: rotationally induced ingress," *ASME J. Turbomach.*, 133(3), pp. 031005.

Owen, J. M., 2011b, "Prediction of ingestion through turbine rim seals. part II: externally induced and combined ingress," *ASME J. Turbomach.*, 133(3), pp. 031006.

Owen, J. M., Pountney, O. J., and Lock, G. D., 2012, "Prediction of ingress through turbine rim seals. part 2: combined ingress," *ASME J. Turbomach.*, 134, p.031013.

Owen, J. M., Zhou, K., Pountney, O. J., Wilson, M., and Lock, G. D., 2012a, "Prediction of ingress through turbine rim seals. Part 1: externally-induced ingress," *ASME J. Turbomach.*, 134, p.031012.

Owen, J.M., Wu, K., Scobie, J.A., Sangan, C.M., Cho, G. and Lock, G.D., 2014, "Use of pressure measurements to determine effectiveness of turbine rim seals," ASME Paper GTP-14-1417. To apprear in *ASME J. Eng. Gas Turbines Power*.

Palafox, P., Ding, Z., Bailey, J., Vanduser, T., Kirtley, K., Moore, K., and Chupp, R., 2013, "A new 1.5-stage turbine wheelspace hot gas ingestion rig (HGIR) – part I: experimental test vehicle, measurement capability and baseline results," ASME Paper GT2013-96020.

Pellé, J., and Harmand, S., 2006, "Study of heat trasnfser in a rotor-stator system: impinging jet and spacing influcence," *J. Enhanc. Heat* 13(4):291-307

Pellé, J., and Harmand, S., 2007a, "Heat trasnfer measurements in an opened rotor-stator system air-gap," *Exp. Thermal. Fluid. Sci.* 31(3):165-180

Pellé, J., and Harmand, S., 2007b, "Heat trasnfer sutdy in a discoidal system: the influence of an impinging jet and rotation," *Exp. Heat Trasnf.* 20(4):337-358

Pellé, J., and Harmand, S., 2008, "Heat trasnfer study in a discoidal system: the influcence of rotation and space between disks," *Int. J. Heat Mass Transf.* 51(13-14):3298-3308

Pellé, J., and Harmand, S., 2009, "Heat trasnfer study in a rotor-stator system air-gap with an axial inflow," *Appl. Therm. Eng.*, 29(8-9):1532-1543

Phadke, U. P. and Owen, J. M., 1983, "An investigation of ingress for an air-cooled shrouded rotating-disk system with radial clearance seals," *ASME J. Eng. Power,* 105(1), pp. 178-183.

Phadke, U. P. and Owen, J. M., 1988a, "Aerodynamic aspects of the sealing of gas-turbine rotor-stator systems. Part 1: the behavior of simple shrouded rotating disk systems in a quiescent environment," *Int. J. Heat Fluid Flow,* 9(2), pp. 98-105.

Phadke, U. P. and Owen, J. M., 1988b, "Aerodynamic aspects of the sealing of gas-turbine rotor-stator systems. part 2: the performance of seals in a quasiaxisymmetric external flow," *Int. J. Heat Fluid Flow,* 9(2), pp. 106-112.

Phadke, U. P. and Owen, J. M., 1988c, "Aerodynamic aspects of the sealing of gas-turbine rotor-stator systems. part 3: The effect of nonaxisymmetric external flow on seal performance," *Int. J. Heat Fluid Flow*, 9(2), pp. 113-117.

Plint, 1980, Pipe flow and nozzle apparatus and fan test set TE50, Berks, England: Plint & Partners LTD.

Pountney, O. J. 2012. "Modelling and measurement of sealing effectiveness and heat transfer in a rotor-stator system with ingress," University of Bath, PhD.

Pountney, O. J., Cho, G., Lock, G. D. and Owen, J. M., 2012b, "Solutions of Fourier's equation appropriate for experiments using thermochromic liquid crystal," *Int. J. Heat Mass Transfer*, 55(21-22), pp. 5908-5915.

Pountney, O. J., Sangan, C. M., Lock, G. D. and Owen, J. M., 2013, "Effect of ingestion on temperature of turbine discs," *ASME J. Turbomach.*, 135, p. 051010.

Rolls-Royce, 1996, *The jet engine*, 5th ed. Derby: Rolls-Royce plc.

Rolls-Royce, 2011, *Making the future*. Rolls Royce plc.

Roy, R. P., Xu, G. and Feng, J., 2001, "A study of convective heat transfer in a model rotor-stator disk cavity," *ASME J. Turbomach.*, 123(3), pp. 621-632.

Roy, R.P., Zhou, D.W., Ganesan, S., Wang, C.Z., Paolillo, R.E. and Johnson, B.V., 2007, "The flow field and main gas ingestion in a rotor-stator cavity," ASME Paper GT2007-27671.

Saini, A., 2012, "High-temperature materials increase efficiency of gas power plants." *Energy Quarterly.*

Sangan, C. M., 2011, "Measurement of ingress through gas turbine rim seals," University of Bath, PhD.

Sangan, C. M., Pountney, O. J., Zhou, K., Wilson, M., Owen, J. M., and Lock, G. D., 2013a, "Experimental measurements of ingestion through turbine rim seals. part 1: externally-induced ingress," *ASME J. Turbomach.*, 135, p.021012.

Sangan, C. M., Pountney, O. J., Zhou, K., Wilson, M., Owen, J. M., and Lock, G. D., 2013b, "Experimental measurements of ingestion through turbine rim seals. part 2: rotationally-induced ingress," *ASME J. Turbomach.*, 135, p.021013.

Sangan, C. M., Pountney, O. J., Scobie, J.A., Wilson, M., Owen, J. M., and Lock, G. D., 2013c, "Experimental measurements of ingestion through turbine rim seals. part 3: single and double seals," *ASME J. Turbomach.*, 135, p.051011.

Sangan, C. M., Lalwani, Y., Owen, J. M., and Lock, G. D., 2014, "Fluid dynamics of a gas turbine wheel-space with ingestion," *Proceedings of the Institution of Mechanical Engineers Part A: J. Power Energy*, 228 (5), pp. 508-524..

Saravanamuttoo, H. I. H., Rodgers, G. F. C., Cohen, H. and Straznicky, P. V., 2009, *Gas turbine theory*, 7th ed. London: Pearson Prentice Hall.

Schlichting, H., 1979, *Boundary-layer theory*, New York: McGraw-Hill.

Schultz, D. L. and Jones, T. V., 1973, "Heat transfer measurements in short duration hypersonic facilities," Agardograph No. 165.

Schüpbach, P., Rose, M., Gier, J., and Abhari, R., 2011, "Influence of rim seal purge flow on the performance of an endwall-profiled axial turbine," *J. Turbomach.,* 133**,** 021011.

Scobie, J. A., Sangan, C. M., Owen, J. M., Wilson, M., and Lock, G. D., 2014, "Experimental measurements of hot gas ingestion through turbine rim seals at off-design conditions," *Proceedings of the Institution of Mechanical Engineers, Part A: Journal of Power and Energy,* 228**,** 491-507.

Stewartson, K., 1953, "On the flow between two rotating coaxial discs," *Proceedings of the Cambridge Philosophical Society*, 49(1), pp. 333-341.

Teuber, R., Wilson, M., Lock, G. D., Owen, J. M., Li, S., and Maltson, J. D., 2013, "Computational extrapolation of turbine sealing effectiveness from test rig to engine conditions," *Proc. IMechE Part A: J. Power and Energy*, 227, 167-178.

Tian, S., Zhang, Y., Su, W., 2014, "Effects of gas-ingestion through turbine rim seals on flow and heat,", ASME paper GT2014-26635.

Thomann, H., and Frisk, B., 1968, "Measruement of heat trasnfer with an infrared camera," *Int. J. Heat Mass Transfer* 11:819-826

Unger, D. and Herzog, H., 1998, Comparative study on energy R&D performance. Massachusetts Institute of Technology Energy Laboratory.

Van Der Linden, S, 1988, "The world's first industrial gas turbine set at Neuchatel (1939)" ASME.

Walsh, P. P. and Fletcher, P., 1998, *Gas turbine performance*, Oxford: Blackwell Science.

Wang, Z., Ireland, P. T., Jones, T. V. and Davenport, R., 1996, "A color image processing system for transient liquid crystal heat transfer experiments," *ASME J. Turbomach.*, 118(3), pp. 421-427.

White, F. M., 1994, *Fluid Mechanics*, 3rd ed. McGraw-Hill, INC.

Winskel, M., 2002, "When systems are overthrown - the dash for gas' in the British electricity supply industry," *Soc. Stud. Sci.*, 32**,** 563-598.

Yan, Y. Y. and Owen, J. M., 2002, "Uncertainties in transient heat transfer measurements with liquid crystal," *Int. J. Heat Fluid Flow*, 23(1), pp. 29-35.

Zhou, D.W., Roy, R.P., Wang, C.-Z., Glahn, J.A., 2011, "Main gas ingestion in a turbine stage for three rim cavity configurations," *ASME J. Turbomach.*, 133, p.031023.

Zhou, K., Wood, S. N., and Owen, J. M., 2013, "Statistical and theoretical models of ingestion through turbine rim seals," *ASME J. Turbomach.*, 135, p.021014.

Zuoan, L., 2012, "Numerical evaluations of transcendental equations for transient experiments," *Int. J. Hydrogen Energy*, 37**,** 8118-8122.

Appendix A. Thermal buffer ratio model

The following note, which forms the basis of Mear *et al.* (2015), was written by Owen and Mear in February 2014.

A.1. Flow structures

Consider an infinite disc rotating in a rotating core of fluid with a concentration c_∞ and a swirl ratio $\beta < 1$. At $x = x_a$, there is a superposed flow rate of fluid with a turbulent flow parameter of $\lambda_T = \lambda_{T,a}$ and a concentration c_a. For $x > x_a$, fluid from the rotating core will be entrained into the boundary layer on the disc, so that the concentration at the disc surface, c_o, will increase as x increases.

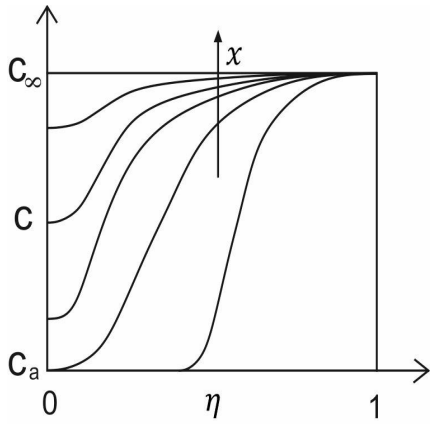

Figure A.1 Axial variation of concentration inside boundary layer on rotating disc as x increase.

Fig. A.1 shows a simplified diagram of the variation of concentration in the boundary layer on the disc as x increases; η is the normalised axial distance from the surface and $\eta = 1$ denotes the edge of the layer. It should be noted that as it takes time for the mass transfer from the core to the disc to occur, it is possible that, for small values of x, $c_o = c_a$.

However, it is not increasing x that determines the increase of $c = c_o$ at $\eta = 0$: it is the increasing ratio of the entrained to the superposed flow rate. *Consequently,* $c_o \rightarrow c_\infty$ as $\lambda_{T,e} / \lambda_{T,a} \rightarrow \infty$, *where* $\lambda_{T,e}$ *corresponds to the entrained flow rate.*

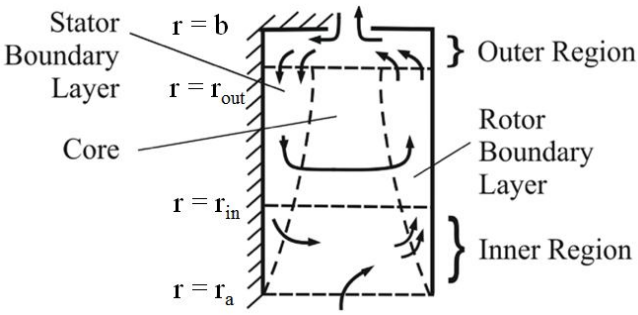

Figure A.2 Simplified flow structure for a rotor-stator system with superposed sealing flow and ingress

Fig. A.2 shows the flow structure in a rotor-stator system for the case where there is a *superposed radial flow, with swirl, together with ingress through the rim seal.* The gap ratio is large enough to ensure separate boundary layers on the two discs, both of which start at $r = a$ ($x = x_a$). Fluid moves radially outward in the boundary layer on the rotor and inward in the boundary layer on the stator.

Fluid moves axially across the rotating inviscid core from the boundary layer on the stator to that on the rotor. (*Note*: the entrainment by the boundary layer on the rotor decreases as the swirl ratio in the core increases. It should also be noted that there can be no axial gradients of the tangential and axial components of velocity in the core and that the radial component must be zero. *Importantly, all radial flow is confined to the boundary layers on the rotor and stator.*)

The superposed flow enters the system through an *inner region* which extends to $r = r_{in}$, where all the available flow has been entrained by the boundary layer on the rotor. In the *outer region* for $r_{out} < r < b$ fluid, with a flow rate equal to that of the superposed flow, leaves the system through the rim seal; the additional fluid entrained by the boundary layer on the rotor flows axially across the outer region to be entrained by the boundary layer on the stator. The inner and outer regions are the sources for the flow in the boundary layers on the rotor and stator respectively. Importantly, if the fluid is fully mixed in the outer region, the concentration of the fluid in the boundary layer on the stator will be equal to that in the adjacent core, and the concentration will be invariant with radius. *Consequently, for fully mixed flow,* $c_s = c_\infty$ *= constant, where* c_s *and* c_∞ *respectively denote the concentration at the surface of the stator and in the core.* (*Note*: if the superposed flow enters the inner region

without swirl then there can be no radial inflow on the stator in this region, and the concentration must therefore remain at the initial value of c_a throughout the inner region.)

A.2. Buffer ratio for rotor

The following definitions of effectiveness are used:

$$\varepsilon_\infty = \frac{c_{an} - c_\infty}{c_{an} - c_a},\ \varepsilon_o = \frac{c_{an} - c_o}{c_{an} - c_a},\ \varepsilon_o' = \frac{c_\infty - c_o}{c_\infty - c_a} \tag{A.1}$$

where the subscript *an* denotes the flow in an external annulus, radially-outward of the rim seal. It follows that

$$\varepsilon_o = \varepsilon_\infty + \varepsilon_o'(1 - \varepsilon_\infty) \tag{A.2}$$

If, as explained above, c_∞ is assumed to be equal to the concentration on the stator then it can be seen that ε_∞ is equivalent to ε_c, the sealing effectiveness obtained from measurements on the stator. Similarly, ε_o is the effectiveness that could, in principle, be measured on the rotor. It follows that ε_o' is equivalent to a buffer ratio: when ε_o' = 1, ε_o = 1 (complete buffering occurs); when ε_o' = 0, $\varepsilon_o = \varepsilon_\infty$ (no buffering).

From the above argument about an infinite disc, it is reasonable to assume that ε_o'= 1 when $\lambda_{T,e}$ = 0, which occurs when $\lambda_{T,a} > \lambda_{T,fd}$, the free-disc entrainment value for the entire rotor; and ε_o' = 0 when $\lambda_{T,a}$ = 0. A reasonable hypothesis is therefore

$$\varepsilon_o' = exp\left(-k\,\lambda_{T,e} / \lambda_{T,a}\right) \tag{A.3}$$

where *k* is an empirical constant.

This hypothesis could be tested using available theoretical, experimental or computational data for ε_o and ε_∞. Eq.A.2 can be written as

$$\varepsilon_o' = exp\left(-k\,\lambda_{T,e} / \lambda_{T,a}\right) = \frac{\varepsilon_o - \varepsilon_\infty}{1 - \varepsilon_\infty} \tag{A.4}$$

or

$$k = -\frac{\lambda_{T,a}}{\lambda_{T,e}} \ln\left(\frac{\varepsilon_o - \varepsilon_\infty}{1-\varepsilon_\infty}\right) \tag{A.5}$$

If values of $\lambda_{T,e}$, ε_o and ε_∞ are known for one value of $\lambda_{T,a}$ and several values of x then linear regression could be used to calculate k from Eq.A.5.

For given inlet conditions, $\lambda_{T,e}$ depends on $\lambda_{T,a}$, and so an alternative hypothesis is that

$$\varepsilon_o' = exp\left(-k' \lambda_{T,a}^{-1}\right) \tag{A.6}$$

where $k' \neq k$ is another empirical constant, which could be calculated from

$$k' = -\lambda_{T,a} \ln\left(\frac{\varepsilon_o - \varepsilon_\infty}{1-\varepsilon_\infty}\right) \tag{A.7}$$

As k' is invariant with x, this method could be used when values of ε_o and ε_∞ are known at one value of x and several values of $\lambda_{T,a}$.

It can be seen from Eqs.A.5 and A.7 that $k'=\lambda_{T,e}\, k$, which implies that k and k' cannot both be constant. As Eq.A.3 is physically more realistic than Eq.A.6, it is probable that k' cannot be independent of $\lambda_{T,a}$.

Now $\lambda_{T,e}$ is proportional to the flow rate down the stator, which increases as β increases. It will therefore be a maximum for the case of a closed system where $\lambda_{T,a} = 0$, and will be zero when $\lambda_{T,a} = \lambda_{T,fd}$. A reasonable hypothesis is that

$$\lambda_{T,e} = A\, exp\,(-B\,\lambda_{T,a}) \tag{A.8}$$

where A and B are empirical constants. Eq.A.4 then becomes

$$\varepsilon_o' = exp\left(-A'\, exp\,(-B\,\lambda_{T,a})/\lambda_{T,a}\right) \tag{A.9}$$

where $A'=kA$. Eq.A.9 can be expressed as

$$-\lambda_{T,a}\, ln\, \varepsilon_o' = A'\, exp\,(-B\,\lambda_{T,a}) \tag{A.10}$$

Hence

$$ln\left(-\lambda_{T,a}\, ln\, \varepsilon_o'\right) = ln\, A' - B\,\lambda_{T,a} \tag{A.11}$$

If $ln(-\lambda_{T,a}\, ln\varepsilon_o')$ is plotted versus $\lambda_{T,a}$ then linear regression can be used to find lnA' and B as the intercept and gradient respectively of the fitted curve.

A.3. Comparison with experiment

In order to find the empirical constants in Eq.A.11 experimental data must be used to find a correlation. In the paper by Pountney *et al.* (2013) measurements of adiabatic rotor effectiveness $\varepsilon_{ad}(\Phi_0)$ for an axial seal were made using a TLC technique, for a range of different sealing flow rates. It happened that $\Phi_0 \approx \lambda_{T,a}$, therefore the data from those experiments can be used as if $\varepsilon_{ad}(\Phi_0) = \varepsilon_o(\lambda_{T,a})$. Concentration measurements were also taken to determine the effectiveness on the stator. It is assumed that these measurements of ε_c are equivalent to ε_∞ in the above analysis.

The experimental measurements are for an axial seal with mitred inserts. The measurements of rotor and stator effectiveness are taken at radial locations x=0.898 and x=0.958 respectively.

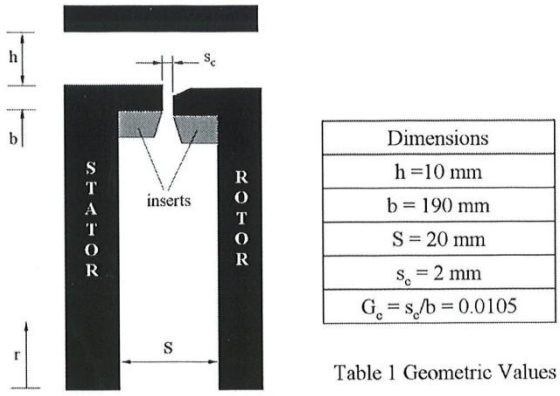

Dimensions
h =10 mm
b = 190 mm
S = 20 mm
s_c = 2 mm
$G_c = s_c/b = 0.0105$

Table 1 Geometric Values

Axial-clearance seal with polycarbonate inserts; key dimensions included

Figure A.3 Wheel-space geometry from Pountney *et al.* (2013)

Firstly values of ε_o' can be found from experimental measurements by setting $\varepsilon_o = \varepsilon_{ad}$ and $\varepsilon_\infty = \varepsilon_c$ within Eq.A.4:

$$\varepsilon_o' = \frac{\varepsilon_o - \varepsilon_\infty}{1-\varepsilon_\infty} = \frac{\varepsilon_{ad} - \varepsilon_c}{1-\varepsilon_c} \tag{A.12}$$

Note that as the stator measurements are not taken at the same $\lambda_{T,a}$ values as ε_{ad} the orifice model fit must be used to calculate the corresponding ε_c. This is done by solving the EI (or RI) effectiveness equation for ε_c:

$$\frac{\Phi_0}{\Phi_{minEI}} = \frac{\varepsilon}{\left[1+\Gamma_C^{-2/3}(1-\varepsilon)^{2/3}\right]^{3/2}}$$

$$\frac{\Phi_0}{\Phi_{minRI}} = \frac{\varepsilon}{\left[1+(1-\varepsilon)^{1/2}\right]\left[1+\Gamma_c^{-2}(1-\varepsilon)\right]^{1/2}}$$

given values of Φ_{min} and Γ_c gained from fitting the experimental concentration measurements.

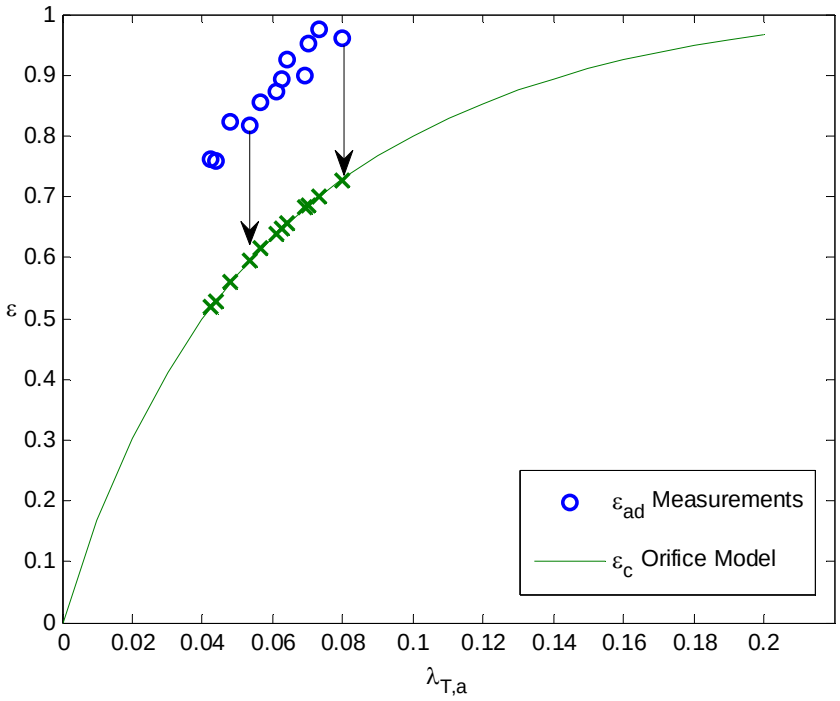

Figure A.4 Using the EI effectiveness equation to calculate stator effectiveness for each $\lambda_{T,a}$ where the rotor effectiveness if known, with Φ_{min}=0.275 and Γ_c=0.348 (On design case of Pountney *et al.* (2013))

Now using the calculated values of ε_o' the left hand side of Eq.A.11, now defined as y for convince, can be evaluated:

$$y = ln\left(-\lambda_{T,a} ln\left(\varepsilon_o'\right)\right) \tag{A.13}$$

The measurements from Pountney *et al.* (2013) were taken 'on design' – so for Re_w/Re_ϕ=0.538. More experimental measurements (for rotor and stator effectiveness) were taken for the same axial seal, but at Re_w/Re_ϕ = 0.326 – so 'overspeed'. Only the value of Re_w was changed. This rotor and stator effectiveness data can be used in the same way as described above (but with Φ_{min} = 0.118 and Γ_c = 0.687) to find more values of ε_o' and therefore more values of y. Linear regression can be used on all these points to find B = 38.5 and A' = 0.233, for the axial seal.

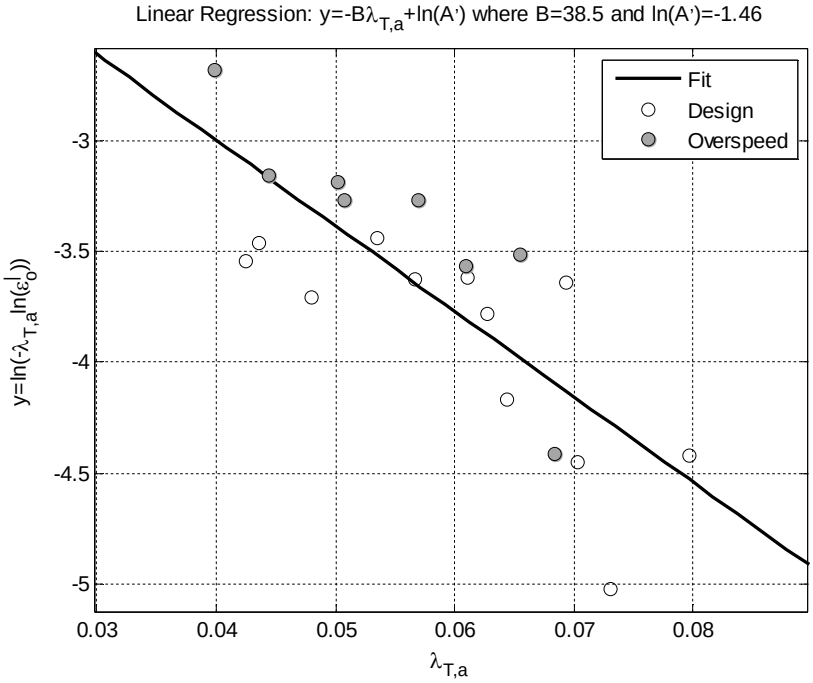

Figure A.5 Fitting the experimental values of the buffer ratio, for the axial heat transfer measurements of Pountney *et al.* (2013) , to find empirical constants *A'* and *B*.

Once these empirical constants have been found, a theoretical fit for the buffer ratio, ε_o', can be plotted for all $\lambda_{T,a}$ values using Eq.A.9. In order to generate a fit for the rotor effectiveness then values of ε_o need to be calculated from ε_o' using Eq.A.2. This requires that the stator effectiveness, ε_∞, is evaluated at many $\lambda_{T,a}$ values. This can be done by once again using the orifice model effectiveness EI equation.

It can be seen from Fig. A.6 that the fit with the empirical constants is in good agreement with the experimental measurements, despite the scattered linear regression shown in Fig. A.5. The shape is representative of an effectiveness curve. As the data are quite close together the same results can be shown on two separate figures for the two cases. The stator measurements fitted using the orifice model are also shown in the following figures. The on-design data is shown in Fig. A.7 and the overspeed in Fig. A.8.

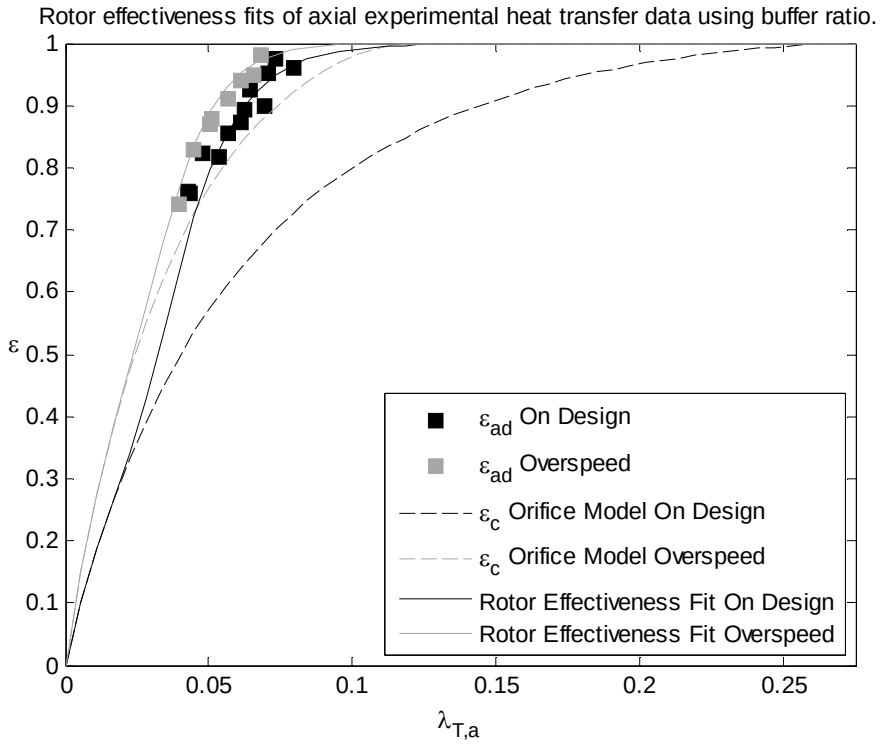

Figure A.6 Comparison between experimental rotor effectiveness measurements of Pountney *et al.*(2013) for the axial seal, fit from buffer ratio and stator effectiveness fit from orifice model (for the axial seal)

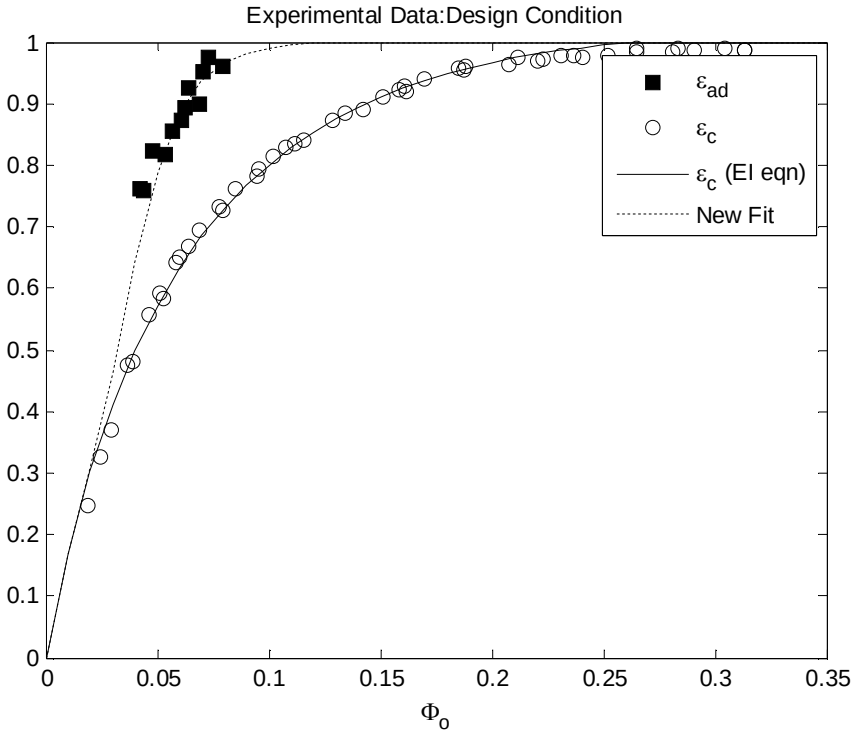

Figure A.7 Buffer Ratio for the design condition experimental results of Pountney *et al.* (2013)

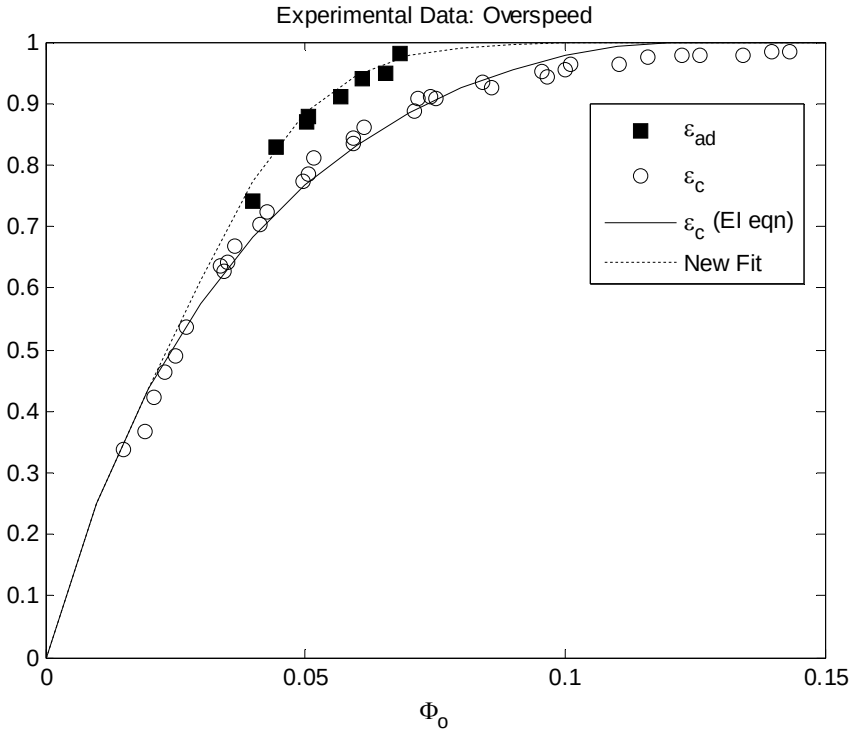

Figure A.8 Buffer Ratio for the overspeed condition experimental results of Pountney *et al.* (2013)